Interdisciplinary Applications of Automated Computational Workflows for XMM-Newton Cross-Calibration and Monte Carlo Simulations of eROSITA and a Breast PET Insert

Dissertation

der Mathematisch-Naturwissenschaftlichen Fakultät

der Eberhard Karls Universität Tübingen

zur Erlangung des Grades eines

Doktors der Naturwissenschaften

(Dr. rer. nat.)

vorgelegt von

Christian Manuel Pommranz

aus Reutlingen

Tübingen

2024

Gedruckt mit Genehmigung der Mathematisch-Naturwissenschaftlichen Fakultät der Eberhard Karls Universität Tübingen.

Tag der mündlichen Qualifikation:	10.09.2024
Dekan:	Prof. Dr. Thilo Stehle
1. Berichterstatter:	Prof. Dott. Andrea Santangelo
2. Berichterstatter:	PD Dr. Christoph Schäfer
3. Berichterstatterin:	Prof. Dr. Magdalena Rafecas

Abstract

Three interdisciplinary scientific projects using automated computational workflows for scalable and reproducible data analyses are presented in this work.

The Corrarea correction is an empirical correction for the remaining relative uncertainties in the on-axis effective area calibration of the XMM-Newton European Photon Imaging Camera (EPIC) instrument. These uncertainties can lead to differences in the fluxes derived from EPIC-MOS and EPIC-pn data on the order of 10 %. In Project I, a generic workflow system was developed and used for the derivation and validation of an updated Corrarea correction. The correction is based on cross-calibration using a large sample of observations and is implemented as an energy-dependent multiplicative factor available as part of the XMM-Newton Current Calibration Files (CCFs). The new correction was validated on several sub-samples based on the science mode, pile-up level, and observation epoch. The validation demonstrated the robustness of the new Corrarea correction. At low energies unaffected by the Corrarea correction, the validation revealed significant remaining relative uncertainties in the time-dependent calibration and the calibration of individual science modes.

Monte Carlo simulations performed with Geant4 for characterizing the Filter Wheel Closed (FWC) background of the eROSITA telescope on board the SRG observatory are described in Project II. A new mass model of the eROSITA camera was created, which provides a detailed description of the geometry and material compositions, including impurities based on manufacturer specifications and measurements. For modeling of detector effects, a new digitizer and data analysis workflow was developed with the focus on precise modeling, using the pattern matching algorithm from the eROSITA Science Analysis Software System (eSASS). The simulated background level agreed with the in-orbit measurements within the uncertainties of the radiation and particle environment, in contrast to pre-launch simulation studies. The simulation results show several prominent fluorescence lines that also exist in the measured eROSITA FWC spectrum, although the absolute strengths of the fluorescence lines could not be reproduced. The simulations demonstrated that impurities in the beryllium shielding are the main contributors to the iron fluorescence line. The aluminium

line was found to be produced predominantly inside the camera instead of in the filter wheel, in contrast to previous expectations.

In Project III, Monte Carlo simulations were performed with GATE to evaluate and compare the PET performance characteristics of three geometries of a future breast PET/MRI insert, that will be operated inside a whole-body PET/MRI scanner. Absolute breast PET insert sensitivities of 3.1 % (Geometry A), 2.7 % (Geometry B), and 2.2 % (Geometry C) were found at the center of the Field Of View (cFOV) of the breast PET insert. Spatial resolutions between 1.4 mm and 2.0 mm were determined close to the cFOV, and the simulations revealed the necessity of using detectors with Depth Of Interaction (DOI) capability to compensate for the parallax error close to the edges of the FOV. Simulations of the Noise Equivalent Count Rate (NECR) showed that the breast PET insert will operate below saturation for typical clinical scenarios. Simulations of an anthropomorphic phantom revealed background single count rates of up to 17.1 Mcps (Geometry A). By collecting mixed coincidences between the breast PET insert and the whole-body PET scanner, dual-system simulations demonstrated an increase in sensitivity at the axillary lymph node region by between 26 % and 52 % compared to using only the whole-body PET scanner coincidences. Furthermore, the simulations showed potential improvements in the mean radial spatial resolution component in the axillary lymph node region using mixed coincidences from 6.9 mm (without breast PET insert) to 4.0 mm (Geometry A, two-layer DOI) and 3.8 mm (Geometry A, three-layer DOI).

Zusammenfassung

Drei interdisziplinäre wissenschaftliche Projekte, die automatisierte computergestützte Workflows für skalierbare und reproduzierbare Datenanalysen nutzen, werden in dieser Arbeit vorgestellt.

Die CORRAREA Korrektur ist eine empirische Korrektur für die verbleibenden relativen Unsicherheiten in der Kalibrierung der effektiven Flächen auf den optischen Achsen des XMM-Newton European Photon Imaging Camera (EPIC) Instruments. Diese Unsicherheiten können zu Differenzen in den mit EPIC-MOS und EPIC-pn bestimmten Flüssen in der Größenordnung von 10 % führen. Für Projekt I wurde ein generisches Workflowsystem entwickelt und für die Erstellung und Validierung einer aktualisierten CORRAREA Korrektur genutzt. Die Korrektur basiert auf einer Kreuzkalibrierung unter Verwendung einer großen Auswahl an Beobachtungen und ist als energieabhängiger multiplikativer Faktor implementiert, der als Teil der aktuellen Kalibrierungsdateien (CCFs) für XMM-Newton verfügbar ist. Die neue Korrektur wurde anhand mehrerer Teilauswahlen validiert, die auf dem Beobachtungsmodus, dem Pile-up-Level und der Beobachtungsepoche basieren. Die Validierung demonstrierte die Robustheit der neuen CORRAREA Korrektur. Bei niedrigen Energien, die nicht von der CORRAREA Korrektur betroffen sind, zeigte die Validierung signifikante relative Unsicherheiten in der zeitabhängigen Kalibrierung und der Kalibrierung der einzelnen Beobachtungsmodi auf.

Monte-Carlo-Simulationen zur Charakterisierung des Hintergrunds bei geschlossenem Filterrad (FWC) des eROSITA Teleskops an Bord des SRG Observatoriums, die mit Geant4 durchgeführt wurden, sind in Projekt II beschrieben. Ein neues Massenmodell der eROSITA Kamera wurde erstellt, das eine detaillierte Beschreibung der Geometrie und Materialzusammensetzungen, inklusive Verunreinigungen basierend auf Herstellerangaben und Messungen, enthält. Für die Modellierung der Detektoreffekte wurde ein neuer Digitalisierungs- und Datenanalyseworkflow entwickelt, mit Fokus auf präziser Modellierung und unter Verwendung des Musterabgleichsalgorithmus aus dem eROSITA Softwaresystem für wissenschaftliche Analysen (eSASS). Das simulierte Hintergrundniveau stimmte mit den Messungen im Orbit im Rahmen der Unsicherheiten des Strahlungs- und Teilchenhintergrunds überein, im Gegensatz zu Simulationsstudien, die

vor dem Start von eROSITA durchgeführt wurden. Die Simulationsergebnisse enthalten mehrere Fluoreszenzlinien, die ebenfalls im gemessenen eROSITA FWC Spektrum enthalten sind, wobei die absoluten Ausprägungen der Fluoreszenzlinien nicht nachgestellt werden konnten. Die Simulationen zeigten auf, dass die Verunreinigungen in den Berylliumabschirmungen den Hauptanteil zur Eisenfluoreszenzlinie beitragen. Die Aluminiumlinie wurde entgegen früherer Erwartungen überwiegend innerhalb der Kamera anstatt des Filterrads erzeugt.

Für Projekt III wurden Monte-Carlo-Simulationen mit GATE durchgeführt, um die PET-Leistungsmerkmale von drei Geometrien eines künftigen Brust-PET/MRI-Inserts zu bestimmen und zu vergleichen, das innerhalb eines PET/MRI-Ganzkörperscanners betrieben werden soll. Absolute Sensitivitäten des Brust-PET-Inserts von 3.1 % (Geometrie A), 2.7 % (Geometrie B) und 2.2 % (Geometrie C) wurden am Zentrum des Gesichtsfelds (cFOV) des Brust-PET-Inserts gefunden. Ortsauflösungen zwischen 1.4 mm und 2.0 mm wurde nahe des cFOV festgestellt, und die Simulationen offenbarten die Notwendigkeit von Detektoren, welche die Interaktionstiefe (DOI) bestimmen können, um dem Parallaxenfehler an den Rändern des Gesichtsfelds entgegenwirken zu können. Simulationen der rauschäquivalenten Zählrate (NECR) zeigten, dass das Brust-PET-Insert in typischen klinischen Szenarios unterhalb der Sättigungsgrenze operieren wird. Simulationen eines anthropomorphen Phantoms führten zu einer Hintergrundzählrate an Einzelevents von bis zu 17.1 Mcps (Geometrie A). Durch die Erfassung von gemischten Koinzidenzen zwischen Brust-PET-Insert und Ganzkörperscanner kann die Sensitivität in der Region der axillären Lymphknoten zwischen 26 % und 52 % im Vergleich zur Sensitivität unter ausschließlicher Verwendung der Koinzidenzen des Ganzkörperscanners gesteigert werden, was durch Simulationen mit zwei Systemen gezeigt wurde. Zusätzlich zeigten die Simulationen mögliche Verbesserungen der durchschnittlichen Radialkomponente der Ortsauflösung in der Region der axillären Lymphknoten für gemischte Koinzidenzen von 6.9 mm (ohne Brust-PET-Insert) auf 4.0 mm (Geometrie A, DOI mit zwei Schichten) und 3.8 mm (Geometrie A, DOI mit drei Schichten).

Contents

List of Figures

List of Tables

List of Abbreviations

ALND	Axillary Lymph Node Dissection
AMS	Alpha Magnetic Spectrometer
ARF	Ancillary Response File
CAD	Computer-Aided Design
CASToR	Customizable and Advanced Software for Tomographic Reconstruction
CCD	Charge-Coupled Device
CCF	Current Calibration File
cFOV	center of the Field Of View
CRDB	Cosmic-Ray DataBase
CRT	Coincidence Resolving Time
CSG	Constructive Solid Geometry
CT	Computed Tomography
CTI	Charge Transfer Inefficiency
CXB	Cosmic X-ray Background
CXO	Chandra X-ray Observatory
DAG	Directed Acyclic Graph
DOI	Depth Of Interaction
EPIC	European Photon Imaging Camera
eRASS1	eROSITA All-Sky Survey 1
eROSITA	extended ROentgen Survey with an Imaging Telescope Array
ESA	European Space Agency
ESAC	European Space Astronomy Centre
eSASS	eROSITA Science Analysis Software System
FBP	Filtered Back Projection
$[^{18}F]$FDG	2-$[^{18}F]$fluoro-2-deoxy-D-glucose
FITS	Flexible Image Transport System
FOV	Field Of View
FWC	Filter Wheel Closed
FWHM	Full Width at Half Maximum

GATE	Geant4 Application for Emission Tomography
GDML	Geometry Description and Mark-up Language
Geant4	Geometry and tracking 4
GPS	General Particle Source
GTI	Good Time Interval
HEO	Highly Elliptical Orbit
HPC	High-Performance Computing
IACHEC	International Astronomical Consortium for High-Energy Calibration
ISIS	Interactive Spectral Interpretation System
ISS	International Space Station
LEAP	Large-sample Epic Analysis Pipeline
LEO	Low Earth Orbit
LOR	Line Of Response
LSO	Lutetium OxyorthoSilicate
LUT	LookUp Table
MIP	Minimum Ionizing Particle
MC	Monte Carlo
MOS	Metal Oxide Semiconductor
MRI	Magnetic Resonance Imaging
NECR	Noise Equivalent Count Rate
NEMA	National Electrical Manufacturers Association
NuSTAR	Nuclear Spectroscopic Telescope ARray
PAMELA	Payload for Antimatter Matter Exploration and Light-nuclei Astrophysics
PET	Positron Emission Tomography
PIXE	Particle Induced X-ray Emission
PRNG	Pseudo Random Number Generator
RF	Radio Frequency
RMF	Redistribution Matrix File
SAS	Science Analysis System

SIXTE	SImulation of X-ray TElescopes
SLNB	Sentinel Lymph Node Biopsy
SPECT	Single Photon Emission Computer Tomography
SPENVIS	Space ENVironment Information System
SQL	Structured Query Language
SRG	Spectrum-Roentgen-Gamma
TOF	Time Of Flight
VP-PET	Virtual Pinhole PET
XCAT	eXtended CArdiac-Torso
XMM-Newton	X-ray Multi-mirror Mission Newton
YAML	YAML Ain't Markup Language

Introduction

Contents

1. Thesis outline

This thesis is divided into five parts. Basic introductions into the automated computational workflows that are used throughout this thesis, the calibration of X-ray instruments, and Monte Carlo (MC) simulations are given in the Introduction. The thesis consists of three scientific projects. The CORRAREA project for cross-calibration of the effective areas of the X-ray Multi-mirror Mission Newton (XMM-Newton) European Photon Imaging Camera (EPIC)-pn and EPIC-Metal Oxide Semiconductor (MOS) instruments, based on a large source sample, is described in Project I. The characterization of the extended ROentgen Survey with an Imaging Telescope Array (eROSITA) filter wheel closed background using MC simulations is described in Project II. Project III contains MC simulation studies of the expected performance characteristics of different variants of a breast Positron Emission Tomography (PET) insert, which is planned for integration into a clinical whole-body PET/Magnetic Resonance Imaging (MRI) scanner. Each of the three projects consists of an introduction, a description of the materials and methods used and developed as part of this work, the results, and a discussion. A joint summary, conclusion, and outlook for the three projects is provided in the Conclusion.

2. On automated computational workflows

Computational data analysis and simulation studies have become ubiquitous in modern physics and science in general. The increase in available computational resources over the last decades has enabled complex and detailed workflows and pipelines, consisting of many individual steps that can be executed on workstations, High-Performance Computing (HPC) clusters, or in cloud environments. However, the increased workflow complexity has posed challenges for the reproducibility of computational methods and data analyses (Mesirov, 2010; Stodden et al., 2016; Gryk and Ludäscher, 2017). These challenges affect not only the reproducibility of results obtained by other groups, but also the reproducibility of one's own results (Baker, 2016).

Automation of computational workflows is key to enabling reproducible data analysis, as the implicit information required for manual step-by-step execution is transferred into the automatic workflow description. Other key concepts for reproducibility include scalability, allowing for parallelized execution of the workflows on different computational platforms, and provenance tracking of the results produced, including logs of the workflow execution (Crusoe et al., 2022).

Even when the same analysis code is run on different computing platforms, such as different UNIX systems, additional variations in scientific results can sometimes occur due to numerical instability (Di Tommaso et al., 2017). This can be avoided by using software containers, such as Docker or Singularity containers (Kurtzer et al., 2017), which provide a consistent software environment across computing infrastructures, including all software dependencies except the kernel (Di Tommaso et al., 2017; Moreau et al., 2023).

In the past years, a variety of workflow and pipeline management systems have been introduced to enable automated and reproducible computational

workflows[1]. As most of the workflow management systems were incompatible with each other, efforts have been started to standardize workflows, such as the Common Workflow Language (CWL) (Crusoe et al., 2022). Although prominent workflow management systems, such as Snakemake (Köster and Rahmann, 2012; Mölder et al., 2021) or Nextflow (Di Tommaso et al., 2017), have often emerged from the field of genomics research in bioinformatics, they can typically be used in other fields as well. The importance of reproducible computational workflows in high energy physics led to the introduction of the open-source REusable ANAlyses (REANA) system, developed at the Conseil Européen pour la Recherche Nucléaire (CERN), which provides a platform for data analyses, supporting various workflow management systems and software containers (Šimko et al., 2019). Nevertheless, workflow management systems do not seem to be widely adopted in physics yet, which is also indicated by the fraction of only 1 % of the total citations of the Snakemake and Nextflow papers (Köster and Rahmann, 2012; Di Tommaso et al., 2017; Mölder et al., 2021) related to physical sciences[2].

Throughout this thesis, Docker and Singularity containers were used to provide fixed computing environments for reliable reproducibility. Snakemake workflows were used for automated data analyses in Project II and end-to-end automated simulation studies in Project III, enabling to automatically split long simulations into many small parts for parallelized execution and analysis. In Project I, a self-written declarative workflow management system was used for fully automated large-sample cross-calibration analyses. Most of the data analysis software developed in the course of this thesis was written in the Python programming language using NumPy arrays (Harris et al., 2020), Astropy tables and input-output functions (The Astropy Collaboration et al., 2013, 2018; Astropy Collaboration et al., 2022), uproot for reading ROOT files (Pivarski et al., 2023), and Matplotlib for data visualization (Hunter, 2007).

[1] A list of open-source pipeline and workflow management systems containing more than 200 entries is available at `https://github.com/pditommaso/awesome-pipeline` (accessed on 2023-08-04).

[2] 34 of 3583 citing publications were related to physical sciences according to Dimensions. Manually aggregated from `https://app.dimensions.ai/details/publication/pub.1018944052`, `https://app.dimensions.ai/details/publication/pub.1084776940`, and `https://app.dimensions.ai/details/publication/pub.1137313608` (accessed on 2023-08-04).

3. Calibration and effective area

Reliable calibration is essential and indispensable for the scientific interpretation of measurement data in general. Particularly for more complex detectors and measurement instruments, such as those used in the fields of molecular imaging and high energy astrophysics, calibration is a critical and continuous process that is never completely finished (which is also demonstrated in Project I), as instruments change over time and require constant calibration adjustments. Furthermore, the understanding of detectors and instrumental effects improves over time, which is also reflected in calibration updates (Arnaud, 2011).

PET not only enables qualitative and visual inspections of reconstructed images, but also quantitative measurements of the activity concentration of the radiotracer (Boellaard, 2013). For multicenter studies, the PET scanners need to be well calibrated to obtain comparable quantitative data (Aide et al., 2017). Thus, calibration procedures are part of the European Association of Nuclear Medicine (EANM) guidelines for PET scanners, which include daily quality control measures and regular cross-calibration of PET scanners with the dose calibrators (Boellaard et al., 2015). Calibration procedures for PET scanners across multiple sites and from different manufacturers were demonstrated to allow for quantitative multicenter studies of diseases with low prevalence (Kist et al., 2016).

Modern X-ray observatories typically have two main calibration phases. Before the launch of an X-ray satellite, on-ground calibration of the detectors and mirrors is performed in specialized X-ray test facilities simulating an astronomical point source, such as the PANTER facility (Bradshaw et al., 2019), which was used for on-ground calibrations of the XMM-Newton EPIC instruments and eROSITA (Salmaso et al., 2022). After launch and prior to the main science phase, an in-orbit calibration and performance verification phase is conducted to test the instrument in space conditions and to overcome typical limitations of the on-ground calibration listed in Lumb (2002), such as technical

limitations of X-ray test facilities and the notoriously short amount of time between instrument completion and launch. As noted above, calibration is never fully complete, and continuous calibration updates are performed throughout the life of the mission. This is particularly important for satellite missions, as in-orbit detectors can degrade over time due to radiation damage, e.g., by funneled soft protons (Kendziorra et al., 2000), contamination (Plucinsky et al., 2018), micrometeoroid hits (Freyberg et al., 2022), and other effects. In the last two decades, cross-calibration efforts between different X-ray instruments, either on a single spacecraft or also across observatories, have gained interest in the calibration community, and the International Astronomical Consortium for High-Energy Calibration (IACHEC)[3] was founded to coordinate synchronized observations of the same source by several X-ray missions, and also to foster high-energy calibration procedures and provide high-energy calibration standards (Sembay et al., 2010).

While many instrumental effects need to be individually calibrated in order to obtain an accurate overall calibration of X-ray instruments, the two most important factors typically dominating the calibration uncertainties are the effective area and the detector response. In the analysis software of X-ray missions and in spectral analysis tools, the effective area and the redistribution function are typically implemented in form of an Ancillary Response File (ARF) containing a vector and a Redistribution Matrix File (RMF), respectively. In addition to the effective area of the X-ray mirrors, the total effective area of an X-ray instrument includes several components, representing absorption and the loss of events from the X-rays entering the optics to their detection. The effective area incorporates the transmission of the filters, the detector quantum efficiency, and the transmission of gratings in the optical path (if any), such as for XMM-Newton. Furthermore, the in-orbit frame processor and the on-ground event analysis software affect the effective area, e.g., by removing Minimum Ionizing Particle (MIP) tracks from frames (see Section 12.8), removing bad pixels, or discarding invalid events in pattern matching, that will result in a reduction of the effective area and have to be taken into account in the calibration.

[3]The IACHEC website is available at `https://iachec.org` (accessed on 2023-08-29).

4. Monte Carlo simulations in X-ray and gamma ray physics

The MC method is a probabilistic method based on repeated random sampling and the law of large numbers, especially useful to investigate problems where analytical descriptions are not feasible, such as calculating the winning chances of a game of solitaire or tracking the particle cascades in the atmosphere produced by cosmic rays (Metropolis and Ulam, 1949). Although the name "Monte Carlo method" was suggested by Nicholas Metropolis in the late 1940s and the method rapidly expanded with the availability of the emerging electronic computers (Metropolis, 1987), the basic principles of the MC method were already used in the 18^{th} century by Georges-Louis Leclerc, Comte de Buffon, to estimate the value of π from dropping needles on a tiled floor (Harrison et al., 2010). Before general availability of electronic computers, Enrico Fermi invented the analog computer FERMIAC, shown in Figure 4.1, for tracking of neutrons through a nuclear device based on random numbers (Metropolis, 1987; Coccetti, 2016). Today, the MC method is used in many fields for problems where analytical approaches are insufficient, especially for systems with many coupled degrees of freedom (Harrison et al., 2010).

The MC method is often used for simulations tracking particles through matter, e.g., in the fields of nuclear medicine, particle physics, and space science (Agostinelli et al., 2003). For modern space-based missions, MC simulations have become critical for the detector design and for the interpretation of the collected data (Allison et al., 2016). In Project II, MC simulations are utilized for the characterization of the eROSITA particle-induced background. The MC method has also become essential for medical imaging, e.g., for simulations necessary for the development of new PET scanners, for improvements of image reconstruction algorithms and scan protocols based on simulation data, and for radiotherapy (Jan et al., 2004, 2011). In Project III, MC simulations supporting the design and development of a breast PET insert are described.

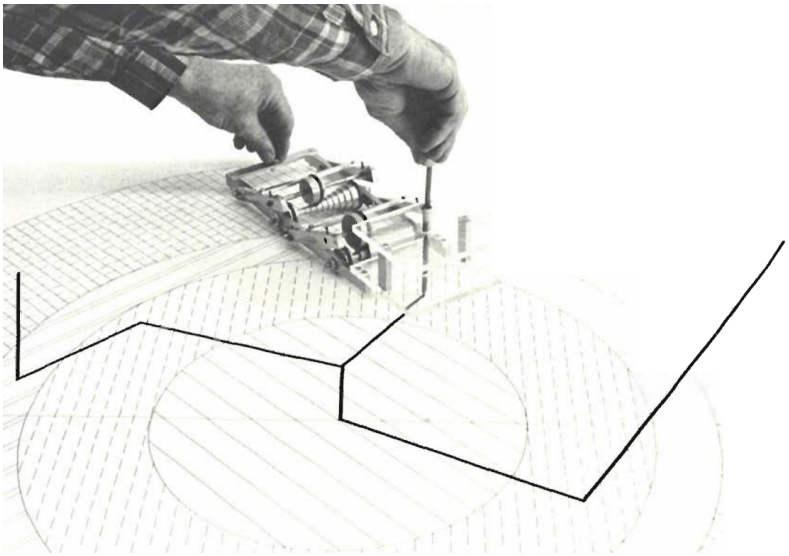

Figure 4.1.: The FERMIAC Monte Carlo trolley. It was invented by Enrico Fermi for tracking neutrons through a material arrangement available as a scale drawing. The trolley consisted of a platform for neutron direction selection and two drums, which were set depending on the neutron velocity and the material properties of the volume where the neutron was tracked. Random numbers were used to determine the tracking and collision properties. The operation of the FERMIAC is described in more detail in Coccetti (2016). Image credit: Metropolis (1987).

Modern MC simulators for tracking particles through matter are complex codes, as simulations have become more detailed and demanding, and because multiple components have to be implemented for exhaustive simulations (Agostinelli et al., 2003). Today, several general purpose particle tracking codes are available and under active development, including Geometry and tracking 4 (Geant4) (Agostinelli et al., 2003), EGSnrc (Kawrakow, 2000), FLUKA (Ferrari et al., 2005), Monte Carlo N-Particle 6 (MCNP6) (Goorley et al., 2016), KASSIOPEIA (Furse et al., 2017), and Particle and Heavy Ion Transport code System (PHITS) (Sato et al., 2018). Throughout this thesis, the Geant4 toolkit was used for particle tracking simulations, either by developing a custom Geant4 application for the simulations shown in Project II, or by using an existing Geant4 application specialized for medical physics simulations described below for the simulations shown in Project III. Geant4, actively developed by the international Geant4 collaboration, is an open-source, modular, well-validated toolkit written in the C++ programming language, and is widely used across many fields and includes implementations of all important simulation aspects, including, among others, the following list of key components (Agostinelli et al., 2003; Allison et al., 2006, 2016):

- **Geometry:** Particle tracking simulations need a description of the detector geometry including the material properties of every volume. The geometry can be constructed from an extensive set of basic solids (e.g., spheres, cylinders, boxes) using the Constructive Solid Geometry (CSG) technique, or using tessellated volumes. The Geant4 toolkit includes the ability to check the user-provided geometry at construction time for compliance with constraints imposed by the internal geometry representation as a tree data structure, such as avoiding volume overlaps of sibling nodes or volumes that extend the volumes of their ancestors (Allison et al., 2016).

- **Transportation:** In Geant4, particles are transported through the geometry with a variable step length determined from the proposed step lengths of all activated physical processes for a given step. The selected physical process is then applied, including the production of secondary particles when applicable, either along the step for continuous processes, at the end of the step, or at rest for stationary particles. As the transportation itself is realized as a generic process in the object-oriented structure of Geant4,

the step length can also be limited by crossing the border between two materials without an actual physical interaction (Agostinelli et al., 2003).

- **Physics:** Multiple well-validated models for physical processes are included in Geant4, and for many processes several alternative models exist, which are optimized for different aspects, such as specific energy ranges, precision, or computational performance, which allows for configuration and optimization of the simulation for specific use cases (Agostinelli et al., 2003). Several pre-defined physics lists exist for different use cases, which strongly simplifies the selection of physical models for the users by providing a consistent set of models as reference and starting points (Allison et al., 2006).

- **PRNGs:** Robust Pseudo Random Number Generators (PRNGs) are essential for MC simulations. In Geant4 applications, the users can choose from several PRNGs that share the same interface, which are provided by the Class Library for High Energy Physics (CLHEP) project (Lönnblad, 1994). For reproducible simulations, an initial seed can be defined by the user. Furthermore, the internal state of the PRNG can be saved and loaded in order to directly reproduce specific events of a simulation run. With version 10.4, Geant4 switched to MIXMAX (Savvidy, 2015) as the default random number generator.

- **Visualization:** Geant4 supports various visualization drivers for visualizing the geometry and particle tracks, either for writing files that can be opened by external viewers, or for direct and interactive visualization. The former class of visualization drivers includes a ray-tracing renderer, which is an important debugging tool for complex geometries because it is based on the internal Geant4 tracking algorithm and therefore gives an impression of the geometry interpretation at simulation time (Agostinelli et al., 2003).

- **User interaction:** While Geant4 applications are written in the C++ language, the users can interact with a Geant4 application at different stages of the simulation using interactive commands, that can either be interactively entered into a user interface, or read from user-provided macro files in the batch mode (Agostinelli et al., 2003). The available

interactive commands can be modified and extended by Geant4 applications, such that a single application can be used for running different simulations, controlled only by interactive commands.

Overall, the object-oriented structure of Geant4 together with the chosen software architecture and design allows the development of highly flexible applications, but application developers need to have a solid understanding of C++ and the Geant4 design choices, which can hinder easy accessibility.

The Geant4 Application for Emission Tomography (GATE) software, originally designed for simulating PET and Single Photon Emission Computer Tomography (SPECT) scanners, builds on the Geant4 interactive commands mechanism and provides an MC simulation application that is completely configured by macro files (Jan et al., 2004). GATE includes functionality specifically useful for medical physics simulations, and introduces the three key concepts `Volumes`, `Actors`, and the `Digitizer` as simplified abstractions of several Geant4 components, allowing for improved clarity and comprehensibility, but reduced capabilities of the macro files used to define simulations[4] (Sarrut et al., 2022). In the past, the scope of the GATE software was extended, including features needed for modeling Computed Tomography (CT) scanners and radiotherapy simulations (Jan et al., 2011). For simulations of PET and SPECT systems, GATE is very well validated by evaluating simulation results against real measurements for different scanners, with 46 and 21 evaluations of PET and SPECT systems referenced in Sarrut et al. (2021), respectively. GATE is open-source software, collaboratively developed by the international OpenGATE collaboration and independent community contributors like myself, and has a strong impact on multiple applications in medical imaging and dosimetry today (Sarrut et al., 2022).

Currently, GATE is in the process of a complete rewrite in the Python programming language using the Geant4 Python bindings. The macro-file based simulation configuration will be completely replaced by user-developed Python scripts. Thus, the new Python-based GATE version will strongly increase the flexibility of simulation creation and will allow for integration of new features

[4] As an example, the Geant4 concepts of `Solids`, `LogicalVolumes`, and `PhysicalVolumes` are represented by a single `Volume` concept in GATE as described in Sarrut et al. (2022), which leads to simplified macro files, but drops some advanced functionality.

like multi-threaded simulations[5]. These features could not be integrated into the aging code base of the current GATE software due to the long-term maintenance challenges posed by the fact that contributions are typically related to individual research projects with limited duration (Sarrut et al., 2022). At the time of writing, the new Python-based GATE version was only available as a beta release. As Geant4 will be used for particle tracking also in the new GATE version and the `Digitizer` design will be based on GATE 9.3, the impact of the new GATE version on the simulation results shown in this thesis will likely be minimal.

[5]More details about the rationale and the technical details of the new Python-based GATE can be found in the user manual available at `https://opengate-python.readthedocs.io` (accesses on 2023-08-10).

Project I.

Cross-calibration of the XMM-Newton EPIC-pn and EPIC-MOS effective areas

Contents

5. Introduction

In this project, a generic workflow system was developed and applied to derive an empirical correction function for the XMM-Newton EPIC on-axis effective areas in collaboration with the European Space Astronomy Centre (ESAC) based on cross-calibration and a large sample of observations. The new correction function was validated based on several sub-samples using the highly automated workflow system.

5.1. The XMM-Newton observatory

The X-ray Multi-mirror Mission Newton (XMM-Newton) of the European Space Agency (ESA) was launched into a 48 h Highly Elliptical Orbit (HEO) around the Earth with an apogee of 114 000 km and a perigee of 7000 km on December 10, 1999, on the first commercial flight of an Ariane 5 rocket from the Guiana Space Center (Jansen et al., 2001). Earlier in the same year, the National Aeronautics and Space Administration (NASA) launched their Chandra X-ray Observatory (CXO) (Weisskopf et al., 2002), and with their complementary capablities, e.g., the large effective area of XMM-Newton and the high angular resolution of the CXO, the two observatories established a new era of X-ray astronomy (Santos-Lleo et al., 2009).

XMM-Newton is a highly successful mission with a yearly average of around 380 refereed publications based on XMM-Newton data (Schartel et al., 2022). Despite its originally planned lifetime of ten years (Kirsch et al., 2014), the XMM-Newton mission is still active and is currently in its 24^{th} year of observation at the time of writing this thesis. Measures have been implemented to extend the potential lifetime of XMM-Newton, such as switching to four-wheel drive operation, which reduces the fuel consumption by using the spare reaction wheel that was originally included as a cold redundancy unit, allowing

operations beyond the originally defined ultimate end of life in 2019 (Kirsch et al., 2014). These measures allow, from a technical point of view, to operate the spacecraft until 2031 (Schartel et al., 2022) and potentially beyond 2033 (Kirsch, 2023).

A technical drawing of the XMM-Newton spacecraft, including the three X-ray mirror modules mounted on the mirror support platform and the focal plane assembly where the X-ray detectors are located, is shown in Figure 5.1. In the foci of the X-ray mirror modules is the European Photon Imaging Camera (EPIC), which consists of two EPIC-MOS detectors (Turner et al., 2001) and one EPIC-pn camera (Strüder et al., 2001). Photographs of the EPIC-MOS and EPIC-pn Charge-Coupled Device (CCD) configurations are shown in Figure 5.2. While EPIC-MOS has better spatial resolution due to the smaller pixel sizes and a slightly better spectral resolution, the back-illuminated EPIC-pn has a higher quantum efficiency, allowing to extend the useful energy range up to around 10 keV, and a much better time resolution of 73 ms compared to the 2.6 s of EPIC-MOS in the full frame modes (ESA: XMM-Newton SOC, 2023a). In addition to the full frame mode, both instrument types can be operated in different science modes where only parts of the CCDs are read out, which leads to increased time resolution and less pile-up for bright sources (Turner et al., 2001; Strüder et al., 2001). The available EPIC science modes are listed in Table 5.1.

In each of the two lines of sight of the EPIC-MOS cameras, an X-ray reflection grating array is mounted that deflects half of the incoming X-rays to the CCDs of the Reflection Grating Spectrometer (RGS), which offers high-resolution spectroscopy in the soft X-rays in the range of 0.3 keV to 2.1 keV (Den Herder et al., 2001). Furthermore, XMM-Newton contains an Optical Monitor (OM), sensitive in the range of 170 nm to 650 nm, providing simultaneous observational data in optical and UV (Mason et al., 2001). All scientific instruments on the XMM-Newton spacecraft are co-aligned such that they observe the same region at the same time, and typically, all instruments are observing simultaneously (Schartel et al., 2022).

Reduction and analysis of XMM-Newton observational data can be performed using the Science Analysis System (SAS) (ESA: XMM-Newton SOC, 2023a) developed by the XMM-Newton Science Operations Center (SOC) and the

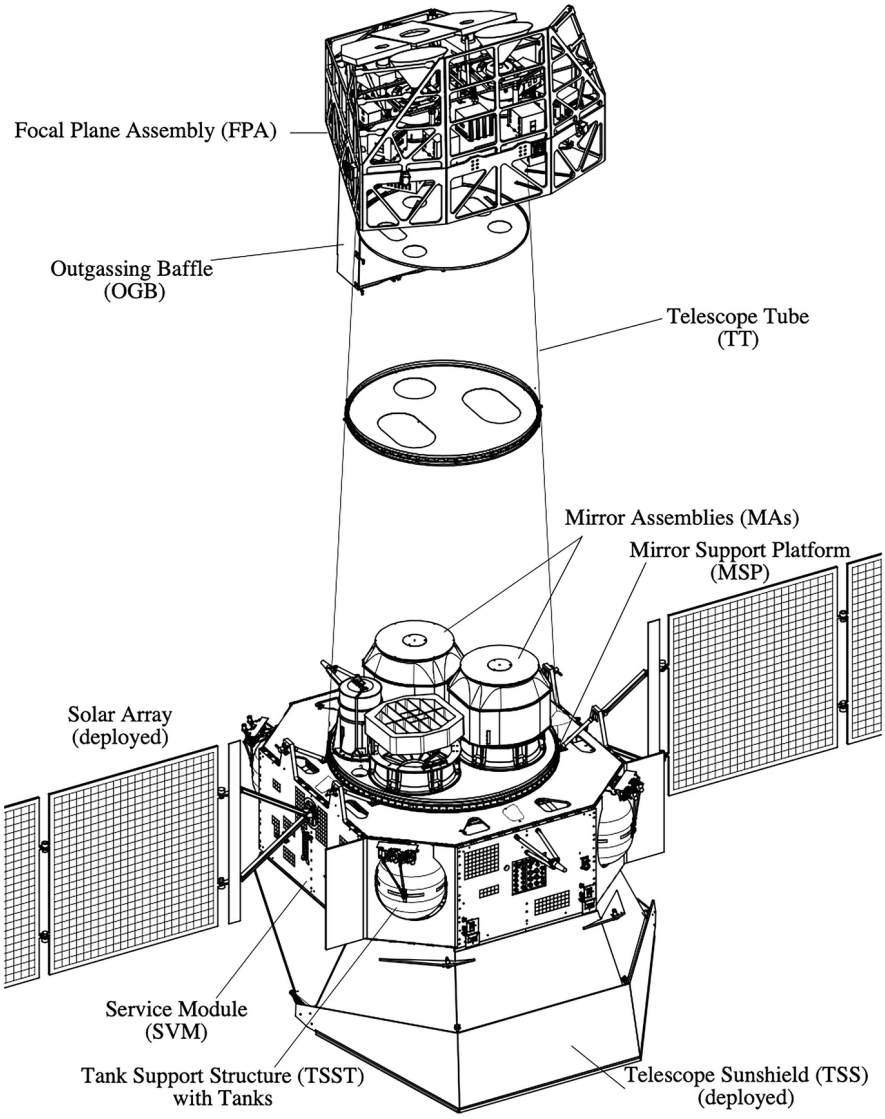

Figure 5.1.: Technical drawing of the XMM-Newton observatory, which has a total length of 10.8 m and a total width of 16 m with unfolded solar panels (Schartel et al., 2022). In the inside view of the mirror assembly, a reflection grating array is shown above the mirror module. Image credit: Schartel et al. (2022). Reproduced with permission from Springer Nature.

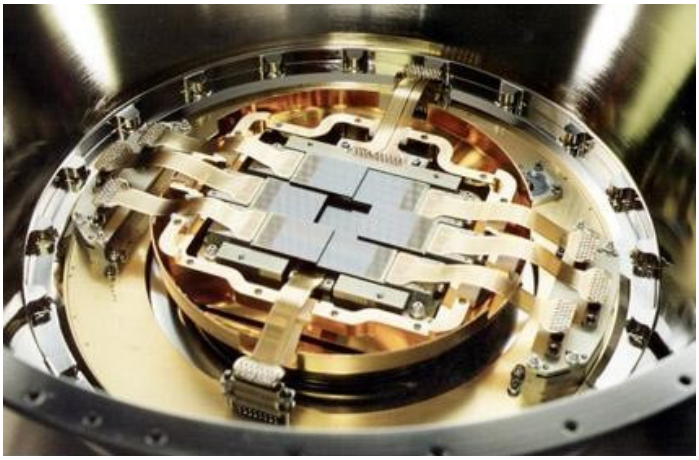

(a) EPIC-MOS detector.

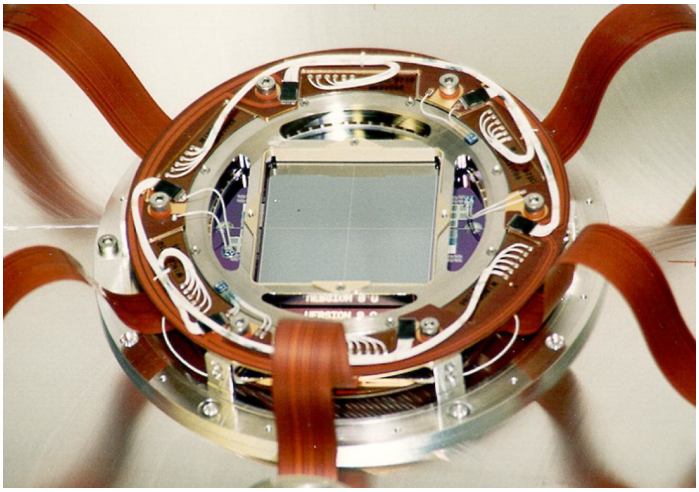

(b) EPIC-pn detector.

Figure 5.2.: (a): EPIC-MOS CCD. Image courtesy of Leicester University, University of Birmingham, CEA Service d'Astrophysique Saclay and ESA. (b): EPIC-pn CCD. Image courtesy of MPI-semiconductor laboratory, MPE, Astronomisches Institut Tübingen, Germany and ESA. Image credit for (a) and (b): ESA/XMM-Newton, used under CC BY-SA 3.0 IGO, cropped from original.

Table 5.1.: Time resolution and live time of the science modes of the EPIC-MOS and EPIC-pn cameras as reported in ESA: XMM-Newton SOC (2023a). The timing (and burst) modes only provide spatial information along one direction.

Science mode	Time res. [ms]		Live time [%]	
	MOS	pn	MOS	pn
Ext. full frame	–	199.1	–	100.0
Full frame	2600	73.4	100.0	99.9
Large window	900	47.7	99.5	94.9
Small window	300	5.7	97.5	71.0
Timing	1.75	0.03	100.0	99.5
Burst	–	0.007	–	3.0

XMM-Newton Survey Science Center (SSC) (Watson et al., 2001). The XMM-Newton calibration is provided as a set of Current Calibration Files (CCFs), available both for the most recent calibration and for earlier calibration snapshots[6]. Together with the availability of Observation Data Files (ODFs), which can be obtained from the XMM-Newton Science Archive (XSA) (Sarmiento et al., 2019), this allows for repeated reprocessing of observational data (ESA: XMM-Newton SOC, 2023a), which is fundamental to enable the empirical cross-calibration studies described in this part of the thesis.

5.2. The CORRAREA correction

The calibration of the effective area of X-ray satellites is challenging and for the XMM-Newton European Photon Imaging Camera (EPIC) instruments, the effective area calibration is assumed to dominate the systematic uncertainties for energies above around 0.5 keV, whereas at low energies the Redistribution Matrix File (RMF) calibration uncertainties are assumed to dominate (Read et al., 2014). In previous cross-calibration studies, the relative calibration

[6]The available methods for retrieving the CCFs are described in `https://www.cosmos.esa.int/web/xmm-newton/current-calibration-files` (accessed on 2023-09-29).

uncertainties were found to yield significant differences in the fluxes determined by the three EPIC instruments, especially between the EPIC-pn and the EPIC-MOS cameras (Stuhlinger et al., 2010; Read et al., 2014; Guainazzi et al., 2014). These relative calibration uncertainties persist in the most recent CCFs available at the time of writing this thesis, and can lead to flux differences on the order of 10 %. This is illustrated by the MOS-to-pn flux ratio distribution from 302 simultaneous (by satellite design) observations of bright and point-like sources from the 4XMM-DR12-v0.1 sample (see Chapter 8), shown in Figure 5.3 for different energy bands. On average, the EPIC-MOS cameras yield higher fluxes than the EPIC-pn camera over all energy bands, but to different extents depending on the energy. Towards high energies (dominated by the effective calibration uncertainties), the MOS-to-pn flux ratios increase strongly, with average ratios of 1.14 and 1.12 for MOS1 and MOS2, respectively.

The remaining calibration uncertainties led to the development of an empirical, energy-dependent correction for the on-axis EPIC effective areas determined by cross-calibration, called the CORRAREA correction (Read et al., 2014). With version 14 of SAS, the CORRAREA correction was released as a non-default multiplicative correction to the EPIC ARFs, that can be enabled by providing the `applyxcaladjustment=yes` option to the SAS `arfgen` tool (Guainazzi et al., 2014).

In a linear approximation, neglecting nonlinear effects such as pile-up, the production of spectral data can be described using

$$n(c) = \int D(c, E) \times A(E) \times F(E) dE + b(c) \tag{5.1}$$

with the count rate n, the energy channel c, the redistribution function D describing the probability of an event with energy E to be assigned to channel c, the effective area A, the photon flux density of the observed source F, and the background count rate b (Davis, 2001; Arnaud and Smith, 2011). A formal derivation of equation 5.1 together with information about the assumptions and simplifications made in the derivation is given in Davis (2001). As the CORRAREA correction is an energy-dependent multiplicative correction factor for the effective area, the corrected count rate n_{corr} can be described using

$$n_{\mathrm{corr}}(c) = \int D(c, E) \times C(E) \times A(E) \times F(E) dE + b(c) \tag{5.2}$$

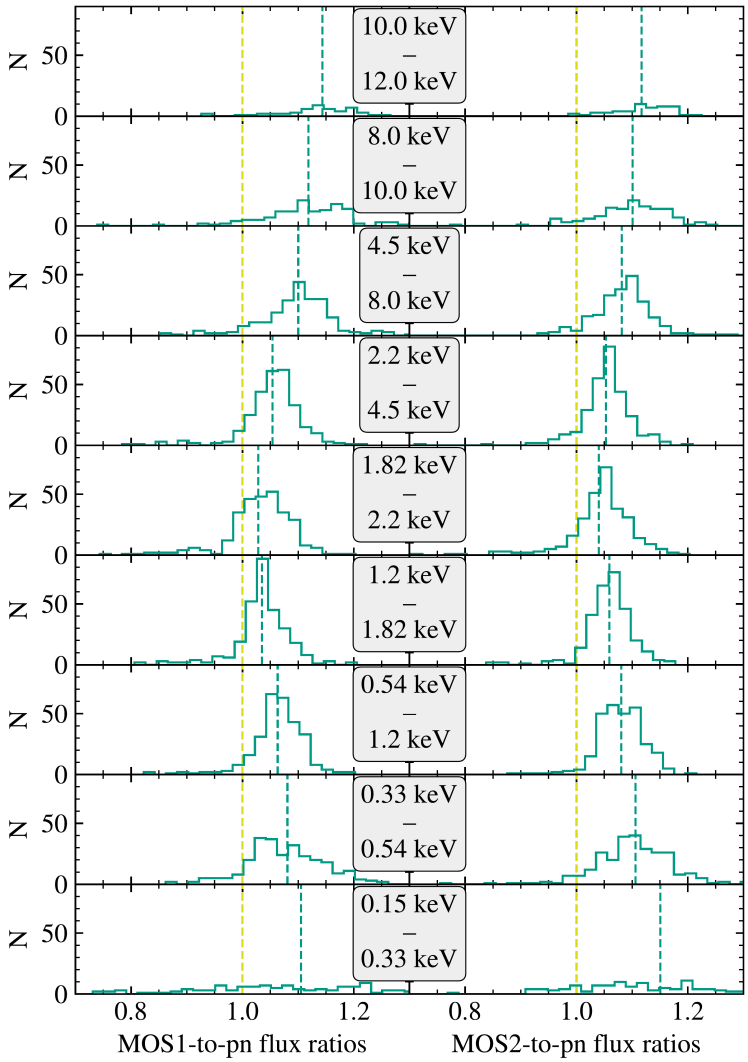

Figure 5.3.: MOS-to-pn flux ratio histograms for 302 observations from the 4XMM-DR12-v0.1 sample using SAS version 21.0.0 and the most recent calibration files. There are a few outliers outside the displayed range of ratios, which are excluded for better visibility, but are included in the calculation of the visualized averages.

with the CORRAREA correction function C. This empirical correction function was derived by cross-calibration from a sample of 46 bright but pile-up free point-like sources (Read et al., 2014).

The CORRAREA correction functions were obtained separately for MOS1 and MOS2 by using the widely adopted stacked residual ratio method, relying on stacking data from several observations and convolving a reference model with the response of the other instrument (Longinotti et al., 2008; Kettula et al., 2013; Read et al., 2014; Schellenberger et al., 2015; Nevalainen and Molendi, 2023). Following these papers, the residuals R_{pn} of the EPIC-pn instrument, which was selected as reference instrument for the CORRAREA correction, are given as

$$R_{\mathrm{pn}} = \frac{\mathrm{data}_{\mathrm{pn}}}{\mathrm{model}_{\mathrm{pn}} \otimes \mathrm{response}_{\mathrm{pn}}} \ , \tag{5.3}$$

and the residuals for one of the EPIC-MOS instruments R_{MOS} can then be obtained by convolving the reference model ($\mathrm{model}_{\mathrm{pn}}$) with fixed parameters with the EPIC-MOS response ($\mathrm{response}_{\mathrm{MOS}}$):

$$R_{\mathrm{MOS}} = \frac{\mathrm{data}_{\mathrm{MOS}}}{\mathrm{model}_{\mathrm{pn}} \otimes \mathrm{response}_{\mathrm{MOS}}} \ . \tag{5.4}$$

Furthermore, by dividing the EPIC-MOS residuals with the EPIC-pn residuals, effects of imperfect spectral models are reduced, and the resulting MOS-to-pn residual ratios α, given by

$$\alpha = \frac{R_{\mathrm{MOS}}}{R_{\mathrm{pn}}} = \frac{\mathrm{data}_{\mathrm{MOS}}}{\mathrm{model}_{\mathrm{pn}} \otimes \mathrm{response}_{\mathrm{MOS}}} \cdot \frac{\mathrm{model}_{\mathrm{pn}} \otimes \mathrm{response}_{\mathrm{pn}}}{\mathrm{data}_{\mathrm{pn}}} \ , \tag{5.5}$$

describes a suitable energy-dependent correction.

The MOS-to-pn residual ratios can be obtained either by fitting spectral models for individual sources and subsequently stacking the residuals ("fit-and-stack"), or by stacking all data and performing a single fit with an empirical model on the stacked data ("stack-and-fit") (Read et al., 2014). Each of these approaches has its own unique advantages and disadvantages, which will be discussed in Section 9.1. For the original CORRAREA correction, the stack-and-fit approach was used on a sample of 46 sources, and the MOS-to-pn residual ratios were fit with an analytical function in order to obtain smooth correction functions and

to avoid the introduction of artificial features into corrected spectral products (Guainazzi et al., 2014).

Recently, the derivation of the CORRAREA correction was strongly improved, including more sophisticated procedures in the filter pipeline for selection of the source sample and data reduction[7], resulting in a source sample of 163 pile-up free observations (Heinitz, 2021). The original CORRAREA correction and the more recently derived correction in the version optimized for full frame mode observations are shown in Figure 5.4. The former correction available since SAS version 14 remained unchanged until the introduction of a new CORRAREA correction described in Chapter 7. The new correction was derived based on the improvements in Heinitz (2021), the highly automated CORRAREA workflow, and the Large-sample Epic Analysis Pipeline (LEAP) tool developed as part of this thesis (described in Chapter 6), using a fit-and-stack approach (Smith et al., 2021).

In addition to cross-calibration of the XMM-Newton instruments, several cross-calibration studies between the XMM-Newton EPIC cameras and instruments on other active X-ray observatories using samples of galaxy clusters were conducted, such as with the X-Ray Imaging Spectrometer (XIS) (Koyama et al., 2007) on board of Suzaku (Kettula et al., 2013) and the Advanced CCD Imaging Spectrometer (ACIS) (Garmire et al., 2003) on board of Chandra (Nevalainen et al., 2010; Schellenberger et al., 2015). Furthermore, several cross-calibration studies were performed with coordinated simultaneous observations of single sources by multiple X-ray observatories in the IACHEC context[8]. Recently, the ABSCORRAREA correction was introduced in SAS version 20, which provides an empirical correction for the EPIC-pn effective area with reference to the Nuclear Spectroscopic Telescope ARray (NuSTAR) observatory and can be enabled by setting the `applyabsfluxcorr=yes` option in the `arfgen` tool (Fürst, 2022a,b). In the CONCORDANCE project, estimates of the systematic uncertainties of the effective area calibration for multiple X-ray missions are taken into account to derive the flux estimation that agrees best with measurements from different instruments (Marshall et al., 2021).

[7] See procedure descriptions in Section 6.1 and Heinitz (2021) for detailed explanations of the improvements.

[8] A list of cross-calibration publications is available on the IACHEC website at `https://iachec.org/papers` (accessed on 2023-09-23).

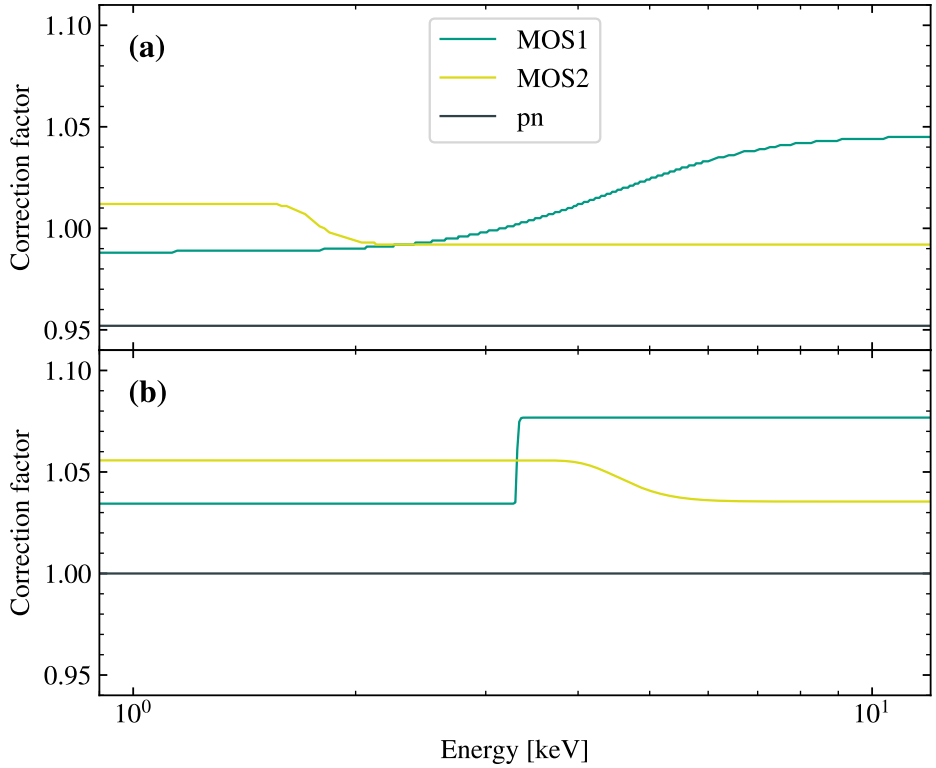

Figure 5.4.: Two previously existing CORRAREA corrections obtained using the stack-and-fit approach. (a): The correction introduced in SAS version 14 (Guainazzi et al., 2014). (b): A correction specifically derived for observations in the full frame mode (Heinitz, 2021), that is currently not available in the official CCFs. While the EPIC-pn effective area is boosted by a constant factor in (a), it remains unchanged in (b).

6. The CORRAREA workflow and the LEAP tool

The determination of appropriate CORRAREA correction functions, based on large initial source samples consisting of hundreds of observations, and the validation of the correction functions on multiple sub-samples requires an automated and scalable computational workflow. As an empirical correction, the CORRAREA correction is planned to be updated in case of calibration updates or new SAS versions that affect the effective area of the EPIC instruments in the relevant energy range. This further reinforces the need for a highly automated workflow, as the effects of the CORRAREA correction functions need to be re-validated on a regular basis following calibration updates. Furthermore, repeated workflow runs using different sub-samples, workflow configurations, and software versions necessitate provenance tracking of the results and traceability of the configuration used for individual runs, which can be facilitated by extensive logging and concise centralized configuration. Thus, one of the goals of this thesis was to implement the strong improvements in the CORRAREA filtering and data reduction methods described in Heinitz (2021) as a reproducible, highly automated, scalable, and generic workflow, that will also enable future XMM-Newton large-sample analyses for investigating calibration issues beyond CORRAREA.

The new CORRAREA workflow is split into two separate tools developed in the course of this thesis. The XMM-Newton LEAP written in the Python programming language consists of classes and `task`s usable for general XMM-Newton large-sample analyses of the EPIC instruments, such as the filtering and data reduction methods. It was designed to be easily modifiable and extensible for specific analyses by providing a plug-in interface usable from external Python code as described below. The CORRAREA tool is based on the LEAP plug-in mechanism and consists of code specifically for the CORRAREA project, such as the implementation of the spectral fitting procedure used to produce the

MOS-to-pn data-to-model ratios and the residual ratios as described in Section 6.2.

The LEAP tool also includes a self-written declarative automated workflow system, that was developed for increased flexibility compared to existing and more generic workflow systems discussed in Chapter 2, especially for the switch from the stack-and-fit approach to the fit-and-stack approach. This switch was expected to lead to fundamental changes in the workflow structure, such as the necessary introduction of the "concurrent exposures" concept discussed in Section 6.1.3. The workflow system of LEAP is based on five key concepts: `task`, `filter`, `obslist`, `obsinfo`, and `config`.

- `task`: A `task` represents a single step of the workflow, similar to the concept of the Snakemake `rule`. While Snakemake determines the Directed Acyclic Graph (DAG) of a workflow from the input and output files defined in the description of the individual `rule`s (Köster and Rahmann, 2012), the workflow in LEAP is explicitly declared by the user by providing a sequence of `task`s to run in the `config`. LEAP provides a task registry inspired by the one of Celery[9], which allows to register `task`s that can later be referenced from the `config` by their names, from anywhere within the Python code of LEAP or from any other Python module, such as the CORRAREA tool. The task registry allows to register either subclasses of the `Task` class, or any Python function using the `@task` decorator as shown in Listing 6.1.

- `filter`: The `filter`s are a special type of `task`s[10], removing all observations from the `obslist` that don't pass the filter definition. For each filter applied, an observation list of removed observations is created to allow for a later investigation of the reason for the removal. As shown in Listing 6.1, a simple observation-based `filter` can be registered in the task registry using the `@filter` decorator for a Python function with a boolean return value, "true" if the observation passes the filter, and "false" to remove the observation from the `obslist`. LEAP contains additional

[9] Celery is a popular distributed task queue with an emphasis on real-time processing. It is written in Python and the documentation is available at `https://docs.celeryq.dev` (accessed on 2023-08-20).

[10] The `Filter` class is implemented as a subclass of the `Task` class.

`filter` classes for simple implementation of `filter`s on the exposure level and `filter`s based on the data available in the `obsinfo`.

- `obslist`: The `obslist` is a plain text file and contains the investigated observation sample for the workflow run, referenced by their unique observation identifiers. An initial `obslist` can be obtained from the XMM-Newton Serendipitous Source Catalogues based on a catalogue query (see Section 6.1) or can be created manually. For each workflow run, the `obslist` is copied to a local directory, where it can be edited by `filter`s and `task`s, e.g., to remove observations from the `obslist` or to add information about concurrent exposures for selected observations.

- `obsinfo`: The `obsinfo` represents the central database with information about the observations and their exposures, obtained from the XMM-Newton Serendipitous Source Catalogues and from the visual screening. Although the `obsinfo` can be configured for each workflow run, a single `obsinfo` is typically used for all workflow runs based on the same data release of the XMM-Newton Serendipitous Source Catalogue, as the `obsinfo` was designed to store only permanent data, such as the science mode used for the individual EPIC instrument, or information that changes infrequently, such as the position of the source in the sky, that can slightly change between catalogue versions due to calibration and software pipeline updates. The `obsinfo` is stored as a YAML file, which allows for easy manual validation, although the file is typically read, written, and updated by LEAP. An example entry for a single observation with one exposure per instrument is given in Listing 6.2.

- `config`: The `config` is the central configuration of the workflow run. It contains all configurable settings and can be imported from the Python code for access to the configuration. The configuration for a specific workflow run is provided by the user in a single YAML file as shown in Listing 6.3. Only specified items are allowed in the `config` to prevent unintended behavior due to mistakes or typing errors in the user-provided configuration files. Configuration items can be added to the `config` from within the Python code as shown in Listing 6.2. Customizable "getter" and "setter" methods are supported to enable sanity checking of the provided configuration and to prepare the directory structure according to the configuration.

```python
from leap.config import Config, config as c
from leap.filter import filter
from leap.observation import Observation
from leap.task_registry import loop_observations, task


@task
@loop_observations(support_ces=False)
def download_obs(obs: Observation) -> None:
    """Download and unpack an observation from the XMM-Newton
    Science Archive."""
    obs.download()


Config.add_item("min_obs_time", default=1000)


@filter
def remove_short_obs(obs: Observation) -> bool:
    """Remove short observations. Note that this function needs
    to return False in order to filter out an observation."""
    limit = c.min_obs_time
    if obs.get_gti_duration() < limit:
        return False
    return True
```

Listing 6.1: Registering a `task` and a `filter` to the task registry, and adding an optional item with default value to the `config`, that is later referenced in the filter function. With the `@loop_observations` decorator, the task is automatically executed for every observation in the `obslist`, here with deactivated support of concurrent exposures for simplicity. As `filter`s are designed to operate on all observations in the `obslist`, the observation loop is implicitly included in the `filter` decorator.

```
0851180401:
  dec: -34.191688566118
  iauname: 4XMM J011908.6-341130
  max_ser:
    mos1: 30
    mos2: 30
    pn: 30
  mos1S002:
    bkg_reg: circle(-3365.3292,-4940.1557,1300,DETX,DETY)
    pileup: no
  mos1_filter: Thin1
  mos1_mode: PrimeFullWindow
  mos2S003:
    bkg_reg: circle(-4796.9609,-1768.0171,1500,DETX,DETY)
    pileup: no
  mos2_filter: Thin1
  mos2_mode: PrimeFullWindow
  pnS001:
    bkg_reg: circle(2365.2392,3279.5718,600,DETX,DETY)
    pileup: no
  pn_filter: Thin1
  pn_mode: PrimeFullWindow
  ra: 19.785963264447
  srcid: 206578201010001
```

Listing 6.2: `obsinfo` entry for observation 0851180401. The entry contains information about the source, the selected science modes, and the selected filters of the three EPIC instruments, which were obtained from the XMM-Newton Serendipitous Source Catalogue. The maximum source extraction radii and the preferred background regions of the individual exposures were obtained during visual screening. Furthermore, a pile-up estimation is given for each exposure, which was automatically determined and stored by a previous run of the pileup `task` in the filter pipeline.

```
obslist: /corrarea-data/OBSLIST_3XMM_DR7_smallwindow.txt
obsinfo: /corrarea-data/3XMM_DR7_obsinfo.yaml

deflaremethod: gauss_snr
fitting_ref_instrument: PN

tasks:
  - deflare
  - find_concurrent_exposures
  - apply_gtis
  - filter_short_observations
```

Listing 6.3: Excerpt from a sample configuration file. References to the `obslist` and `obsinfo` files are given together with two exemplary `config` items. The tasks list contains four `task` names that will be executed in the given order.

The command line interfaces of LEAP and the CORRAREA tool are simplistic, as all configuration is provided in the central configuration file, and follow the structure `leap CONFIG_FILE [TASK]...` and `corrarea CONFIG_FILE [TASK]...`, respectively. By providing a list of `task`s in the command line interface, the list of `task`s in the configuration file can be overwritten, which is useful for repeated execution of selected `task`s during visual screening, spectral model definition, or workflow development. However, manual selection of `task`s via the command line interface is disregarded for running the full CORRAREA workflow, as it might lead to a more complicated provenance tracking for the results of the workflow. A list of all `task`s registered at runtime can be obtained using `leap --help` or `corrarea --help`. Since all user-defined configurations are stored in human-readable YAML or plain text files, that include also the performed `task`s, applied `filter`s, and their execution order, version control systems can be conveniently used to keep track of the performed analyses.

The major components of the CORRAREA workflow are shown in Figure 6.1. Starting from the XMM-Newton Serendipitous Source Catalogues, a sample of suitable observations (see Section 7.1) is filtered, visually screened, and used for determining the stacked data-to-model ratios, residual ratios, and the correction functions using the fit-and-stack approach. In the CORRAREA workflow implementation, these components are split into six different meta

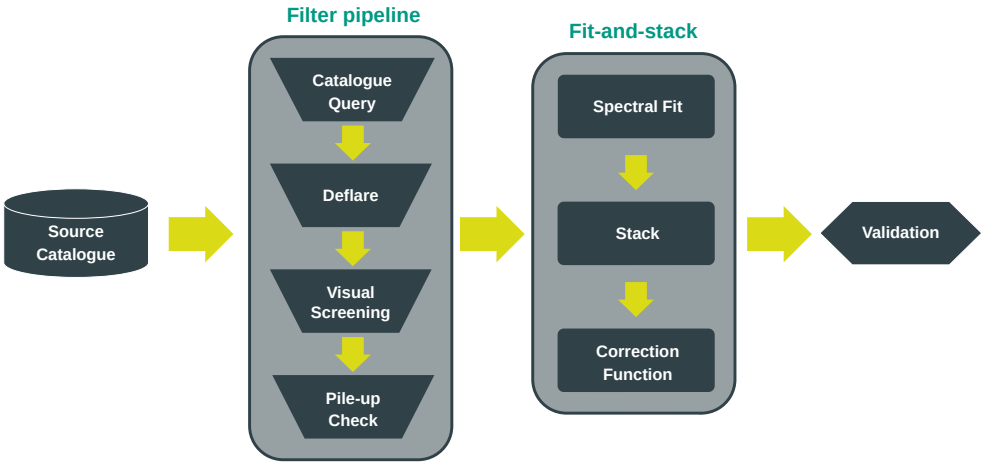

Figure 6.1.: The CORRAREA workflow and its major components. An initial selection of observations is based on data from the XMM-Newton Serendipitous Source Catalogue, followed by further filter steps including visual screening. The workflow implements a fit-and-stack approach followed by the derivation of the CORRAREA correction functions and a final validation step.

`task`s or "stages", each representing a collection of workflow `task`s.

- `Stage 0`: Catalogue query.
- `Stage 1`: Basic processing of observations, deflaring, and preparation of the images needed for visual screening.
- `Stage 2`: Filtering of observations, pile-up estimation, and extraction of the spectral products based on the information from the visual screening.
- `Stage 3`: Spectral fitting.
- `Stage 4`: Stacking of data-to-model ratios and residual ratios.
- `Stage 5`: Calculating MOS-to-pn flux ratios for validation.

For the validation and sub-sample analyses shown in this thesis, the CORRAREA tool was used in version 1.0, based on LEAP version 1.0, together with the most recent CCFs available at the time of writing, referenced as XMM-CCF-REL-399[11]. The XMM-Newton SAS was used in version 21.0.0 together with the High Energy Astrophysics Software (HEASoft) (Nasa High Energy Astrophysics Science Archive Research Center (Heasarc), 2014) version 6.30.1.

6.1. The filter pipeline

The filter pipeline of the CORRAREA workflow provides a filtered set of observations, and extracts the spectral products for the source and the background region required for the spectral fitting during the fit-and-stack method. It consists of `Stage 0`, `Stage 1`, and `Stage 2`, although `Stage 0` is omitted in the default CORRAREA workflow, as it is only needed to obtain new observation lists from the catalogue. The filter pipeline is a reimplementation of the scripts from Heinitz (2021) for the LEAP infrastructure, leaving the methods of the data processing, deflaring, visual screening, and pile-up steps largely unchanged.

6.1.1. Catalogue query

In the catalogue query step, an initial source sample is filtered from the XMM-Newton Serendipitous Source Catalogue in the 3XMM (Rosen et al., 2016) or 4XMM (Webb et al., 2020) version and from a configurable data release. The filtering is performed by LEAP using a Structured Query Language (SQL) query built from a set of filter expressions given in the configuration file. An SQLite[12] version of the source catalogue is required, produced from the SQL statements included in the source catalogue data releases. In addition to the observation list, an `obsinfo` is produced containing a configurable set of fields filled from the source catalogue for later reference during the workflow runs.

[11] A list of CCF updates and release notes is available at `https://www.cosmos.esa.int/web/xmm-newton/ccf-release-notes` (accessed on 2023-08-20).

[12] `https://sqlite.org` (accessed on 2023-08-21).

6.1.2. Data processing

In the data processing step, the observations are downloaded from the XMM-Newton Science Archive, a calibration index file referencing the appropriate CCFs for each observation is produced using `cifbuild`, and housekeeping data required by the subsequent SAS commands is extracted using `odfingest`. Furthermore, calibrated event lists of the EPIC instrument exposures are produced using the SAS meta tasks `emproc` and `epproc`.

As the SAS tools use randomization for rebinning, which can lead to different data-to-model residuals across workflow runs (Dennerl, 2019), a fixed random seed can be set in the configuration of the Corrarea workflow, which is used together with the observation identifier to obtain a reproducible random seed for each observation.

6.1.3. Finding good time intervals and concurrent exposures

The Good Time Intervals (GTIs) of the individual exposures, describing time intervals without high background activity induced by proton flares, are determined from the single-event pattern lightcurves at high energies (10 keV to 12 keV for EPIC-pn and >10 keV for the EPIC-MOS instruments). Two count rate thresholds are determined using different methods. The first method is based on a Gaussian fit and the count rate threshold is set at $\mu + 3\sigma$. For the second method, the signal-to-noise ratio is calculated for count rate ranges with different upper limits, and the upper limit corresponding to the maximum signal-to-noise ratio is chosen as threshold (Piconcelli et al., 2004). Finally, the more conservative of the two thresholds is chosen for the selection of common GTIs between the three instruments.

Although each XMM-Newton observation typically consists of one exposure per instrument, sometimes multiple exposures per instrument can be contained in an observation, e.g., when an instrument had to be restarted during an observation. This can lead to common GTIs across exposure boundaries. In the previous stack-and-fit approach, the source and background counts were stacked for the exposures of a single observation. However, for the fit-and-stack method the common GTIs must be split at the exposure boundaries into individual “concurrent exposures”, as different exposures of a single instrument

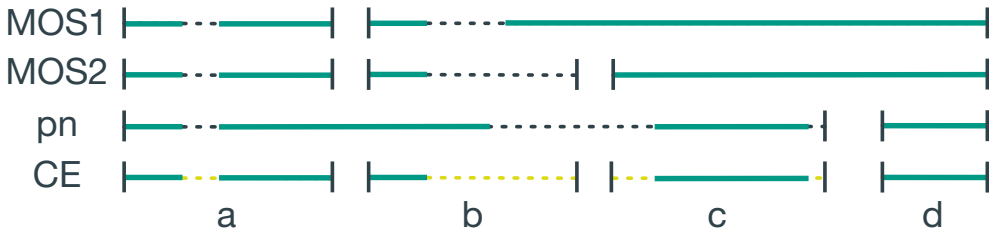

Figure 6.2.: Visualization of the concurrent exposure (CE) principle for an exemplary observation with multiple exposures per instrument and common GTIs including intervals of different exposures. The concurrent exposures are designed to contain only one exposure per instrument and a single observation can be split into multiple concurrent exposures. Exposures are illustrated in gray, concurrent exposures in yellow, and GTIs in green.

might require adapted spectral modeling, such as different valid energy ranges. The concurrent exposures principle is illustrated in Figure 6.2. LEAP can automatically detect concurrent exposures and supports individual handling of every concurrent exposure in the subsequent steps of the workflow. The identifiers of concurrent exposures are constructed from the observation identifier by appending a lowercase letter in ascending order, such as `0673730101a`, `0673730101b`, and `0673730101c`.

6.1.4. Visual screening

Before it can be added to the source sample, every new observation and all of its exposures must be visually screened. The visual screening procedure is a manual process, but has to be done only once, as all of the user-provided information is automatically stored in the `obsinfo` for further workflow runs. The visual screening is an integral part of the LEAP workflow and optimized for ease of use by guiding the user through the visual screening process. Exposures are automatically opened in the SAOImage DS9 (Joye and Mandel, 2003) image viewer, and the user information is collected directly using the interface of the image viewer and by terminal prompts.

In the visual screening process, every exposure is manually tested for suitability,

and exposures are marked as excluded otherwise, e.g., in case of chip gaps or bad CCD columns that are located very close to the source, in case of a chip loss affecting the source, or in case of broken exposures. The whole observation is excluded in case of extended sources[13], or when other sources are located close to the observed source, such that it is not possible to select a suitable maximum source extraction radius without containing events from the nearby source. Furthermore, maximum source extraction radii are defined for every exposure, and a suitable background region is selected based on a set of instrument and science-mode specific recommendations that are automatically displayed in the image viewer, as shown in Figure 6.3. In LEAP version 1.0, the user can define the most suitable background region by selecting and optionally modifying the recommended regions directly in the image viewer, which is then automatically saved to the `obsinfo` for further use.

More details about the visual screening procedure and the preferred background regions for each instrument and science mode are available in Heinitz (2021). Details about the realization of the visual screening procedure in the LEAP workflow can be found in Lober (2023).

6.1.5. Estimating the level of pile-up

In addition to the mode-dependent count rate filter available in `Stage 0` that can be used to remove heavily piled-up observations, three different methods for pile-up estimation are available in the LEAP workflow, that are described in detail in Heinitz (2021).

For the EPIC-MOS camera, the pile-up is determined from the fraction of diagonal pattern events and "clean" pattern events up to quadrupels[14]. Diagonal pattern events are assumed to be produced almost only from pattern pile-up of two single pattern events due to geometrical considerations of the electron charge cloud extent produced in the detector. Therefore, the diagonal pattern method gives a solid pile-up estimation for the EPIC-MOS cameras, and the exposure pile-up level is either set to `yes` (piled-up) or `no` (pile-up free).

[13] Although a point-like filter is included in the catalogue query, some extended sources were found to be present in the initial sample of potentially useful observations.

[14] More precisely, the SAS pattern codes 0 to 12 are considered.

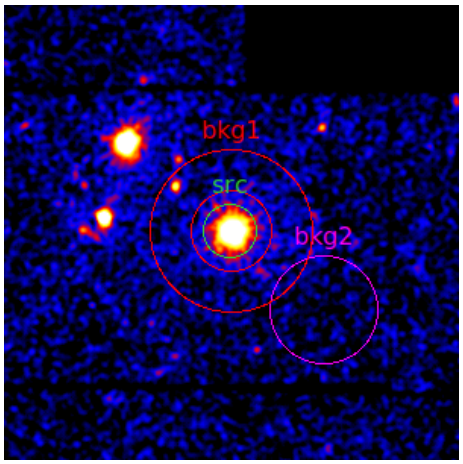

(a) Full frame mode EPIC-MOS.

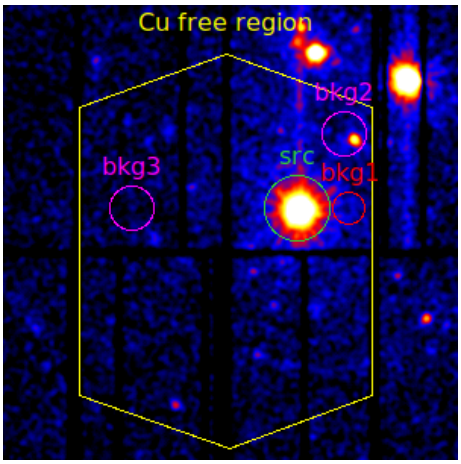

(b) Full frame mode EPIC-pn.

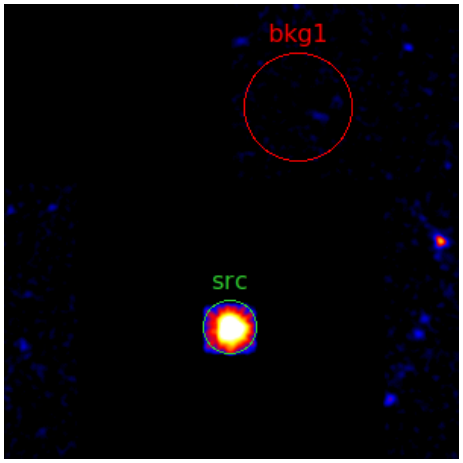

(c) Small window mode EPIC-MOS.

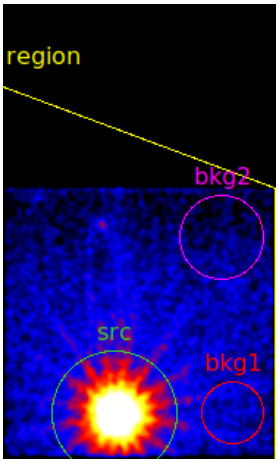

(d) Small window mode EPIC-pn.

Figure 6.3.: For the manual background region selection during the visual screening process, a set of mode-dependent static background region recommendations are displayed. The user can select a suitable background region by interactively adapting the shown background regions. The screenshots shown in (a)-(b) were obtained from observation `0006220201`, the ones shown in (c)-(d) from observation `0690870501`.

The diagonal pattern analysis is impractical for the EPIC-pn camera, as diagonal patterns are not available in the transmitted data. Thus, the pile-up level of EPIC-pn exposures is estimated from the source region count rate calculated using the SAS `eregionanalyse` tool and the mode-dependent count rate limits from ESA: XMM-Newton SOC (2023b). The count rate limits are only an indirect indication of the pile-up possibility, and for many cases it is not possible to tell with confidence if an exposure is piled-up. Therefore, four pile-up levels are available in LEAP for the EPIC-pn detector. Exposures above the count rate limit are either marked as `yes` (piled-up) if the count rate exceeds the count rate limit by at least 10 %, or `(yes)` (likely piled-up) otherwise. Exposures below the count rate limit are set to the pile-up level `(no)` (likely pile-up free) if the count rate is above 90 % of the limit, or `no` (pile-up free) otherwise. Based on these pile-up levels that are determined automatically, the exposures can be filtered in the future steps of the workflow to enable analyses with sub-samples of, e.g., only pile-up free observations.

For a further manual investigation of pile-up, which is optional and typically only needed if a more solid pile-up estimation for the EPIC-pn detector is required, LEAP produces a pattern plot series using the SAS `epatplot` tool for annuli around the source with different inner radii. While the pattern plot series is produced automatically, the interpretation of the results and the update of the `obsinfo` need to be done manually. Exemplary pattern plots produced by `epatplot` of a piled-up and a pile-up free EPIC-pn exposure including the source center are shown in Figure 6.4. In the piled-up exposure, the deviations of the pattern fractions from a model describing the expected pattern fractions without pile-up can be clearly seen, while the pattern fraction is consistent with the model in the pile-up free exposure. In these two exemplary cases, the manual `epatplot` based analysis confirmed the pile-up level estimates that were automatically produced using the methods described above.

6.2. The fit-and-stack approach

In the fitting part, the manually provided spectral models are fitted to the EPIC-pn spectra independently for every exposure to obtain the best fit EPIC-pn model. The source and background spectra are extracted by LEAP following the source and background region definitions from the visual screening, and an

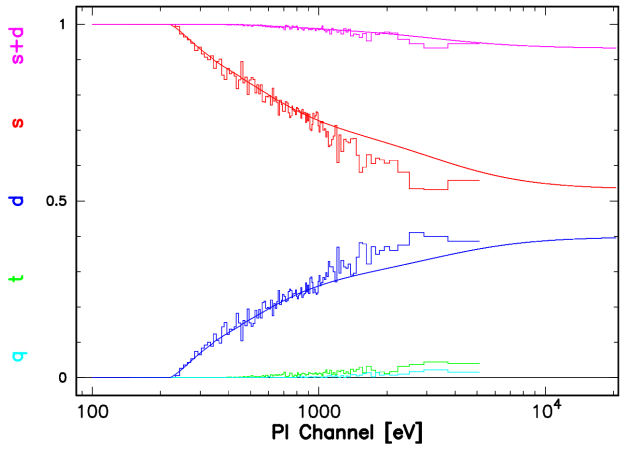

(a) Piled-up exposure of observation `0101440601`.

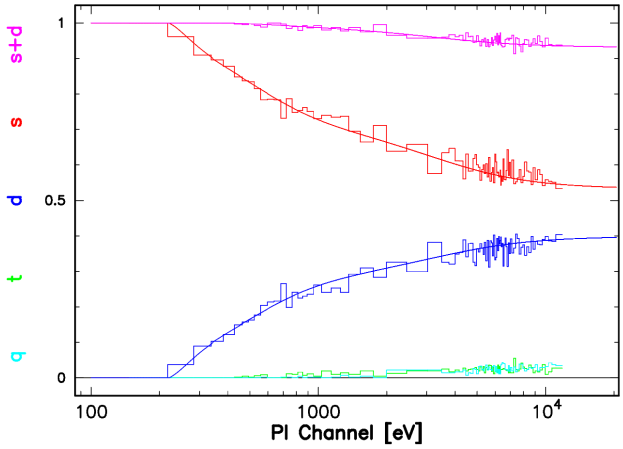

(b) Pile-up free exposure of observation `0006220201`.

Figure 6.4.: Pattern fraction plot for a piled-up and a pile-up free EPIC-pn exposure produced by `epatplot` (modified for improved clarity). Single, double, triple, and quadruple patterns are denoted by s, d, t, and q, respectively. For the exposure marked as piled-up in the automated count rate based method using `eregionanalyse` (a), the fraction of single patterns is clearly lower than the model prediction, which is a strong indication for pile-up.

optional configuration of a source extraction radius in the CORRAREA workflow configuration. This best fit EPIC-pn model is then fitted with fixed parameters to the EPIC-MOS data.

Spectral fitting is performed using the Interactive Spectral Interpretation System (ISIS) (Houck and Denicola, 2000) and the Cash statistic (Cash, 1979), that can optionally be replaced by other statistics in the workflow configuration. The concurrent exposure specific information needed by the fitting stage, such as the source-specific spectral model, start parameters, and a suitable valid energy range, are provided in a single configuration file per concurrent exposure. Based on this file, the CORRAREA workflow creates the ISIS scripts for the individual fits and runs the fit-and-stack stage automatically. Together with the spectral and model data, the fitting stage produces plots for every performed fit for optional visual quality verification, and by default, the CORRAREA workflow performs fits with free and pn-tied parameters for all three EPIC instruments.

Source, background, and model counts as determined by ISIS are then stacked by the workflow. Subsequently, the stacked EPIC-MOS data is rebinned to the energy grid used for EPIC-pn. The EPIC-pn and EPIC-MOS data-to-model ratios are calculated as described by equation 5.3 and equation 5.4, respectively, and the MOS-to-pn ratios are determined following equation 5.5.

For better visibility in the produced ratio plots, the data-to-model ratios and MOS-to-pn ratios are rebinned for a minimal signal-to-noise ratio starting from the highest energy bin. The minimum signal-to-noise ratio can be set in the workflow configuration, and throughout this thesis, a lower threshold of 50 was used. The MOS-to-pn ratios can be used for determining correction functions either by fitting analytic functions to the ratios or by interpolation with cubic splines. However, for the derivation of the new CORRAREA correction functions, a more sophisticated pre-convolutional method was used as described in Section 7.2, that is currently not implemented in the automated CORRAREA workflow.

6.3. Validation of the correction

Automated validation of correction functions for single sources and large source samples is an integral part of the CORRAREA workflow, and parts of the data produced in the fit-and-stack approach are directly suitable for validation. By

setting `applyxcaladjustment: true` in the workflow configuration, optionally combined with the `additional_ccfs: /path/to/my/ccfs` parameter for validating customized and non-official CCFs, the CORRAREA workflow can be executed with activated CORRAREA correction. As part of `Stage 3`, plots of the best fit results and data-to-model residuals are produced for each instrument with free and fixed parameters, which can be used for visual investigation of the correction effects on single sources. Furthermore, plots of the stacked data-to-model ratios and MOS-to-pn ratios (if pn is chosen as reference instrument) are created as part of `Stage 4`, which provide a useful measure for validation as discussed in the following chapters. In `Stage 5`, the validation stage, MOS-to-pn flux ratio histograms and average flux ratios are calculated and visualized as shown in Figure 5.3 for different energy bands. The energy bands can be configured as part of the CORRAREA workflow configuration. In this thesis, the same flux bands were used as in Smith et al. (2021) for consistency. Combining the MOS-to-pn ratios and flux ratio histograms from workflow runs with activated and deactivated correction provides an intuitive basis for analyzing the effects of the correction on a source sample.

7. The new correction functions

In the course of this thesis, new CORRAREA correction functions were derived in collaboration with the ESAC and were published in 2021 as an update to the official XMM-Newton CCFs (Smith et al., 2021). The contributions by the Institute for Astronomy and Astrophysics Tübingen (IAAT) included the automated computational CORRAREA workflow based on the LEAP tool that was used, e.g., for data reduction, production of spectral products for the source and background regions for the default and CORRAREA-corrected effective areas, automated fitting of the individual spectra, and stacking of the data-to-model and MOS-to-pn residual ratios. The definition of the mainly physically motivated spectral models, the original fitting code, and the derivation routine of the final new CORRAREA correction functions was contributed by M. Smith (ESAC).

One mode-independent correction function for energies above 2 keV was derived and published for each EPIC instrument, keeping the EPIC-pn effective area unchanged. The new correction functions and their effect on the EPIC-MOS effective areas are shown in Figure 7.1. The implementation of the CORRAREA correction in SAS remained unchanged and only the CCFs were updated, such that the new CORRAREA correction can be applied as previously in the `arfgen` tool by providing the `applyxcaladjustment=yes` option. Currently, the CORRAREA correction is not activated by default, as such severe changes to the effective areas of up to 20 % for MOS2 at the highest energies require solid testing by the community beyond the validation studies performed as part of the update. Depending on the feedback from the community, activating the CORRAREA correction in the `arfgen` tool by default might be a subject for discussion in the future[15].

[15] Private communications with M. Smith (ESAC).

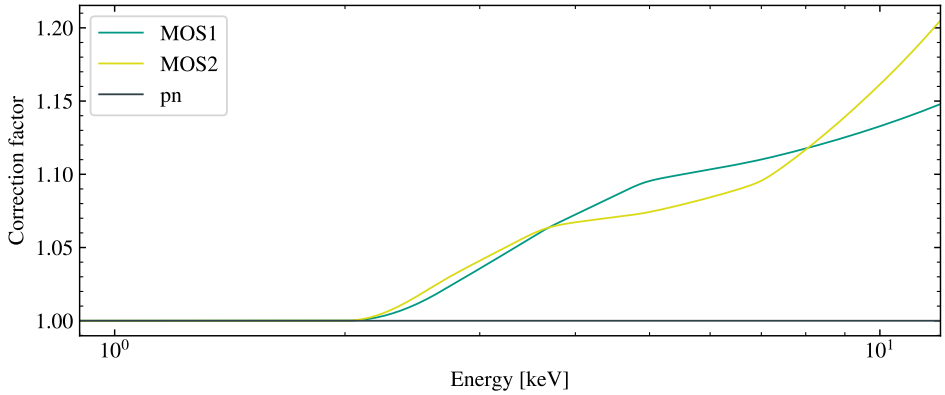

(a) CORRAREA correction functions.

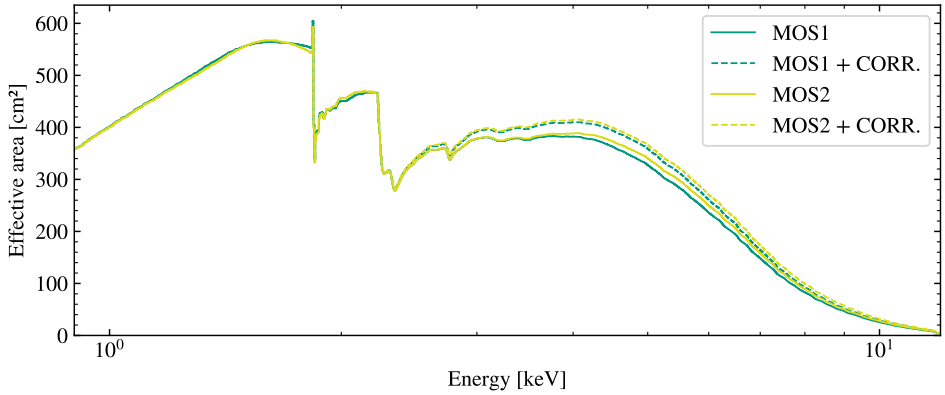

(b) Effective areas.

Figure 7.1.: (a): The new CORRAREA correction functions for MOS1, MOS2, and pn as implemented in SAS. The corrections for MOS1 and MOS2 only apply to energies above 2 keV, and the EPIC-pn effective area remains unchanged. (b): The impact of the new CORRAREA correction functions available in SAS on the MOS1 and MOS2 effective areas. The effective areas were computed by the SAS `arfgen` task for observation `0006220201`. Only the mirror effective areas and detector quantum efficiencies were modeled by `arfgen`, without corrections for the point spread function or bad pixels, and without modeling the filter transmission or contamination.

7.1. Source selection and the source sample

The source sample used for deriving the new CORRAREA correction functions was based on the XMM-Newton Serendipitous Source Catalogue in the 3XMM-DR7 version containing information about around 9700 observations. The catalogue was filtered for bright but pile-up free point-like sources in the `Stage 0` catalogue query, and the selection criteria described below were consistent with the extended sample described in Heinitz (2021).

- **Point-like:** Only point-like sources were considered, and extended sources were removed from the sample by filtering for `EP_EXTENT=0`.
- **On-axis:** As CORRAREA is a correction for the on-axis effective area, only on-axis sources with a maximum boresight-to-source distance of $2'$ were considered by filtering for `EP_OFFAX<2`.
- **Outside of the Galactic plane:** Sources located at absolute Galactic latitudes of less than 15° were removed from the sample to prevent possible effects due to absorption, introduced by accumulating the counts of multiple highly absorbed sources in the Galactic plane in the stack-and-fit approach (Read et al., 2014). This requirement was kept for consistency with earlier CORRAREA studies and might be removed in the future to allow for larger source samples (see Section 9.3).
- **Science mode:** Full frame, large window, and small window modes were considered. Mixed modes, where the EPIC-MOS and EPIC-pn instruments were operated in different science modes in a single observation, were allowed.
- **Filter:** Thin, medium, and thick filters were allowed, also in mixed configurations.
- **Total number of counts:** An instrument-specific minimum total number of source counts, 5000 for EPIC-MOS and 13 500 for EPIC-pn, was used to filter for bright sources.
- **Count rate:** An instrument and science mode specific maximum source count rate was applied based on the values given in ESA: XMM-Newton SOC (2023b) to remove sources that are expected to show strong pile-up from the sample. For the EPIC-MOS instruments, the count rate

limits were 0.7 counts s^{-1}, 1.5 counts s^{-1}, and 4.5 counts s^{-1} for the full frame, large window, and small window modes, respectively. For EPIC-pn, the limits were 6.0 counts s^{-1}, 3.0 counts s^{-1}, and 25.0 counts s^{-1} for full frame, large window, and small window, respectively. In the current version of the XMM-Newton Users Handbook, lower count rate limits are given for the EPIC-MOS and EPIC-pn in the full frame modes. The former higher limits were kept for consistency with previous CORRAREA studies and because of the more sophisticated pile-up analysis later in the workflow as described in Section 6.1.5, that allows to remove piled-up sources.

- **Isolated sources:** Only isolated sources were considered. Crowded fields, where other sources were located too close to the central source on the detector, were removed from the sample. This filter is performed after the SQL query by removing all observation identifiers that appeared more than once in the filtered list, which indicates that more than one bright source was detected in the catalogue, matching the selection criteria including the on-axis restriction for a single observation.

These selection criteria resulted in an initial sample size of 347 observations that was selected from the total of about 9700 observations in the 3XMM-DR7 catalogue. In `Stage 1` of the CORRAREA workflow, 13 of those observations were removed due to very short common GTIs below 1000 s. In the visual screening, one or several exclusion reasons were found for 71 observations, mainly extended emission in the vicinity of the source (65 cases) and crowded fields (38 cases). Thus, the sample contained 262 suitable observations, which are listed in Heinitz (2021). For each of the 262 observations, individual spectral models were defined by M. Smith (ESAC) to allow this sample to be used together with the fit-and-stack method.

The pile-up analysis in the CORRAREA workflow detected 163 pile-up free, 70 piled-up and 29 vaguely piled-up observations. The pile-up free sample was then manually curated by M. Smith (ESAC) to obtain a very clean final sample for the derivation of the new CORRAREA correction, e.g., by removing soft sources, by reducing the number of different observations of the same source to reduce the impact of a few sources with many counts on the sample, or by removing sources with lower goodness of the fit compared to the other fits in the sample. The final sample contained 120 concurrent exposures in 116

observations and is listed in Smith et al. (2021) including the science modes and filter configurations for each concurrent exposure.

7.2. Derivation and validation of the new correction functions

The new CORRAREA correction was derived using the fit-and-stack approach in a pre-convolution variant explained below, and is described in Smith et al. (2021), whereupon this section is based. Concurrent exposures were found and spectral products were produced by the LEAP tool as described in Chapter 6, using the maximum source extraction radii and background regions as defined in the visual screening. The stacked EPIC-MOS and EPIC-pn data-to-model ratios for the final sample of 120 concurrent exposures were obtained by independently fitting the concurrent exposures and stacking and rebinning of the source and model counts as described in Section 6.2. The data-to-model ratios were subsequently normalized to the EPIC-pn data-to-model ratios.

The uncorrected data-to-model ratios and the ratio of the data-to-model ratios are shown in Figure 7.2, as automatically reproduced by the CORRAREA workflow with the most recent SAS and CCFs available at the time of writing this thesis. While the pn-to-pn ratios are unity by design, the MOS-to-pn ratios would also be unity in case of a perfectly consistent calibration of the instruments. Towards higher energies above around 3 keV, the MOS-to-pn ratios increase similarly for MOS1 and MOS2, with slight differences in the respective slopes. At the highest energy bin, a strong increase in the MOS-to-pn ratios is found, which was also apparent in the data produced with earlier CCFs and used for the derivation of the new CORRAREA correction; as the reasons for this jump remained unclear, and since the EPIC-pn data-to-model ratios drop at the highest few energy bins potentially indicating modeling issues at the highest energies that notoriously suffer from little counts and low signal-to-noise, the highest bin was excluded and the correction functions were extrapolated in the range of 10 keV to 12 keV (Smith et al., 2021). At the lowest energies, the MOS-to-pn ratios significantly differ from the ratios shown in Smith et al. (2021), which dropped below unity below around 0.22 keV. This is likely due to

a recent update of the EPIC-MOS RMFs (Rosen et al., 2023), underlining the effect of the detector response calibration on the lower energies.

The new CORRAREA correction functions were derived using a cubic spline model with five nodes at manually chosen energies, and were designed to apply only for energies above 2 keV, as corrections of the effective area at lower energies were found to be unstable for several sources, indicating relative uncertainties in the redistribution calibration, despite an on-average improvement for the whole sample (Smith et al., 2021). Expanding the CORRAREA correction towards lower energies in future work requires further investigation and is discussed in Section 9.2.

A pre-convolution derivation method was used, where the effective area correction was applied before convolving the EPIC-pn model with the RMF. The method is based on minimizing the data-to-model ratios by varying the spline model and using a simultaneous fit for all observations (Smith et al., 2021). In contrast to the more conventional post-convolution stacked residual ratio method, this method allows to minimize the EPIC-MOS data-to-model ratios without including redistribution effects introduced in the final correction. A detailed description of the post-convolution and pre-convolution methods together with a comparison of the two methods is given in Nevalainen and Molendi (2023). Following this paper, the modified EPIC-MOS data-to-model ratios for the pre-convolution method are of the form

$$R'_{\mathrm{MOS}} = \frac{\mathrm{data}_{\mathrm{MOS}}}{(\mathrm{model}_{\mathrm{pn}} \cdot J_{\mathrm{corr}} \cdot \mathrm{arf}_{\mathrm{MOS}}) \otimes \mathrm{rmf}_{\mathrm{MOS}}} \tag{7.1}$$

with a correction function J_{corr}, representing the cubic spline model for the new CORRAREA correction, where the optimal parameters are found by minimizing the modified EPIC-MOS data-to-model ratios R'_{MOS}. In a study based on a sample of galaxy clusters, the post-convolution and pre-convolution methods showed similar results, with a largest difference of 3 % at the highest investigated energy of 6 keV (Nevalainen and Molendi, 2023).

The new CORRAREA correction functions were validated by producing corrected MOS-to-pn ratios and flux histograms for different source samples, e.g., the CORRAREA sample, the full 3XMM-DR7 sample, and an independent sample of 42 bright blazars (Smith et al., 2021). MOS-to-pn ratios for the CORRAREA sample of 120 concurrent exposures with default and corrected effective area

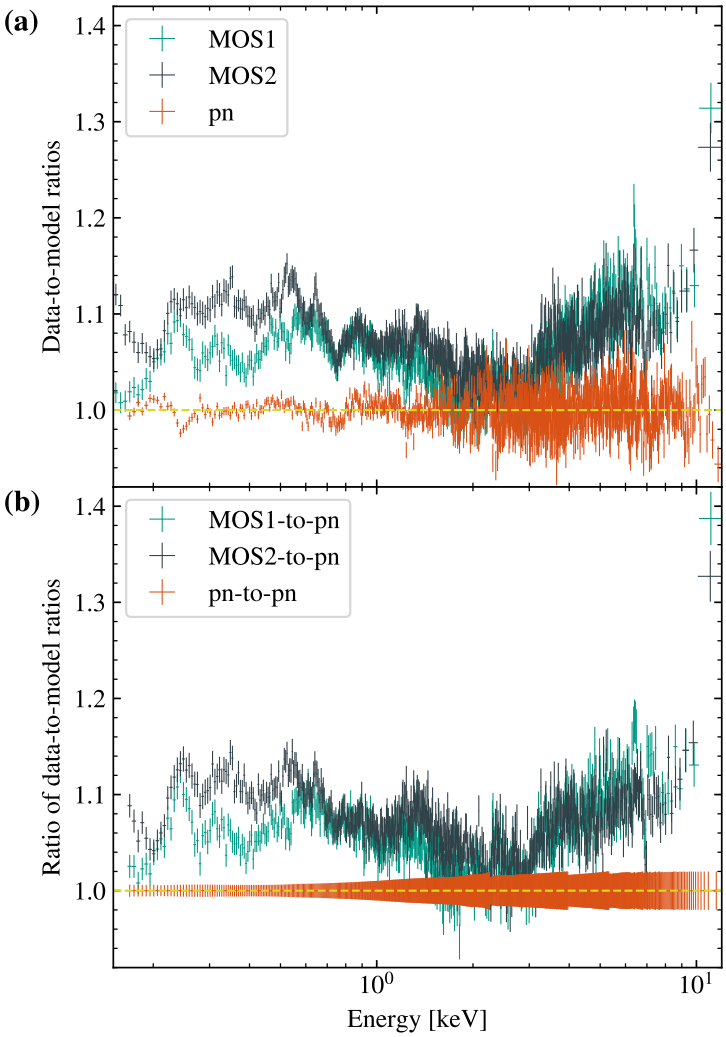

Figure 7.2.: Residuals for the CORRAREA sample, determined using SAS version 21.0.0 and the most recent calibration files. (a): Data-to-model ratios. (b): MOS-to-pn ratios and pn-to-pn ratios. The EPIC-pn data-to-model ratios represent the stacked residuals of the best-fit models for the EPIC-pn data and, by construction, the residuals are shifted to unity upon normalization.

calibrations are shown in Figure 7.3. The corrected ratios are much closer to unity compared to the uncorrected ratios, while the ratios below 2 keV remain unchanged.

The same trend exists for the flux ratio histograms obtained from the default and corrected effective area calibration, where the corrected distributions are located much closer to unity, as shown in Figure 7.4 for the energy bands affected by the new CORRAREA correction. By construction, the lowest displayed energy band in the range of 1.82 keV to 2.2 keV is only slightly affected by the correction, as the correction functions only start to slowly deviate from a factor of 1.0 (no correction) above 2 keV due to the cubic spline model with a fixed no-correction node at 2 keV. As the data in this section was produced with the most recent SAS version 21.0.0 and CCFs (XMM-CCF-REL-399), Figure 7.3 and Figure 7.4 prove the validity of the new CORRAREA correction for both EPIC-MOS instruments with the most recent calibration for the observation time period covered by the CORRAREA sample. Hence, no evidence was found that the correction needs to be updated for the current XMM-Newton calibration.

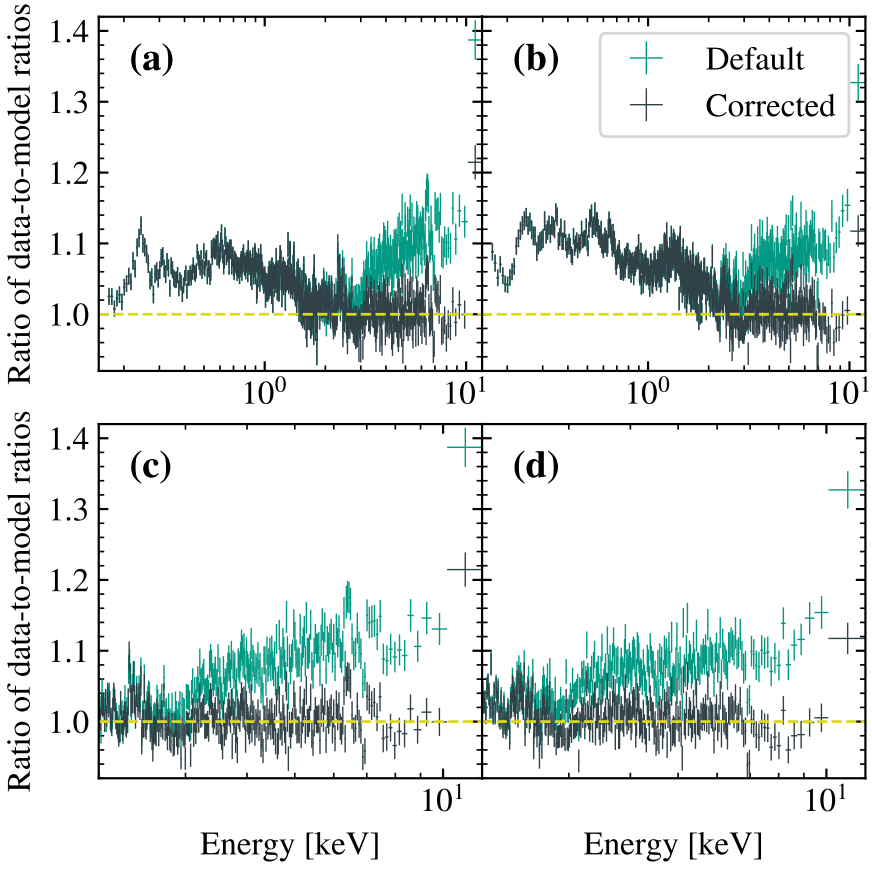

Figure 7.3.: MOS-to-pn ratios for the CORRAREA sample for MOS1 (a) and MOS2 (b). Above 2 keV the corrected ratios are much closer to unity (dashed yellow line) than the default ratios that are increasing towards high energies. At energies below 2 keV, the ratios are not affected by the correction. (c) and (d): Same as (a) and (b), but limited to the energy range affected by the CORRAREA correction for better visibility.

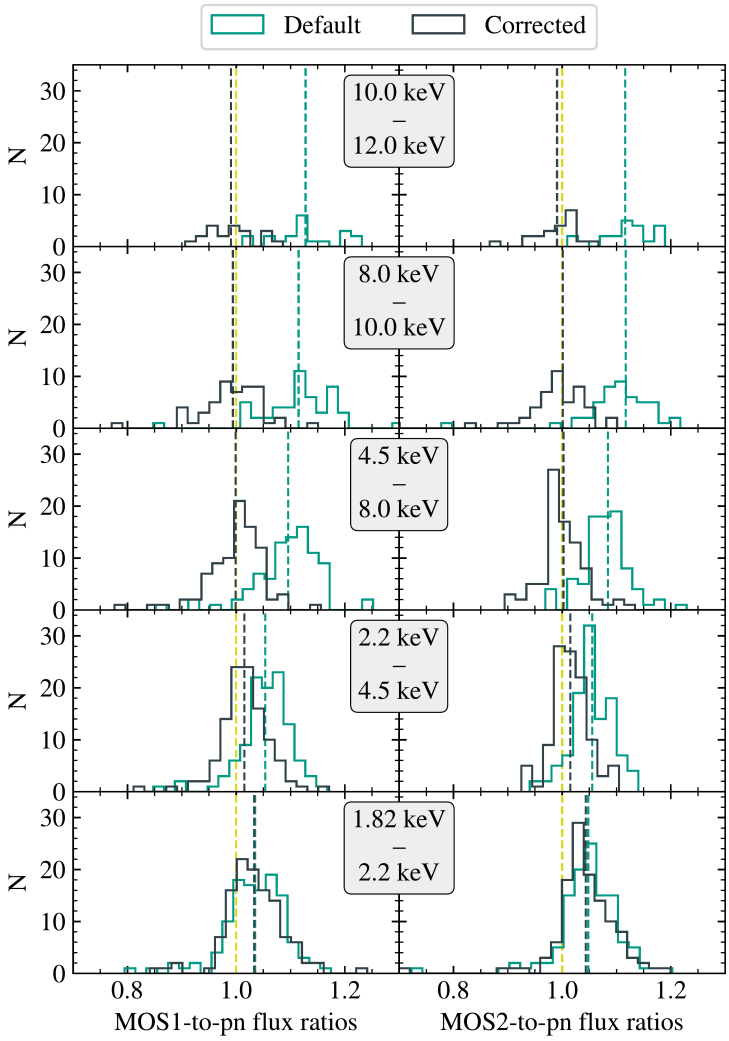

Figure 7.4.: MOS-to-pn flux ratio histograms for the CORRAREA sample for the default calibration and with activated CORRAREA correction for different energy bands. The average flux ratio values are depicted as dashed lines. The corrected flux ratios are shifted close to unity (dashed yellow lines). A few outliers are excluded for better visibility, but are included in the calculation of the displayed averages.

8. Sub-sample analyses using the new correction functions

In the following sections, sub-sample analyses were performed to investigate the dependency of the new CORRAREA correction on the science mode, the pile-up level, and the epoch when the observation was conducted. In order to extend the time period of observations included in the sample, and to allow for validation of the new CORRAREA correction for recent observations not included in the CORRAREA sample, a new sample was created based on the 4XMM-DR12 version of the XMM-Newton Serendipitous Source Catalogue using the selection criteria listed in Section 7.1, that were also used for obtaining the 3XMM-DR7 sample.

The 4XMM-DR12 catalogue incorporates observations from five additional data releases compared to the 3XMM-DR7 version. Together with more robust flux estimations for EPIC-pn introduced with the 4XMM catalogue (see discussion in Section 9.3), the number of potentially suitable observations before visual screening is more than doubled, with 749 and 347 observations for 4XMM-DR12 and 3XMM-DR7, respectively. To include recent revolutions in the time stability analysis, screening and modeling of more recent observations was prioritized and performed with the support of a student (Lober, 2023). The 4XMM-DR12-v0.1 sample, representing an intermediate step towards the full 4XMM-DR12 sample, contains 40 concurrent exposures from 39 observations not present in the 3XMM-DR7 catalogue, which are listed in Table 8.1.

The sub-samples were derived by filtering suitable concurrent exposures from the 4XMM-DR12-v0.1 sample. Although the new CORRAREA correction was derived from the smaller and cleaner CORRAREA sample, the 4XMM-DR12-v0.1 sample was used for the sub-sample analyses to include more recent observations in the time stability analysis, and to increase the signal-to-noise ratio in the investigated sub-samples, especially at high energies.

Table 8.1.: Observations in the 4XMM-DR12-v0.1 sample that are not part of the 3XMM-DR7 Serendipitous Source Catalogue. In addition to the observation identifier (Obs. ID), the science mode, filter configuration, and estimated pile-up level are given for the MOS1 (M1), MOS2 (M2), and pn exposures. The science modes are abbreviated as FF (full frame), LW (large window), and SW (small window). The filters are given as Tn (thin), Md (medium), and Tk (thick).

Obs. ID	Mode			Filter			Pile-up		
	M1	M2	pn	M1	M2	pn	M1	M2	pn
0823780701	LW	LW	LW	Md	Md	Md	no	no	(no)
0830470101	LW	LW	LW	Md	Md	Tk	no	no	no
0840220701	SW	SW	SW	Tk	Tk	Tk	no	no	no
0840740101	SW	SW	SW	Tn	Tn	Tn	no	no	no
0840800401	SW	SW	SW	Tn	Tn	Md	no	no	no
0840800501	SW	SW	SW	Tk	Tk	Tk	no	no	no
0841480101	LW	LW	SW	Tn	Tn	Tn	yes	yes	no
0841480401	LW	LW	FF	Tn	Tn	Tn	no	no	yes
0841480501	LW	LW	LW	Tn	Tn	Tn	no	no	(no)
0841481501	FF	FF	FF	Tn	Tn	Tn	no	no	no
0841481601	FF	FF	FF	Tn	Tn	Tn	yes	yes	(no)
0841481901	FF	FF	FF	Tn	Tn	Tn	no	no	no
0841482101	FF	FF	FF	Tn	Tn	Tn	yes	yes	(no)
0841482301	FF	FF	FF	Tn	Tn	Tn	yes	no	no
0841800201	FF	FF	FF	Tn	Tn	Tn	no	no	no
0842340201	FF	FF	FF	Md	Md	Md	no	no	no
0844341401	SW	SW	SW	Tn	Tn	Tn	no	no	no
0844350101	LW	LW	LW	Md	Md	Md	no	no	no
0850180201	LW	LW	LW	Md	Md	Md	no	no	no
0852210101	SW	SW	SW	Tn	Tn	Tn	no	no	no
0852380101a	SW	SW	FF	Md	Md	Tn	no	no	yes
0852380101b	SW	SW	FF	Md	Md	Tn	no	no	yes
0853980201	FF	FF	FF	Tn	Tn	Tn	no	no	no
0853980901	FF	FF	FF	Tn	Tn	Tn	yes	yes	no
0862230101	FF	FF	FF	Tk	Tk	Tk	yes	yes	yes
0863050201	LW	LW	LW	Tn	Tn	Tn	no	no	no
0863560101	LW	LW	LW	Tk	Tk	Tk	no	no	no

Table 8.1.: (continued)

Obs. ID	Mode			Filter			Pile-up		
	M1	M2	pn	M1	M2	pn	M1	M2	pn
0864810101	FF	FF	FF	Tn	Tn	Tn	no	no	no
0865040401	FF	FF	FF	Md	Md	Md	no	no	no
0870850101	FF	FF	FF	Tn	Tn	Tn	no	no	no
0870920101	FF	FF	FF	Tk	Tk	Tk	no	yes	no
0870930101	SW	SW	SW	Tn	Tn	Tn	no	no	no
0870930301	SW	SW	SW	Tn	Tn	Tn	no	no	no
0870930401	SW	SW	SW	Tn	Tn	Tn	no	no	no
0870930501	SW	SW	SW	Tn	Tn	Tn	no	no	no
0870931001	SW	SW	SW	Tn	Tn	Tn	no	no	no
0871190101	SW	SW	SW	Md	Md	Md	yes	yes	no
0872390801	SW	SW	SW	Md	Md	Tn	no	no	no
0872390901	LW	LW	LW	Tn	Tn	Tn	no	no	no
0872392901	SW	SW	SW	Tn	Tn	Tn	no	no	no

8.1. Investigating the science mode dependency

Three sub-samples containing concurrent exposures that were conducted in full frame mode, large window mode, and small window mode, excluding mixed modes where individual instruments were operated in different science modes, were investigated. To limit possible pile-up related effects, only clearly pile-up free and likely pile-up free exposures (pile-up levels `no` and `(no)`) were considered. The full frame, large window, and small window samples included 75, 52, and 51 concurrent exposures from 73, 48, and 50 different observations, respectively.

The default and corrected MOS-to-pn ratios and the MOS-to-pn flux ratio histograms in the energy bands affected by the correction are shown in Figure 8.1 and Figure 8.2, respectively. For the large window science mode, the highest energy band in the range of 10 keV to 12 keV was removed from the analysis after stacking and prior to signal-to-noise rebinning due to very low statistics, as only one source spectrum allowed for a flux estimation in this energy band. Although the Corrarea correction worked very well for that single observation

in the highest energy band with MOS-to-pn flux ratios of 0.99 for both MOS instruments, it was excluded also from the flux ratio histogram in Figure 8.2, as more observations would be needed to obtain a solid estimate of the average correction for the large window science mode at the highest energies.

For all science modes, the new CORRAREA correction resulted in a strong improvement in the consistency of the EPIC-MOS and EPIC-pn fluxes. However, a small overcorrection was revealed in the flux ratio histograms for MOS2 in the full frame and large window modes in the energy bands above 8 keV. This is also reflected in the MOS-to-pn ratios at high energies for the full frame mode above 4 keV and the large windows mode above around 7 keV, while the MOS-to-pn ratios are closer to unity for the small window mode. For MOS1, only a few overcorrected bins could be found in the ratios for the full frame mode, and the correction was very robust also for energies in the range of 8 keV to 10 keV. Although the small window mode was the least common mode in the CORRAREA sample with 30 (MOS1), 31 (MOS2), and 26 (pn) exposures out of the total 120 concurrent exposures, it contributed most of the source counts (12.5×10^6 counts of the total 19.9×10^6 counts) to the derivation of the new CORRAREA correction, which could potentially contribute to the improved correction of the MOS-to-pn ratios for the small window mode in Figure 8.1.

At energies below the CORRAREA energy range, the analysis determined strong differences depending on the science mode, with flux differences between MOS2 and pn of up to the order of 20 % for several energy bins in the large window mode. Furthermore, inconsistencies between the MOS1 and MOS2 cross-calibrations were observed in all investigated science modes. Hence, this analysis demonstrates the suitability of the CORRAREA workflow and the LEAP tool to probe the consistency of the EPIC cross-calibration also at energy ranges not affected by CORRAREA.

8.2. Investigating the effect of pile-up

Two sub-samples including observations of different pile-up levels were analyzed to investigate the effect of pile-up on the new CORRAREA correction. The pile-up free sample included 191 concurrent exposures from 184 observations, where all exposures were marked as clearly not piled-up (pile-up level `no`) by the pile-up

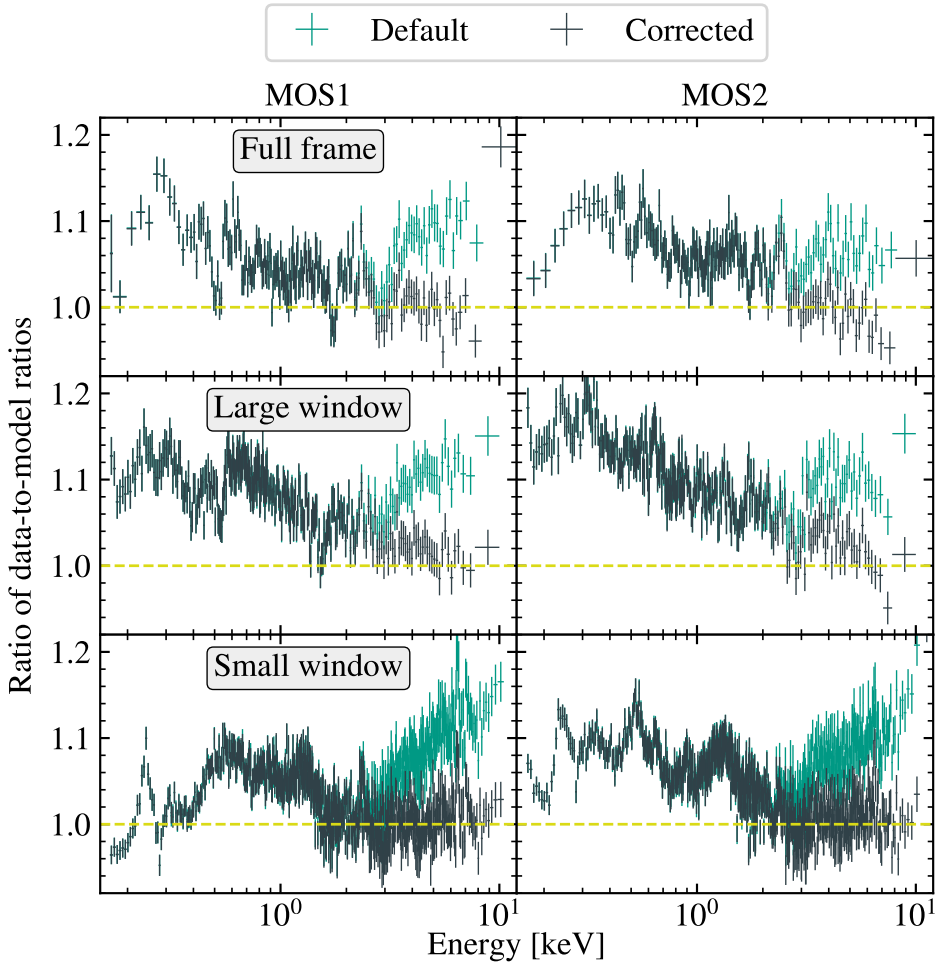

Figure 8.1.: MOS-to-pn ratios for the full frame, large window, and small window science modes for the default calibration and with activated CORRAREA correction. The corrected ratios are closer to unity than the ratios from the default calibration. For several high energy bins in the full frame mode, the corrected ratios are below unity. Inconsistencies between the science mode as well as MOS1 and MOS2 cross-calibrations are visible at lower energies.

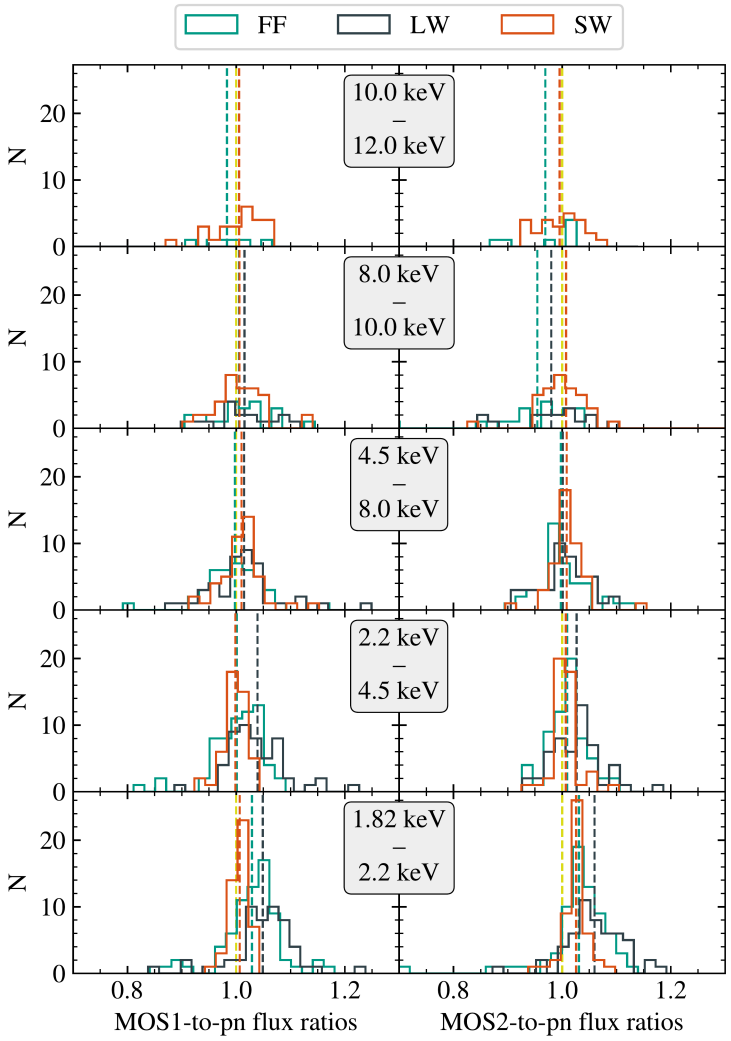

Figure 8.2.: MOS-to-pn flux ratio histograms for different energy bands with activated CORRAREA correction for the full frame, large window, and small window science modes. The average flux ratios are depicted as dashed lines. A few outliers are excluded for better visibility, but are included in the calculation of the displayed averages.

estimation stage of the LEAP tool described in Section 6.1.5. As the number of observations with clear pile-up in all EPIC exposures is low (8 observations) in the 4XMM-DR12-v0.1 sample due to the maximum count rate filter in the `Stage 0` catalogue query, the piled-up sample included all concurrent exposures with at least one exposure with clear pile-up detection (pile-up level `yes`), resulting in 109 concurrent exposures from 105 observations.

The MOS-to-pn ratios for the pile-up free and piled-up sub-samples are shown in Figure 8.3. The ratios for both sub-samples were found to be comparable for both EPIC-MOS instruments, however, the signal-to-noise ratio for the piled-up sub-sample was too low to probe the increase in the MOS-to-pn ratios at energies above 10 keV, that was present in the pile-up free sub-sample.

The flux ratio histograms of the pile-up analysis shown in Figure 8.4 demonstrate the robustness of the new CORRAREA correction for both sub-samples, and the distributions of the MOS-to-pn flux ratios are comparable across most of the energy bands for MOS1 and MOS2. While the average flux ratios for the pile-up free sub-sample are close to unity for all affected energies, slight overcorrections for the piled-up sub-sample in the order of a few percent occurred at high energies for MOS1 (8 keV to 12 keV) and MOS2 (10 keV to 12 keV). For future studies, the piled-up sub-sample could be extended by removing the count rate limits in `Stage 0`, followed by visual screening of the new candidate observations and manual spectral model selection. This will allow to also investigate the effect of the CORRAREA correction on strongly piled-up sources, which are not present in the 4XMM-DR12-v0.1 sample.

8.3. Investigating the time stability of the correction

For validating the new CORRAREA correction for observations from different time points in the more than two decades long lifetime of the XMM-Newton observatory, the 4XMM-DR12-v0.1 sample was divided into four epochs depending on the revolution of the observation and containing only exposures with the pile-up levels `no` and `(no)`. Each epoch spanned 1000 revolutions[16]. The number of observations varied for the different epochs, with 39, 44, 82, and

[16]The most recent observation available in the 4XMM-DR12 catalogue was performed at revolution 4027 in December, 2021.

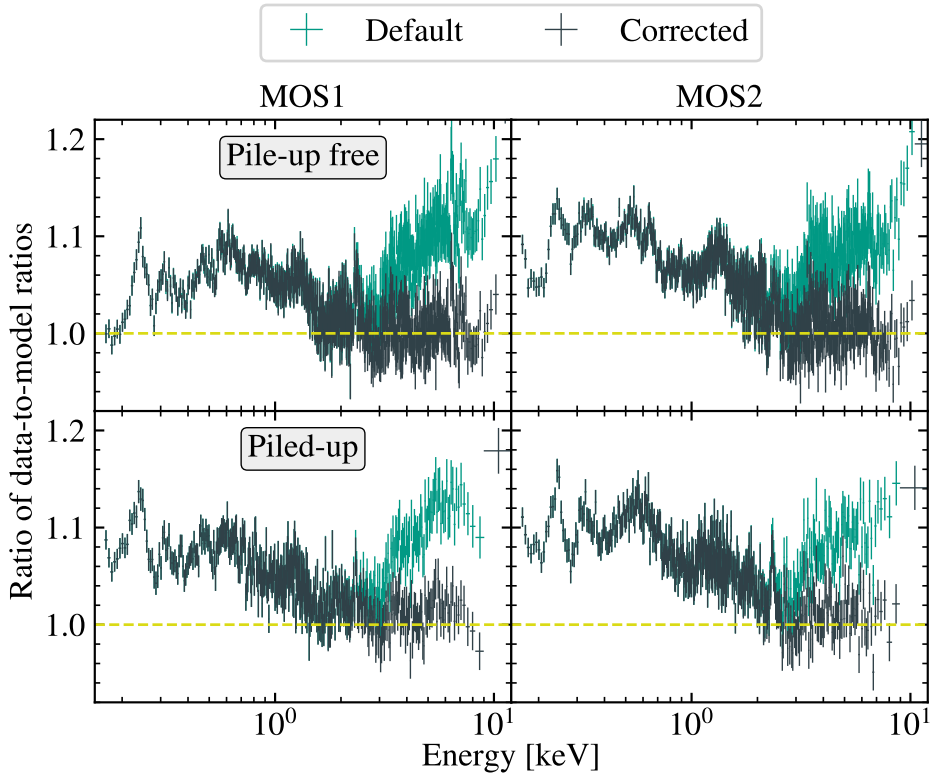

Figure 8.3.: MOS-to-pn ratios for sub-samples of piled-up and pile-up free observations for the default calibration and with activated CORRAREA correction. The CORRAREA corrected ratios are close to unity above 2 keV, demonstrating the stability of the correction also for the slightly piled-up observations included in the sub-sample.

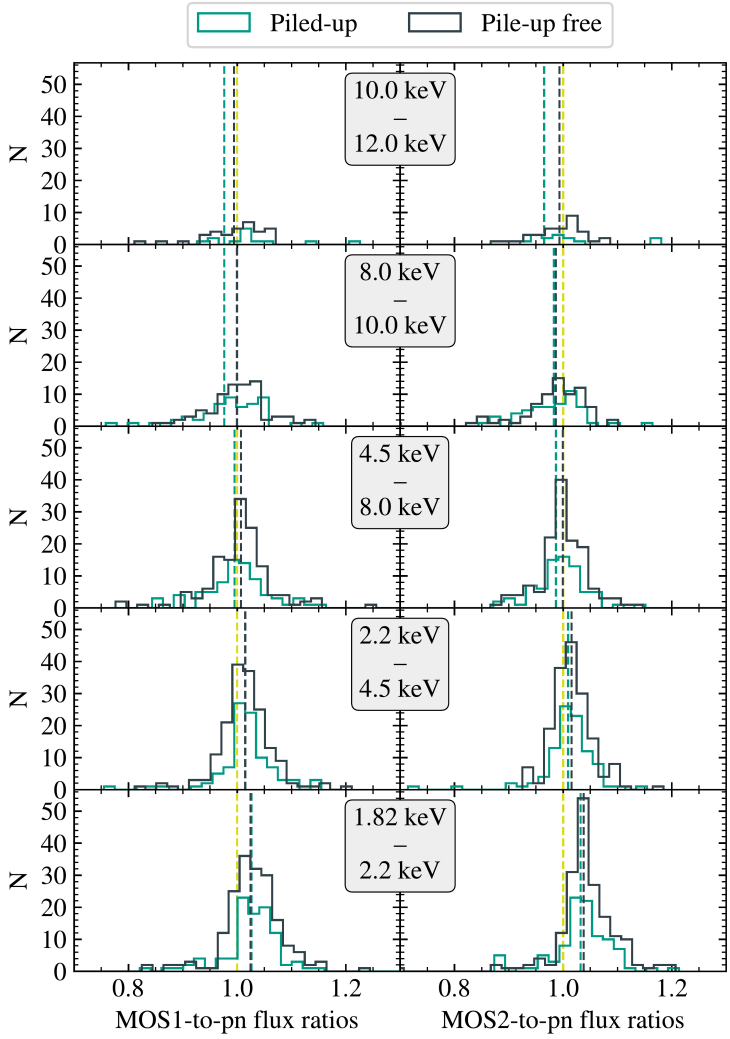

Figure 8.4.: MOS-to-pn flux ratio histograms for different energy bands with activated CORRAREA correction for sub-samples of piled-up and pile-up free observations. The average flux ratios are depicted as dashed lines. A few outliers are excluded for better visibility, but are included in the calculation of the displayed averages.

37 concurrent exposures from 38, 43, 76, and 37 observations for epochs one to four, respectively.

The MOS-to-pn ratios shown in Figure 8.5 revealed good overall agreement in the four epochs for the CORRAREA related energies above 2 keV. However, differences exist in the energy range around 1 keV to 2 keV, that also manifested in a spread of the average MOS-to-pn flux ratios in the lowest energy band affected by CORRAREA shown in Figure 8.6. The reasons for these discrepancies are unclear, as the effective area calibration uncertainties should dominate at this energy range and the effective area at these energies is not expected to change significantly during the in-orbit time of XMM-Newton. For the most recent epoch, only four EPIC-MOS exposures could be used for determining the fluxes in the energy range of 10 keV to 12 keV, so the potential overcorrection for MOS2 could result from low statistics and should be interpreted with caution.

At the lowest energies, the MOS-to-pn ratios reveal a time dependency described in the following for both EPIC-MOS cameras. Furthermore, MOS1 and MOS2 revealed significant cross-calibration uncertainties at lower energies in the two recent epochs. In the earliest epoch, the MOS1-to-pn ratios below 0.7 keV significantly deviate from unity with MOS1-to-pn ratios between 1.05 and 1.19, while in the epoch between revolutions 2000 and 2999 and towards the lowest energies below 0.6 keV, the MOS1-to-pn ratios are decreasing to unity (minimum MOS1-to-pn ratio of 0.97) except for a peak of 1.10 at around 240 eV. In the most recent epoch, the MOS1-to-pn decrease below 0.6 keV is less pronounced, with a minimum ratio of 1.02. For MOS2, the earliest and most recent epochs show different trends than the epochs between revolutions 1000 and 2999. In the epoch between revolutions 2000 and 2999, the MOS2-to-pn ratios are almost flat below 0.6 keV and only drop towards a minimum of 1.03 below a peak at around 240 eV (similar to the peak described for MOS1). However, in the same energy range, the MOS2-to-pn ratios in the most recent epoch show a different trend and significantly larger deviations from unity with ratios between 1.09 and 1.19, similar to the earliest epoch, where the ratios are between 1.07 and 1.15.

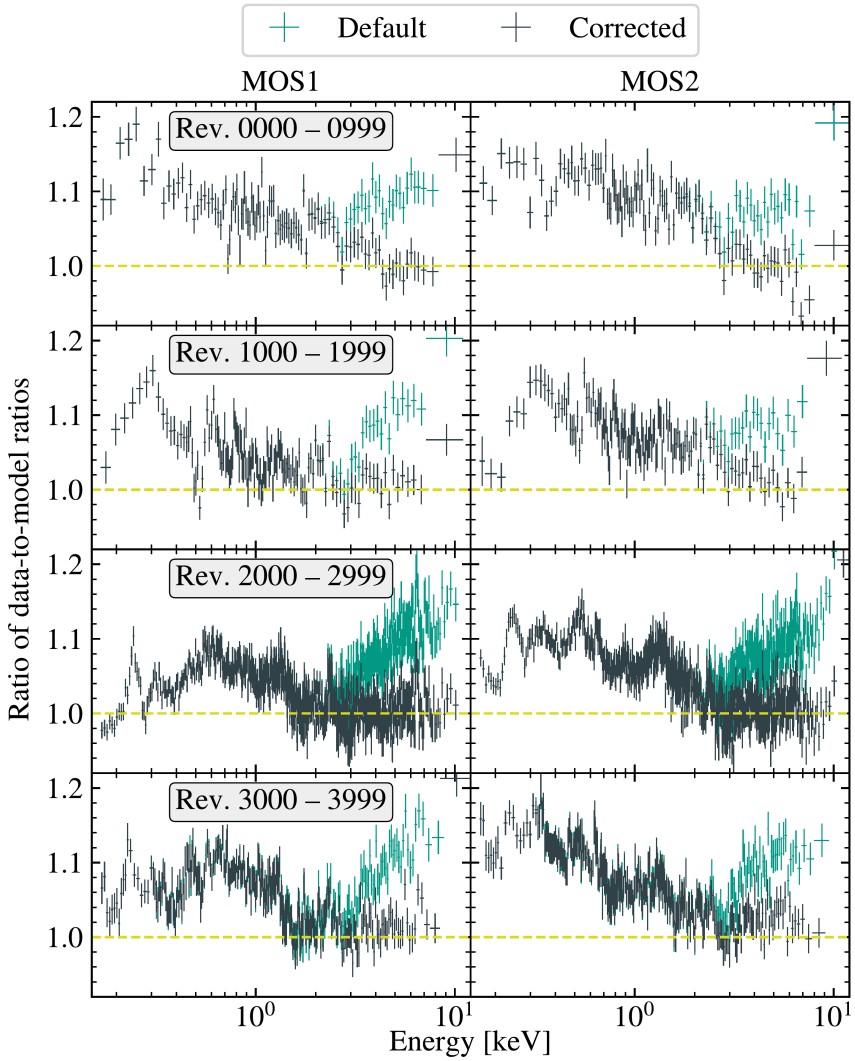

Figure 8.5.: MOS-to-pn ratios in four epochs obtained with default calibration and with activated CORRAREA correction. For energies above 2 keV, the ratios in the different epochs are comparable and apart from some deviations especially for MOS2, the CORRAREA corrected ratios are shifted close to unity. At lower energies, the ratios are time-dependent and in the most recent epoch, MOS2 ratios show a different trend than in earlier epochs.

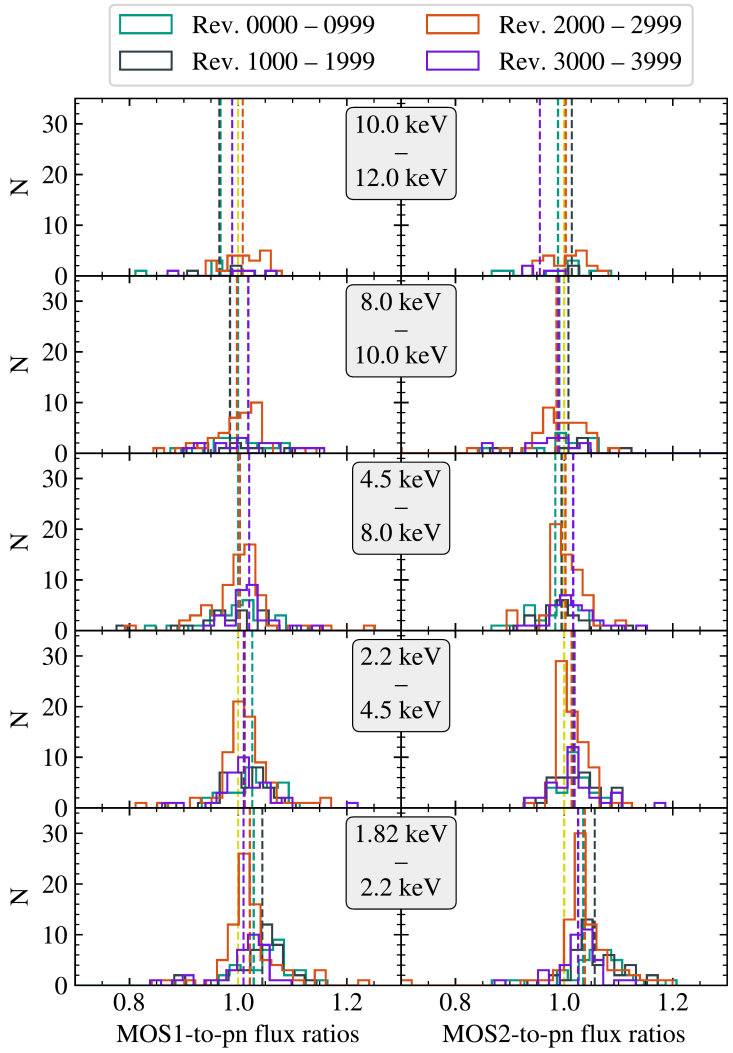

Figure 8.6.: MOS-to-pn flux ratio histograms for different energy bands with activated CORRAREA correction in four XMM-Newton epochs. The average flux ratios are depicted as dashed lines. A few outliers are excluded for better visibility, but are included in the calculation of the displayed averages.

9. Discussion

The CORRAREA correction was derived from a large source sample and, thus, is also designed to represent a mean effective area correction for large source samples. For individual observations, the outcome of the CORRAREA correction may vary, and for some observations, the correction can even increase the relative difference of the fluxes derived from EPIC-MOS and EPIC-pn. However, on average, the new CORRAREA correction functions lead to a strong improvement in the relative effective area calibration and consequently to decreased differences in the derived fluxes.

The sub-sample analyses conducted in the course of this thesis demonstrate the robustness of the new CORRAREA correction functions across science modes, pile-up levels, and time epochs. The small differences in some energy bands discussed in Chapter 8 provide useful information about the potential origin of parts of the remaining uncertainties. However, the differences revealed in the sub-samples analyses are too small to explain the overall relative difference in the EPIC-MOS and EPIC-pn effective area calibrations that led to the development of the CORRAREA correction. Hence, the main contributions to the relative differences of the effective area calibrations are independent of calibration effects considering science mode, pile-up, and time variability. Furthermore, the sub-sample analyses yielded significant differences in the relative MOS-to-pn calibration at lower energies and demonstrated the suitability of the CORRAREA workflow to provide useful data and validation based on large source samples also for calibration topics besides the effective area calibration.

The generic and flexible LEAP tool can be extended to support instruments on other missions. LEAP, the CORRAREA workflow, and the large sample of physically motivated spectral models are a powerful combination that enables the investigation of further calibration aspects based on large source samples.

With the selection of the EPIC-pn instrument as reference instrument for the

correction, the EPIC-MOS fluxes are modified to be more consistent with the EPIC-pn fluxes. However, this does not imply that the fluxes of the EPIC-pn instrument are closer to reality than the EPIC-MOS fluxes, and in essence, the selection of the EPIC-pn instrument as reference is arbitrary. The selection of EPIC-pn is supported by the stability of its calibration over the XMM-Newton lifetime (Saxton, 2022) and the missing grating in its line of sight corresponding to a larger absolute effective area compared to the EPIC-MOS instruments (Smith et al., 2021). Furthermore, the EPIC-pn instrument is also used for deriving the ABSCORRAREA correction based on cross-calibration with the NuSTAR mission (Fürst, 2022a,b).

The CORRAREA correction is an empirical correction specifically for the on-axis effective area of the XMM-Newton EPIC instruments, based on a large sample of point-like sources, and was not optimized or validated for off-axis sources. Effective area calibration effects for off-axis positions, such as vignetting, could be included into the effective area cross-calibration, e.g., by considering extended sources such as galaxy clusters (Nevalainen and Molendi, 2023), or by selecting a sample of point-like sources at off-axis positions.

The high degree of automation of LEAP and the CORRAREA workflow is crucial to allow for a continuous validation of the CORRAREA correction included in the official CCFs in case of published calibration changes, as performed as part of Chapter 7. In case of a physically motivated calibration change affecting the relative MOS-to-pn flux differences at energies above 2 keV, the CORRAREA functions, as an empirical correction, would need to be updated to account for the changes. These validations can be performed in a fully automated manner using the CORRAREA workflow, except for potential interface-breaking changes in SAS updates.

9.1. The fit-and-stack and stack-and-fit approaches

In the course of this thesis and the derivation of the new correction functions (Smith et al., 2021), the CORRAREA project switched from the previously used stack-and-fit approach (Read et al., 2014; Guainazzi et al., 2014; Heinitz, 2021) to the fit-and-stack method. While both methods have their own advantages

and disadvantages, this change was made for several reasons discussed in this section.

The fit-and-stack method is more established in the high-energy calibration community than stack-and-fit[17], which is also reflected in XMM-Newton related cross-calibration efforts, where mostly fit-and-stack is used (Longinotti et al., 2008; Stuhlinger et al., 2010; Kettula et al., 2013; Schellenberger et al., 2015; Fürst, 2022a,b; Nevalainen and Molendi, 2023) rather than stack-and-fit (Read et al., 2014; Guainazzi et al., 2014; Heinitz, 2021). Using fit-and-stack consistently across cross-calibration projects simplifies the combination of subsamples and the comparison of residual ratios from different corrections, and in the course of this thesis, initial work had started to find a common sample of observations to investigate the effect of using the CORRAREA correction together with the ABSCORRAREA (pn-to-NuSTAR) correction (Fürst, 2022a,b) on the EPIC-MOS-derived fluxes.

The derivation of correction functions mixing exposures from different science modes is simplified, as stacking of the ARFs and RMFs is not necessary, which posed challenges for proper exposure-weighting including the mode-specific live time of the detectors for the stack-and-fit approach (Heinitz, 2021).

One of the main differences between both methods is the use of mainly physically motivated spectral models for individual sources in the fit-and-stack method, while the stack-and-fit method needs to rely on a purely empirical model that fits the stacked data sufficiently well. With the source-specific spectral models, differences in the EPIC-MOS and EPIC-pn instrumental responses, such as different energy resolutions, can be considered in the fitting process. In the stack-and-fit method, these differences could potentially result in slightly different features in the stacked spectra. In contrast, the source-specific spectral models commonly lead to small features in the residuals resulting from imperfect physical modeling of the source. However, the normalization of the data-to-model ratios to the pn-to-model ratios should minimize remaining systematical errors, such that the effect in the stacked residuals can be expected to be minimal. Regardless, small differences in the stacked MOS-to-pn ratios are washed out in the derivation of smooth correction functions. Thus, the choice of the correction model, e.g., a Gompertz function (Guainazzi et al., 2014; Heinitz, 2021) or cubic splines with a fixed number of pre-defined nodes (Smith

[17] Private communications with M. Smith (ESAC).

et al., 2021), has arguably more impact on the final correction functions than potential slight differences resulting from the chosen stacking method.

In Read et al. (2014) and Heinitz (2021) the concern was discussed that the fit-and-stack method could potentially lead to an underestimation of the MOS-to-pn ratios at the highest energies due to stacking bins with low statistics and probably negative counts resulting from background subtraction. However, no evidence for such an underestimation was found in this work, since the produced MOS-to-pn ratios and the derived new CORRAREA corrections are higher than the stack-and-fit derived corrections from Guainazzi et al. (2014) and Heinitz (2021) at high energies.

Adding new observations to the source sample in case of the fit-and-stack method results in additional manual work due to the required spectral model, in addition to the visual screening that must be done for both methods. However, these spectral models are not only used for the derivation of the correction functions, but are also indispensable for the generation of the MOS-to-pn flux ratios, which, as also demonstrated in this thesis, are a valuable tool for the validation of the correction functions. Furthermore, individual spectral modeling of the observations, considering absorption effects when needed, will allow to include sources located in the Galactic plane in the source sample, which will allow to significantly increase the number of sources before visual screening (see Section 9.3).

9.2. Expanding the correction functions to lower energies

The new CORRAREA correction only affects energies above 2 keV due to the conservative approach focused on the prevention of the introduction of artificial features in the corrected source spectra. While an expansion of the correction towards lower energies is possible in principle and planned as future work, the impact of the redistribution calibration is increasing with lower energies and dominates the calibration uncertainties at the very low energies below 0.5 keV (Read et al., 2014). Thus, for expanding the correction of the effective area to lower energies, the derivation of the correction based on the MOS-to-pn residual ratios must be adapted, as the residual ratios also include redistribution

effects, which should be corrected for in the redistribution calibration instead of in the effective area calibration. An extension of the CORRAREA correction towards lower energies, investigated during the derivation of the new CORRAREA correction, resulted in reduced relative flux uncertainties for large samples, but increased the relative difference in flux for some individual observations, which could be a consequence of redistribution effects included in the effective area correction (Smith et al., 2021).

In the effective areas of the EPIC instruments shown in Figure 7.1, pronounced features are visible at the silicon K-α edge of 1.7 keV and at the gold M-α edge of 2.1 keV, linked to the detector quantum efficiency and the mirror effective area, respectively (ESA: XMM-Newton SOC, 2023b). In the new CORRAREA correction, the silicon feature is not affected by the correction, and the multiplicative correction factor at the gold feature is small due to the fixed spline node of unity at 2 keV. For expanded correction functions, careful validation is necessary to ensure that no artificial features are introduced at the silicon and gold edges despite flat functions, e.g., by amplifying potential relative calibration uncertainties.

9.3. Increasing the source sample

As shown above, sub-sample analyses are a useful approach to disentangle and probe the relative uncertainties of the calibration of isolated detector effects and settings on the total effective area calibration. However, filtering sub-samples reduces the available statistics and can easily lead to low sub-sample sizes that are not sufficient to draw reliable conclusions. Thus, increasing the sample size is important to support and enable further sub-sample analyses. New data releases are regularly published for the XMM-Newton serendipitous source catalogue, that typically contain sets of recent observations suitable for enlarging the source sample.

With the introduction of the 4XMM catalogue version and the accompanied changes to the software and calibration used for catalogue construction as described in Webb et al. (2020), 212 observations that previously had been filtered out in the `Stage 0` catalogue query for the 3XMM catalogue versions now passed the query. In the course of this thesis, the 50 oldest of those

observations with observation identifiers between `0005010101` and `0203260101` were manually investigated for their exclusion reasons in the 3XMM catalogue versions. For 47 of the 50 investigated observations, the EPIC-pn-related fields were unfilled in the 3XMM catalogue versions, which caused their removal by the maximum EPIC-pn count rate and minimum total counts filters in the catalogue query, while valid values were included in the 4XMM catalogue versions. Thus, the more robust EPIC-pn pipeline used for the 4XMM catalogue construction allows for a large increase of the source sample size. On the other hand, 14 observations were removed from the initial sample with the 4XMM versions due to slightly increased EPIC-MOS count rates in the catalogue. In the 3XMM-DR7 sample, 10 of those 14 observations were excluded in visual screening due to crowded fields or extended emission in the source region, and the EPIC-MOS exposures of the remaining four observations were piled-up.

A further increase in the number of sources can be achieved by including sources located in the Galactic plane. These sources were originally excluded from the CORRAREA samples because of the stack-and-fit approach, which could be susceptible to the introduction of possible absorption-based effects by stacking counts from sources with high column densities (Read et al., 2014). Since the fit-and-stack approach allows the use of physically motivated spectral models, absorption models can be added for individual sources, and the suitability of observations can be decided on a case-by-case basis. Thus, the general requirement of a minimum Galactic latitude of 15° can be removed from the catalogue query in the future.

The potential increase in the source sample size is shown in Figure 9.1 by visualizing the source positions of the observations that pass the `Stage 0` catalogue query for the 3XMM-DR7 catalogue (347 observations), the 4XMM-DR12 catalogue (749 observations), and the 4XMM-DR12 catalogue with the Galactic latitude filter removed (1076 observations). In total, the initial sample that was used to determine the CORRAREA correction can be more than tripled, which will require significant screening and spectral modeling efforts. This effort could be supported by students new to the field, as the user-friendly automation of the visual screening procedure and the ISIS-based spectral fitting make the preparation of new sources for the sample a suitable way for students to familiarize themselves with the data analysis methods and tools used in X-ray astrophysics.

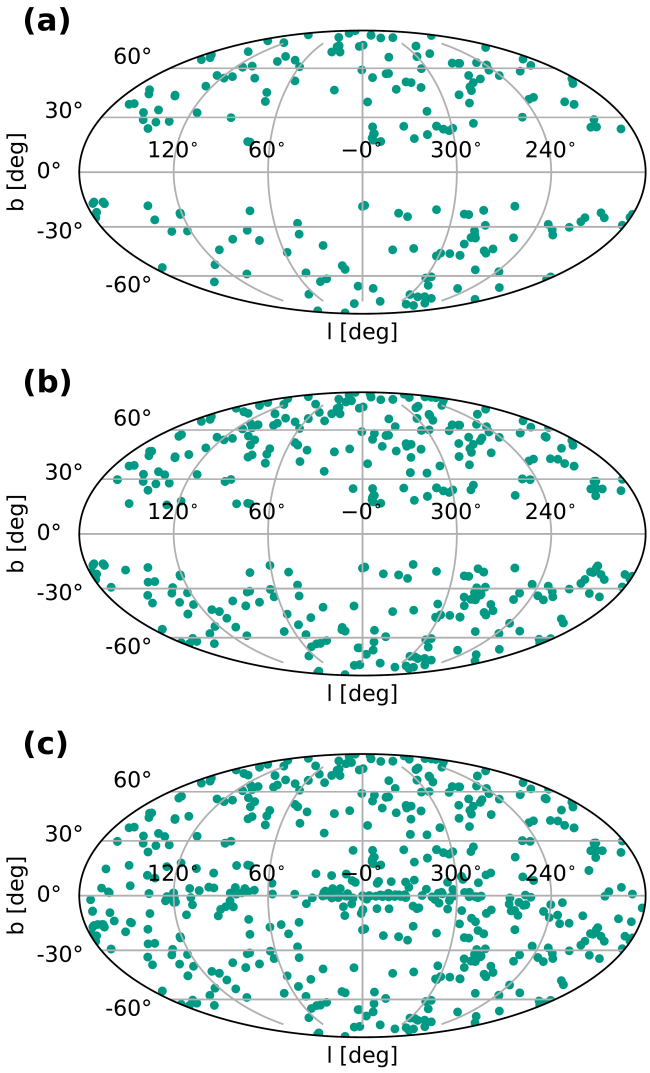

Figure 9.1.: Source positions in Galactic coordinates using the Mollweide projection for three different observation samples after `Stage 0`. The samples were obtained using the criteria described in Section 7.1 from the 3XMM-DR7 catalogue (a) and the 4XMM-DR12 catalogue (b). (c): The 4XMM-DR12 catalogue sample including sources in the Galactic plane.

Project II.

Characterizing the eROSITA particle-induced background

Project II

Contents

Project II

10. Introduction

MC simulations were conducted in this project to reproduce and characterize the Filter Wheel Closed (FWC) background of the extended ROentgen Survey with an Imaging Telescope Array (eROSITA) instrument. The simulations incorporated a new camera mass model, as well as a new digitizer and data analysis workflow developed as part of this project. Based on the simulation results, the origins of the prominent fluorescence lines in the FWC background were investigated.

10.1. The eROSITA instrument

The Spectrum-Roentgen-Gamma (SRG) mission was successfully launched into a *Halo* orbit around the second Lagrangian Point L_2 on July 13, 2019, by a Proton-M rocket from the Baikonour Cosmodrome (Sunyaev et al., 2021). The mission goal is to accomplish an all-sky survey using the two scientific instruments with grazing incidence optics on board of the spacecraft. The primary instrument is the eROSITA X-ray telescope observing in the 0.2 keV to 8 keV energy range (Predehl et al., 2021), which is complemented towards higher energies by the *Mikhail Pavlinsky* Astronomical Roentgen Telescope – X-ray Concentrator (ART-XC) telescope observing in the 4 keV to 30 keV energy range (Pavlinsky et al., 2021). Eight scans of the sky were originally planned in the scan mode of SRG, where the spacecraft performs a constant rotation. The eight scans correspond to a time frame of four years, since the full sky is covered over the six months duration of one *Halo* orbit. After the all-sky survey, a phase of pointed observations was planned. However, after having finished four of the eight scans, eROSITA was put into safe mode pausing science operation on February 26, 2022, following the Russian invasion

of Ukraine[18], and until the time of writing of this thesis science operation was not restarted.

The eROSITA instrument consists of seven separate cameras placed in the focal planes of seven individual mirror modules with a focal length of 1600 mm, each consisting of 54 Wolter-1 mirror shells (Friedrich et al., 2008; Ferrario et al., 2017). Pictures of the mirror modules assembled at the front side of the instrument and the electronics boxes and cameras at the rear side of the instrument are shown in Figure 10.1.

Each camera contains a back-illuminated, fully-depleted, 450 µm thick CCD, which is an improved version of the EPIC-pn instrument on board of XMM-Newton (Strüder et al., 2001), with 384 × 384 pixels and a pixel size of 75 µm × 75 µm, corresponding to a field of view of 1.0° (Meidinger et al., 2014). Besides better energy resolution, the main improvement is the integration of a frame-store area, which leads to a strongly reduced number of out-of-time events for bright sources shown in Figure 10.2, achieved by quickly shifting the charges from the imaging area into the X-ray-shielded frame-store area, where the almost two orders of magnitude slower read-out takes place using three CMOS Amplifier and MultiplEXer (CAMEX) Application-Specific Integrated Circuits (ASICs) (Meidinger et al., 2008). The frame-store CCD layout is shown in Figure 10.3 and the read-out cycle is described in more detail in Section 12.4. Five of the seven CCDs (TM1, TM2, TM3, TM4, and TM6; in the following this selection is referred to as TM8) include an on-chip aluminium filter with a thickness of 200 nm for blocking optical light and a 200 nm thick polyimide foil in the filter wheel, while a 100 nm thick optical light filter is placed on the 200 nm thick polyimide foil in the filter wheel for TM5 and TM7 (Meidinger et al., 2021).

The CCD is placed inside a 3 cm thick copper shield for protection against the cosmic radiation environment. To protect against fluorescence X-rays produced in this copper shield, which would lead to strong copper K-α and K-β fluorescence lines at around 8.0 keV and 8.9 keV, respectively, a graded-Z shield is used to effectively reduce the fluorescence yield and transform the

[18] See the MPE "Statement on the status of the eROSITA instrument aboard Spektr-RG (SRG)" from March 2, 2022 (`https://www.mpe.mpg.de/7856215/news20220303` (accessed on 2023-10-09)) and from November 17, 2022 (`https://www.mpe.mpg.de/7912248/news20221117` (accessed on 2023-10-09)).

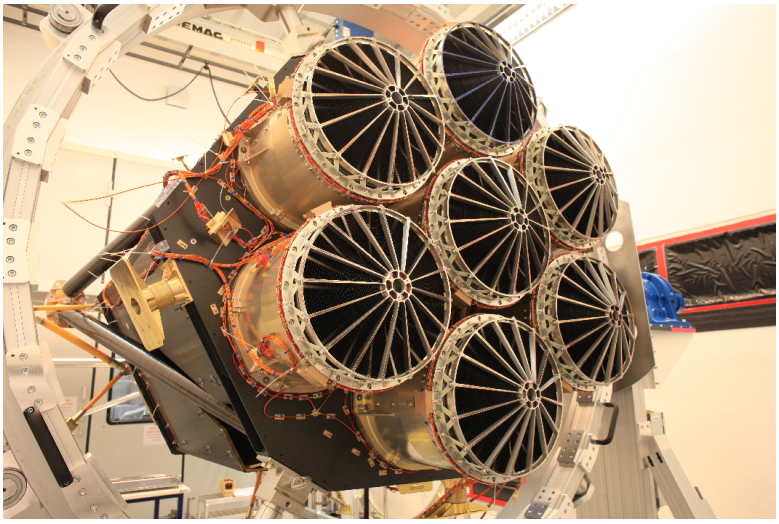

(a) Front view.

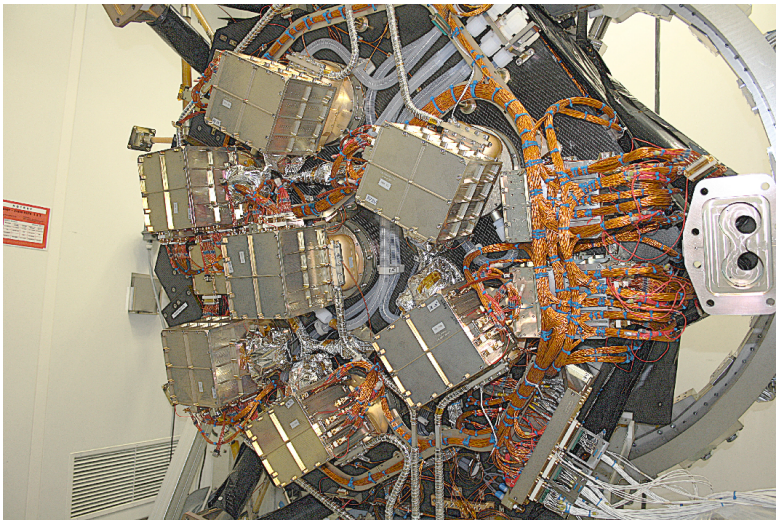

(b) Rear view.

Figure 10.1.: Pictures of the eROSITA telescope during assembly. Front-view of the seven eROSITA mirror modules (a) and rear-view of the seven eROSITA cameras and electronics boxes (b). Image credit: Predehl et al. (2021), used under CC BY 4.0.

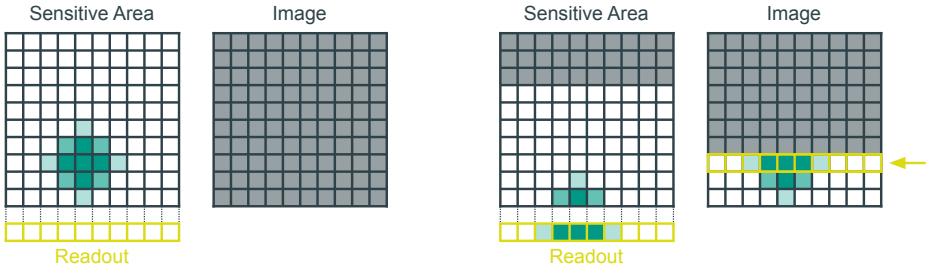

(a) After integration.

(b) Row-by-row read-out.

(c) X-ray detected during read-out.

(d) X-ray detected during read-out.

(e) Final image.

Figure 10.2.: Out of time events during CCD read-out. As illustrated in the time series from (a) to (e), the out of time events detected in (c) and (d) lead to read-out streaks in read-out direction in the final image. The complete and animated gif is available at: `http://astro.uni-tuebingen.de/~pommranz/outoftime.gif` (accessed on 2024-01-04).

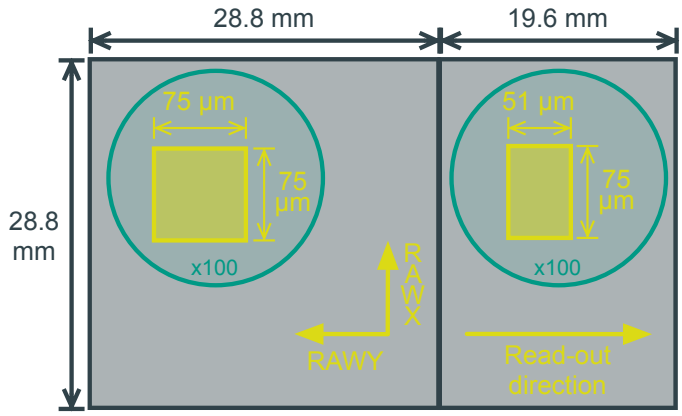

Figure 10.3.: The eROSITA frame-store CCD. The imaging area on the left consists of square 75 µm × 75 µm pixels and the frame-store area on the right consists of rectangular 75 µm × 51 µm pixels. Note that the pixels in the green circles are enlarged by a factor of 100 for better visibility. Both CCD parts are divided into 384 × 384 pixels.

fluorescence line energies to energies below the lower end of the eROSITA energy range of 200 eV by using layers of materials with gradually lower atomic number Z absorbing the fluorescence lines produced in the outer layers and re-emitting fluorescence lines of lower energy (Meidinger et al., 2008). The outer layer of the three-layer eROSITA graded-Z shield is represented by the copper shield, the middle layer is implemented in the form of an aluminium housing around the detector, and the inner layer consists of beryllium plates below the CCD and around the aperture and boron-carbide plates mounted above the frame-store area (Meidinger et al., 2021).

The all-sky image in the 0.3 keV to 2.3 keV energy band from the eROSITA All-Sky Survey 1 (eRASS1) completed in June 2020 is shown in Figure 10.4. While this image shows all of the sky, the eROSITA data are split at a galactic longitude of 180°: data with $l < 180°$ belong to the Russian consortium and data with $l > 180°$ belong to the German consortium (Predehl et al., 2021). The release of the eRASS1 X-ray catalogues with around 930 000 sources in the 0.2 keV to 2.3 keV energy band and around 5500 sources in the harder 2.3 keV to 5.0 keV energy band, and the first eROSITA Data Release (DR1), both

containing data only from the German consortium, were conducted in 2024 (Merloni et al., 2024).

During eRASS1, the eROSITA instrument showed a high observing efficiency of around 96.5 % with the main efficiency loss attributed to Single Event Upsets (SEUs) in the Camera Electronics (CE) and Interface and Thermal Controller (ITC) units, which don't include Triple Module Redundancy (TMR) for additional radiation hardening (Merloni et al., 2024; Predehl et al., 2021). In the first two years of operation, the eROSITA CCDs were hit several times by micrometeoroids, which caused only small damage to the detectors, such as bad pixels or bright columns, and did not lead to a significant performance decrease (Freyberg et al., 2022). The cameras with off-chip optical light filters (TM5 and TM7) are prone to a light leak irradiating the lower part of the CCDs with optical light depending on the Sun angle. As the light leaks led to increased telemetry rates, the energy thresholds for TM5 and TM7 had to be increased from 80 eV to around 125 eV to 140 eV, causing decreased performance of these cameras at low energies (Predehl et al., 2021).

10.2. The radiation environment at the second Lagrangian point

The radiation environment for X-ray satellites is strongly depending on the individual mission orbit. While many X-ray detectors have been operated in Low Earth Orbits (LEOs) and Highly Elliptical Orbits (HEOs) with large eccentricities, SRG is the first X-ray mission at the second Lagrangian Point L_2 (Grant et al., 2022). The L_2 point shows a highly dynamic radiation environment due to its position in the geomagnetic field tail (Campana, 2022). However, since SRG is placed in a *Halo* orbit around the L_2 point with large maximum distances from L_2 of more than 750 000 km and 400 000 km in the axes perpendicular to the Sun-Earth axis (Sunyaev et al., 2021), it is operating well outside of the geomagnetic field tail. This leads to a background with only little short-term variations for eROSITA (Freyberg et al., 2020).

The radiation environment at the *Halo* orbit around the L_2 point is considerably less well studied than the LEO and HEO orbits. Since SRG also lacks a particle monitor on board, primary particle fluxes for Monte Carlo (MC) simulations

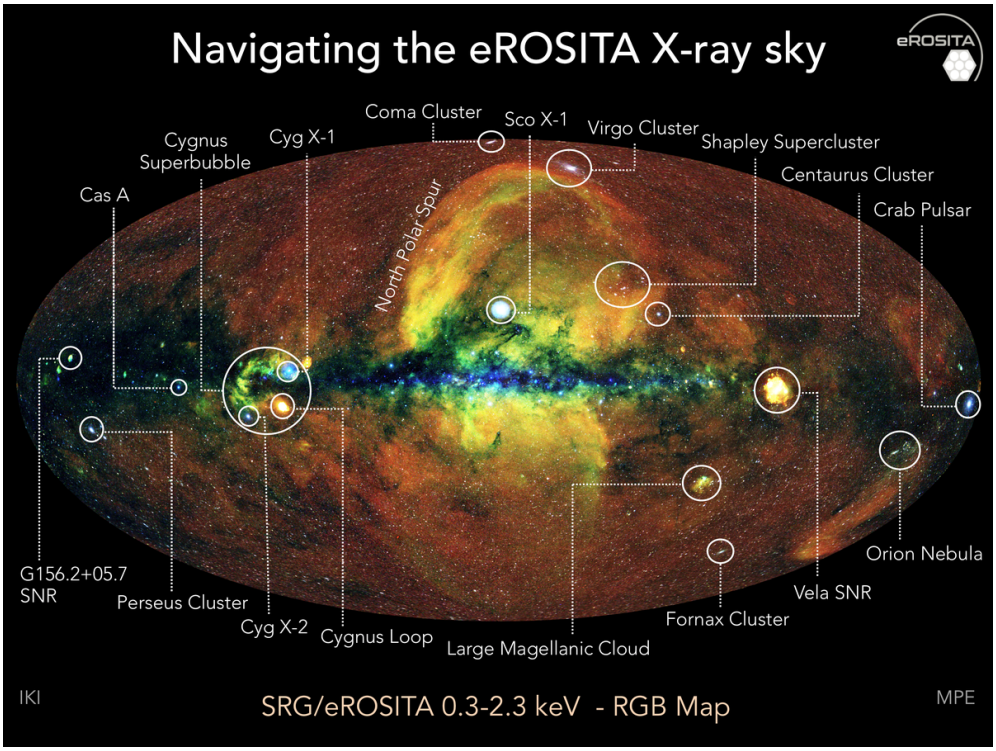

Figure 10.4.: eROSITA eRASS1 all-sky image with annotations. The annotated features include nearby bright point sources, extended sources, and clusters of galaxies at cosmological distances. The Galactic disk is visible as the central plane in the image and the image is centered on the supermassive black hole Sagittarius A* at the center of the Milky Way. The large-scale structures north and south of the Galactic disk are referred to as eROSITA bubbles and are likely due to energy release from the Galactic center (Predehl et al., 2020). Image credit: Jeremy Sanders, Hermann Brunner, Andrea Merloni and the eSASS team (MPE); Eugene Churazov, Marat Gilfanov (on behalf of IKI).

of the eROSITA filter wheel closed background have to be estimated from empirical models based on satellite missions and particle monitors in other orbits.

10.2.1. Cosmic rays

Cosmic rays are charged particles with a composition of about 98 % protons and nuclei – consisting of about 87 % protons, 12 % helium nuclei, and 1 % heavier nuclei – and 2 % electrons, covering a wide energy range up to more than 1×10^{20} eV (Longair, 2011). Cosmic rays are of galactic origin outside the solar system and also come from extra-galactic sources (Drury, 2012). The cosmic-ray flux shows long-term variability, especially at lower energies of the cosmic-ray spectrum, anti-correlated with the 11-year solar-activity cycle and it is known since many decades that models describing the cosmic-ray intensity need to incorporate the solar modulation potential determined i.e. from the sunspot number together with a time-lag between the sunspot number and the prediction time (Campana, 2022; Ross and Chaplin, 2019; Gleeson and Axford, 1968; Forbush, 1958). The solar modulation heavily affects cosmic rays at energies below 1 GeV nucl^{-1} and the total integral cosmic-ray flux varies by about a factor of two during one solar-activity cycle (Campana, 2022). The cosmic-ray flux can be better described in dependence of the 22-year Hale cycle rather than the 11-year cycle, as differences can be observed in the cosmic-ray flux for even and uneven solar-activity cycles (Thomas et al., 2014). Today, several sophisticated empirical models based on measurement data from multiple instruments exist for flux predictions for the individual cosmic-ray components. However, for certain epochs the available cosmic-ray models fail to reproduce energy spectra that are fully consistent with measurements (Mrigakshi et al., 2012).

A selection of helium nuclei fluxes obtained from commonly used cosmic-ray models are shown in Figure 10.5 together with data from the Alpha Magnetic Spectrometer (AMS) on the International Space Station (ISS) measured between May and August 2011 (Aguilar et al., 2019). The figure includes flux predictions from the Nymmik et al. (1996) model (Nymmik et al., 1996, 1994), the ISO 15390 model (International Organization for Standardization, 2004), the CREME96 model (Tylka et al., 1997) based on Nymmik et al. (1992), and the Kuznetsov

et al. (2017) model (Kuznetsov et al., 2017). The ESA Space ENVironment Information System (SPENVIS) (Heynderickx et al., 2004) implements the CREME86 (Adams, 1986), CREME96, ISO 15390 and Nymmik et al. (1996) models for the atomic nuclei component of the galactic cosmic rays ranging from hydrogen to uranium. Flux predictions can be obtained via the SPENVIS web interface in the energy range from 1 MeV nucl^{-1} to 100 GeV nucl^{-1} for a custom defined mission epoch. For the simulations described in this thesis, a single-segment mission duration of two years starting from October 1, 2019, was configured in SPENVIS and placed in a near Earth interplanetary orbit at a distance of 1.01 AU from the Sun. The AMS measurement data were obtained from the Cosmic-Ray DataBase (CRDB) (Maurin et al., 2020, 2014). The models agree well at high energies above about 300 MeV but slightly overestimate the AMS measurement, which is expected since the measurement time corresponds to a time of less solar activity compared to the modeled mission epoch. The Kuznetsov et al. (2017) model shows a less pronounced effect of solar modulation compared to the other models, which could be due to the idealistic assumption of a sunspot number of zero, thus marking the maximum flux of the model. At energies below about 300 MeV, the models show large differences due to the inclusion of a Solar Energetic Particle (SEP) component in the Nymmik et al. (1996) and CREME96 spectra. The plateau seen in the CREME96 spectrum is due to Anomalous Cosmic Rays (ACRs) originating from interstellar pickup ions (Giacalone et al., 2022; Tylka et al., 1997). For the interpretation of the flux prediction quality, it is important to understand that measuring the absolute flux of particles is a difficult task (see also Project I) and that the experimental uncertainties of particle flux measurements have to be assumed on the order of 20 % (Kuznetsov et al., 2017).

10.2.2. Cosmic X-ray background

The Cosmic X-ray Background (CXB) is a diffuse and nearly isotropic background mainly from extra-galactic point sources that cannot be resolved to individual detected sources by a given instrument due to limited angular resolution (Campana, 2022). In the eROSITA eRASS1 *Main* catalogue in the 0.2 keV to 2.3 keV energy band, the CXB is the largest contributor to the total number of calibrated events with 32 % of the total 338 million events assigned to it

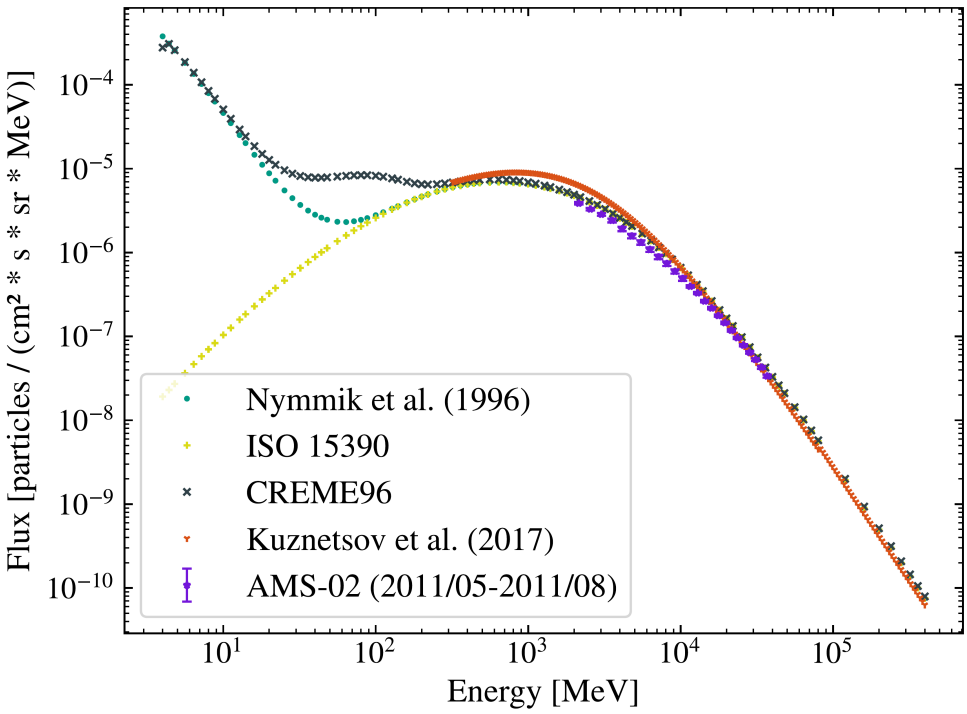

Figure 10.5.: Cosmic-ray spectra for helium nuclei. The Nymmik et al. (1996), ISO 15390, and CREME96 flux predictions were produced by SPENVIS. The Kuznetsov et al. (2017) flux predictions were calculated using a custom implementation of the model assuming no sunspots. The AMS-02 data measured between May 2011 and August 2011 were retrieved from the CRDB.

(Merloni et al., 2024). While these low-energy X-rays are typically absorbed by the detector shielding and the filter wheel in closed position, X-rays with higher energies of up to hundreds of keV can potentially deposit energy in the detector and are sufficiently abundant to contribute to the filter wheel closed background of X-ray detectors (Pommranz, 2019; Tenzer, 2008). The CXB can be described by the empirical Gruber et al. (1999) model for photon energies between 3 keV and 100 keV as shown in Figure 11.2a. Similar to the uncertainties of the cosmic-ray measurements, the uncertainties for the absolute flux measurements are expected to be of the order of 20 % (Campana, 2022).

10.3. The eROSITA filter wheel closed background

An important contribution to the background of X-ray satellites is caused by high-energy particles of the radiation environment in the satellite orbit from solar, galactic, and extra-galactic origin. These particles can penetrate the camera and deposit energy in the CCD either directly or via secondary particles produced in interactions with the camera components. As these high-energy particles penetrate the camera shielding, this background component is also visible when the filter wheel is in closed position blocking soft protons, soft electrons, and incident X-rays from astrophysical background and sources. The contribution of this FWC background to the total eROSITA background in all-sky survey mode is shown in Figure 10.6. At lower energies, the dominating contributor to the total eROSITA background in all-sky survey mode is the CXB. In the 0.2 keV to 2.3 keV energy band of the eRASS1 catalogue, 19 % of all calibrated events are assigned to the instrumental background, and at higher energies the backgrond is dominated by it. Therefore, the characterization and understanding of the FWC background is crucial for the interpretation of the eROSITA data, especially at high energies.

In the FWC background, spectral features corresponding to the energies of the K_α or K_β fluorescence lines of several chemical elements are present, as shown in Figure 10.6 and Figure 13.3. Pronounced fluorescence lines are seen for aluminium, iron, zinc, nickel, and copper, while less pronounced lines also exist for additional elements like calcium. As the fluorescent X-rays would be effectively blocked by the 3 cm thick copper shield and the 4 mm thick aluminium filter wheel, they must be originating from within the camera

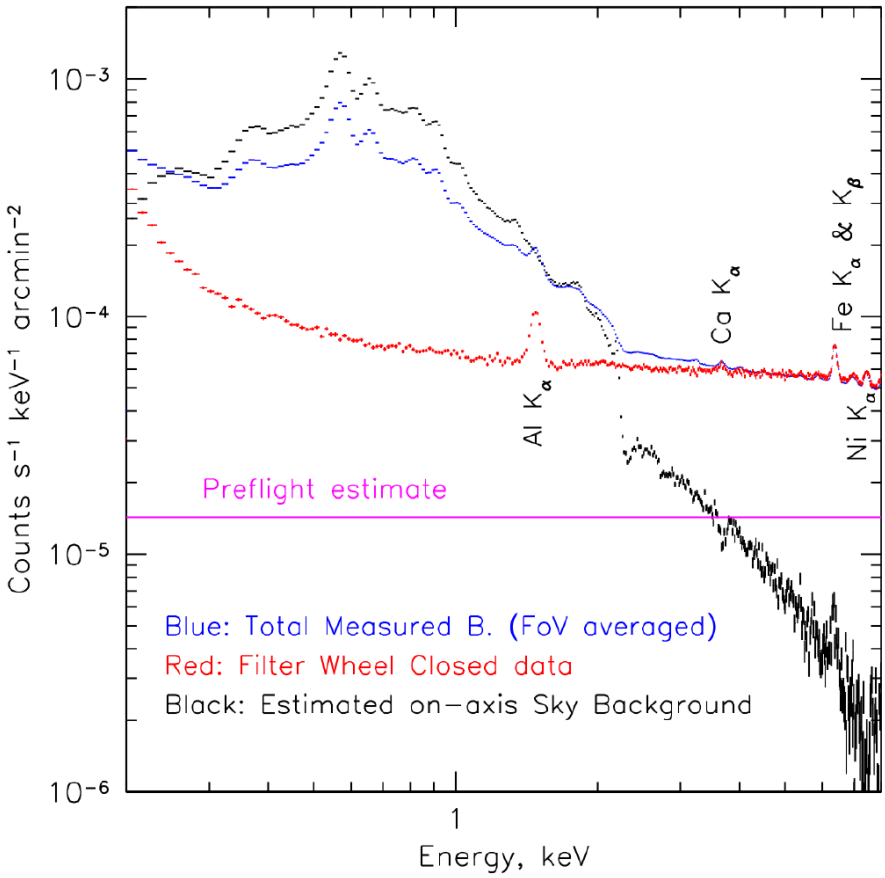

Figure 10.6.: Stacked background spectrum of eROSITA in the all-sky survey, normalized for a single telescope module. The total measured background is depicted in blue, the estimated vignetting-corrected on-axis CXB is depicted in black, the measured FWC background is depicted in red, and the pre-launch FWC background estimate from Tenzer et al. (2010) is depicted in magenta. Image credit: Predehl et al. (2021), used under CC BY 4.0.

itself (Predehl et al., 2021). The appearance of these fluorescence lines in the FWC spectrum was unexpected – apart from the aluminium contribution from the filter wheel directly in the unshielded line of sight of the CCD – as the fluorescence photons were thought to be transformed to energies below the CCD detection threshold in the graded-Z shield, which was also observed in pre-launch simulations (Tenzer et al., 2010). The fluorescence lines seen in the eROSITA FWC spectrum are much weaker than the ones of the XMM-Newton EPIC-pn instrument and are likely due to impurities in the inner beryllium layer of the graded-Z shield, as they show no significant spatial inhomogeneity in contrast to the features in the EPIC-pn FWC spectrum (Freyberg et al., 2020; Predehl et al., 2021).

Pre-launch simulations of the eROSITA FWC background published in Tenzer et al. (2010) and Perinati et al. (2012) reported consistent expected particle-induced background levels of $6.4 \times 10^{-3}\,\mathrm{counts\,cm^{-2}\,s^{-1}\,keV^{-1}}$ and 6.2×10^{-3} $\mathrm{counts\,cm^{-2}\,s^{-1}\,keV^{-1}}$, respectively, thus underestimating the measured FWC background processed with the eROSITA Science Analysis Software System (eSASS) pipeline version 020 in the 2 keV to 6 keV energy range by about a factor of four ($2.53 \times 10^{-2}\,\mathrm{counts\,cm^{-2}\,s^{-1}\,keV^{-1}}$). This difference can be potentially explained by two main reasons. Firstly, the pre-launch simulations anticipated a launch date close to the solar maximum, while the final SRG launch was close to the solar minimum. Due to the anti-correlation of solar activity and particle fluxes described in Section 10.2.1, the particle input spectra used in the simulations therefore were lower than for the actual launch date. Secondly, the simulation studies used simplified detector mass models that represented the earlier variants of the eROSITA camera, which differ from the final version.

Project II

11. A Geant4 application for X-ray satellites

In the course of this thesis, a simulation environment designed for background studies of X-ray satellites was developed and is described in this chapter. A highly detailed mass model suitable for background simulation studies was manually derived from the final Computer-Aided Design (CAD) model of eROSITA (Section 11.2). Furthermore, a highly automated read-out, digitizer and data analysis workflow was developed, that uses adapted parts of the eROSITA data analysis pipeline where possible and enables using the existing eSASS (Brunner et al., 2018; Predehl et al., 2021) for further analysis of the simulation data (Chapter 12). The new simulation environment, mass model, and workflow were used together to simulate the eROSITA filter wheel closed background (Chapter 13).

A Geant4 application was developed to simulate the eROSITA filter wheel closed spectrum, based on the Geant4 application described in Pommranz (2019) with additional sensitive detectors and extended output. In contrast to the approach taken in GATE, the Geant4 application was designed to have only minimal features but to provide detailed output of unprocessed physical data on the `Hit` level. This way, the computationally expensive MC simulations needed to be performed only once for the final detector mass model and physics description, and the comparatively less computationally expensive processing and analysis described in Chapter 12 could then be performed multiple times with different sets of parameters on the raw simulation data produced by the Geant4 application.

The simulation output is stored in ROOT (Brun and Rademakers, 1997) files in separate trees for the imaging and frame-store areas. For every `Hit` in the sensitive detector volume, the trees contain information about the primary particle (initial energy, initial position, direction, and event identifier), the secondary particle interacting with the detector (particle type, position and volume of production, and track identifier), and the `Hit` (energy, deposited

energy, position, physical process, direction of momentum, time since production of the primary particle, and volume of interaction).

Geant4 version 11.0.3 was used with the QBBC Geant4 reference physics list activated for simulation of hadronic processes, which was specifically created for optimized precision in space radiation environment simulations (Ivantchenko et al., 2012). Standard electromagnetic physics modeling was used in option four (EMZ), which provides a combination of the best electromagnetic models available in Geant4 (Allison et al., 2016). Fluorescence, Auger electron emission, and Particle Induced X-ray Emission (PIXE) (Mantero et al., 2011; Pia et al., 2009) were activated for modeling of atomic deexcitation. A global range cut of 0.5 µm was used in the detector mass model volumes and sensitive detectors together with a lower energy cut of 100 eV. In a study with a simplified mass model consisting only of a spherical shell of aluminium around the CCD, performed in the course of this thesis, these values were found to be a suitable compromise between simulation precision and computational cost as well as raw data file sizes.

The Geant4 application is independent of the detector geometry, which allows to simulate different variants or parts of the eROSITA detector mass model described in Section 11.2 without the need to adapt the application. The detector mass model file in the Geometry Description and Mark-up Language (GDML) schema (Chytracek et al., 2006) needs to be provided as an argument to the Geant4 application and is read and interpreted by Geant4 at runtime (Apostolakis et al., 2009). The CCD imaging and frame-store area volumes can be marked as sensitive detectors using a GDML `auxiliary` tag with `auxtype="SensDet"`.

An isotropic background was simulated using the Geant4 General Particle Source (GPS) by shooting particles following Lambert's cosine law from uniformly distributed positions on a spherical surface around the mass model. For each primary particle type, the corresponding in-orbit time t was calculated from the number of simulated primary particles N and the energy-integrated flux Φ in counts $\mathrm{cm}^{-2}\mathrm{s}^{-1}\mathrm{sr}^{-1}$ using the well-known normalization formula described in Pommranz (2019) based on Santin (2007), in Fioretti et al. (2012), Zhao et al. (2013), and in internal working group documents, such as Fioretti et al.

(2018) and Hubbard (2021)[19]:

$$t = \frac{N}{\Phi \cdot 4\pi^2 R^2 \cdot (\sin^2 \theta_{max} - \sin^2 \theta_{min})} \quad , \tag{11.1}$$

where the radius of the sphere in cm^2 is denoted by R and the maximum and minimum source biasing angles, used to exclude the simulation of primary particles that are not directed towards the mass model, are denoted by θ_{max} and θ_{min}, respectively.

11.1. Primary particle input spectra

As protons are the most important component of the cosmic-ray radiation background (see Section 10.2.1), a proton input spectrum currently used for Athena Wide Field Imager (WFI) background simulations based on Perinati et al. (2017) and on-going eROSITA background simulations based on Perinati et al. (2012) was used for improved comparability and cross-checks of the simulation results. The input spectrum is based on data by the Payload for Antimatter Matter Exploration and Light-nuclei Astrophysics (PAMELA) mounted on the Resurs DK1 satellite operating in a semi-polar orbit at altitudes between 350 km and 600 km (Picozza et al., 2007; Orsi, 2007) and is shown in Figure 11.1a. The input spectrum was derived from data measured in 2010 (Martucci et al., 2018)[20], and the total proton particle flux was $0.41\,cm^{-2}\,s^{-1}\,sr^{-1}$. Although PAMELA is operating at low altitudes, it is suitable for estimating the particle energies at higher altitudes, as the cosmic-ray proton variabilities on short and

[19] This normalization formula has been the focus of the long-standing "factor of two conundrum", as a full consensus about this equation has not been achieved in the background simulation community and individual scientists were claiming a missing factor of two in the denominator, which directly translated into a factor of two difference in the simulated count rates and fluxes (Hubbard, 2021). In the course of this thesis, it was possible to reach a consensus on the correctness of the equation without the additional factor of two when used together with the widely adopted Geant4 GPS by presenting a detailed step-by-step course on how the production of an isotropic flux is realized in the Geant4 GPS in one of the regular eROSITA background/foreground meetings. Overall, it must be taken care that the normalization formula is consistent with the implementation details of the used code.

[20] The input spectrum was provided by E. Perinati in June 2021 (private communications).

long timescales are consistent, i.e. for the AMS mounted on the ISS and the Chandra X-ray Observatory in a highly elliptical orbit (Grant et al., 2022).

Atomic nuclei with Z between 2 and 28 were used as primary particles for the eROSITA background simulations with the particle fluxes from the Nymmik et al. (1996) model (see Section 10.2.1). For every element, only the most abundant stable isotope was considered for conversion of energy units and as primary particles in the simulation. Total particle fluxes for the atomic nuclei are given in Table 11.1 for energies between $1\,\mathrm{MeV\,nucl^{-1}}$ and $100\,\mathrm{GeV\,nucl^{-1}}$. The spectra for helium, carbon, magnesium, and iron nuclei are shown in Figure 11.1b. For the simulation of primary photons from the CXB the Gruber et al. (1999) model (see Section 10.2.2) was used between 3 keV and 100 GeV as shown in Figure 11.2a with a total particle flux of $8.6\,\mathrm{cm^{-2}\,s^{-1}\,sr^{-1}}$. Primary cosmic-ray electrons were simulated based on PAMELA data measured between July 2009 and December 2009 (Adriani et al., 2015) as shown in Figure 11.2b, obtained from the CRDB. The total electron particle flux was $9.6 \times 10^{-3}\,\mathrm{cm^{-2}\,s^{-1}\,sr^{-1}}$.

A complete MC simulation study for space-based detectors requires the simulation of multiple types of primary particles. The individual input spectra are typically retrieved from different sources – such as SPENVIS, the CRDB, or custom implemented empirical models – that offer the data in custom data formats and in different normalization units, which can make the handling of multiple input spectra a tedious task. To simplify the handling of particle input spectra, the small `geant4-space-input-spectra` toolkit was developed in the course of this thesis[21]. The toolkit contains useful helper tools for automatic spectra conversion from the SPENVIS and CRDB output formats to the Geant4 macro format and implementations of selected empirical models, such as the Gruber et al. (1999) model and the Kuznetsov et al. (2017) model. In addition, normalization tools to calculate the number of particles corresponding to a given in-orbit time (and vice versa) as well as a tool to calculate the total flux for a given spectrum by integration in the energy domain using different interpolation methods are included. The toolkit contains a plotting tool for easy visualization of spectra and all the figures in this section were produced using this plotting tool.

[21] The `geant4-space-input-spectra` toolkit is available at `https://github.com/cpommranz/geant4-space-input-spectra` (accessed on 2023-11-06).

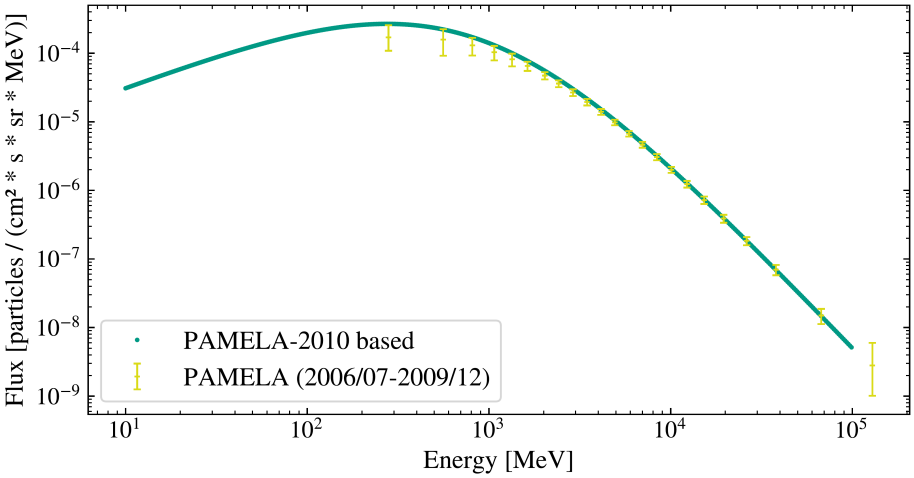

(a) Protons.

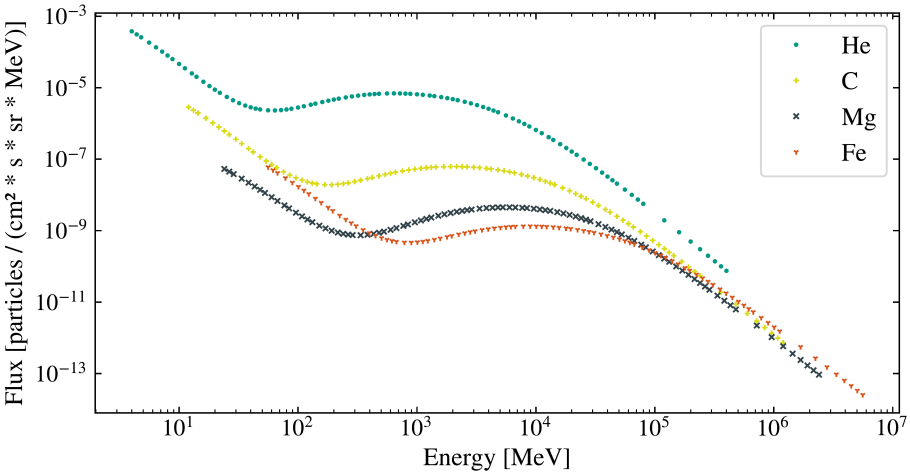

(b) Helium, carbon, magnesium, iron.

Figure 11.1.: Input spectra for protons based on PAMELA data measured in 2010 (a) and for helium, carbon, magnesium, and iron nuclei based on Nymmik et al. (1996) (b). The PAMELA data measured between July 2006 and December 2009 were retrieved from the CRDB. The input spectra for the helium, carbon, magnesium, and iron nuclei are shown between 1 MeV nucl^{-1} and 100 GeV nucl^{-1}.

Table 11.1.: Total particle fluxes Φ of the cosmic-ray atomic nuclei components between $1\,\mathrm{MeV\,nucl^{-1}}$ and $100\,\mathrm{GeV\,nucl^{-1}}$ calculated from the SPENVIS produced spectra for the eROSITA orbit based on the Nymmik et al. (1996) model.

Nucleus	Z	A	Φ ($\mathrm{cm^{-2}\,s^{-1}\,sr^{-1}}$)
He	2	4	3.32×10^{-2}
Li	3	7	1.29×10^{-4}
Be	4	9	7.03×10^{-5}
B	5	11	2.55×10^{-4}
C	6	12	9.18×10^{-4}
N	7	14	2.37×10^{-4}
O	8	16	8.51×10^{-4}
F	9	19	1.96×10^{-5}
Ne	10	20	1.48×10^{-4}
Na	11	23	3.51×10^{-5}
Mg	12	24	1.60×10^{-4}
Al	13	27	3.24×10^{-5}
Si	14	28	1.41×10^{-4}
P	15	31	6.66×10^{-6}
S	16	32	2.77×10^{-5}
Cl	17	35	5.97×10^{-6}
Ar	18	40	1.09×10^{-5}
K	19	39	8.03×10^{-6}
Ca	20	40	2.10×10^{-5}
Sc	21	45	4.00×10^{-6}
Ti	22	48	1.35×10^{-5}
V	23	51	7.20×10^{-6}
Cr	24	52	1.45×10^{-5}
Mn	25	55	9.07×10^{-6}
Fe	26	56	9.47×10^{-5}
Co	27	59	7.41×10^{-7}
Ni	28	58	4.42×10^{-6}

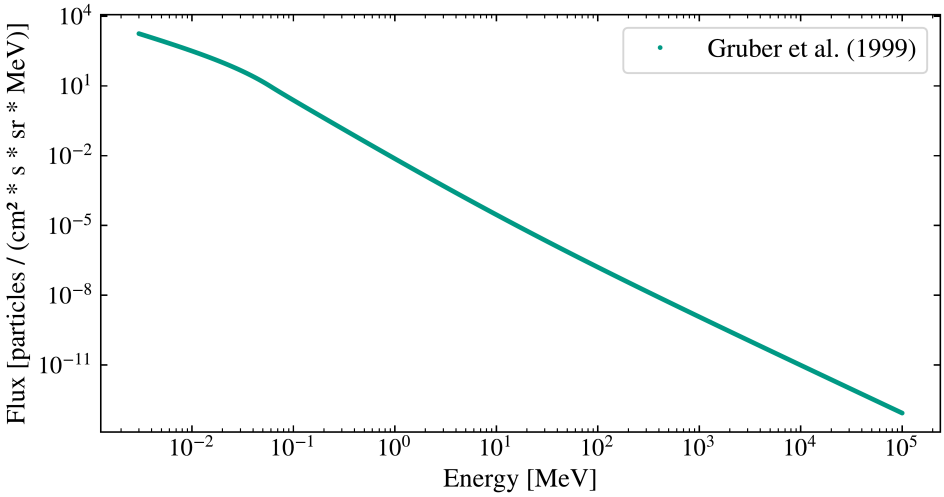

(a) CXB photons.

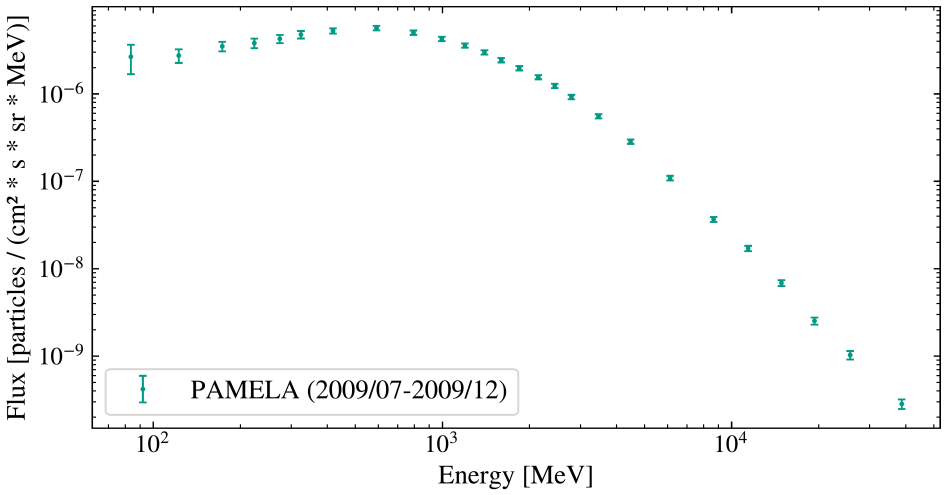

(b) Electrons.

Figure 11.2.: Input spectra for CXB photons calculated using the Gruber et al. (1999) model (a) and cosmic-ray electrons from PAMELA measurements (b). The PAMELA data measured between July 2009 and December 2009 were retrieved from the CRDB.

11.2. A highly detailed mass model

A new eROSITA camera mass model suitable for Geant4 simulations was developed in the course of this thesis and was described in more detail in Pommranz et al. (2022). It was manually derived from the final eROSITA CAD model obtained from MPE with the aim to incorporate geometrical and material details needed to investigate the origin of the fluorescence lines in the eROSITA FWC spectrum. To enable a reasonable simulation speed despite the high level of detail, the mass model was constructed from CSG volumes instead of using tessellated volumes. In addition, the level of detail was gradually reduced with the amount of attenuation between the volume and the CCD, such that volumes close to the CCD or its line of sight were modeled in more detail than volumes further apart. The mass model was implemented in GDML (Chytracek et al., 2006). The assembled eROSITA camera is shown in Figure 11.3a. CAD and GDML representations for parts of the camera interior are shown in Figure 11.3c. The filter wheel is modeled with a high level of detail, such as notches and screws, due to its placement directly in the line of sight of the CCD. In contrast, the filter wheel case and the components mounted on top of it are modeled with less details, as these volumes are shielded from the CCD by the filter wheel and other volumes. A simplistic model of the rest of the eROSITA instrument that is optionally available as part of the mass model is shown in Figure 11.3b together with one detailed camera and mirror module. The mirror module includes two-cone approximations of the 54 mirror shells, therefore, the mass model is also suitable for mirror scattering and ray-tracing simulations using Geant4.

The mass model was constructed with the help of a student assistant (Tim Wildfang) by identifying suitable geometrical solids for sub-volumes in the CAD model and rebuilding them in GDML using the Artenum ExtendeD GDML Editor (EDGE)[22] with positions and rotations retrieved from the CAD model. The individual GDML solids were then manually combined to more complex solids using the CSG technique and arranged in a hierarchical volume structure. The mass model presented in Pommranz et al. (2022) was further improved by including CSG variants of the upper and lower copper case volumes that passed extensive particle tracking validations performed using Geant4 version 11.0.3,

[22] `https://www.artenum.com/EN/Products-Edge.html` (accessed on 2023-06-02).

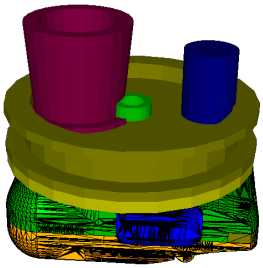

(a) The eROSITA camera.

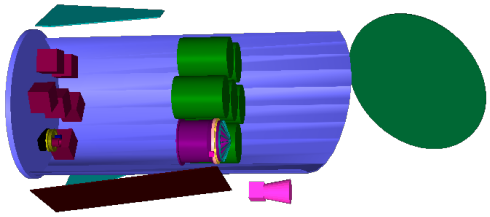

(b) The eROSITA instrument.

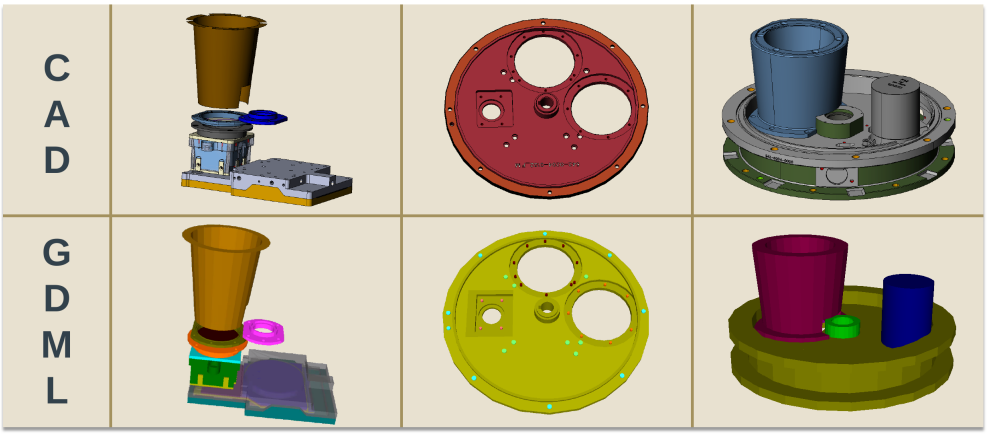

(c) CAD and GDML versions of parts of the camera assembly.

Figure 11.3.: The eROSITA GDML mass model. The eROSITA camera assembly with the tessellated variants of the upper and lower copper shield volumes (a). The whole eROSITA instrument with one detailed camera and mirror module (b). Comparison of the CAD and GDML representations of a partly assembled camera, the filter wheel, and the filter wheel case with an aluminium cone and the stepping motor (c), from left to right. Image credit: Pommranz et al. (2022).

Table 11.2.: Material composition of the beryllium volumes used in the eROSITA mass model. The mass fractions for the individual components are given in %.

Comp.	Fraction	Comp.	Fraction	Comp.	Fraction
Be	99.0534	Cr	0.0031	Mo	0.0004
BeO	0.7000	Mn	0.0023	Zr	0.0004
Fe	0.0920	Pb	0.0020	B	0.0003
Al	0.0460	Ag	0.0010	Li	0.0003
N	0.0300	Sn	0.0010	Ca	0.0002
Ni	0.0220	K	0.0008	Cd	0.0002
Si	0.0200	U	0.0007	Mg	0.0002
C	0.0100	W	0.0007	P	0.0002
Cu	0.0083	Na	0.0006	V	0.0001
Ti	0.0034	Co	0.0004		

and by implementing the mass model as a template in the Jinja[23] templating engine. The template implementation of the mass model allows to produce different versions of the mass model according to a central configuration. Thus, mass models can be rendered including all or only a subset of specific parts of the camera with different levels of detail, such as screw models or switching between the tessellated and non-tessellated variants of the copper case. Camera variants with on-chip and off-chip optical light filters can be produced.

The mass model contains detailed chemical material compositions for every volume including impurities following the manufacturers' specifications, as the impurities were discussed as the potential cause for the unexpected fluorescence lines in the eROSITA FWC spectrum (Freyberg et al., 2020). Typically, the impurities were given as upper limits in the manufacturers' specifications. In these cases, the upper limits were used for the material compositions in the GDML mass model. The material compositions of the beryllium parts of the mass model are critical for the FWC background due to their proximity to the CCD as the inner layer of the graded-Z shield. Therefore, the impurities were

[23] `https://jinja.palletsprojects.com` (accessed on 2023-06-02).

Table 11.3.: Material composition of the aluminium alloys used in the eROSITA mass model. The mass fractions are given in %.

Element	AW-7075	AW-5056	AW-5083	AW-6082-T6	AW-6061-T6	AW-1050A
Al	87.32	92.20	92.55	95.35	96.65	99.08
Zn	6.10	0.20	0.25	0.20	0.25	0.07
Mg	2.90	5.60	4.90	1.20	1.00	0.05
Cu	2.00	0.10	0.10	0.10	0.30	0.05
Fe	0.50	0.50	0.40	0.50	0.70	0.40
Si	0.40	0.40	0.40	1.30	0.60	0.25
Mn	0.30	0.60	1.00	1.00	0.15	0.05
Cr	0.28	0.20	0.25	0.25	0.20	-
Ti	0.20	0.20	0.15	0.10	0.15	0.05

taken from an analysis of a spare eROSITA beryllium plate performed in 2021 on behalf of the MPE instead of the manufacturer's specification. The composition of beryllium including impurities is given in Table 11.2. For impurities that were not listed in the report of the new analysis but were contained in the original report of the manufacturer's measurement, the latter values were used. The material compositions of the six aluminium alloys used for parts of the eROSITA camera in the mass model are listed in Table 11.3. The need to include accurate material compositions in the mass model is underlined by the wide range of aluminium contents and impurities in the alloys.

For the simulations shown in this thesis, an on-chip optical light filter variant of the GDML mass model was used with all available details except for the copper case, which was included in the CSG variant. While the CSG variant of the copper case introduced some simplifications compared to the tessellated variant, it allowed for significant improvements in simulation speed. In a test simulation with 1×10^5 primary protons, switching to the CSG variant of the copper case for the camera mass model with full details showed a 53 % improvement in primary particle simulation rate compared to the same camera mass model with the tessellated copper case variant.

Project II

12. The digitizer and data analysis workflow

As part of this thesis, the `erosita_background_analysis` (`eba`) project and the `eba digitizer` module were designed and developed from scratch and integrated in a highly automized digitizer and data analysis workflow using Snakemake. The `eba digitizer` module contains multiple tasks modeling different aspects of instrumental effects similar to the modules concept of the GATE digitizer chain. In contrast to the GATE digitizer chain, the eROSITA digitizer and data analysis workflow can be run on a set of ROOT files from a split simulation run, which are merged to a single event list as part of the workflow, and it operates in an offline processing mode by design, as the workflow is not part of the Geant4 application and it is run after the Geant4 simulation is finished. This allows to run the workflow multiple times with different parameters on the results of a single Geant4 simulation run.

The digitizer and data analysis workflow was optimized for a precise modeling of the instrumental effects, including specific effects for the frame-store CCD concept, and effects from in-orbit and on-ground software algorithms in order to reduce discrepancies introduced by differences in the event processing and analysis stages for simulation and measurement. Therefore, one of the design goals of the workflow was to produce eSASS-compatible Flexible Image Transport System (FITS) files early in the workflow to enable the use of the original eSASS pattern matching algorithm as part of the workflow. Furthermore, this allows the same analysis tools to be used for simulated and measured event lists.

The DAG representing the flow of the digitizer and data analysis workflow, which is determined by Snakemake from the rule-based input and output workflow definition, is shown in Figure 12.1 up to the production of the event list FITS file for a simplified case of two primary particle types and three ROOT files.

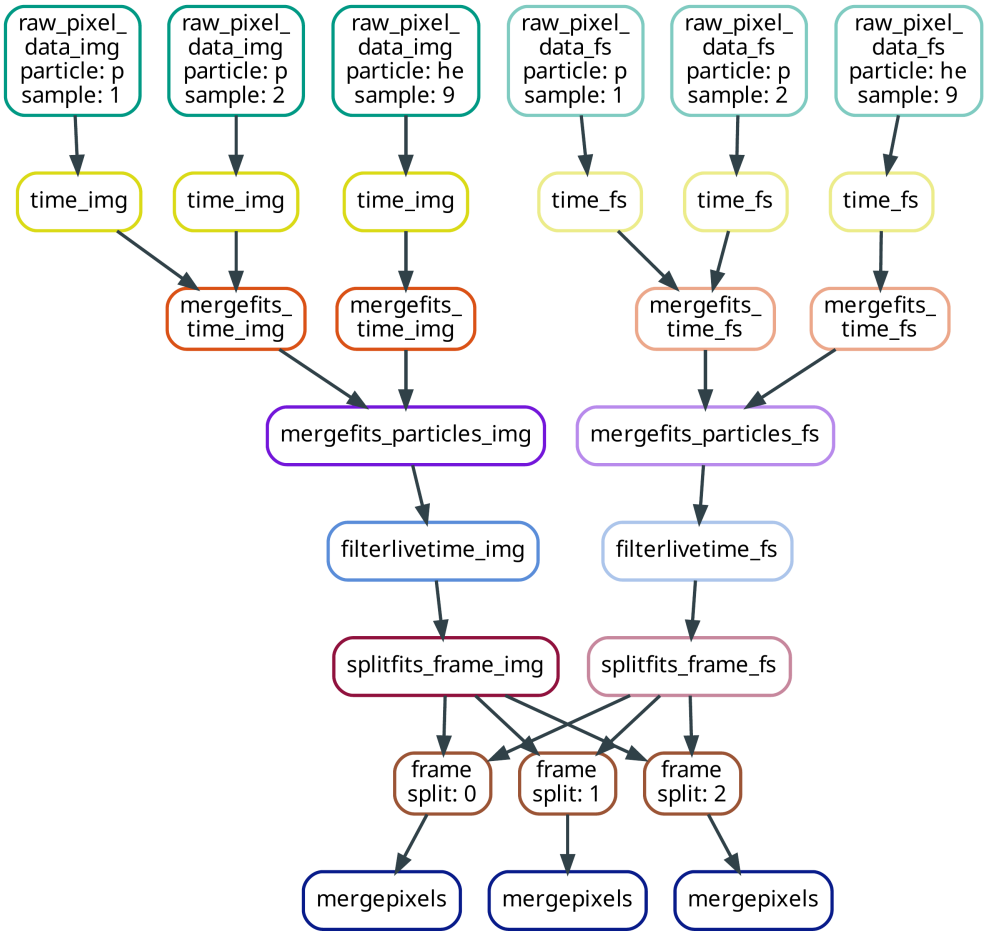

Figure 12.1.: The directed acyclic graph of the digitizer and data analysis workflow implemented in the Snakemake workflow management system. For illustration purposes, only two proton samples and one helium nuclei sample are shown and analysis and plotting steps are omitted.

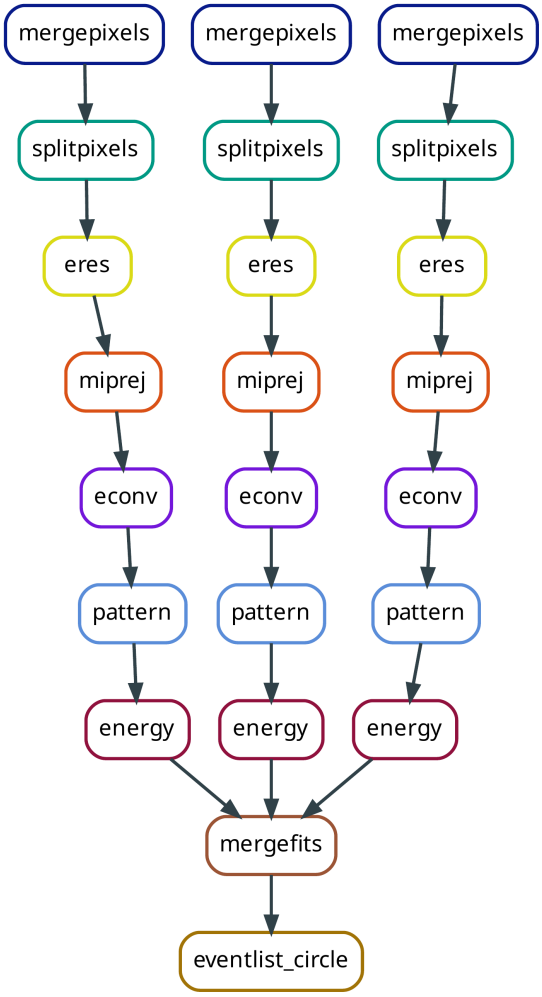

Figure 12.1.: (continued)

The initial workflow tasks are performed separately for the output of different primary particles, samples, and areas of the CCD. The outputs are merged to single event lists for the imaging and frame-store areas, which are then split into event lists of shorter exposure time to allow for parallelized computation of the remaining workflow tasks (Section 12.3). All `eba digitizer` tasks follow the same command line interface: `eba digitizer TASK [OPTIONS] INFILE[S] OUTFILE[S]` with task-specific options.

12.1. Pixelization with the `raw-pixel-data` task

The simulation output stored in the ROOT file as described in Section 11 contains the `Hit` data with sub-pixel precision in separate trees for the imaging and frame-store areas. In the first step of the `eba digitizer` workflow, the `Hit` information of a single tree is aggregated separately for each event on a CCD pixel level. The aggregated `Raw Pixel Data` (`RPD`) is then converted and written into a FITS[24] file (Hanisch et al., 2001) using astropy.

The data format of the `RPD` is listed in Table 12.1. The `RPD` only contains a subset of the information stored in the ROOT output file that is needed by the `eba digitizer` workflow to produce output files compatible with the eROSITA data analysis pipeline and the eSASS. In addition, Geant4 track and event identifiers are stored together with the primary particle type and sample number, that can be used as a pointer to the particle track in the ROOT output. With this pointer, the analysis steps can obtain more information of the event that led to the energy deposition in the given pixel directly from the simulation ROOT output.

Each pixel with deposited energy is represented by a single `RPD` entry where the total energy of the pixel is calculated as the sum of the energy that is deposited in that pixel by the individual `Hits` of the event. The energy-weighted centroid of all `Hits` in the pixel is calculated and stored in the `SUBX` and `SUBY` fields as relative pixel offsets in the interval $[-0.5, 0.5)$, which is used for the electron charge cloud modeling described in Section 12.6 later in the workflow. The `Hits` and the aggregated `RPD` are illustrated in Figure 12.2.

[24] Documentation and formal definition of the FITS format are available at `https://fits.gsfc.nasa.gov` (accessed on 2023-10-09).

Table 12.1.: The RPD data format. Information about the pixel, sub-pixel, and deposited energy are contained together with the information needed to identify the original Geant4 track in the ROOT output. The data types are given in the NumPy notation.

Field	Data type	Description
RAWX	int16	Pixel number on the x-axis $[1, 384]$.
RAWY	int16	Pixel number on the y-axis $[1, 384]$.
ENERGY	float64	Energy deposited in the pixel in eV.
SUBX	float64	Location on the x-axis of the energy-weighted centroid in the pixel $[-0.5, 0.5)$.
SUBY	float64	Location on the y-axis of the energy-weighted centroid in the pixel $[-0.5, 0.5)$.
TRACKID	int32	Geant4 track identifier of the particle impinging the CCD.
EVENTID	int32	Geant4 event identifier.
SAMPLE	int32	Sample number used as run identifier.
PARTICLE	bytes_	Geant4 byte string representation of the primary particle type.

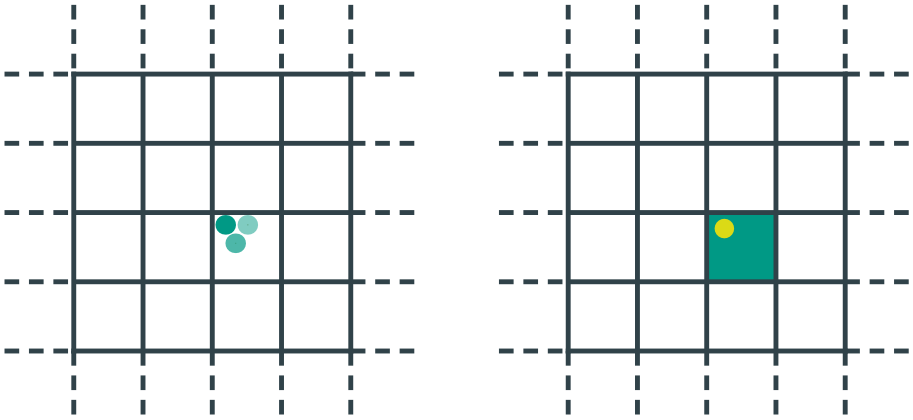

(a) Simulation raw data. **(b)** Simulation `RPD`.

Figure 12.2.: Illustration of the pixelization concept. The individual `Hits` of the simulation raw data are aggregated per pixel. The energy of the pixel is calculated as the total energy deposited by the `Hits` in that pixel. The dot depicted in yellow represents the energy-weighted centroid, which is stored as part of the `RPD`.

The Geant4 track identifiers are stored only for the tracks that impinge the CCD volume. Pixels that were hit only by tracks originating from within the CCD volume are assigned with the track identifier `0`, which allows for fast separation of particles produced outside and inside of the CCD in the analysis of the final FITS data without consulting the ROOT files.

The pixelization workflow task is named `raw-pixel-data`. The most important options are `--particle`, `--sample`, and `--hit-tree` corresponding to the primary particle type, the sample number of the analyzed run, and the name of the tree containing the `Hit` data in the ROOT output, respectively. Additional options exist to support generic CCDs with customized pixel numbers and pixel sizes, which are needed for the non-square pixels of the frame-store area, as well as simulation setups where the origin of the ROOT output coordinate system is not located in the CCD center.

12.2. Assigning in-orbit timestamps with the time task

The RPD produced in the raw-pixel-data lacks in-orbit time information that is needed for eROSITA read-out modeling and integrating events into frames (see Section 12.4). The time task adds an additional float64 field named TIME to the RPD FITS file, which contains in-orbit timestamps for the individual event. Each event is randomly assigned to an in-orbit time by sampling from a uniform distribution between 0 s and the corresponding total in-orbit time of the analyzed run. The same timestamp is assigned to pixels with the same EVENTID. The resulting FITS file is sorted in ascending order by in-orbit time.

The in-orbit time of the run is calculated in the time task following equation 11.1 using the number of primaries from the --primaries option, the flux in counts $\mathrm{cm}^{-2}\,\mathrm{s}^{-1}\,\mathrm{sr}^{-1}$ from the --flux option, the radius in cm from the --radius option, and the minimum and maximum opening angles in degrees from the --min-angle and --max-angle options, respectively. For reproducible workflow runs and unit testing, an initial seed can be provided to the random number generator using the --seed option.

12.3. Merging runs

In the simulation environment described in Section 11, the Geant4 simulations are split into separate runs for every primary particle type. Furthermore, for every primary particle type the simulations can be split into multiple samples with a smaller number of primary particles per run. The individual FITS files must therefore be merged per primary particle type and subsequently to a single FITS file for the CCD imaging and frame-store areas. Multiple samples for the same primary particle type are merged using the mergefits_time task. Merging is performed by concatenation and by applying an offset to the TIME field. The offset corresponds to an integer multiple of the in-orbit time of a single run and is calculated from the same options as for the time task described in Section 12.2. The subsequent merge of the different primary particle type results is performed by concatenation using the mergefits_particles task. The resulting FITS file is then sorted in ascending order by the TIME field using

the `eba digitizer timesort` program and cut after a configurable maximum live time, since the simulation parts of the individual primary particle types can have different corresponding in-orbit durations. The cut is performed at the frame border of the last complete frame in the live time using the `filter` task by setting the `--live-time` and `--cycle-time` options.

To allow for parallelized execution of the following workflow parts, the merged FITS file can be split into a number of smaller files of the same duration using the `splitfits_frames` task and the `--num` option. The splits are performed at the frame borders, which are calculated from the `--cycle-time` option.

12.4. Read-out cycle modeling with the `frame` task

The following explanation of the eROSITA CCD read-out cycle in this Section is based on Freyberg et al. (2020), where more details about the read-out can be found. A sketch of the eROSITA read-out cycle in the frame-store mode is shown in Figure 12.3. The imaging area accumulates charges and events from the beginning of the read-out cycle for a time t_{int} before the fast transfer of the charges from the imaging area to the frame-store area is performed during t_{ft}. After the fast transfer of charges into the frame-store area from the previous read-out cycle, the frame-store area is left in an integrating state at the beginning of the next cycle for a delay time t_{del}, before the read-out is performed during t_{ro}. After the read-out, the frame-store area is in an idle mode until the next fast transfer of charges from the imaging area into the frame-store area, where charges accumulated during the idle phase are cleared. All read-out times are listed in Table 12.2.

The `frame` task expects the arguments `INFILE_IMAGE_AREA`, `INFILE_FRAME-STORE` and `OUTFILE`. The input FITS files for the imaging and frame-store areas must be of the same structure and the task performs a check that both files use the same column names, data types, and units. The structure is adopted for the newly created combined output FITS file, extended with an additional `int32` column `FRAME` that stores the frame number assigned to each active pixel. The frame number, the corresponding state in the read-out cycle as well as the time since the beginning of that state ("time in state") are calculated from the `TIME` column. If an event happened in the fast transfer or read-out state, the

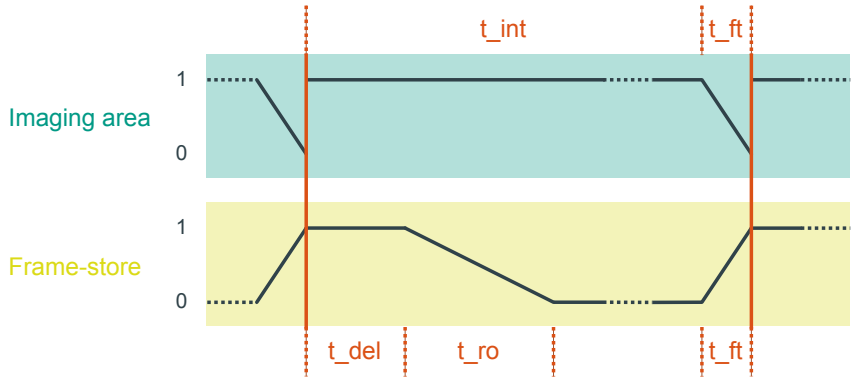

Figure 12.3.: Sketch of the eROSITA read-out cycle in the frame-store mode for the imaging and frame-store areas. State 1 represents an integrating state, where charges in the respective CCD area are accumulated for the next read-out, while state 0 represents an idle state, where charges accumulated in that state are cleared and discarded in the next read-out. For intermediate states, charges are either shifted out of the CCD area (transition from state 1 to state 0) or into the CCD area (transition from state 0 into state 1). Note that the sketch is not to scale.

`RAWY` value will be adapted based on the time in state and the read-out cycle time for that state. If the frame-store area is in the idle state, the active pixel will be dropped and will not be copied to the output file.

For spatially homogeneous incident radiations M_{im} and M_{fr} for the imaging and frame-store areas, respectively, an analytical model was proposed in Freyberg et al. (2020) to describe the total intensity M_{tot} in dependence of `RAWY`:

$$M_{tot}(\texttt{RAWY}) = M_{im} + M_{fs} \cdot \frac{A_{fs}}{A_{im}} \cdot \frac{t_{del}}{t_{cyc}} + M_{fs} \cdot \frac{A_{fs}}{A_{im}} \cdot \frac{t_{ro}}{t_{cyc}} \cdot \frac{\texttt{RAWY}}{N_Y} \tag{12.1}$$

where the pixel sizes of the imaging and frame-store areas are denoted as A_{im} and A_{fs}, respectively, the number of pixels in read-out direction is denoted by N_Y, the cycle time is denoted by t_{cyc}, and the delay and read-out times of the frame-store area are denoted as t_{del} and t_{ro}, respectively. For eROSITA, this leads to an additional 12.1 % contribution to the background from the

Table 12.2.: eROSITA read-out cycle times as reported in Freyberg et al. (2020).

Name	Description	Time in ms
t_{cyc}	Total cycle time	50.058 40
t_{int}	Integration time	49.943 25
t_{ft}	Fast transfer time	0.115 15
t_{del}	Delay time	4.284 85
t_{ro}	Read-out time	9.178 40

frame-store area when the same incident radiation is assumed for the imaging and frame-store areas ($M_{im} = M_{fs}$).

To demonstrate the `RAWY` dependency for the frame-store area as introduced by the read-out model in the `eba digitizer` workflow, 1×10^6 single events in consecutive frames were produced for the frame-store area. Each event was produced by directly creating one `RPD` with an additional time field. For each event, the time was randomly sampled from a uniform distribution in the cycle time of its frame. Only one row was considered in `RAWX` direction, as the read-out model does not introduce features perpendicular to the read-out direction. The imaging area was not illuminated and did not contain any active pixels, thus $M_{im} = 0$. The `frame` task was run with the empty imaging area file and the frame-store area file containing the produced single events. Since the single-event frames are produced independent of the pixel size and every frame contains exactly one event, the pixel sizes must be assumed equal in the analytical model ($A_{im} = A_{fs}$). Therefore, for this simulation, equation 12.1 simplifies to

$$M_{tot}(\texttt{RAWY}) = M_{fs} \cdot \left(\frac{t_{del}}{t_{cyc}} + \frac{t_{ro}}{t_{cyc}} \cdot \frac{\texttt{RAWY}}{N_Y} \right) \tag{12.2}$$

and the average background is 17.7 % of M_{fs} assuming the timing values of eROSITA and 384 pixels in read-out direction.

The results of the `frame` task are shown in Figure 12.4. The simulated total intensity of the frame-store area in dependence of `RAWY` is consistent with the

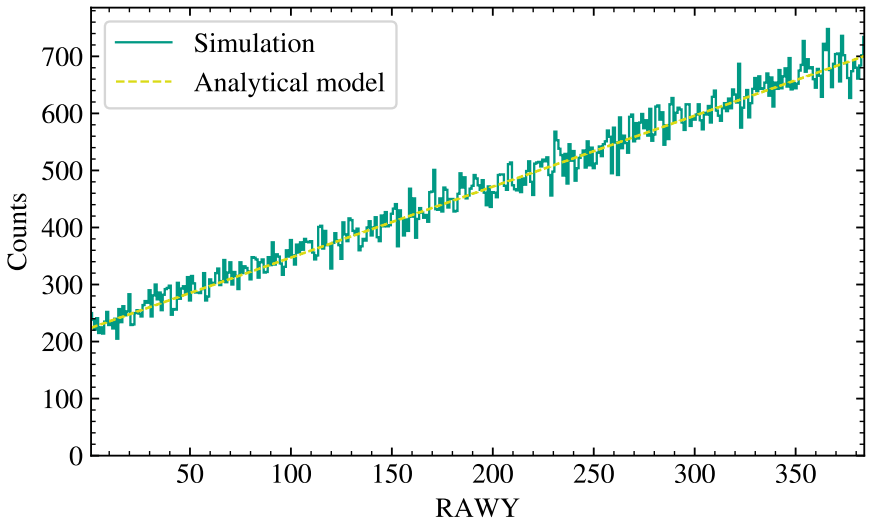

Figure 12.4.: Linear gradient introduced by the read-out model of the `eba digitizer` workflow for the frame-store area. 1×10^6 single-event frames were produced at random times in the eROSITA read-out cycle for the frame-store area. In `RAWX` direction, only one pixel was considered in order to speed up the simulation and since the read-out model is not introducing features along the `RAWX` direction.

analytical model using equation 12.2. The small variations from the model are due to the MC approach used in the simulation.

12.5. Merging duplicate active pixel entries with the `merge-pixels` task

Since the `frame` task processes the events in the input files independently, the combined output file may contain multiple entries for the same pixel in the same frame. For example, one pixel in a single frame could contain two entries originating from different input particles. Since these events are impossible to distinguish in the eROSITA measurements, these multiple entries must be

aggregated, such that every active pixel for a given frame is represented by exactly one entry in the FITS file with the total deposited energy.

While the energy of the duplicate entries can easily be summed up for the aggregated single entry, the pointers to the particle tracks in the ROOT output described in Section 12.1 must also be merged in the `merge-pixels` task. For duplicate entries from different tracks, events, samples, or particles, the respective identifiers are set to the negative number of different values, rendering the pointer invalid. For example, duplicate entries originating from the same input particle and sample, but from two different events and tracks, will be merged into a single entry with track and event identifiers set to `-2` and keeping the original particle and sample identifiers. The track identifier `0` representing tracks starting inside the CCD (see Section 12.1) is not considered.

12.6. Electron charge cloud modeling with the `split-pixels` task

The production and tracking of electron charge clouds in the CCD is inhibited in the eROSITA Geant4 simulation environment because of the selected cut length. Therefore, spill-over of electrons with low energy created in a physical interaction in one pixel into a neighbor pixel is not considered in the simulations. This leads to a concentration of the deposited energy on fewer pixels in the `RPD` than it would be the case for measurements. To compensate for this effect, a simple empirical electron charge cloud model is implemented in the `eba digitizer` workflow. The model was originally proposed by K. Dennerl (MPE) – who also suggested to use this model for the purpose of the `split-pixels` task[25] – and is also implemented in the SImulation of X-ray TElescopes (SIXTE) end-to-end simulator (Dauser et al., 2019). For every active pixel in the input FITS file, the `split-pixels` task calculates the two closest edges to the energy-weighted centroid from the `SUBX` and `SUBY` fields of the `RPD`. The energy of the active pixel is then distributed into the 2×2 pixel square spanning along the

[25] Private communication in the regular eROSITA-DE background/foreground meetings.

closest edges according to an exponential model of the form

$$\xi_{pix,i} = \exp\left(-\left(\frac{r_i}{z}\right)^2\right) \tag{12.3}$$

$$E_{pix,i} = E_{tot} \cdot \frac{\xi_{pix,i}}{\sum_{i=1}^{4} \xi_{pix,i}} \tag{12.4}$$

where the energy distributed in the pixel i and the total energy of the event are denoted by $E_{pix,i}$ and E_{tot}, respectively, the non-normalized fraction of energy distributed in pixel i is denoted by $\xi_{pix,i}$, and the distance between the energy-weighted centroid and the geometric center of pixel i in units of pixels is denoted by r_i. The parameter of the originally proposed electron charge cloud model was $z = 0.355$. In this thesis, the effect of the electron charge cloud model parameter on the pattern fractions was investigated using MC simulation data and an optimal parameter of $z = 0.310$ was found (Chapter 13). An illustration of the electron model principle and a physical electron charge cloud is shown in Figure 12.5.

The `split-pixels` task provides the options `--numx` and `--numy` in order to support generic CCDs with different numbers of pixels. Since the model is applied for every active pixel in the input FITS file separately, it is typically necessary to subsequently merge the active pixels using the `merge-pixels` task described in Section 12.5. In the Snakemake workflow, the `merge-pixels` call is part of the `splitpixels` rule.

12.7. Energy resolution modeling with the `eres` task

The simulation output contains events with perfect energy resolution, limited only by the precision of the used floating-point format. Therefore, an energy resolution modeling step is included in the workflow to simulate the physical energy resolution of the eROSITA detector. The model is derived from a fit of a hyperbolic function of the form

$$\Delta E = \frac{1}{a \cdot E + b} + c \tag{12.5}$$

with the energy resolution ΔE, the energy E, and the free fit parameters a, b, and c, to pre-flight calibration measurements of the eROSITA cameras reported

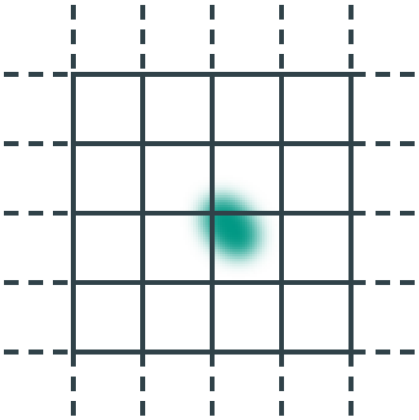

(a) Physical electron charge cloud.

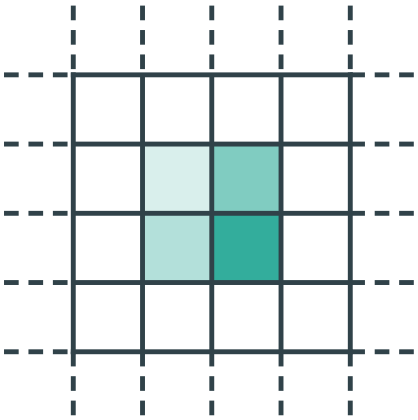

(b) Physical split pixel event.

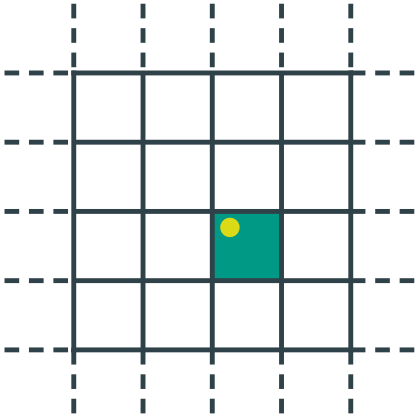

(c) Simulation RPD.

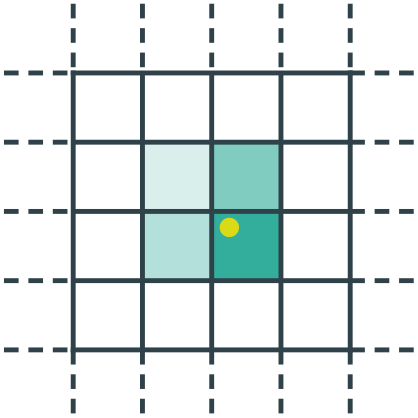

(d) Simulation split pixel event.

Figure 12.5.: Split pixels in measurement and simulation. For the physical CCD, the electron charge cloud produced by the impinging X-ray partially distributes the charge into the neighbor pixels, which leads to a split pixel event for charges above the energy threshold. In the simulation, the spill-over charges into the neighbor pixels are calculated from the energy-weighted centroid in the RPD using an exponential model.

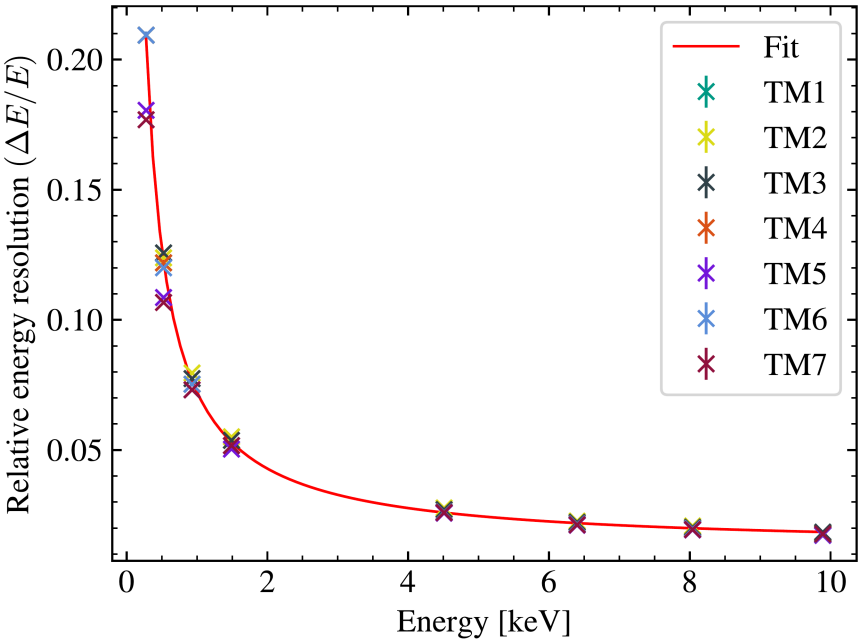

Figure 12.6.: Energy resolution model determined by fitting a hyperbolic function to pre-flight eROSITA energy resolution measurements for TM8. Reported measurement errors are included in the plot but are constrained inside the marker symbols. Note that the slightly better energy resolution at lower energies of the TM5 and TM7 cameras with off-chip optical light filter were excluded from the TM8 fit shown.

in Predehl et al. (2021). The `eba eres fit` command can be used to obtain a file containing the best fit parameters, which is needed to set the energy resolution model in the `eres` task. Best fit parameter files can be created for individual eROSITA cameras as well as any set of cameras. In this work, the hyperbolic function was fitted to all of the TM8 cameras in order to produce an energy resolution model representing an average of all eROSITA cameras with the on-chip optical light filter. The resulting fit is shown in Figure 12.6. The energy resolution modeling workflow step applies the energy resolution for each detected event by randomly sampling from a Gaussian distribution with the FWHM calculated from the hyperbolic model at the detected energy.

12.8. MIP rejection with the `miprej` task

The Bethe-Bloch equation describing the energy loss of a charged particle in matter through ionization and excitation shows a material-dependent minimum energy loss at around $3\,\beta\gamma$ to $4\,\beta\gamma$, with the Lorentz factor $\gamma = 1/\sqrt{1-\beta^2}$ and $\beta = v/c$ (Eidelman and Shwartz, 2012). Particles at these energies are commonly referred to as Minimum Ionizing Particles (MIPs) and are known to cause tracks of bright pixels in CCDs (and other imaging detectors), which have to be cleared from the observation data. The following explanation of the eROSITA MIP rejection is based on Freyberg et al. (2020), where the rejection methods are described in more detail. During science operation, the eROSITA detectors perform a MIP rejection algorithm directly on-board to reduce the telemetry rate by sending only MIP rejection rates instead of the raw data to Earth. The MIP rejection algorithm removes pixels above a given `adu` threshold ("trigger pixels") and in addition removes all pixels in a square with a length of five pixels around the trigger pixel, such that a total of 25 pixels is removed ("rejected pixels"). For MIP tracks, the rejected pixels will include other trigger pixels, such that the ratio of rejected pixels and trigger pixels is lower than 25 and the ratio thus yields information about the pattern of the trigger pixels. eROSITA typically observes a ratio of around 8, which suggests that the MIP rejection algorithm mostly removes MIP tracks and not isolated trigger pixels. In the beginning of the eROSITA mission, the trigger threshold was set to 12 288 adu (3000 adu in hexadecimal notation), which corresponds to energies of around 9 keV to 10 keV depending on calibration, and was later increased to 13 568 adu (3500 adu in hexadecimal notation)[26]. The MIP rejection algorithm of eROSITA is illustrated in Figure 12.7 for a single trigger pixel and a MIP track together with a single event. To allow for dedicated investigations of the MIPs, the MIP rejection on eROSITA can be switched off to retrieve raw frames.

The eROSITA MIP rejection algorithm is implemented in the `miprej` task. The Geant4 simulation and the `eba digitizer` workflow operate directly in the energy domain without the necessity for gain calibration. Therefore, the `miprej` task expects the trigger threshold provided as the `--threshold` option to be in eV. For this work, the trigger threshold in `adu` was converted to `eV`

[26] Private communication in the regular eROSITA-DE background/foreground meetings.

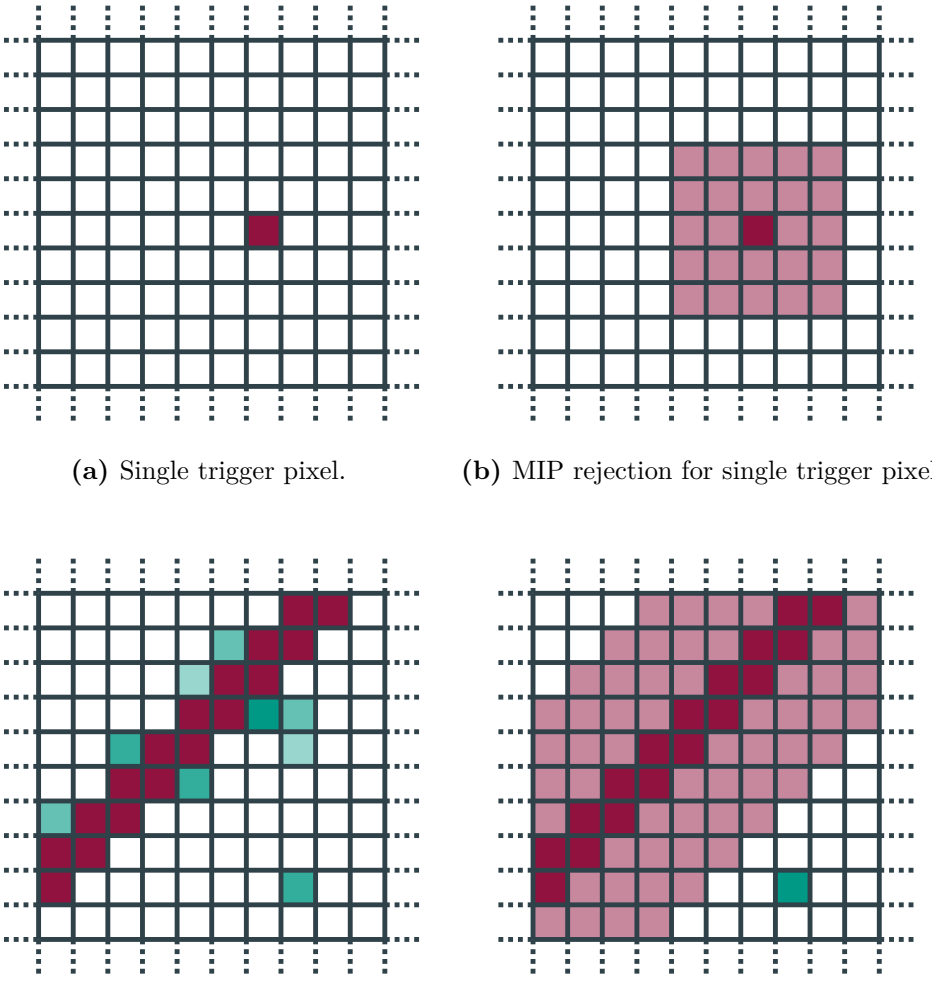

(a) Single trigger pixel.

(b) MIP rejection for single trigger pixel.

(c) MIP track and single event.

(d) MIP rejection for MIP track.

Figure 12.7.: Illustration of the eROSITA MIP rejection algorithm. (a) and (b): A single trigger pixel leads to a rejection of a 5×5 pixel square around the trigger pixel. (c) and (d): For a MIP track, a 5×5 pixel square is rejected around each of the trigger pixels. The single event in the bottom right corner is outside of the rejected squares and thus remains unaffected by the MIP rejection algorithm.

using the eROSITA average of 1 adu ≈ 0.78 eV as reported in Freyberg et al. (2020). The number of trigger pixels, rejected pixels, as well as their ratio is reported by the `miprej` task for the analyzed FITS file and can be written to a text file for analysis later in the workflow using the `--info` option.

The size of the rejected pixel rectangle can be adjusted with the `--rejx` and `--rejy` options. Generic CCDs are supported using the `--numx` and `--numy` options.

12.9. Energy conversion with the `econv` task

The energy of an active pixel is stored in the `RPD` as `float64` for high precision. However, the adapted tasks `PATTERN` and `ENERGY` of the eROSITA data analysis pipeline expect the energy to be stored in an `int16` field called `PHA` (Pulse Height Amplitude) in eV[27] in the FITS file. The conversion from `float64` to `int16` is performed by the `econv` task. To prevent overflow, active pixels with high energies outside the `int16` range – relevant only for analyses with deactivated MIP rejection – are set to the maximum energy of 32 767 eV[28].

12.10. X-ray event pattern analysis and photon energy calibration

At this stage of the workflow, the event list data includes modeling of the read-out as well as the eROSITA on-board processing, and the FITS file format is partly compatible with the FITS files produced by the preprocessor of the eROSITA data analysis pipeline described in Brunner et al. (2018). Thus, the X-ray event pattern analysis and the photon energy calibration can be performed with adapted tasks of the telescope (`TEL`) chain, and the final simulation event list FITS file is compatible for further interactive analysis with the eSASS. Customized versions of the existing eSASS tasks `PATTERN`

[27] For measurement data, the `PHA` values are typically given in adu. However, as the Geant4 simulation environment described in Section 11 operates directly in the energy domain, the simulated `PHA` values are given in eV.

[28] The maximum value of a 16-bit signed integer is $2^{15} - 1 = 32\,767$.

and `ENERGY` specifically adapted for handling the simulation FITS files were developed and provided by K. Dennerl (MPE)[29].

The adapted `PATTERN` task is used for X-ray event pattern analysis of the simulation event list data. Since the pattern matching algorithm is essentially the same as for measured eROSITA data, the differences between simulation and measurement introduced in this crucial task are presumably smaller than for customized and simplified pattern matching algorithms typically used in the analysis of MC background simulation data. The `PATTERN` task adds three additional columns to the FITS file: `PAT_TYP` (pattern type), `PAT_IND` (pattern index) containing a per frame index needed by the `ENERGY` task, and `PAT_INF` (pattern information). For valid patterns, the `PAT_TYP` field is filled with the number of pixels belonging to the pattern. For invalid patterns, the field will contain a negative value, and for patterns below the energy threshold it is set to zero. `PAT_INF` contains further information about the pattern encoded in a three-digit decimal value.

Photon energy calibration is performed using an adapted version of the `ENERGY` task. The `PI` (Pulse Invariant) column is added to the FITS file and contains the total reconstructed energy for the pattern in eV. Since the Geant4 simulation and the `eba digitizer` workflow operate directly in the energy domain and don't include modeling of the gain and the Charge Transfer Inefficiency (CTI), the combined energy calibration factor is unity. The total energy is only assigned to the main pixel of each pattern. For the secondary pixels of the pattern, the total energy is multiplied by -1. Thus, the main pixels of all valid patterns can be found in the later analysis by filtering for `PI` > 0 in addition to the filter for valid patterns described above.

[29] Detailed manuals of the eSASS `PATTERN` and `ENERGY` tasks are available in the eROSITA wiki pages. At the time of writing this thesis, the access to the manuals was restricted to members of the German eROSITA consortium.

Project II

13. Simulation of the filter wheel closed spectrum

For the simulation of the eROSITA FWC spectrum, the new camera mass model was used with all optional details activated, but with the slightly simplified CSG variant of the copper shield to reduce simulation time. A single camera was placed in the center of the simulation world without the other parts of the mass model, such as mirrors or the satellite structure. This allowed to use strong source biasing and enabled a long corresponding in-orbit time of 100 ks. Primary protons, electrons, atomic nuclei from helium to nickel, and CXB photons were simulated in separate runs following the input spectra described in Section 11.1. The simulations for individual primary particle types were further split into smaller jobs, each with a different fixed random seed to allow for highly parallelized job execution using many independent single-core jobs. The simulation environment was provided as Singularity containers (Kurtzer et al., 2017) to allow for reproducible simulation runs across different computers. More than 4500 individual jobs were executed with a total of more than 24 billion simulated primary particles. Most of the jobs were executed on the HPC cluster bwHPC bwForCluster BinAC.

The digitizer and data analysis workflow runs were performed on a local workstation. For the final event list, a circular extraction region was applied to match the detector map applied to the measured FWC data. The digitizer workflow described in Chapter 12 was run with different parameters of the electron charge cloud model in $z \in [0.1, 1.0]$ (see Section 12.6) in order to derive an optimal parameter based on the simulated pattern fractions, that was then used for the final digitizer workflow run and FWC background analysis.

Simulated fractions of single, double, triple, quadruple, and invalid event patterns for electron charge cloud model parameters of $z = 0.355$ and $z = 0.310$ are shown in Figure 13.1 in addition to the pattern fractions of the FWC

measurements of TM1 and TM4 with live times of 264 ks and 289 ks, respectively. The measurement data were processed, cleaned and provided by M. Yeung (MPE) using the newest collaboration-internal version 020 of the eSASS pipeline. Events with invalid patterns were removed from the FWC measurements as part of the processing and cleaning of the datasets. The simulation using the original electron charge cloud model parameter of $z = 0.355$ resulted in an overestimation of the patterns involving multiple pixels (double, triple, and quadruple events) compared to the measurements. As the mass models and digitizer parameters of TM1 and TM4 are identical in the simulation and would lead to consistent pattern fractions[30], the significant differences in the measured pattern fractions of both cameras could not be reproduced and the model parameter of $z = 0.310$ was found to be a suitable compromise (Section 14.1).

The effect of different electron charge cloud model parameters on the MIP trigger pixel rate, the ratios of rejected and trigger pixels, and the average count rate of the simulated FWC background spectrum between 2 keV and 6 keV are shown in Figure 13.2. As the distribution of low-energetic electrons produced in the CCD to neighboring pixels in the digitizer workflow is controlled by the model parameter, the MIP trigger pixel rates and the rejected-to-trigger pixel ratio are also affected by changes to this parameter. While the reduction of the parameter from 0.355 to 0.310 resulted in significant changes of the simulated pattern fractions, the effects on the MIP rejection and the simulated FWC background count rates were minimal. An additional run of the digitizer and data analysis workflow with a deactivated electron charge cloud model resulted in a trigger pixel rate of 545 counts s^{-1}, a ratio of 7.6, and a 2 keV to 6 keV count rate of 2.21×10^{-2} counts $\mathrm{s}^{-1}\,\mathrm{keV}^{-1}\,\mathrm{cm}^{-2}$. Using the final updated model parameter $z = 0.310$, a MIP trigger pixel rate of 540 counts s^{-1} was found, which is 18 % to 25 % lower than the measurement in the range of 660 counts s^{-1} to 720 counts s^{-1} (Freyberg et al., 2020), and the simulated ratio of rejected pixels to MIP trigger pixels was 7.6, which is consistent with the measured value of around eight (Freyberg et al., 2020) (see Section 14.1).

The simulated eROSITA FWC background spectrum is shown in Figure 13.3 together with the contribution of different primary particles to the simulated background spectrum and the background levels detected by the imaging and frame-store areas. The error bars represent the statistical errors assuming

[30] Both TM1 and TM4 have an on-chip optical light filter.

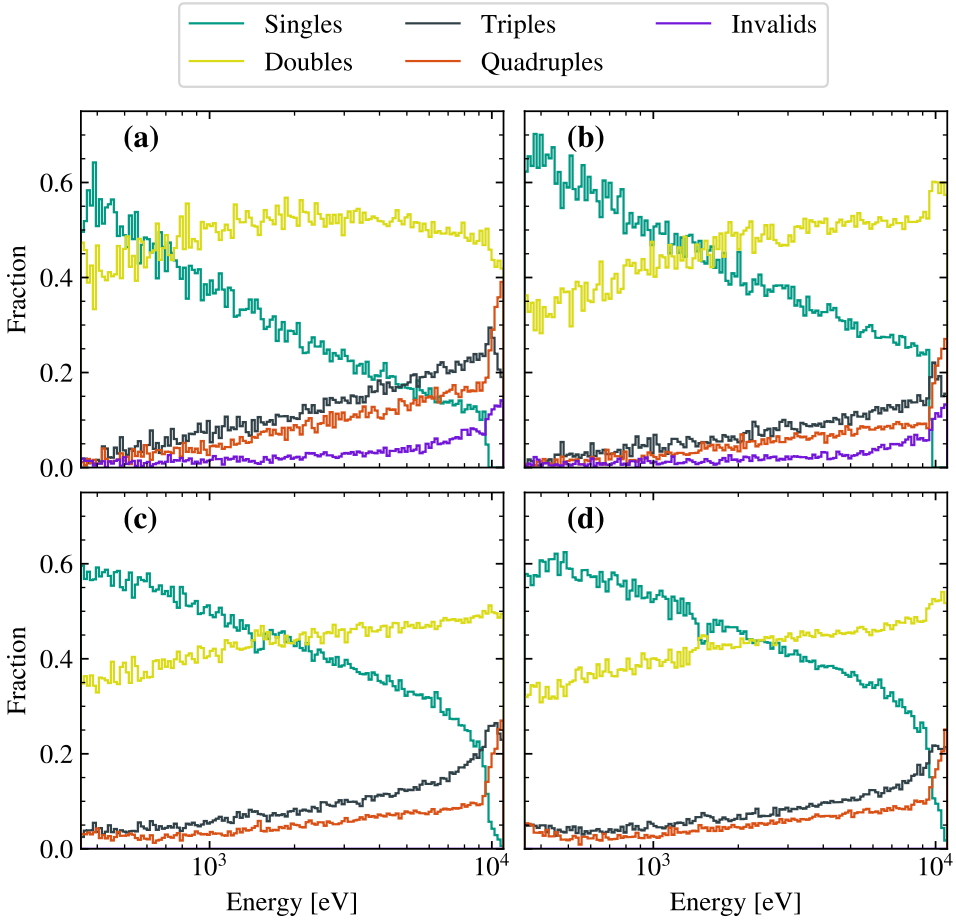

Figure 13.1.: Pattern fractions from simulations with the original electron charge cloud model parameter $z = 0.355$ (a) and the updated model parameter $z = 0.310$ (b), and pattern fractions from FWC measurements for TM1 (c) and TM4 (d) processed with the eSASS pipeline version 020.

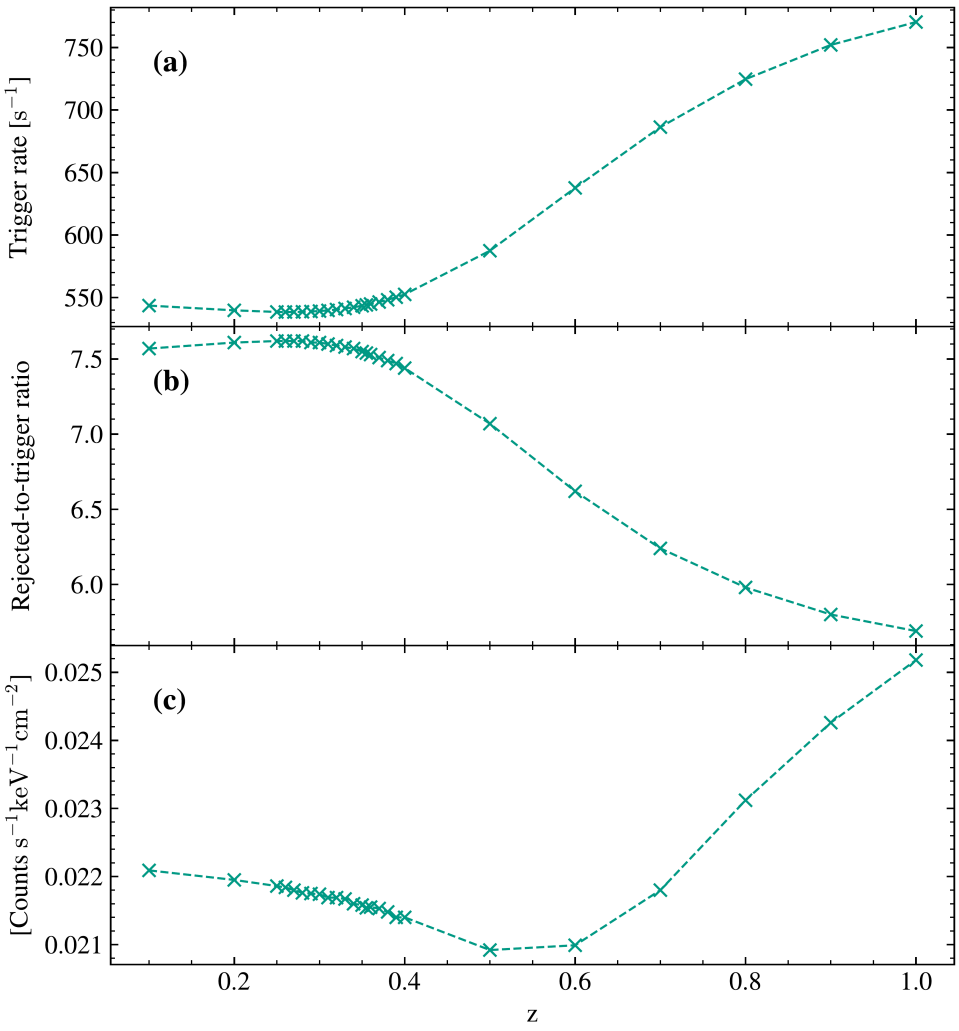

Figure 13.2.: Simulated MIP trigger pixel rates (a), ratios of rejected pixels and MIP trigger pixels (b), and count rates in the energy range of 2 keV to 6 keV (c) for different electron charge cloud model parameters z.

Poisson distributed counts and the light green shaded area represents a 20 % systematical uncertainty of the input spectra used in the simulation (see Chapter 14). The simulated background level in the 2 keV to 6 keV range, where no pronounced fluorescence lines were seen, was 2.17×10^{-2} counts s^{-1} keV^{-1} cm^{-2}. Thus, the simulated background level was 14 % lower than the instrument-averaged combined TM8 FWC measurement with a background level of 2.53×10^{-2} counts s^{-1} keV^{-1} cm^{-2} between 2 keV and 6 keV. The simulated spectrum reproduced the raise towards lower energies and the drop towards high energies seen in the measured spectrum. For the primary particle contributions, the astrophysical definition of metals is used (i.e. all elements besides hydrogen and helium). The most important contribution was seen from protons and the contribution from the CXB was found to be negligible. Helium nuclei, electrons, and metals had similar contributions to the background. In the 2 keV to 6 keV range, the frame-store area contributed 12 % to the total background. While the imaging area spectrum showed similar fluorescence lines as seen in the total simulated spectrum, only minimal fluorescence lines were visible in the frame-store area spectrum.

Pronounced fluorescence lines were visible in the simulated FWC spectrum at the aluminium, iron, copper, and zinc K-α transmission energies. The aluminium line was stronger for the simulation compared to the measurement, while the iron line appeared less pronounced than it did in the measurement. The contributions of mass model volumes to the simulated aluminium, iron, and zinc K-α fluorescence lines are shown in Figure 13.4, where volumes contributing less than 5 % individually were combined as "other".

Filtering of the fluorescent X-rays for subsequent analysis of their production positions was conducted based on the results of the `filterlivetime` tasks (see Figure 12.1) before energy resolution modeling and separately for the imaging and frame-store areas. The events were filtered based on the fluorescence line energies used in Geant4. In addition, events were considered fluorescence events only if the particle impinging on the detector was a photon.

The main contribution to the aluminium line were the aluminium housing around the detector and the clamping frame that holds the beryllium plate below the CCD with 59 % for the imaging area and 78 % for the frame-store area. The filter wheel contribution to the total aluminium K-α line was 16 %.

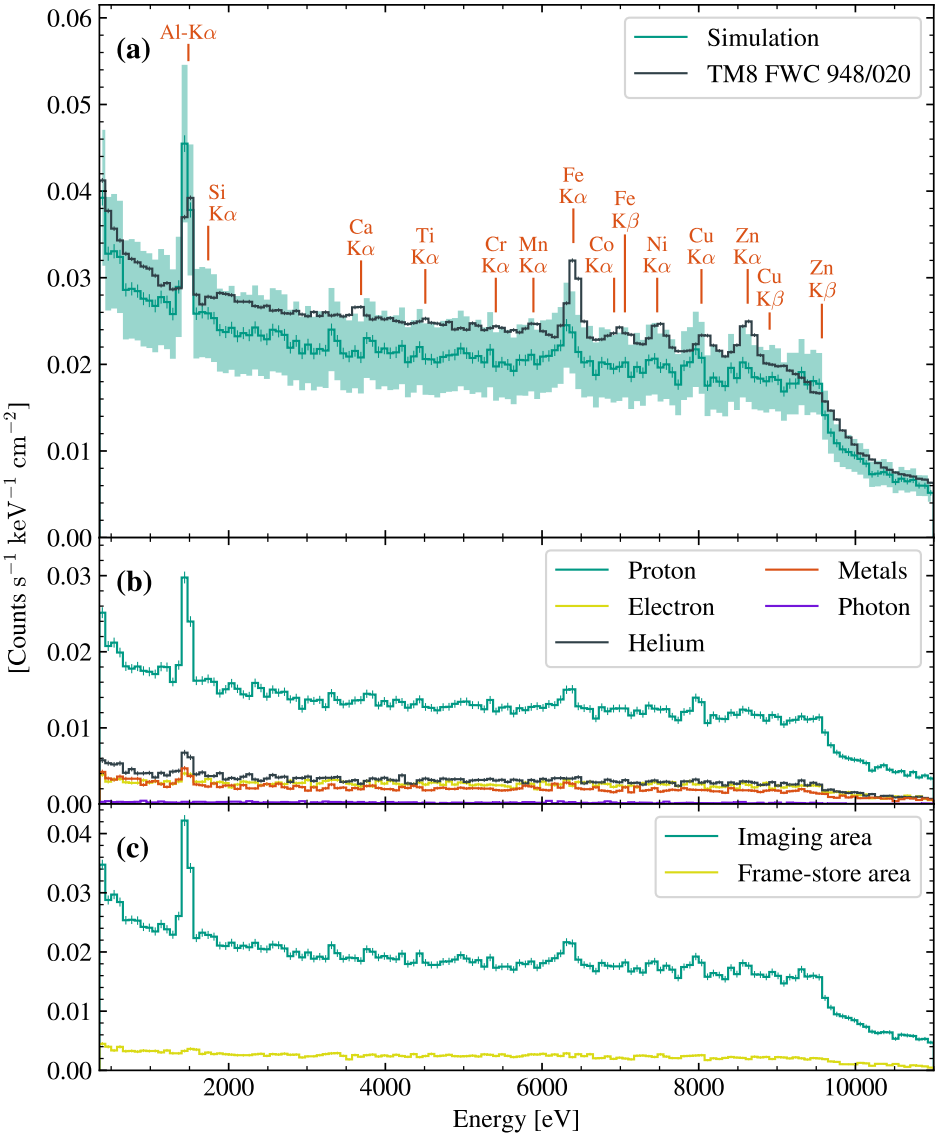

Figure 13.3.: (a): Simulated and TM8 measured eROSITA FWC spectra. (b): Contribution of primary particles from the isotropic background to the simulated FWC background. (c): Simulated background contributions from the imaging and frame-store areas of the CCD.

The imaging area detected 89 % of the total 2721 aluminium K-α X-rays in the simulation.

The iron K-α line seen in the simulated FWC spectrum predominantly originated from impurities in the beryllium with 80 % of the fluorescent X-rays in the imaging area coming from the beryllium shielding lid below the CCD and the beryllium layer of the graded-Z shield mounted at the aperture. The beryllium shielding lid was also the largest contributor for the frame-store area with 77 % of the fluorescent X-rays assigned to it. 72 % of the total 557 detected iron K-α photons were detected in the imaging area.

The main contributions to the zinc K-α line were from the closed filter wheel with 55 % and from the flange with 27 %. The frame-store area was well shielded from the zinc fluorescence X-rays and detected only 6 % of the total 393 detected events.

The origins of the fluorescence X-rays detected in the CCD are shown as a three-dimensional scatter plot in Figure 13.5, where the center of the imaging area was placed at $(-50,\ 0,\ -60)$ mm. The fluorescence X-rays detected by the frame-store area were mainly produced in close proximity to the frame-store area, whereas fluorescence X-rays detected by the imaging area were also produced along the line of sight to the filter wheel. Parts of the filter wheel, the flange insert, the graded-Z aperture, the aluminium housing, and the beryllium plate below the CCD can be clearly distinguished. For the aluminium housing, only the parts close to the CCD are visible in the scatter plot, and the other parts appear well shielded, e.g. by the beryllium plate.

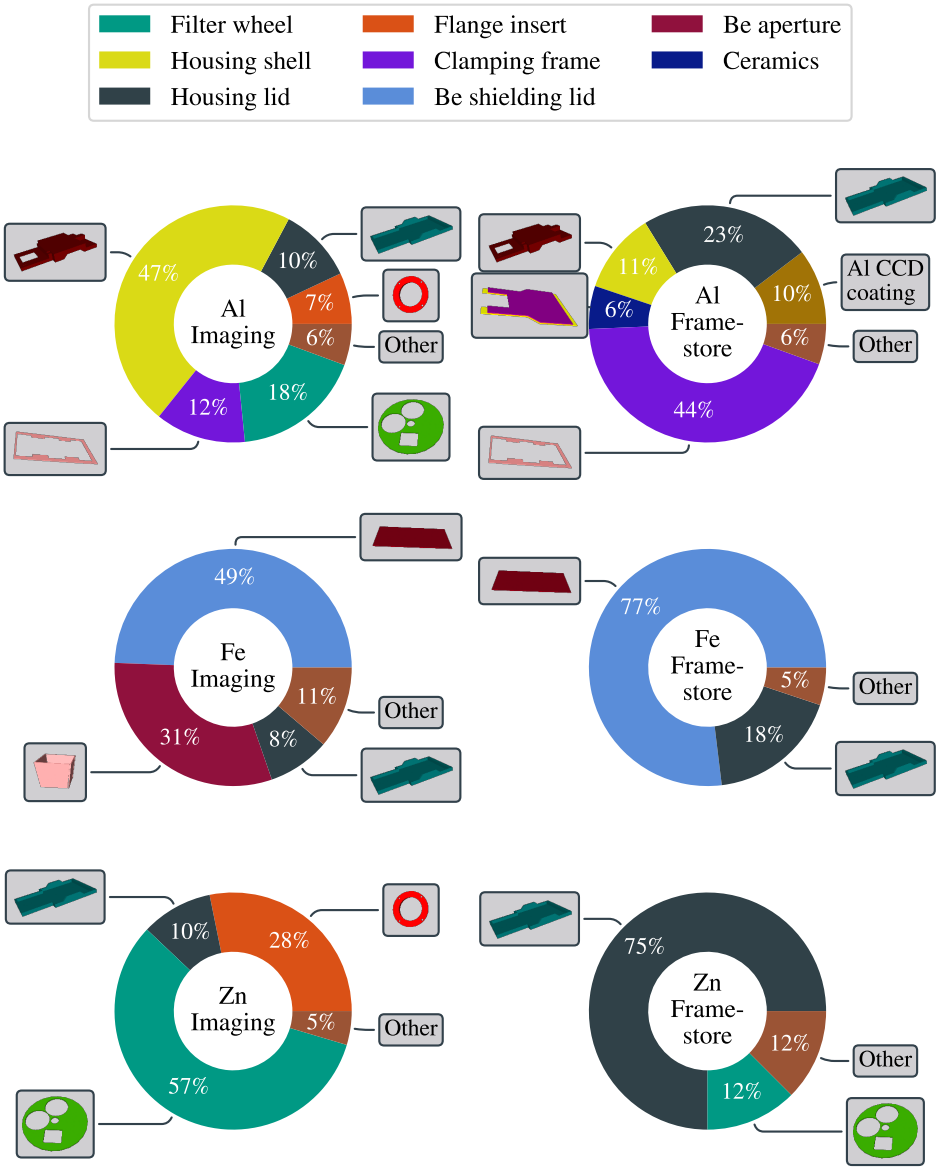

Figure 13.4.: Contributions of mass model volumes to the aluminium, iron, and zinc K-α fluorescence lines.

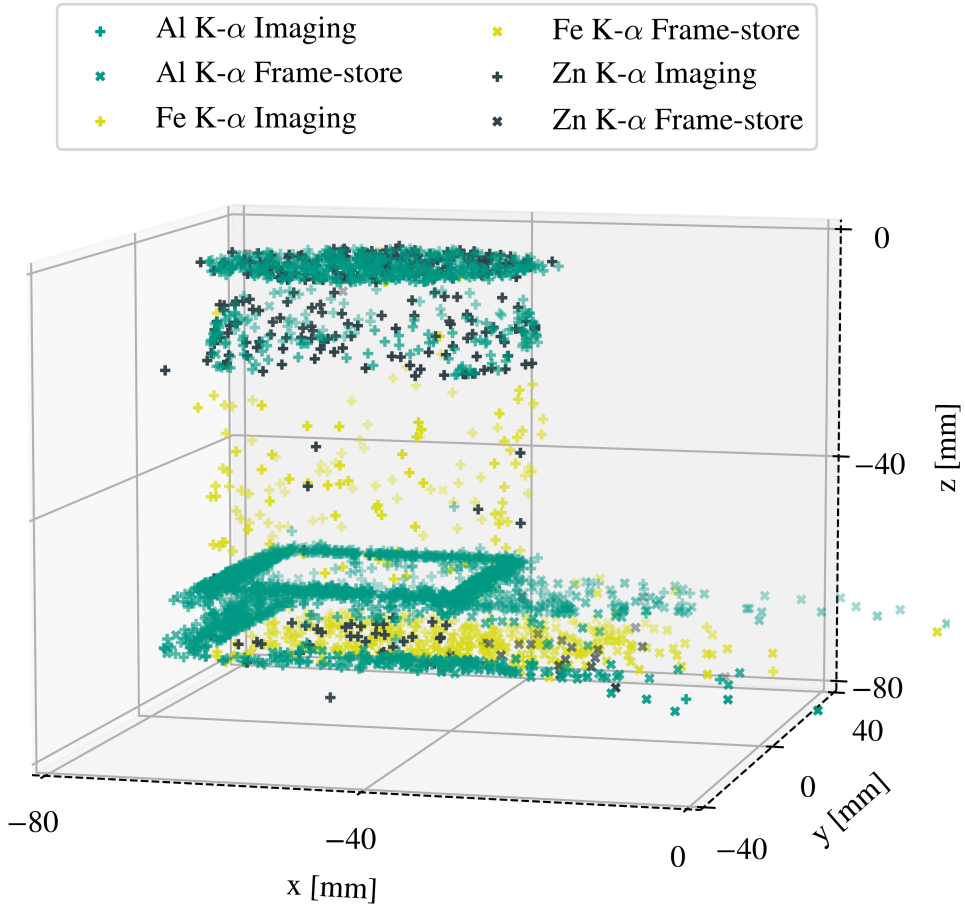

Figure 13.5.: Origins of the fluorescence X-rays detected in the CCD. X-rays detected in the imaging and frame-store areas are visualized as different markers.

Project II

14. Discussion

The main conceptual differences between this work and earlier eROSITA background simulation studies are the detailed mass model and the workflow for digitization and data analysis, which were developed in the course of this thesis. The new workflow incorporates modeling of additional detector effects such as the read-out of the frame-store CCD and uses the pattern matching algorithm of eSASS. This enabled to retrieve additional observables from the simulations, such as pattern fractions, MIP trigger pixel rates, and the ratio of rejected pixels to MIP trigger pixels, that are discussed in Section 14.1. Furthermore, the eSASS-compatible format of the final event list allows to fit the existing empirical eROSITA FWC model to the simulated data using the same process as for the measured data. Thus, the simulation together with the simulation ground truth information for the detected events potentially allows to foster the understanding of the physical processes behind not yet fully understood features in the FWC spectrum (i.e. the raise at lower energies) and to transform the empirical FWC model into a more physically motivated model.

In Section 14.1, the optimization of the electron charge cloud model parameter and the effect of this parameter on the pattern fractions and MIP rejection are discussed. The simulated filter wheel closed background level is discussed in Section 14.2. The new mass model enabled the precise investigation of the origin of the fluorescence lines seen in the filter wheel closed spectrum, which is discussed in Section 14.3.

14.1. Pattern fractions and MIP rejection

The simulated pattern fractions shown in Figure 13.1 with the original electron charge cloud model parameter of $z = 0.355$, which is also used in the SIXTE simulator, was found to underestimate the single event fractions and overestimate the triple and quadruple event fractions at higher energies. This can be explained by an overestimation of the fraction of the charge distributed to the neighboring pixels with the given electron charge cloud model parameter. Several electron charge cloud model parameters were investigated in order to find the optimal parameter for the background simulations.

The measured FWC pattern fractions showed significant differences depending on the individual telescope module with differences also among the cameras with on-chip optical light filters as shown in Figure 13.1 for TM1 and TM4. Since the mass models and the electron charge cloud model were identical for all of the TM8 cameras, the final model parameter had to be chosen to represent a combination of the pattern fractions for the TM8 measurements. Furthermore, the slope of the simulated single event fraction was found to be too steep for the electron charge cloud model parameters that reproduced the slopes of the triple and quadruple event fractions. Therefore, the final model parameter represents a trade-off between overestimation of the single event fraction at lower energies due to a lower model parameter and an overestimation of the triple and quadruple event fractions at higher energies due to a higher model parameter. Since this work is mainly focused on the energies above 1 keV where the fluorescence lines visible in the FWC spectrum are located, a final electron charge cloud model parameter of $z = 0.310$ was chosen, which leads to similar triple and quadruple event fractions in that energy range, but significantly overestimates the single event fraction at lower energies.

The sharp drop in the single event fraction at 9.6 keV is due to the MIP rejection task in the digitizer and data analysis workflow, where single event patterns with energies above the MIP trigger threshold of 12 288 adu are removed. The drop is more pronounced in the simulations than in the measurements for two main reasons. Firstly, the simulations operated directly in the energy domain, which corresponds to a universal adu to eV calibration factor, while the measurement data were folded through the Redistribution Matrix File (RMF). Thus, the sharp drop introduced by the MIP rejection in the adu domain is slightly

washed out in the energy domain for the measurements. To partly reproduce this effect in future simulation work, modeling of gain and CTI effects could be added to the digitizer and data analysis workflow. Secondly, the in-orbit MIP trigger threshold was increased in the course of the eROSITA mission (Section 12.8). Therefore, in contrast to the simulations, the FWC measurements contain data obtained with two different in-orbit MIP trigger thresholds. This effect could be simulated in future work by introducing a time-dependent MIP trigger threshold.

The impact of the electron charge cloud model and the model parameter on simulated observables was investigated for the trigger pixel rates, the ratios of rejected and trigger pixels, and the count rates in the 2 keV to 6 keV energy band. In general, these quantities are strongly affected by the model parameter, especially in the case of overestimated charge cloud sizes, which lead to a broadening of MIP tracks and therefore increased trigger pixel rates and decreased trigger ratios. However, the fine-tuning of the model parameter from $z = 0.355$ to $z = 0.310$ only had minimal impact on the trigger pixel rates, ratios, and background count rate.

The eROday averaged MIP trigger pixel rates measured by all of the eROSITA cameras between October 2019 and November 2020 were typically between 660 counts s^{-1} and 720 counts s^{-1} and showed simultaneous long-term temporal variability related to the solar activity cycle and short-term variabilities in the range of 27 d to 29 d potentially related to different solar influences, but without a clear single correlation parameter (Freyberg et al., 2020). Thus, the simulated MIP trigger pixel rate – without systematic variations by construction of the simulation – is lower than the measured rates by roughly 20 %, which is similar to the relative differences between the simulated and measured background count rates discussed in Section 14.2. The ratio between pixels rejected by the MIP rejection algorithm and MIP trigger pixels exceeding the energy threshold is consistent for simulation and measurement with a simulated ratio of 7.6 and a measured ratio on the order of about eight[31], as reported in Freyberg et al. (2020). This ratio represents an important metric, as it depends on the average geometrical shape of the MIP particle tracks in the CCD. Therefore, the consistent ratios suggest that the range cut and production cut configuration

[31]The precise values are typically slightly lower than eight. Private communication in the regular eROSITA-DE background/foreground meetings.

used in the simulation is suitable to produce realistic MIP particle tracks.

14.2. Filter wheel closed background level

To compare the simulated and measured FWC background levels, the 2 keV to 6 keV range between the aluminium K-α and the iron K-α lines is of special interest due to the lack of strong fluorescence lines in that energy range, as shown in Figure 13.3. The 14 % lower background level of the simulation is roughly consistent with the simulated MIP trigger pixel rate underestimating the measured trigger pixel rate on the order of 20 %. Thus, increasing the input primary fluxes by about 15 % to 20 % could potentially lead to consistent background levels and MIP trigger rates for simulation and measurement. Indeed, such an increase of the input fluxes would be consistent with the empirical models due to the estimated systematical and statistical uncertainties of observational data measured at the same energy range and at the same time of about 20 % (Kuznetsov et al., 2017). Further uncertainties for the input fluxes were introduced by the fact that the measurements were conducted in orbits different from the eROSITA orbit. Dedicated particle monitors in one of the future missions to L_2, measuring fluxes and spectra for different charged particles, could deliver useful input fluxes data for future simulation studies.

The frame-store area of the eROSITA CCD is typically either excluded from simulations, e.g., it is not included yet in the official eROSITA simulator SIXTE (Dauser et al., 2019), or included with simplified modeling. For example, in recent FWC studies based on (Perinati et al., 2012), the frame-store area was not included in the mass model and was modeled by increasing the FWC background level from the imaging area by 12 %. The inclusion of the frame-store area in the mass model together with the implementation of the precise frame-store CCD read-out as part of this thesis allowed to investigate the background levels and fluorescence lines separately for the imaging and frame-store areas. The background level contributed by the frame-store area in the 2 keV to 6 keV range was found to match exactly the analytical prediction of 12 % given in Freyberg et al. (2020) based on the read-out cycle times and assuming the same incident flux on the imaging and frame-store areas. The frame-store area spectrum appeared almost free of visible fluorescence lines. Even for the case of the always-on frame-store area (integrating over the complete cycle

time or $t_{int} = t_{cyc}$) in the fluorescence line analysis reported in Chapter 13, the frame-store area only contributed between 6 % (zinc K-α) and 28 % (iron K-α), although the frame-store area represents 40 % of the geometrical area of the CCD. This emphasizes the effectiveness of the eROSITA frame-store area shielding from fluorescence lines generated inside the camera.

Pre-launch MC simulation studies of the expected particle-induced background and predictions whether scientific requirements for the background level can be achieved are essential for designing future missions such as Athena. Therefore, improved simulations of existing missions leading to better consistency with measurements can also help to improve pre-launch simulations, increase confidence in the predicted results, and potentially allow to reduce the safety buffers that need to be added to the predicted background levels for future missions.

14.3. Fluorescence lines

The highly detailed mass model used in the simulation enabled the investigation of the exact camera parts responsible for the fluorescence lines seen in the FWC spectrum. Understanding the origin of the fluorescence photons is critical for developing further improved camera designs and potential counter measures reducing the strengths of the fluorescence lines in future missions. Furthermore, it can improve the characterization of the particle-induced background that is present in the case of the filter wheel in "FILTER" position[32] during the survey, e.g. by estimating the aluminium line contribution by the closed filter wheel.

While in pre-launch simulations fluorescence lines from the detector surroundings were either not found when the graded-Z shield was in place (Tenzer et al., 2010) or less pronounced than in the measurements (Perinati et al., 2012), fluorescence lines for aluminium, iron, copper, and zinc were visible even with activated energy resolution modeling and a bin size of 75 keV as shown in Figure 13.3. This improvement is mainly due to the new highly detailed mass model with precise material compositions including impurities. Furthermore, the Geant4 version used for this simulation incorporates improvements in the modeling of physical processes from more than a decade over the Geant4 versions

[32]The filter wheel contains a 200 nm thick polyimide foil also for the cameras with on-chip optical light filter.

available at the time of the pre-flight simulations. In addition, the increase in available computing capacity and the possibility to use the HPC cluster allowed to produce simulation data with better statistics with the simulation corresponding to an in-orbit exposure time of 100 ks for a single eROSITA camera. The reasons for the clearly visible overestimation of the aluminium K-α line were unclear at the time of writing this thesis. Since the volumes contributing to the aluminium line were modeled in detail with only small simplifications made to enable the CSG approach, the mass model is expected to only contribute small differences and it is unlikely to be the main cause. Potential inaccuracies in the PIXE cross sections used at low energies, which would translate directly into yield differences, will be investigated in future work with special emphasis on the aluminium and iron K-α lines (see below).

In Predehl et al. (2021), the aluminium K-α line in the measured FWC spectrum was expected to originate mainly from the closed filter wheel (thickness of 4 mm, made of aluminium). In contrast, the simulation results show that the filter wheel contributes only 18 % of the total aluminium K-α line seen in the imaging area of the CCD and 16 % when including the frame-store area. The simulations suggest that the major part of this line is originating from inside the camera and thus will be part of the background also during the survey with the filter wheel in "FILTER" position. For the zinc K-α line, the filter wheel is the main contributor due to the large zinc mass fraction of 6.1 % in the simulated aluminium AW-7075 alloy. Thus, the strength of the zinc line is expected to be strongly reduced when the filter wheel is not in closed position.

The iron K-α line seen in the simulation results predominantly originates from impurities in the beryllium, which is in line with previous assumptions discussed in Freyberg et al. (2020). However, since the iron line is underestimated in the simulation results and the independent analysis of the spare eROSITA beryllium plate is roughly consistent with the manufacturer's analysis with a difference of 15 % in the iron fraction, the origin of the "missing" part of the iron line remains unclear. A possible contribution to the iron line could be from potential impurities in the boron-carbide layer of the graded-Z shield placed on top of the frame-store area, which were excluded in the used version of the new mass model due to the lack of solid information about the abundances in the plates used for eROSITA. However, since the boron-carbide plate is only placed close to the frame-store area, a strong contribution to the iron line can be excluded from the measured FWC background, as it would have introduced

a steep gradient along the RAWY direction due to the read-out cycle (see Section 12.4).

The only calcium presence in the mass model is in the form of an impurity in the beryllium material with a very minor mass fraction of 0.0002 %, that is not sufficient to explain the calcium line seen in the measured FWC spectrum. Therefore, it is expected that the origin of the calcium line is not in the volumes that are part of the mass model, and the search for its origin is still actively ongoing.

In general, the simulation results confirmed the effectiveness of the graded-Z shielding and the aluminium case in suppressing the strong copper line, that would be expected from the 3 cm thick copper shielding around the camera. Furthermore, the simulations confirmed the assumption, that impurities in the material compositions inside the camera significantly contribute to the fluorescence features in the FWC background (Predehl et al., 2021; Freyberg et al., 2020). This is particularly important for the design of future X-ray missions, and future pre-launch simulation studies should include the expected impurities in the mass models.

Since the analysis of the origins of the fluorescence lines was performed before read-out modeling, MIP rejection, electron charge cloud modeling, pattern matching and circular extraction, the results represent the fluorescent X-rays that were absorbed by the CCD, including also events that would eventually be removed from the final event list in later steps of the workflow. Fluorescent X-rays that deposit energy in multiple pixels in the Geant4 tracking are not considered. However, due to the mono-energetic analysis and the small pixel sizes, the effect on the analysis of the originating volumes is assumed to be stochastic and minimal.

The fluorescence lines visible in the FWC spectrum were shifted to lower energies compared to the eROSITA measurement and experimental X-ray fluorescence data reported in Thompson et al. (2009) based on Bearden and Burr (1967), which was clearly visible for spectra with smaller bin sizes (data not shown). This is a known effect for simulation of atomic relaxation with Geant4 (Guatelli et al., 2007). The reason for the visible energy differences are simplifications in the calculation of the transition energies in the LLNL Evaluated Atomic Data Library (EADL) (Perkins et al., 1991), which uses transition energies approximated from neutral atoms (Salvat and Fernández-Varea, 2009). Since

the Geant4 version 10.1, it is possible to use the more accurate experimental transition energies reported in Bearden and Burr (1967) (Allison et al., 2016). Future work will be conducted using these experimental transition energies for the eROSITA FWC simulations. Furthermore, the effect of different PIXE ionization cross sections available in Geant4 (Bakr et al., 2021, 2018) on the FWC spectrum will be investigated. These studies are planned to be performed first using a simple spherical shell approximation of the mass model before conducting a new iteration of the detailed simulation because of the high computational cost of the FWC simulations with the detailed mass model.

Project III.

Design and simulation studies of a breast PET insert

Project III

Contents

Project III

15. Introduction

In this project, MC simulations of a future breast PET/MRI insert designed for operation inside a whole-body PET/MRI scanner were performed. The expected PET performance characteristics were evaluated for three breast PET insert geometries. In addition to the performance characteristics within the Field Of View (FOV) of the breast PET insert, the potential improvements in sensitivity and spatial resolution outside of the FOV from collecting mixed coincidences between the breast PET insert and the whole-body PET scanner were estimated.

15.1. PET in breast cancer

Among women, breast cancer corresponds to a fraction of 24.5 % of all diagnosed cancers, and breast cancer is the leading cause of cancer death with a fraction of 15.5 % according to the GLOBOCAN 2020 estimates by the International Agency for Research on Cancer (IARC) (Sung et al., 2021). However, the breast cancer mortality rates vary widely across countries, and for many countries, the mortality rate has decreased significantly over the last decade (Sedeta et al., 2023).

Medical imaging techniques are crucial for breast cancer diagnosis and treatment in modern oncology in general, including tumor detection and classification, treatment planning, treatment response assessment, and screening (Rembielak et al., 2016). For breast cancer imaging, in addition to the long established mammography, ultrasound, and Magnetic Resonance Imaging (MRI) modalities, Positron Emission Tomography (PET) for tumor staging has become more important in the clinical routine (Koolen et al., 2012). Based on the detection of two 511 keV gamma rays produced in an electron-positron annihilation, PET is a non-invasive molecular imaging modality that allows for quantification of the

distribution of positron-emitting radiotracers (Cherry et al., 2012). Together with the commonly used 2-[^{18}F]fluoro-2-deoxy-D-glucose ([^{18}F]FDG) radiotracer as a glucose analogon, PET provides accurate functional data of the glucose metabolism, which is increased in most tumor cells compared to normal tissue. Furthermore, several other radiotracers are available in the clinical setting to obtain functional data of different processes in breast cancer imaging, such as tracers targeting estrogen receptors (Peñuelas et al., 2012). While PET is highly useful and widely used in modern breast cancer imaging, the limited spatial resolution of clinical whole-body PET scanners and the so-called partial volume effect hinder the detection of small lesions and metastases (Zhang-Yin, 2023).

As PET lacks accurate imaging of the anatomical structure, PET is often combined with CT in hybrid PET/CT scanners, which provide a fusion of the functional data from the PET modality and the structural information from the CT (Townsend, 2008). In addition to the widely adopted PET/CT scanners, whole-body clinical PET/MRI scanners have become available, facilitating the high soft tissue contrast of the MRI and reducing the radiation dose compared to PET/CT, which is especially advantageous for pediatric patients (Pichler et al., 2008; Nensa et al., 2014; Wehrl et al., 2015; Mannheim et al., 2018). For primary breast cancers, [^{18}F]FDG-PET demonstrated higher specificity compared to MRI (Moy et al., 2007; Botsikas et al., 2016), while dynamic contrast-enhanced MRI has the highest sensitivity for breast cancer detection (Umutlu and Herrmann, 2018). Hybrid PET/MRI was found to be useful for breast cancer imaging (Catalano et al., 2017), and the differentiation between benign and malignant enhancements improved by the functional data of PET/MRI might lead to less unnecessary breast biopsies (Pinker et al., 2014; Pujara et al., 2019).

Breast cancer is characterized by a high degree of morphological and molecular diversity, both between multiple patients (intertumor heterogeneity) and within an individual patient or single tumor (intratumor heterogeneity), necessitating individualized cancer treatment and precise diagnoses (Polyak, 2011; Martelotto et al., 2014; Aleskandarany et al., 2018). It has been reported that the multiparametric information from simultaneous PET/MRI can be suitable for intratumoral classification in breast cancer to further improve diagnostic strategies (Schmitz et al., 2016).

15.2. Axillary lymph node staging

In addition to the imaging of the breast, accurate axillary lymph node staging is crucial, as it is an important predictor of disease progression and treatment planning (Caudle et al., 2014). Two surgical procedures are frequently performed for axillary lymph node staging: Axillary Lymph Node Dissection (ALND), where lymph nodes are removed from the axilla, and the minimally invasive Sentinel Lymph Node Biopsy (SLNB), where only the first lymph nodes in the lymphatic drainage of the breast are removed (Harris et al., 2014). Compared with the potential long-term complications of ALND, such as lymphedema and chronic pain, SLNB is associated with less postoperative morbidity (Burak et al., 2002). Therefore, today SLNB is the standard approach in clinically node-negative patients, while in the past, ALND was standardly performed for axillary lymph node staging (Caudle et al., 2014). If the SLNB is negative for metastases, the axillary lymph nodes can be expected to be unaffected, as the lymphatic drainage of the breast follows an orderly pattern as shown in Figure 15.1a, and ALND is not required (Chang et al., 2020).

Several studies were performed to investigate the potential of PET imaging for axillary lymph node staging, either as non-invasive replacement for surgical procedures or for combined use together with SLNB (Crippa et al., 2008). [^{18}F]FDG-PET was found to show low sensitivity, but high specificity for detecting metastases in the axillary lymph nodes (Veronesi et al., 2007). The combined use of [^{18}F]FDG-PET and surgical procedures can be beneficial, e.g., as the high specificity of PET allows direct ALND in patients with detectable [^{18}F]FDG uptake in the axillary lymph nodes, rather than SLNB and subsequent ALND, or for whole-body staging in clinically node-positive or equivocal patients (Crippa et al., 2008). A recent study demonstrated that whole-body PET/MRI combined with a machine learning algorithm could potentially avoid invasive procedures for newly diagnosed breast cancer patients (Morawitz et al., 2023). However, a major problem of [^{18}F]FDG-PET for axillary lymph node staging is the insufficient capability of the currently available whole-body PET scanners to reliably detect small metastases, which is attributed to limited spatial resolution of the PET scanners (Guller et al., 2003; Crippa et al., 2008). Therefore, designing a PET insert specifically for breast imaging that improves the spatial resolution in the breast and the axillary lymph node regions can potentially

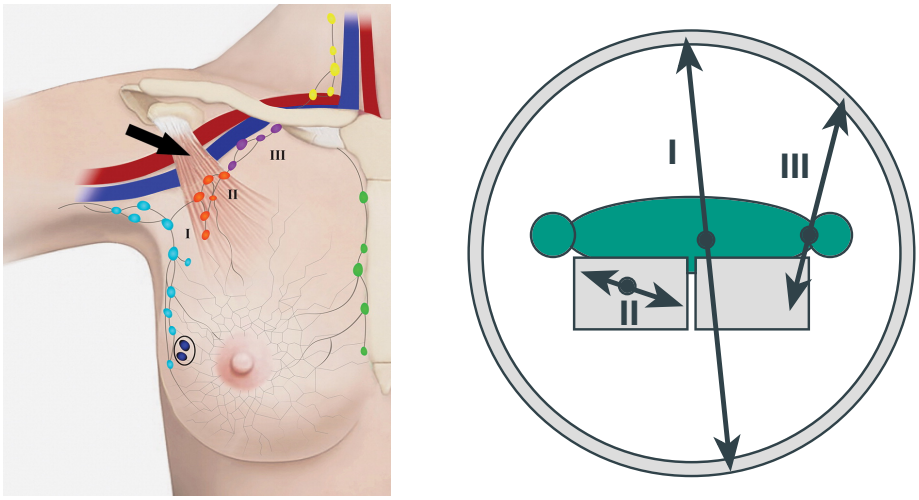

(a) Lymphatic drainage of the breast. **(b)** Three types of coincidences.

Figure 15.1.: (a): Level I, II, and III axillary lymph nodes of the lymphatic drainage of the breast. The typical location of the sentinel lymph nodes is indicated by the black ellipse. The black arrow points to the pectoralis minor muscle. (b): Three types of coincidences can be recorded by the breast PET insert (two boxes in the center) and the whole-body PET scanner (outer circle, figure not to scale). The patient is depicted in green and the back-to-back gamma rays of the exemplary coincidences are visualized as arrows pointing to the location of detection in the scanners. Type I coincidences are whole-body-only, Type II coincidences are insert-only, and Type III coincidences are mixed between both scanners. The Lines Of Response (LORs) of the Type III coincidences penetrate the location of the axillary lymph nodes. Image credit for (a): Chang et al. (2020). Reproduced with permission from Radiological Society of North America.

provide important improvements for PET in breast cancer imaging and axillary lymph node staging.

15.3. Designing a breast PET insert

PET inserts, designed to operate inside an MRI scanner for enabling simultaneous PET/MRI, first emerged from the preclinical setting, where today several PET inserts are available (a list of preclinical PET inserts is given in Disselhorst et al. (2022)). In the clinical setting, PET inserts were developed for brain imaging (Kolb et al., 2012; Gonzalez et al., 2019; Won et al., 2021; Scipioni et al., 2023). Dedicated breast PET inserts are currently in development by the HYPMED consortium (Schulz et al., 2020), and by our group (Pommranz et al., 2023).

The main concept of organ-specific PET inserts is to improve the PET imaging quality compared to whole-body PET systems. This can be achieved by using smaller crystal sizes than in the whole-body PET scanners for improved spatial resolution, and by placing the crystals closer to the region of interest for increased solid angle coverage by the scintillators, leading to increased sensitivity. The breast PET insert planned by our group will be operated inside a whole-body PET/MRI scanner (Biograph mMR, Siemens Healthineers, Erlangen, Germany). The combination of two PET systems in the whole-body scanner and the breast insert will allow to improve the spatial resolution not only inside of the FOV of the breast PET insert, but also outside of the breast PET insert FOV using "mixed coincidences" between both devices (see Section 15.4 and Figure 15.1b).

For whole-body PET/MRI scanners, multichannel Radio Frequency (RF) coils dedicated for the breast can be used to improve the organ-specific MRI quality (Aklan et al., 2013; Dregely et al., 2015). The breast PET insert is planned for integration into an RF breast coil (breast biopsy coil, NORAS MRI products, Höchberg, Germany), which will result in a hybrid breast PET/MRI insert, improving both modalities for breast imaging in a single scan, the MRI through the brest coil and the PET through the insert.

The planned detector block for the breast PET insert is illustrated in Figure 15.2. It contains 16×16 Lutetium OxyorthoSilicate (LSO) crystals with a

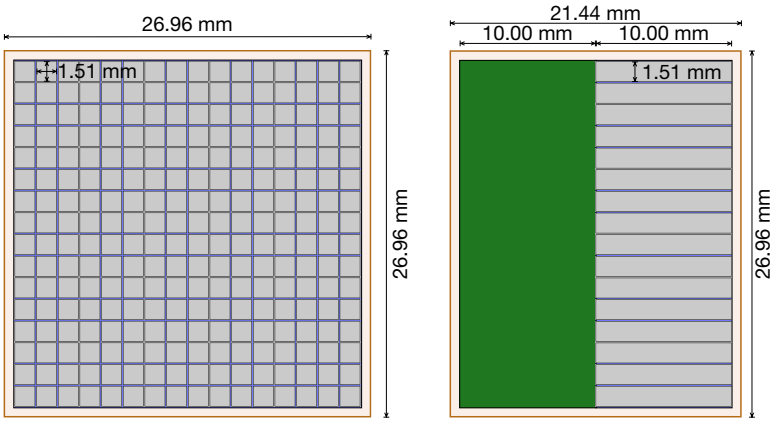

(a) Front view. **(b)** Side view.

Figure 15.2.: Sketch of the breast PET insert detector block including a grid of 16×16 crystals. The detector block is wrapped with a 0.7 mm thick Acrylonitrile Butadiene Styrene (ABS) layer and 18 µm copper for magnetic shielding. The volume depicted in green is reserved for the front-end electronics.

crystal dimension of $1.51 \times 1.51 \times 10.00\,\text{mm}^3$, with 80 µm of Enhanced Specular Reflector (ESR) between the individual crystals. A 10 mm thick volume behind the crystals is reserved for the Silicon PhotoMultiplier (SiPM) and the front-end electronics.

As depicted in Figure 15.3 (a), the detector blocks are planned to be placed between the upper and lower RF coils, and the coarse size of the breast PET insert is predetermined by the breast coil with an upper coil diameter of about 20 cm and a distance between the upper and lower RF coils of about 12 cm. Three geometries for the breast PET insert were previously suggested (Pommranz, 2019; Pommranz et al., 2023) and are shown in Figure 15.3 (b). Geometry A represents a conventional approach consisting of two separate full cylinders with four layers of detector blocks each, resulting in an axial length of 10.8 cm. Each cylinder ring consists of 22 detector blocks per layer, which are evenly distributed with a front-face diameter of 19.9 cm. The total number of detector blocks is 176. The integration of Geometry A in the existing RF breast

coil would require adaptations of the breast coil, because the back-to-back detector blocks in the center of Geometry A don't fit in the available space between the two coils. Therefore, Geometries B and C were introduced, which would fit in the breast coil without the need for geometrical adaptations. For Geometry B, the 24 central detector blocks are removed and the two part cylinders are moved closer to the center by 1.1 cm per cylinder, resulting in a distance of the two cylinder centers of 22.0 cm. Geometry C consists of two half cylinders, and the space between them is filled with two plain grids of 7×4 detector blocks. In total, Geometries B and C consist of 152 and 144 detector blocks, respectively.

Building a PET insert for integration into an MRI scanner poses challenges for the detectors and system integration, as the PET must be capable to operate in the strong magnetic field of the MRI scanner, and the PET scanner must be carefully shielded to not deteriorate the MRI quality (Muzic and DiFilippo, 2014; Vandenberghe and Marsden, 2015). Hence, simulation studies of the planned breast PET insert are crucial, as they allow for geometry and data driven optimizations early in the development phase. Furthermore, the use of automated workflows will enable repeated re-evaluation of the PET performance characteristics for detector geometry adaptations during the ongoing development of the breast PET insert. As the MRI compatibility of the detector blocks was already demonstrated in measurements (Schmidt, 2022), no degradation of the PET detector performance due to the operation in the Biograph mMR were assumed in the simulations described below.

15.4. Mixed coincidences and the virtual pinhole effect

Operating a PET insert inside of a whole-body PET scanner enables to collect a third type of coincidences in addition to the conventional coincidences of the whole-body PET scanner and the breast PET insert, which will be referred to as Type I and Type II coincidences in this thesis, respectively, as shown in Figure 15.1b. The third type of coincidences consists of one single event detected by the whole-body PET scanner and one detected by the PET insert and will be referred to as Type III coincidences or "mixed coincidences". For the breast PET

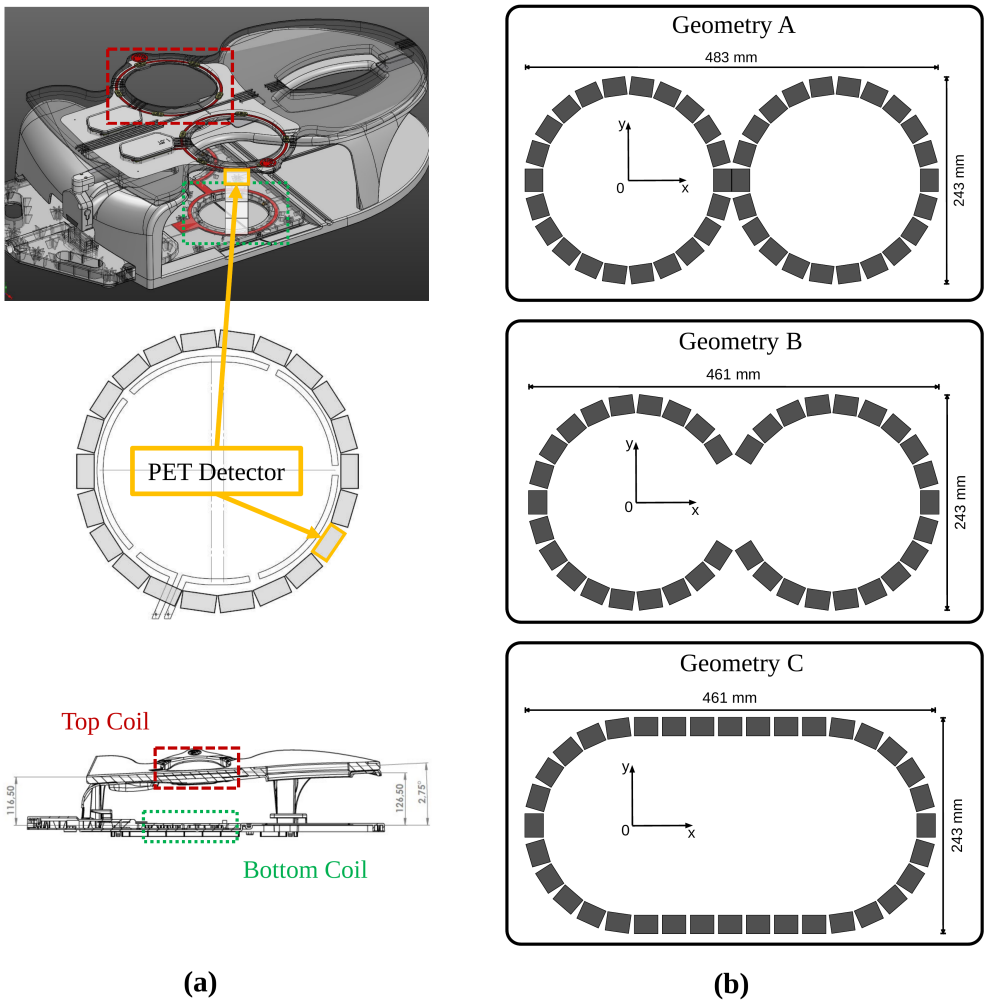

Figure 15.3.: Integration of the breast PET insert into the RF breast coil (a), and sketches of the three investigated breast PET insert geometries (b). Each geometry consists of four detector block layers in axial direction. Image credit: Pommranz et al. (2023). Breast coil drawings in (a) courtesy of NORAS MRI products.

insert geometries, the LORs of the mixed and the Type I coincidences cover the axillary lymph node region, which will enable to perform a simultaneous PET scan of this region. Furthermore, the small crystal dimensions of the breast PET insert will improve the spatial resolution of the mixed coincidences through the Virtual Pinhole PET (VP-PET) effect (Tai et al., 2008) as shown in Figure 15.4, and therefore potentially improving the PET imaging quality of the axillary lymph node region compared to the stand-alone whole-body PET scanner resolution.

For detection elements of different widths, the Full Width at Half Maximum (FWHM) detection profile R_{det} is determined from its base width w_b and plateau width w_p using

$$\begin{aligned} w_b &= \frac{(D-x)\cdot w_1 + x\cdot w_2}{D} \\ w_p &= \frac{|(D-x)\cdot w_1 - x\cdot w_2|}{D} \\ R_{det} &= \frac{w_b + w_p}{2} \ , \end{aligned} \tag{15.1}$$

where the detection element widths w_1 and w_2, the separation of the detection elements D, and the distance from the surface of the first detection element x are defined as shown in Figure 15.4 (Tai et al., 2008). For detection elements of the same width w, equation 15.1 simplifies to

$$R_{det} = \frac{w}{2}\cdot\left(1 + \left|1 - 2\frac{x}{D}\right|\right) \ , \tag{15.2}$$

which is consistent with the symmetric detection profiles seen in Figure 15.4 and the well-known FWHM spatial resolution of $R_{det} = \frac{w}{2}$ for a point source centered between the detectors (Moses, 2011). Equations 15.1 and 15.2 only hold if the detector front faces are parallel. Otherwise, a parallex error is introduced as observed in PET ring-design scanners that can degrade the spatial resolution.

Several groups reported on improved spatial resolution based on simulation studies and experimental data using the VP-PET principle, implemented in

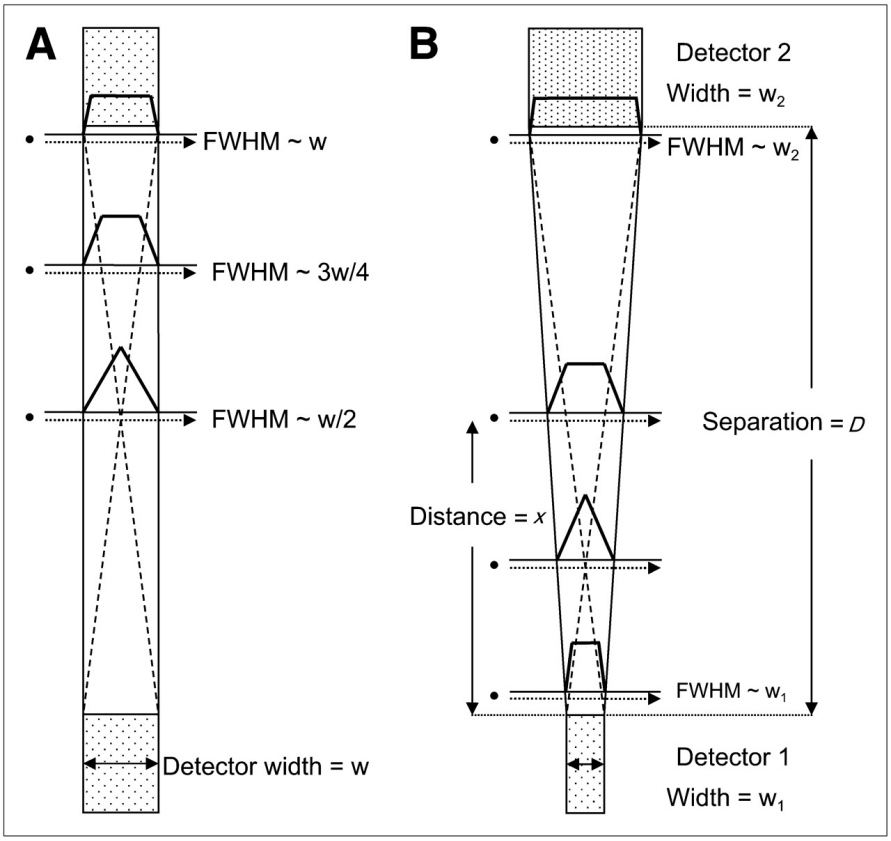

Figure 15.4.: Spatial resolution and the VP-PET principle. For two detector elements of the same width, the detection profile is symmetric with the best FWHM spatial resolution at the center (A). For two detector elements of different widths, the location of the best FWHM spatial resolution is shifted towards the detector element with smaller width (B). Image credit: Tai et al. (2008).

different detector designs, either utilizing silicon detectors or LSO scinitillators and covering a broad range of system geometries from single probe inserts to full-ring inserts, optimized for pre-clinical and clinical scanners. For the silicon inserts, detector probes (Brzeziński et al., 2014, 2016), partial-ring (Grkovski et al., 2015), and full-ring geometries (Park et al., 2007; Clinthorne et al., 2013) were investigated. The inserts using LSO scintillators included detector probes (Huh et al., 2007; Tai et al., 2008; Zhou and Qi, 2009), half-ring (Wu et al., 2008b; Mathews et al., 2013), full-ring (Janecek et al., 2006; Wu et al., 2008a), and plate geometries (Jiang et al., 2020). Furthermore, research for operating detector probes inside the new generation of total-body PET scanners has started (Ros et al., 2021).

Project III

16. Materials and methods

A performance simulation study comparing the three geometries, based on the simulated performance characteristics of the stand-alone breast PET insert obtained in the course of this thesis, was previously published (Pommranz et al., 2023). Those simulations were performed with GATE version 9.1 and Geant4 version 10.7.2 and will be referred to as "previously published results" throughout this part of the thesis. For the stand-alone breast PET insert simulations shown in this thesis, GATE version 9.3 and Geant4 version 11.1.2 were used and the previously published stand-alone breast PET insert simulations were reconducted using the updated versions. Thus, the results presented here incorporate the changes of two new GATE and Geant4 releases compared to the previously published results. As the digitizer was rewritten in large parts for GATE 9.3 and included changes breaking compatibility with earlier GATE versions, the new simulation study can also be seen as a test run comparing the effects of the new GATE digitizer to the previous and well validated version. The simulations were fully automated, implemented as Snakemake workflows, and the runs were performed on a local workstation. For the new simulations, the same data analysis was used as for obtaining the previously published results. The dual-system simulations collecting coincidences between the Biograph mMR and the breast PET insert were conducted with GATE version 9.1, and GATE's new unified "Tree" output was used for saving simulation data. For the stand-alone breast PET insert simulations, the simulated list-mode data was stored in ROOT files, while NumPy arrays were used for the dual-system simulations.

16.1. A template-based macro generator for GATE

GATE relies on the Geant4 macro mechanism for configuration and interaction with the simulation (see Chapter 4). While this approach results in a gentle

learning curve and easy to modify simulations, for large-scale simulation studies it can easily lead to a large number of macro files that are difficult to manage, especially when exploring different versions and configurations of digitizer chains or geometries. To simplify the macro file management for GATE simulations, the `gate-template` tool was developed in the course of this thesis, that allows to render macro files from a simple YAML configuration file using the Jinja[33] templating engine. Jinja templates can be provided by the user for individual parts of the macro file (e.g., sources, actors, digitizers). Control structures and filters can be used in the templates to allow for a concise configuration file. Individual templates are versioned, so that version numbers can be set in the configuration file to generate different variants of the macro files, e.g. for compatibility with a specific GATE version. An example configuration file is shown in Listing 16.1.

16.2. Implementing the system geometries

The detector block was modeled according to Figure 15.2, using a material composition mixture of Printed Circuit Board (PCB) and copper resulting in a density of $2.03\,\mathrm{g\,cm^{-3}}$ for the 10 mm thick volume behind the crystals. The breast PET insert geometries described in Section 15.3 were implemented in GATE using the generic repeater on the detector block level. In contrast to the other repeater modules in GATE, where the placement of the volume copies are calculated by the repeater (see Chapter 4), the generic repeater reads the positions and orientations of the volumes from a placement file provided by the user. Therefore, the generic repeater allows the simulation of geometries that cannot be described by the other repeaters, such as Geometries B and C. The placement files for the three geometries were produced by the self-written `gate-generic-geometries` tool, which includes repeaters similar to the GATE repeaters, but with increased flexibility, such as the possibility to skip specific volume copies to allow for partial geometrical shapes and the support of arbitrary combinations of repeaters. In addition, the tool allows to produce Customizable and Advanced Software for Tomographic Reconstruction (CASToR)-compatible (Merlin et al., 2018) binary LookUp Table (LUT) files. These files contain the dimensions, positions, and orientations of all crystals in the system geometry,

[33] `https://jinja.palletsprojects.com` (accessed on 2023-06-02).

```
systems:
  - type: petinsert_breast

blocks:
  - type: petinsert_breast

repeaters:
  - type: petinsert_breast_peanut

digitizers:
  - type: petinsert_breast
    version: v3
    arguments:
      deadtime: 200 ns
      deadtime_mode: nonparalysable

sources:
  - type: nema_na22
    arguments:
      activity: 100 kBq

outputs:
  - type: tree_root

duration: 30
time_start: 0
time_stop: 30
```

Listing 16.1: Example configuration of a 30 s long simulation of a point-like ^{22}Na source placed inside Geometry B. A specific version of the digitizer is chosen to ensure compatibility of the produced macro file with GATE 9.3. For illustration purposes, the default dead time module was changed to model a 200 ns non-paralyzable dead time. This example configuration is translated into a 358 line GATE macro file by `gate-template`, which also produces all additional files needed for running the GATE simulation.

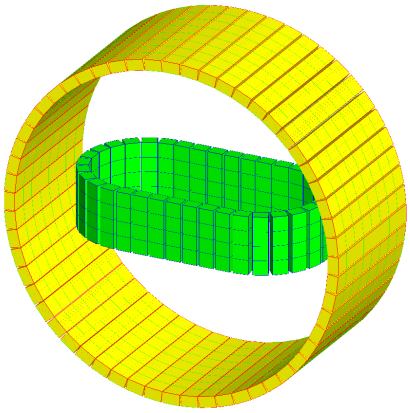

Figure 16.1.: Placement of Geometry C inside the Biograph mMR. For better visibility, the patient bed is not shown. The placement of Geometries A and B is analogous to Geometry C, with the center of the insert located at the cFOV of the Biograph mMR.

calculated from user-specified crystal positions inside a single detector block, e.g., by using a grid repeater. The LUT export of the `gate-generic-geometries` tool was also used for the dual-system geometries, producing a single LUT file including all crystals of both PET systems.

For the dual-system and mixed coincidences simulations, an existing GATE model of the Biograph mMR was used, that was previously validated against measurements according to the National Electrical Manufacturers Association (NEMA) NU-2 2007[34] (National Electrical Manufacturers Association, 2007) protocol using GATE in version 6.2 (Aklan et al., 2015). The mass model included eight rings with 56 detector blocks per ring. A single detector block contained 8×8 LSO crystals with crystal dimensions of $4.0 \times 4.0 \times 20.0\,\mathrm{mm}^3$. The breast PET insert was placed inside the Biograph mMR, such that the center of the breast PET insert system geometry was located at the center of the Field Of View (cFOV) of the whole-body scanner. A patient bed model was included and placed below the breast PET insert. The placement of the breast PET insert inside the Biograph mMR is shown in Figure 16.1 for Geometry C.

[34]The NEMA NU-2 standard is optimized for clinical PET scanners.

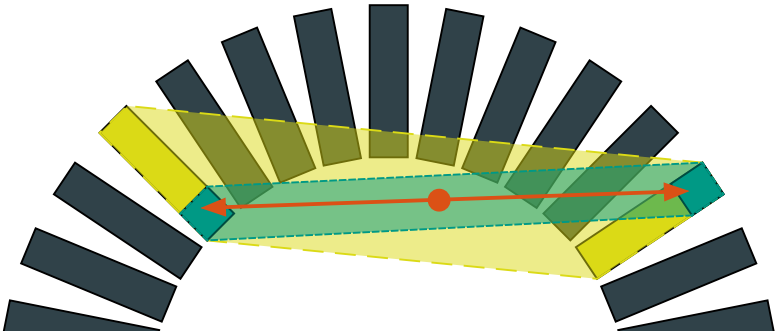

Figure 16.2.: Working principle of DOI detectors, reducing the parallax error for source positions close to the edge of the FOV and, thus, improving spatial resolution. With the DOI information constraining the location of the gamma ray detection to a specific sub-crystal volume (green crystal parts), the possible location of the electron-positron annihilation can be constrained to a smaller region (depicted in green) compared to the region without DOI information (depicted in yellow). The electron-positron annihilation and the two 511 keV gamma rays are visualized as an orange circle and orange arrows, respectively.

For the stand-alone breast PET insert and the dual-system spatial resolution simulations described in Section 16.4.2 and Section 16.4.6, respectively, detectors capable of obtaining the Depth Of Interaction (DOI) of the incident gamma ray with two and three layers were simulated. Thus, the effect of including the DOI information in the reconstruction process on the spatial resolution was assessed. Using information about the DOI of the detected gamma ray in the crystal, the possible region where the electron-positron annihilation took place can be further restricted due to a reduced parallax error compared to non-DOI crystals, especially for regions close to the edge of the FOV as illustrated in Figure 16.2. The DOI capability of the detectors was simulated by dividing each crystal into virtual sub-crystals without changing the volume and shape of the total crystal volume. For the two-layer DOI detector, the sub-crystal lengths were 4.0 mm (front) and 6.0 mm (back), and for the three-layer DOI detector the sub-crystal lenghts were 2.5 mm (front), 3.1 mm (middle), and 4.4 mm (back).

16.3. Modeling digitization and read-out effects

The GATE read-out and digitizer chain for the stand-alone breast PET insert is shown in Figure 16.3. Although the same parameters were used as for obtaining the previously published results, the read-out and digitizer scheme was considerably different due to the restructuring of modules as part of the rewrite of the digitizer functionality in GATE 9.3. Geant4 `Hits` in a single crystal were first combined to a single `pulse` using the `adder` module. Since GATE in version 9.3, this is done separately for every sensitive detector logical volume. Thus, for simulations with DOI sub-crystals of different lengths and logical volumes (see Section 16.4.2), one digitizer per logical sub-crystal volume was spawned and the `adder` module was executed separately per digitizer. In the case of multiple digitizers, the added `pulse`s were merged into a single digitizer using the `merger` module to allow for a combined read-out at the detector block level. The read-out was performed using the `readout` module and the "TakeEnergyWinner" policy, which assigned the event to the crystal or sub-crystal, where the highest energy contribution was deposited. The `energyResolution` module was used to simulate an energy resolution of 15 % at a reference energy of 511 keV. The detector efficiency was set to 85 %, which corresponded to the `efficiency` module randomly dropping 15 % of the events. A timing resolution of 350 ps was modeled using the `timeResolution` module. The dead time was modeled at the detector block level with a 120 ns paralyzable model using the `deadtime` module. In the paralyzable mode, each detected event opened a dead time window of the configured duration, regardless of whether the detector was already in dead time state or not, so that the detector could remain in dead time state for a prolonged period of time in the case of very high activities. Lower and upper energy thresholds of 430 keV and 610 keV were applied using the `energyFraming` module. The coincidence sorter with a coincidence time window of 2 ns operated in the "takeWinnerOfGoods" mode, considering only the valid coincidence pair between the single events with the highest energy when multiple coincidences occurred per coincidence window. As the source position can occupy the entire FOV, the "minSectorDifference" parameter was set to one, so that coincidences between neighboring detector blocks are considered as valid. When not needed for the data analysis, the output of singles or coincidences was deactivated individually to reduce the size of the ROOT file.

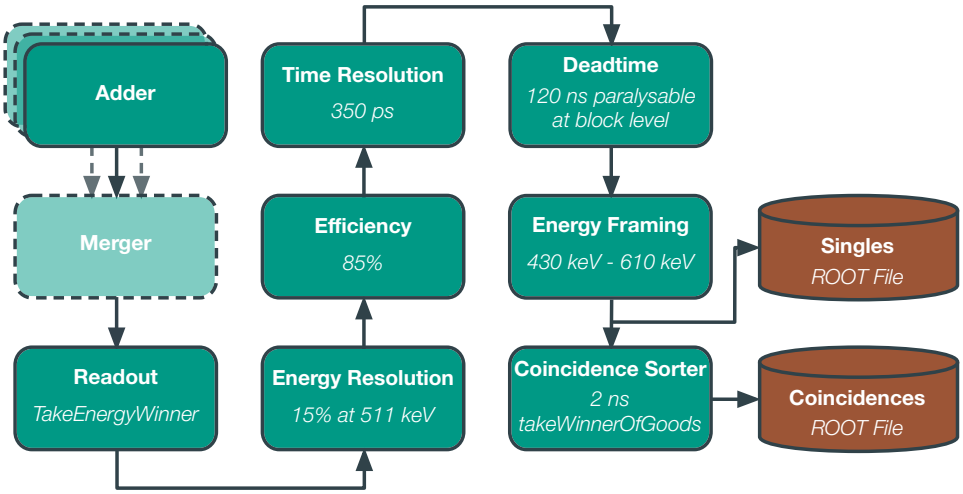

Figure 16.3.: Read-out and digitizer scheme of the stand-alone breast PET insert. The dashed modules are used for DOI detectors only.

The parameters for the `efficiency` and `deadtime` modules are crucial for accurate simulations of imaging systems, as the efficiency parameter scales linearly with the single-event sensitivity at low activities, and the dead time strongly affects the scanner response at high activities. Therefore, these parameters were obtained based on measurement data of a single prototype detector block at different activities by optimization based on simulations of the measurement setup using different parameter values.

The GATE read-out and digitizer chain together with the custom coincidence processor for the dual-system is shown in Figure 16.4. The breast PET insert and the whole-body PET scanner were modeled as separate systems in a single GATE simulation, and read-out and digitization were modeled independently of the other system up to the production of single events. The parameters reported in Aklan et al. (2015) were used for the Biograph mMR read-out and digitizer chain, with energy and time resolutions of 15 % and 3.6 ns, respectively, a detector efficiency of 76 %, a dead time of 355 ns in the nonparalyzable mode, and lower and upper energy thresholds of 430 keV and 610 keV, respectively.

The single event output files were then processed with self-written coincidence

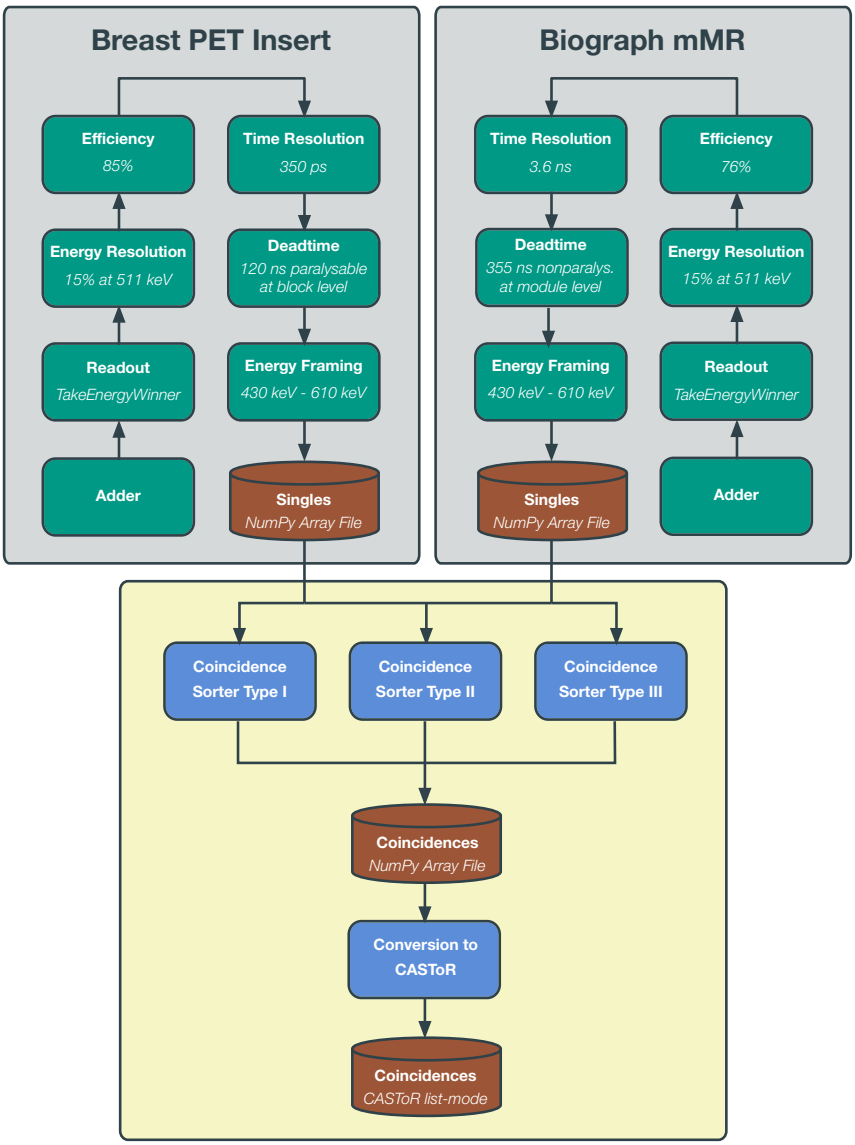

Figure 16.4.: Read-out and digitizer scheme of the dual-system. The modules for the breast PET insert and the Biograph mMR are part of the GATE software. The modules in the lower box were developed as part of this thesis.

sorters to produce coincidences of all three types separately. The coincidence time windows for the Type I and Type II coincidences were unchanged from the single scanner simulations with 5.9 ns (Aklan et al., 2015) and 2.0 ns, respectively. For the Type III coincidences, a coincidence time window of 6.0 ns was assumed, which will be refined in future studies based on simulations and measurements, and which is not expected to significantly affect the dual-system simulations performed in this work due to the low activity of the simulated sources. For all three coincidence sorters, only the coincidence pair between the two single events with the highest energy was considered in case of more than two single events in a single coincidence time window, similar to GATE's "takeWinnerOfGoods" policy. Coincidences were allowed between all pairs of distinct blocks, so that all LORs were considered as valid. The coincidences were converted to a CASToR-compatible binary list-mode data file for subsequent image reconstruction. As part of the workflow, the coincidence sorters could be configured to store only a subset of the three coincidence types, allowing to evaluate the spatial resolution based on individual coincidence types.

16.4. Estimation of the expected breast PET insert performance

The stand-alone breast PET insert performance characteristics were determined similar to the previously published results and this section is based on the recent publication Pommranz et al. (2023). Initial simulation results for the sensitivity and spatial resolution of the three geometries in stand-alone configuration were shown in Pommranz (2019) utilizing early versions of the digitizer configuration and the spatial resolution workflow, which were considerably improved in the course of this thesis.

The simulated performance characteristics are based on the NEMA NU-4 2008 (National Electrical Manufacturers Association, 2008) standard specifically targeting preclinical PET scanners and hence more applicable to the breast PET insert due to the smaller crystal sizes and FOV compared to clinical PET scanners and the corresponding NEMA NU-2 standard. The positioning of the breast inside the breast PET insert differs from conventional clinical PET scanners, for which the main region of interest is typically placed at the

cFOV, utilizing the best imaging capabilities of the scanners. Therefore, for the breast PET insert, additional source placements closer to the edge of the FOV were investigated as well, and an adapted cylindrical scatter phantom with a diameter of 170 mm was used. The positions of the point source and phantom are shown in Figure 16.5 together with the coordinate system used for the breast PET insert simulations. The dual-system sensitivity and spatial resolution simulations (including Type III coincidences between the whole-body PET scanner and the breast PET insert) were conducted similar to the NEMA NU-4 2008 standard but with adapted source positions located at the expected positions of the axillary lymph nodes outside of the FOV of the breast PET insert.

All analyses were performed directly on the simulated list-mode data, as the conventional approach of transforming the list-mode data into sinograms would lead to ambiguous LORs for Geometry B due to its unconventional and non-cylindrical geometry. Thus, to achieve a fair comparison of the expected performance characteristics between the investigated breast PET insert geometries, sinogram-based modifications described in the NEMA NU-4 2008 standard were omitted, which is described for the individual performance characteristics in the following sections (Sections 16.4.1-16.4.6). This is further motivated by the positioning of the breast inside the breast PET insert, which can be located very close to the edges of the FOV both in axial and transaxial directions.

Due to the unconventional shapes of Geometries B, C, and the combined dual-system geometries, iterative image reconstruction was used for estimating the spatial resolution instead of the Filtered Back Projection (FBP) algorithm required by the NEMA NU-4 2008 standard. Image reconstruction was done for the stand-alone breast PET insert and the dual-system case using the simulated list-mode data with CASToR in version 3.1. For both cases, an iterative reconstruction was used with ten iterations and 16 subsets using the 3D Maximum Likelihood Expectation-Maximization (MLEM) algorithm (Shepp and Vardi, 1982) and the accelerated Siddon projector (Jacobs et al., 1998) without smoothing or point spread function modeling. The attenuation map at 511 keV was obtained from the GATE MuMap actor and converted to the CASToR coordinate system for attenuation correction as part of the Snakemake workflow. Normalization was not included in the image reconstruction, and

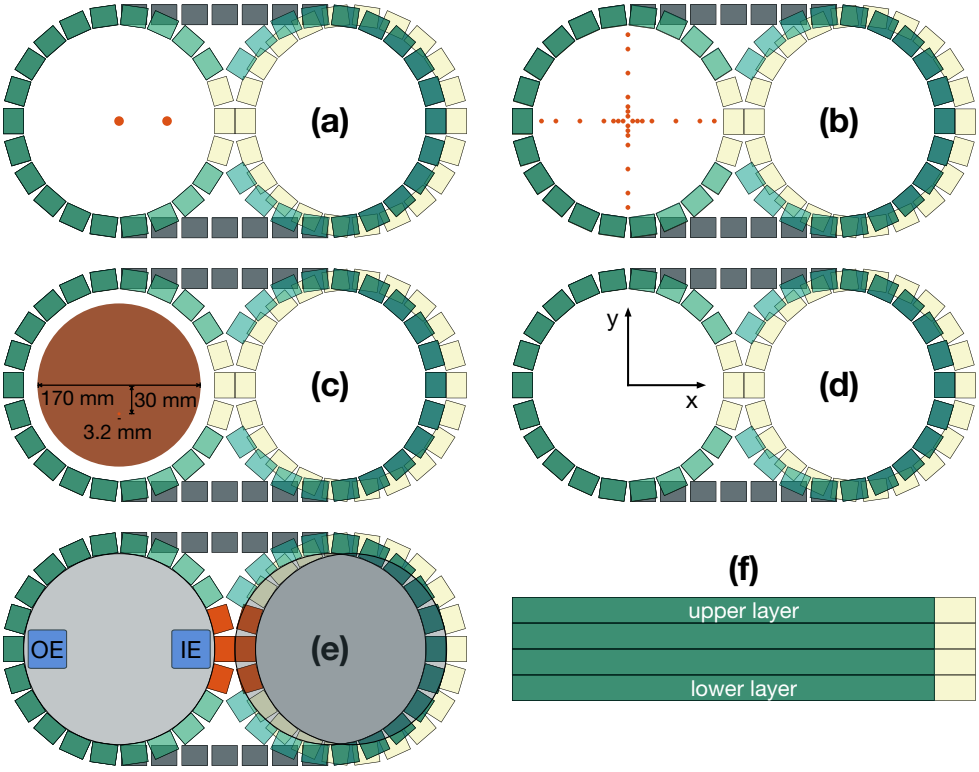

Figure 16.5.: Positions of the point sources used for the sensitivity (a) and spatial resolution (b) simulations, and placement of the scatter phantom used for the count rate evaluation (c) for Geometries A (yellow), B (green), and C (gray). (d): Coordinate system used for the standalone breast PET insert simulations. The origin is located at the axial center and the z-axis is in the axial direction. (e): Positions of the two FOVs (gray), the outer edge (OE) and inner edge (IE) of the FOV, and the central detectors (orange). (f): Side view of the three geometries.

will be implemented together with an optimized image reconstruction once a final geometry was selected.

Similarly to the Geant4 application for X-ray satellites described in Section 11, the standard electromagnetic physics list was used in option four to include the most precise electromagnetic models available in Geant4 in the simulation[35] (Allison et al., 2016). This physics list is known to yield high accuracy for medical physics simulations using Geant4 or GATE (Beaudoux et al., 2019; Salvadori et al., 2020).

Magnetic fields were not included in the stand-alone breast PET insert simulations. For the dual-system simulations, a static 3.0 T magnetic field in axial direction of the whole-body PET scanner was simulated. Due to limitations of the magnetic field modeling capabilities in the current versions of GATE, the magnetic field homogeneously filled the entire world volume. The LSO background was not modeled in the simulations, and to save computation time, hadronic processes were excluded in the simulations. These simplifications are expected to have only negligible effects on the simulation results[36].

16.4.1. Sensitivity

The sensitivity of a PET scanner is a measure of its ability to detect coincident pairs of gamma rays and is calculated as the fraction of detected coincidences and the source activity (National Electrical Manufacturers Association, 2008). For estimating the sensitivity of the breast PET insert, a 100 kBq point-like source with a spherical ^{22}Na volume and a diameter of 0.3 mm placed inside

[35] For the background single count rate simulation, the electromagnetic physics list was used in option three, as option four frequently caused infinite loops and stuck particles in the voxelized phantom. This issue was observed neither in the other performance characteristics simulations nor in the earlier background single count rate simulations performed to obtain the previously published results. The issue has been reported to the GATE community and at the time of writing this thesis, the issue was unresolved and under investigation: `https://github.com/OpenGATE/Gate/issues/628` (accessed on 2023-10-09).

[36] In addition to the simulations without hadronic processes, the sensitivity simulations (Section 16.4.1) were also conducted with the QBBC_EMZ physics list used in Project II including hadronic effects, and no significant differences were found in the simulated sensitivity results.

a 10.0 mm acrylic cube was simulated using an ion source. The source was transaxially centered and measured at axial positions between −50 mm and 50 mm with a step size of 5 mm. Each source position was simulated separately for 30 s. The absolute sensitivity S_{abs} was calculated using

$$S_{abs} = \frac{1}{0.9060} \cdot \frac{n}{A} \tag{16.1}$$

with the ^{22}Na positron decay branching fraction of 90.60 %, the coincidence count rate n, and the source activity A. The coincidence count rate was obtained from the simulated list-mode file. For Geometry A, coincidences between the two cylinders were discarded.

16.4.2. Spatial resolution

The spatial resolution of a PET scanner is calculated from the width of its point spread function determined from a point source scan (National Electrical Manufacturers Association, 2008). The spatial resolution of the breast PET insert was estimated using the same point source as used for the sensitivity simulations, which included modeling of the positron path in the 10 mm cubic envelope of the source. To prevent potential overestimation of the spatial resolution due to the use of iterative image reconstruction, a background activity was included in the simulations as recommended in Gong et al. (2016). The radioactive background was placed in a cubic volume around the point source with an activity concentration of 25 kBq cm^{-3} and an edge length of 20 mm. Voxels with a size of 0.6×0.6×0.6 mm^3 were used for the reconstructed image. The spatial resolution was determined from the FWHM of the line profiles of the reconstructed images in three orthogonal directions following the NEMA NU-4 2008 protocol. For a single FWHM spatial resolution value at a given source position, only the largest spatial resolution component – i.e., the most conservative value of the spatial resolution triplet for a single source placement – was considered. For the four source placements at 5 mm offset from the cFOV in the transaxial plane, the average of these values was calculated to obtain the mean spatial resolution close to the cFOV. To ensure the same number of prompts per source placement and geometry, the list-mode data was cut after a total of 1×10^6 prompts including coincidences from the point source and the background.

16.4.3. Count rates and scatter fraction

The count rates and Noise Equivalent Count Rate (NECR) measures characterize the detector dead time effects and the effect of random coincidences on the performance of the scanner at different source activities, and the relative number of detected scattered gamma rays is indicated by the scatter fraction (National Electrical Manufacturers Association, 2008). A line source filled with water and different activities of ^{18}F with a length of 10.8 cm and a radius of 1.6 mm was simulated. The line source was placed inside a cylindrical scatter phantom made of polyethylene with a density of 0.96 g cm^{-3} with a length of 10.8 cm and a radius of 85 mm, and the line source was located at 30 mm offset from the transaxial cFOV towards the negative y-axis as shown in Figure 16.5. The GATE ion source was used to also include the electron capture decay mode with the production of a 1.7 keV X-ray in the simulation. Simulations were performed with activities from 600 MBq to 10 MBq with a step size of 10 MBq, and 1×10^6 prompts were collected per simulation. An additional simulation was performed at a low activity of 0.1 MBq to estimate the system scatter fraction with low count losses. The count rates for true coincidences n_t, for scattered coincidences n_s, and for random coincidences n_r were determined directly from the simulation ground truth information available in the ROOT output files. The NECR n_{NEC} was calculated using

$$n_{NEC} = \frac{n_t^2}{n_t + n_s + n_r}\,, \tag{16.2}$$

and the scatter fraction S was calculated using

$$S = \frac{N_s}{N_t + N_s}\,, \tag{16.3}$$

where the total number of scattered and true coincidences are denoted by N_s and N_t, respectively.

An excerpt of the NECR simulation Snakemake workflow DAG is shown in Figure 16.6. The GATE simulations were split into multiple short simulation parts, which allowed for highly parallelized job execution. Prior to the analysis step, the list-mode event data of the simulation parts were merged into a single ROOT file per simulated activity.

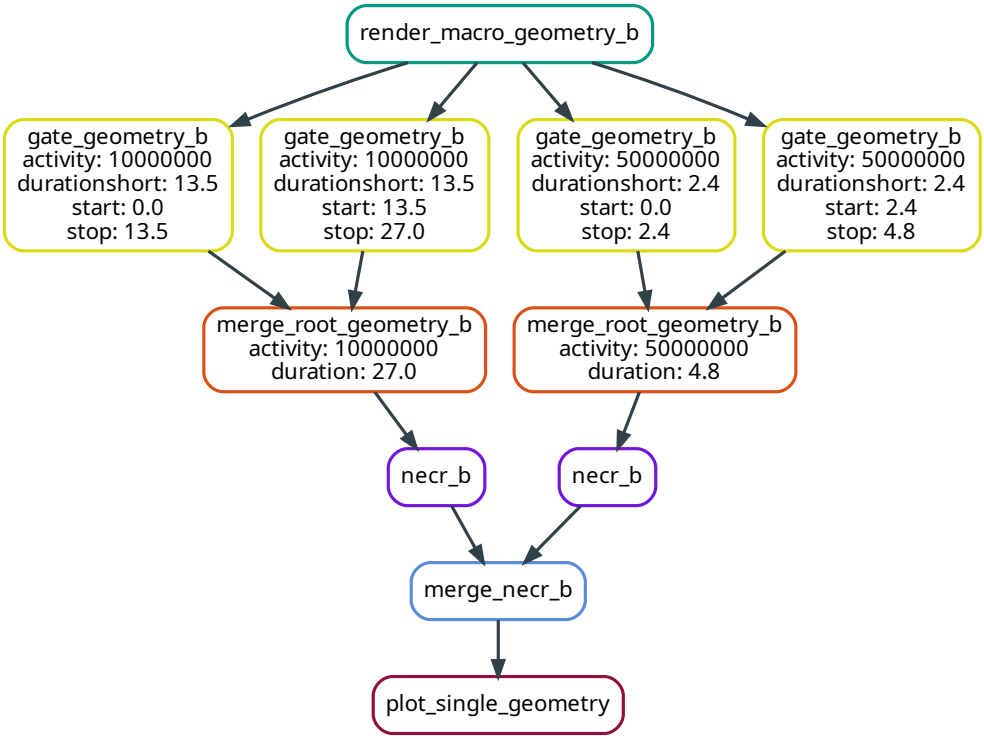

Figure 16.6.: Excerpt of the DAG of the count rates and NECR simulation workflow implemented in the Snakemake workflow management system. For improved visibility, only two simulated activities split in two GATE runs are shown for Geometry B. The workflow includes similar simulations for Geometries A and C. In the `necr_b` task, the count rates and NECRs are determined from the list-mode event data.

16.4.4. Background single count rate

The maximum expected single event count rate is an important measure for the system electronics design of the breast PET insert (Schmidt, 2022). Especially for dedicated breast PET scanners, other organs with high uptakes, such as the heart and the liver, are located close to the detectors and are expected to contribute a considerable number of background single events originating from outside of the FOV (Vandenbroucke et al., 2010). Anthropomorphic phantoms can be used to predict the maximum expected background single count rate from a GATE simulation. The simulation ground truth information enables to detect the contributions of individual organs to the background count rate.

To simulate the background single count rate, including single events from inside and outside of the breast PET insert FOV, a female 4D eXtended CArdiac-Torso (XCAT) phantom (Segars et al., 2010) was used in a static configuration without modeling of respiratory and cardiac motions. The distribution of the activity in the phantom with a total activity of 217 MBq was based on organ-specific mean Standardized Uptake Values (SUVs) for [^{18}F]FDG reported in Ramos et al. (2001); Wang et al. (2007), and was rendered as a voxelized phantom with a voxel size of $3.1\times3.1\times3.1\,\mathrm{mm}^3$. To include the chemical composition of the phantom in the GATE simulation for accurate particle tracking through the phantom, a second phantom of the same geometric shape was created and filled with unique identifiers corresponding to the material for each voxel. These identifiers were then mapped to a set of different materials with available chemical compositions, that was selected from the materials available in the GATE and Geant4 distributions. The mid-coronal planes of the activity and material assignment phantoms are shown in Figure 16.7.

The phantom was placed in the breast PET insert and simulated for 5 s. Since the simulation was performed to provide an estimate of typical background single count rates rather than precise results for an individual phantom configuration, a back-to-back gamma source ignoring the mean free positron path in the tissue was used to reduce the computational time. The lower energy threshold was reduced to 10 keV to include scattered events in the count rate estimation.

The origin of each background single event was determined from the production position of the detected gamma rays, which was included in the ROOT output files. A third XCAT phantom of the same geometric shape was created including

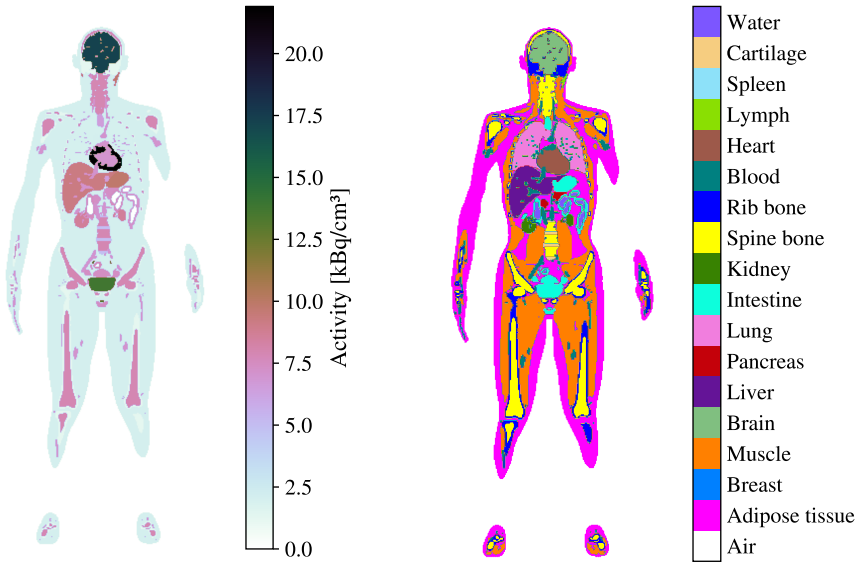

(a) Activity map.

(b) Material assignment map.

Figure 16.7.: Phantom activity and material assignment maps of the mid-coronal plane. The chemical compositions of the assigned materials were obtained from the GATE and Geant4 distributions.

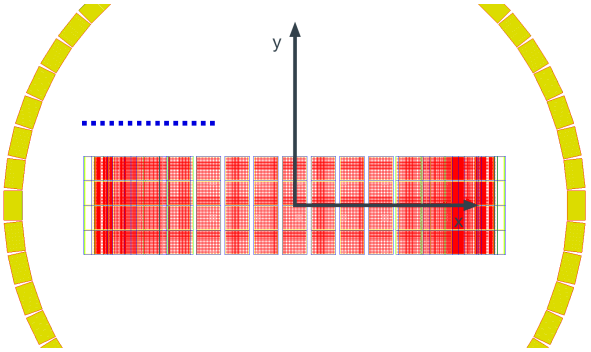

Figure 16.8.: Source placements outside of the breast PET insert FOV to determine the dual-system sensitivity and spatial resolution. The placements of the point source are depicted in blue.

identifiers for a set of ten organs and was used for mapping of the production positions to the originating organs in the analysis step.

16.4.5. Dual-system sensitivity

The simulation of the dual-system sensitivity including Type III coincidences was performed similar as for the stand-alone breast PET insert described in Section 16.4.1. The point source was placed axially centered at 90 mm above the cFOV of the breast PET insert and at x-coordinates between −90 mm and −230 mm with a step size of 10 mm and simulated for 30 s at each of the positions. This set of source positions is shown in Figure 16.8 and was selected to represent typical positions of axillary lymph nodes (exemplary positions were obtained from MRI breast scans obtained with the Biograph mMR of the University Hospital Tübingen (UKT)). The sensitivity was determined separately for the Type I and Type III coincidences and the coordinate system origin was in the cFOV of the whole-body PET scanner.

16.4.6. Dual-system spatial resolution

The dual-system spatial resolution was determined in a similar manner as for the stand-alone breast PET insert described in Section 16.4.2 from reconstructed

images of a simulated point source placed at the source positions shown in Figure 16.8. The point source was placed in a cubic warm background with an edge length of 40 mm and a total activity of 400 kBq. 1×10^6 prompts were collected for each source position including events from the radioactive background. The image reconstruction was performed for Type III coincidences using cubic voxels with a length of 1.0 mm. The same image reconstruction was performed also for Type I coincidences for simulations without integration of the breast PET insert in order to obtain comparable spatial resolution results for the whole-body scanner.

Project III

17. Results

17.1. Sensitivity

The absolute sensitivity for the breast PET insert along the axial axis at the transaxial center and at a transaxial offset of 5 cm towards the center of the insert geometries is shown in Figure 17.1. At the transaxial center, peak absolute sensitivities were 3.1 %, 2.7 %, and 2.2 % for Geometries A, B, and C, respectively, and were thus fully consistent with the previously published results (Pommranz et al., 2023). At 5 cm transaxial offset, the simulations revealed lower peak sensitivities than at the transaxial center, with peak absolute sensitivites of 2.7 %, 2.5 %, and 2.1 % for Geometries A, B, and C, respectively. The simulated sensitivities correspond to non-DOI crystals. However, as the LSO volume and geometrical shape remains unchanged for the DOI crystals, the sensitivity is assumed to be similar.

17.2. Spatial resolution

The combined FWHM spatial resolutions for the four investigated source positions at 5 mm from the cFOV in the axially centered plane are listed in Table 17.1. For the non-DOI variants, Geometry A showed the best spatial resolution. The spatial resolution was improved by the two-layer DOI variant for all geometries, and for the three-layer DOI variants, all geometries revealed the same FWHM spatial resolution of 1.4 mm. The results are consistent with the previously published results, with only minor increases of the spatial resolution by 0.1 mm for Geometry B in the non-DOI variant, and Geometry C in the two-layer DOI variant.

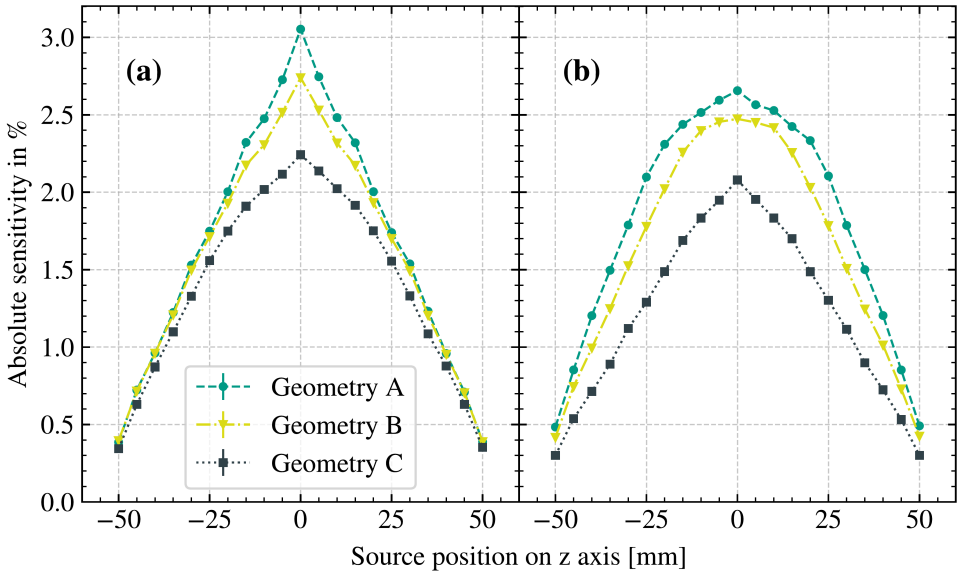

Figure 17.1.: Breast PET insert sensitivity at transaxially centered source positions (a), and at a transaxial offset of 5 cm (b).

Table 17.1.: Average FWHM spatial resolution for the source positions at 5 mm transaxial offset of the cFOV for non-DOI, two-layer DOI, and three-layer DOI variants of Geometries A, B, and C.

	Geom. A [mm]	Geom. B [mm]	Geom. C [mm]
Non-DOI	1.7	1.9	2.0
Two-layer DOI	1.4	1.5	1.6
Three-layer DOI	1.4	1.4	1.4

The FWHM spatial resolution components for source positions at different x-coordinates and at the axial cFOV are shown in Figure 17.2 for non-DOI, two-layer DOI, and three-layer DOI variants of Geometries A, B, and C. For reference, the coordinate systems in the axially centered plane and the source positions are shown in Figure 16.5. For the non-DOI variants, a deterioration of the spatial resolution component along the x-axis was detected for all geometries towards the outer edge of the FOV with FWHM spatial resolution components along the x-axis of up to 6.9 mm, 6.5 mm, and 6.4 mm for Geometries A, B, and C, respectively. Towards the geometrical center of the breast PET insert geometries (i.e. the inner edge of the FOV), a similar effect was seen for Geometries A and B, while the spatial resolution did not deteriorate for Geometry C. For the two-layer DOI variants, this radial elongation effect was strongly reduced, with improvements at the −90 mm source position of 3.6 mm for Geometry A, and 3.2 mm for Geometries B and C compared to the non-DOI variants. For the three-layer DOI variants, this was further improved by 1.2 mm for all three geometries. All geometries showed a comparable spatial resolution across the FOV in the three-layer DOI variant with FWHM spatial resolution components along the x-axis of up to 2.3 mm, 2.3 mm, and 2.0 mm for Geometries A, B, and C, respectively.

In Figure 17.3, the FWHM spatial resolution components are shown for source positions at different y-coordinates at the axial cFOV. A similar radial elongation effect was seen towards the edges of the FOV, this time for the spatial resolution component along the y-axis. The effect was symmetric for all geometries, and the average improvements for the two-layer DOI variants at the ±90 mm source positions were 3.4 mm for Geometries A and B, and 3.6 mm for Geometry C. The three-layer DOI variant further improved the spatial resolution by 1.1 mm for Geometries A and B, and 1.3 mm for Geometry C.

17.3. Count rates and scatter fraction

The NECRs and the individual event types for different activities inside the FOV of the breast PET insert are shown in Figure 17.4 for Geometries A, B, and C. Geometry A revealed the highest NECR of the three geometries at all evaluated activities, with an increase of between 17 % and 26 % compared to Geometry B. At lower activities, Geometry B showed higher NECRs than

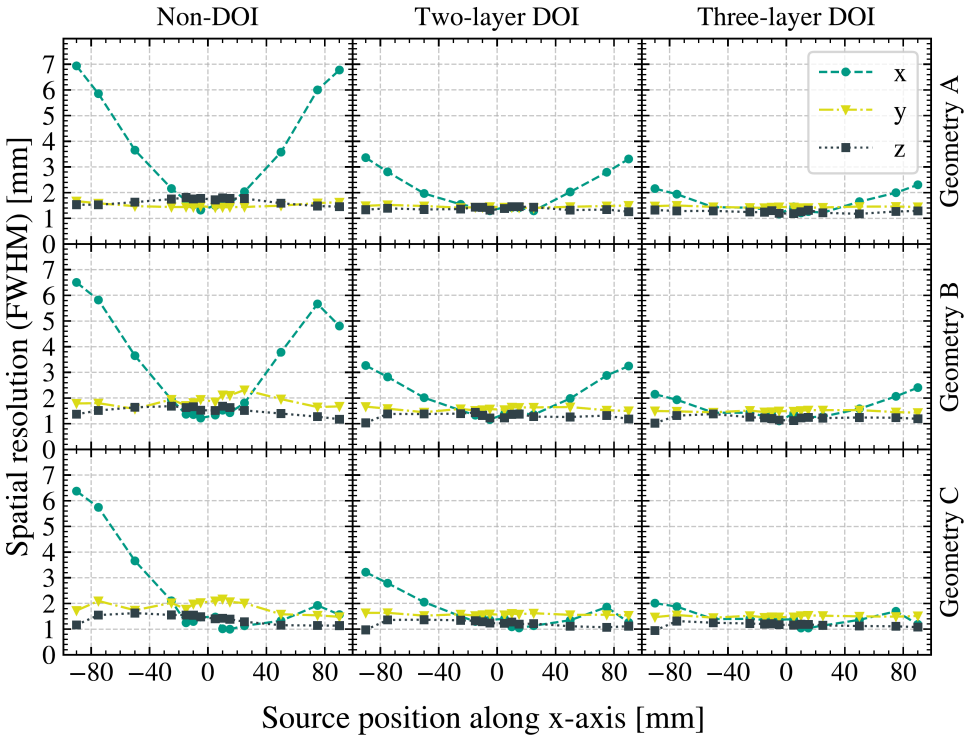

Figure 17.2.: Spatial resolution of the breast PET insert for axially centered source positions on the x-axis. Image credit: Adapted and modified from Pommranz et al. (2023).

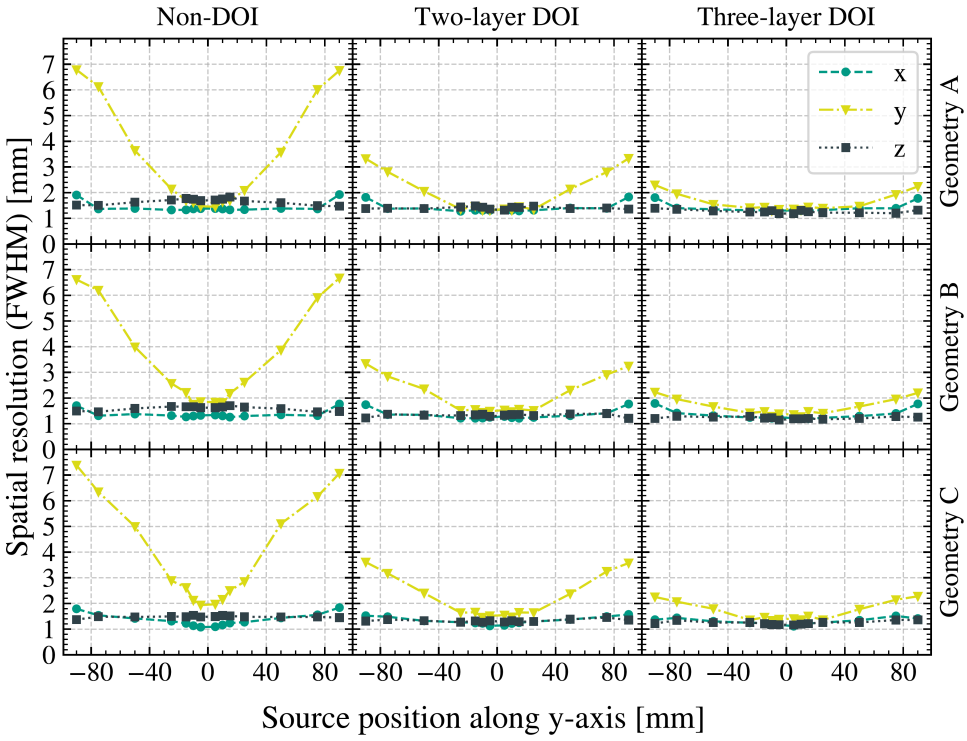

Figure 17.3.: Spatial resolution of the breast PET insert for axially centered source positions on the y-axis. Image credit: Adapted and modified from Pommranz et al. (2023).

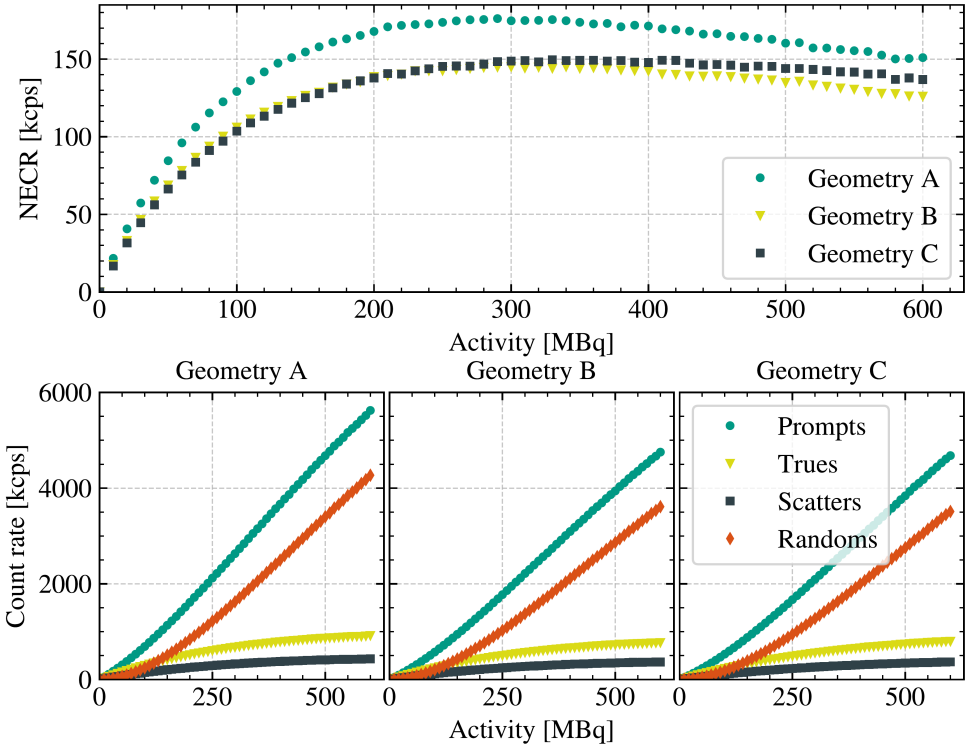

Figure 17.4.: NECR, count rates for true, scattered, and random coincidences, and the total prompt count rate for Geometries A, B, and C. Image credit: Adapted and modified from Pommranz et al. (2023).

Geometry C by up to 8 %, while at high activities, Geometry C demonstrated higher NECRs than Geometry B by up to 10 %. The peak NECR values were 176 kcps at an activity of 290 MBq for Geometry A, 145 kcps at 300 MBq for Geometry B, and 150 kcps at 330 MBq for Geometry C. The peak NECRs were identical with the previously reported results (Pommranz et al., 2023), however, at 10 MBq lower activities (one data point) for all three geometries.

The scatter fractions at an activity of 100 kBq were found to be similar for the three geometries, with 33.0 % for Geometry A, 33.1 % for Geometry B, and 32.4 % for Geometry C. The results were consistent with the previously

published results (Pommranz et al., 2023), with only slightly increased absolute scatter fractions of 0.1 % for Geometries A and C.

17.4. Background single count rate

The background single count rates and the contributions of the individual organs are shown in Figure 17.5. Geometry A demonstrated the highest count rate with 17.1 Mcps, whereas Geometry B and C revealed similar count rates with 15.3 Mcps and 14.9 Mcps, respectively. The background single count rates were consistent with the previously published results (Pommranz et al., 2023) with only a minor increase of 0.1 Mcps for Geometry C. The organ contributions were similar for the three geometries, with major contributions from the "body" region, the liver, and the heart. The breast contributed to 3.3 % of the total single events for Geometry A, 2.9 % for Geometry B, and 2.6 % for Geometry C, which was fully consistent with the previously published results (Pommranz et al., 2023).

The distribution of the background single count rates per detector block is shown in Figure 17.6. The count rates per block were strongly dependent on the layer in axial direction, with the highest count rates observed in the upper layer, and on the position in the transaxial plane where detector blocks closer to the center of the geometries showed the highest count rates. The count rate distributions were symmetric for both FOVs for Geometry A and B. The two different peaks seen in Geometry C refer to the plane grid of detector blocks towards the head and the plane grid towards the feet due to the different detector block orientations. The symmetry analogous to the results for Geometries A and B can be observed as mirror symmetries of the two sides of the peaks.

The maximum and minimum total background single count rates aggregated over the detector block layers and columns are listed in Table 17.2. The results were consistent with the previously published results (Pommranz et al., 2023), except for the maximum total count rate per column for Geometry C, which was increased by 2.9 %.

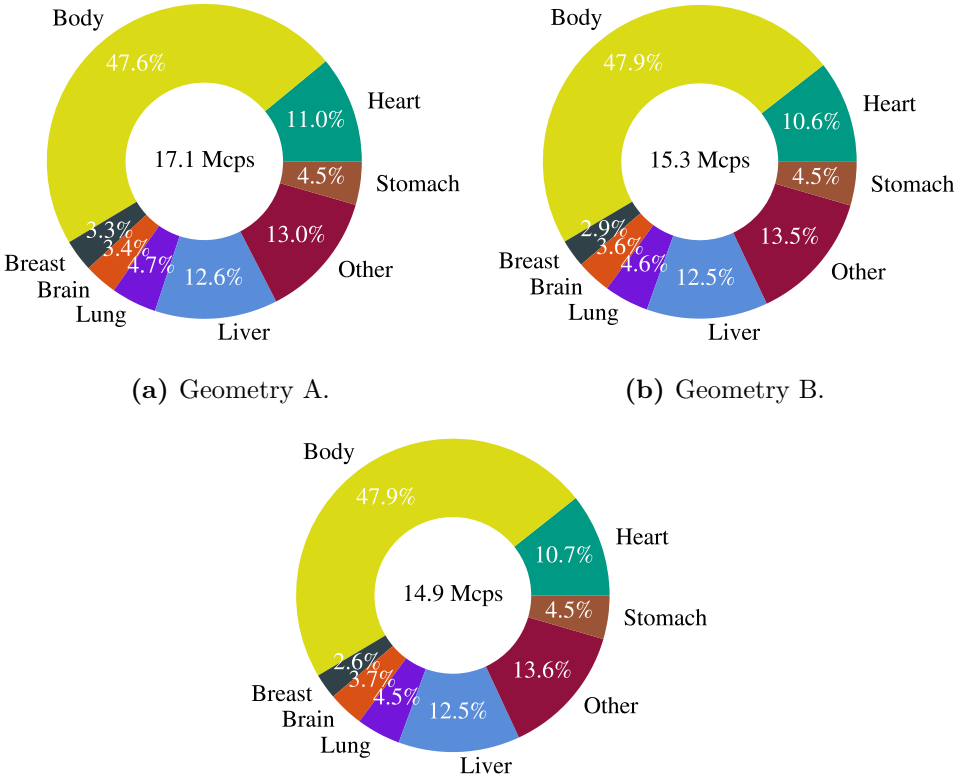

(a) Geometry A.

(b) Geometry B.

(c) Geometry C.

Figure 17.5.: Organ contributions to the background single count rate for Geometries A, B, and C. The "body" volume consists of muscles, bones, and adipose tissue. In the center of the charts, the total background single count rate is given.

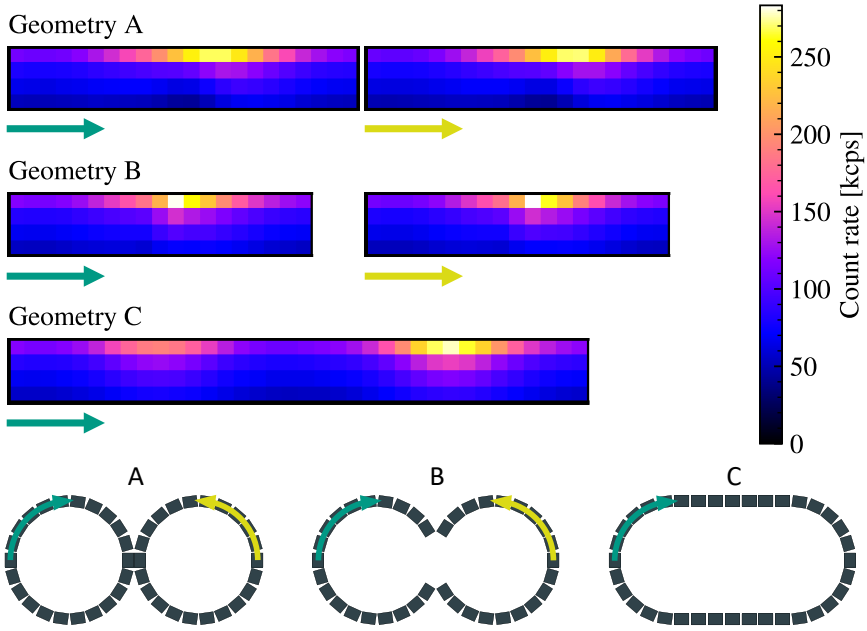

Figure 17.6.: Simulated background single count rates per detector block. The green and yellow arrows indicate the orientation of the mapping between the detector blocks, depicted by single pixels in the corresponding grid. The four rows in the grids correspond to the four detector block layers in the breast PET insert geometries. Image credit: Adapted and modified from Pommranz et al. (2023).

Table 17.2.: Background single count rates per detector block layer and column. Maximum and minimum count rates are reported for layers and columns, respectively. The relative difference is calculated based on the previously published results (Pommranz et al., 2023).

Geometry	Layer max. [kcps]	Diff. [%]	Layer min. [kcps]	Diff. [%]
Geometry A	7326	0.2	2414	0.2
Geometry B	6160	0.2	2339	0.2
Geometry C	5710	0.2	2432	0.2
	Col. max. [kcps]	Diff. [%]	Col. min. [kcps]	Diff. [%]
Geometry A	548	0.2	293	0.3
Geometry B	601	0.2	306	0.0
Geometry C	637	2.9	309	0.3

17.5. Dual-system sensitivity

Absolute sensitivities for Type I, Type II, and Type III coincidences for the three geometries are shown in Figure 17.7. For all geometries, Type I coincidences showed the highest sensitivity at all evaluated source positions with sensitivities between 8.3 % and 5.1 %. Type II sensitivities were below 0.2 % for all geometries and only contained scattered events due to the source placements outside of the breast PET insert FOV. Sensitivities for Type III coincidences were between 3.3 % and 2.4 % for Geometry A, between 2.9 % and 1.9 % for Geometry B, and between 2.9 % and 1.5 % for Geometry C along the investigated positions. By including the Type III coincidences, the whole-body PET sensitivity (Type I) could be improved by a range of 52 % and 35 % for Geometry A, 44 % and 28 % for Geometry B, and 43 % and 26 % for Geometry C for the investigated source positions.

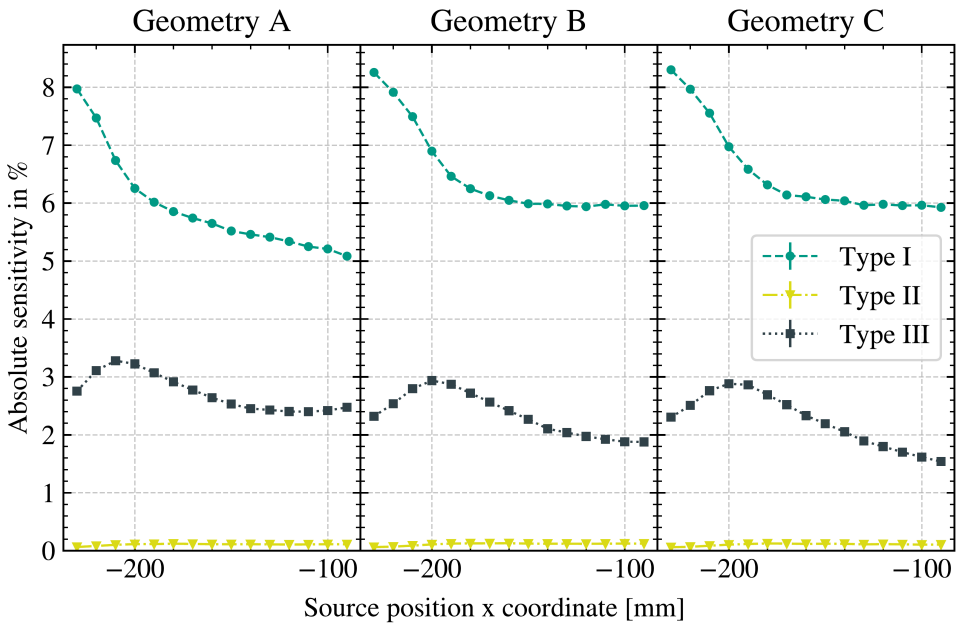

Figure 17.7.: Dual-system absolute sensitivity for Type I, Type II, and Type III coincidences for axially centered source placements and at 90 mm offsets from the cFOV.

17.6. Dual-system spatial resolution

The FWHM spatial resolution components for the individual source positions are shown in Figure 17.8a for the Biograph mMR without integrated breast PET insert, and in Figure 17.8b for the Type III coincidences between the Biograph mMR and the breast PET insert. The two-layer DOI variants of the three geometries resulted in strong improvements of the x-component compared to the non-DOI variants especially for the outer source positions, which were only slightly improved by the three-layer DOI variants.

The mean Type III spatial resolution components of the investigated source positions and the improvements of the spatial resolution compared to the Biograph mMR-only (Type I) are listed in Table 17.3. The Type III coincidences showed strong spatial resolution improvements for the x-component with mean

Table 17.3.: Mean FWHM spatial resolution components for Type III coincidences for the investigated source positions for Geometries A, B, and C in the non-DOI, two-layer DOI, and three-layer DOI variants. The spatial resolution components and the improvements of the spatial resolution compared to the mean Biograph mMR spatial resolution components (Δx, Δy, and Δz) are given in mm.

Geometry	Layers	x	Δx	y	Δy	z	Δz
Geom. A	1	4.8	2.1	4.0	0.8	2.5	1.0
Geom. A	2	4.0	2.9	3.3	1.5	2.4	1.1
Geom. A	3	3.8	3.1	3.1	1.7	2.4	1.1
Geom. B	1	4.8	2.1	4.0	0.8	2.5	1.0
Geom. B	2	4.1	2.8	3.4	1.4	2.5	1.0
Geom. B	3	3.9	3.0	3.2	1.6	2.5	1.0
Geom. C	1	5.0	1.9	4.1	0.7	2.5	1.0
Geom. C	2	4.1	2.8	3.5	1.3	2.5	1.0
Geom. C	3	3.9	3.0	3.3	1.5	2.5	1.0

improvements of 2.1 mm for Geometries A and B, and 1.9 mm for Geometry C in the non-DOI variants, and mean improvements of 3.1 mm for Geometry A and 3.0 mm for Geometries B and C in the three-layer DOI variants. The mean improvement of the z-component of the spatial resolution was between 1.0 mm and 1.1 mm and was almost not affected by introducing DOI capability.

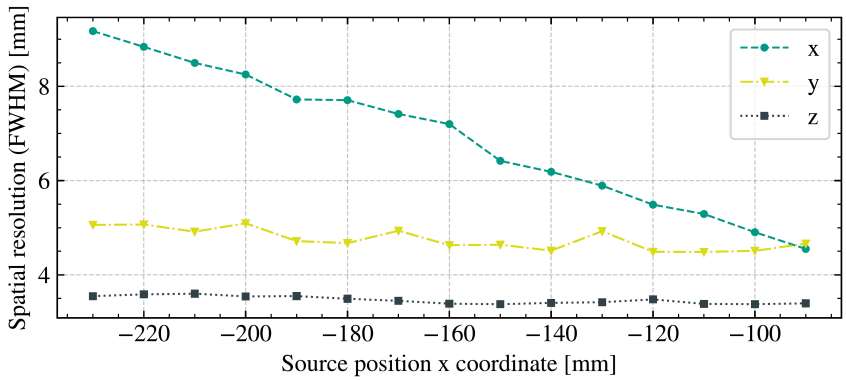

(a) Type I spatial resolution without breast PET insert.

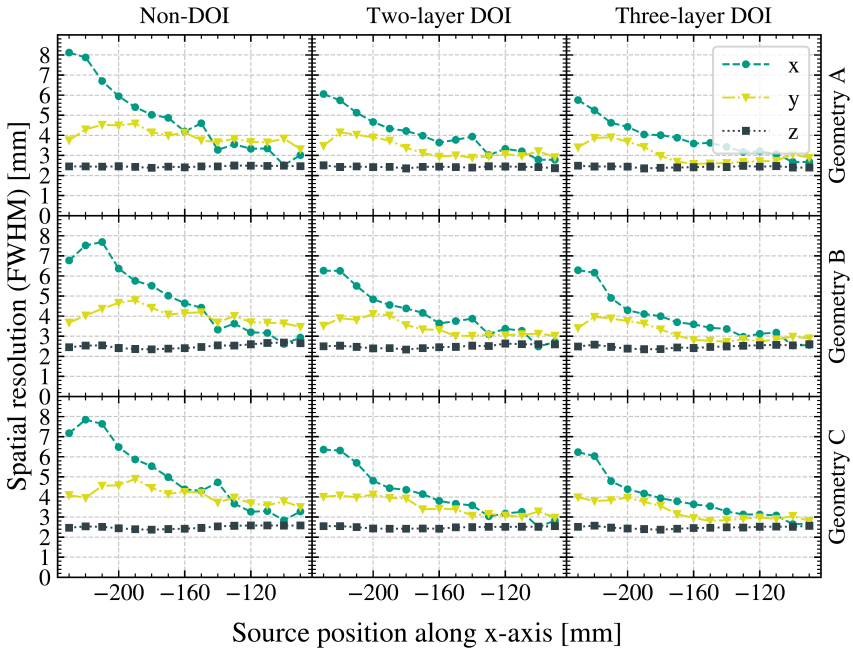

(b) Type III spatial resolution for Geometries A, B, and C.

Figure 17.8.: FWHM spatial resolution for Type I coincidences without integration of the breast PET insert (a), and for Type III coincidences for Geometries A, B, and C in the non-DOI, two-layer DOI, and three-layer DOI variants (b).

Project III

18. Discussion

A simulation study, based on the performance characteristic measurements described in the NEMA NU-4 2008 standard, was conducted to compare the expected performance characteristics of three previously suggested breast PET insert geometries. The expected sensitivity and spatial resolution was determined inside of the breast PET insert FOV and also outside of the FOV using mixed coincidences between the breast PET insert and the whole-body PET scanner.

The subsequent discussion is split into two parts. The first part is focused on the FOV of the breast PET insert (see Section 18.1), summarizing and discussing the results from Pommranz et al. (2023) and the results obtained with the updated Geant4 and GATE versions. In the second part, the dual-system simulation results are discussed (see Section 18.2).

Overall, the performed simulations are independent of the implementation of the DOI capability, read-out, and electronics of the final detector, as long as the final detector will achieve the estimated performance parameters used for read-out and digitizer modeling as described in Section 16.3, such as a dead time of 120 ns or an overall detection efficiency of 85 %. A realistic set of detector requirements was selected for the simulations, and a recent study demonstrated a Coincidence Resolving Time (CRT) of 354 ps and an energy resolution of (14.1 ± 2.0) % using the same crystal dimensions as in the simulations (Schmidt et al., 2023), which agrees well with the modeled time resolution of 350 ps and the energy resolution of 15 % used in the simulations. As the performance characteristics are highly dependent on the detector design, such as crystal dimensions or scintillation material, and the detector is not yet completely finalized, automation of the simulations are important. The fully automated Snakemake implementation of the presented simulations and analyses will allow to easily adapt and reconduct the simulations in case of changes to the detector design during detector development, except for the computationally

expensive nature of MC particle tracking codes. While adapted read-out and digitizer model parameters can be simulated by simple adjustments in the YAML configuration files, changes to the detector block or crystal dimensions would require a one-time manual modeling of the new geometries for GATE and CASToR using the `gate-generic-geometries` tool described in Section 16.2.

18.1. Stand-alone breast PET insert

The sensitivity profiles revealed approximately triangular shapes with highest sensitivities in the center and reduced sensitivities towards the axial edges, which is a well-known result for cylindrical PET scanners (Bailey et al., 2005). For Geometries B and C, the sensitivity profiles appeared compressed towards the axial center. This is due to the reduced solid angle coverage of the scanners compared to a cylindrical scanner, which is caused by the missing detectors in the center of the breast PET insert for these geometries. The simulated sensitivities were higher than the reported measured sensitivities for another breast PET device of 1.8 % (Moliner et al., 2012) and 2.0 % (García Hernández et al., 2016), which uses the same crystal length of 10 mm but with a smaller axial FOV of 4.0 cm per frame compared to the axial FOV of 10.8 cm of the breast PET insert.

In general, the sensitivity of the breast PET insert could be increased by using longer crystals, which was demonstrated for other breast PET devices with longer crystals, where typically higher sensitivities were reported (Tai et al., 2006; Zhang et al., 2007; Ravindranath et al., 2008; Furuta et al., 2009; Lee et al., 2013; Miyake et al., 2014; Zeng et al., 2021). However, from a geometric perspective, longer crystals would potentially decrease the spatial resolution close to the edge of the FOV due to an increased parallax error. Furthermore, extension of the crystals needs to be investigated from a technical point of view, as it would further reduce the available space for the front-end electronics, especially close to the center of Geometry A, which could be mitigated by reducing the diameter of the two cylinders.

Close to the cFOV, the breast PET insert demonstrated FWHM spatial resolutions of 1.4 mm for the three-layer DOI versions, and up to 2.0 mm for

Geometry C without DOI, hence strongly improving the spatial resolution of the Biograph mMR with 4.3 mm FWHM at 10 mm transaxial offset from the cFOV (Delso et al., 2011). The simulations showed, that at least a two-layer DOI detector is needed to achieve decent spatial resolution near the edges of the FOV, with spatial resolutions of 3.6 mm (Geometry C) or better for the two-layer DOI version of the three geometries. At the edge of the FOV, the absolute difference in spatial resolution was larger between the two-layer DOI and non-DOI versions (3.6 mm for Geometry A and 3.2 mm for Geometries B and C) than between the three-layer DOI and two-layer DOI versions (1.2 mm for all geometries). The three-layer DOI versions of all three geometries had similar spatial resolutions across the FOV, with spatial resolutions between 1.3 mm and 2.3 mm for Geometries A and C, and between 1.3 mm and 2.4 mm for Geometry B. Thus, the three-layer DOI versions demonstrated improved uniformity across the FOV compared to the other versions. However, the realization of DOI detectors with three or more layers is more complex than two-layer DOI detectors (Hong et al., 2008; Ito et al., 2010). Although the estimated spatial resolutions were likely limited by the generic image reconstruction used in this work that lacked geometry-specific optimizations and normalization correction, the two-layer DOI versions of the breast PET insert had slightly improved spatial resolutions by between 0.2 mm and 0.8 mm for Geometry A compared to several other breast PET scanners with spatial resolutions in the range of 1.6 mm to 2.2 mm (Tai et al., 2006; Moliner et al., 2012; Lee et al., 2013; García Hernández et al., 2016; Zeng et al., 2021). Other breast PET scanners with four-layer DOI detectors achieved spatial resolutions of below 1.0 mm (Furuta et al., 2009; Miyake et al., 2014).

The signal-to-noise ratio could potentially be improved by using detectors with Time Of Flight (TOF) capability. As the expected CRT of the planned detector was unclear at the time when the simulations were conducted (Schmidt, 2022), the TOF information was not included in the image reconstruction. As the anticipated time resolution of 300 ps in this work and the measured CRT of 354 ps for this detector (Schmidt et al., 2023) would be sufficient to use TOF image reconstruction, future studies are planned to include the TOF information in the CASToR reconstruction process, which is capable of performing TOF image reconstruction, to improve the signal-to-noise ratio.

The simulated NECRs revealed that all three geometries operated below saturation at activities typically seen in clinical breast cancer imaging scenarios with

injected [^{18}F]FDG activity concentrations in the range of about 3 MBq kg^{-1} to 5 MBq kg^{-1} (Niederkohr et al., 2021; Sah et al., 2018), i.e. a total injected activity of about 210 MBq to 350 MBq for a 70 kg patient. While in the NECR simulation all activity was within the FOV of the breast PET insert, in clinical imaging scenarios only a fraction of the activity will be within the FOV at scan time due to uptake in organs outside of the breast PET insert as shown in Figure 16.7a. The simulated NECR was highly dependent on the module configuration of the digitizer and read-out scheme, especially on the dead time and the dead time model, and therefore the simulation needs to be reconducted if key parameters of the detector change during further detector development.

In the final design of the breast PET insert, multiple detector blocks will be combined into a single detector module (Schmidt, 2022). In addition to the expected background single count rates, which are an important figure for the development of the final design of the detector electronics, the simulated aggregated background single count rates showed, that combining detector blocks from different layers and a single column will lead to more evenly distributed count rates across the detector modules than single-row combinations of detector blocks. The simulated contributions of individual organs to the background count rate is important for the design of suitable gamma shielding.

Overall, the three-layer DOI variant of Geometry A had the best PET performance characteristics of the investigated geometries. However, the final design of the breast PET insert will not only be determined from simulations, but will represent a compromise between PET performance characteristics based on the simulation results, manufacturing effort, cost, and detector development feasibility. In the two-layer DOI variant, Geometry B demonstrated only slightly degraded spatial resolution values compared to the two-layer variant of Geometry A, and was therefore identified as a suitable candidate geometry for the breast PET insert, since it will be easier to realize than Geometry A due to the missing back-to-back detector blocks in the center. When considering breast coil adaptations, such as reduced coil diameters or a larger distance between the coils, which would increase the available volume in the center and thus simplify the realization of the back-to-back detector blocks, Geometry A in the two-layer DOI variant would be the more favorable geometry due to easier image reconstruction, and since cylindrical PET scanners are commonly used and well studied.

The re-evaluation of the breast PET insert performance studies using the up-to-date GATE and Geant4 versions showed no major differences compared to the previously published results (Pommranz et al., 2023) that were also conducted in the scope of this thesis. While no decisive changes were expected from the updated Geant4 version, as the electromagnetic physics processes in the energy ranges relevant for PET scanners are well validated and did not show any major changes relevant for the basic PET performance evaluations for previous Geant4 updates, the rewrite of large parts of the GATE digitizer modules could potentially have led to severe differences. This is especially the case since implementation details of single digitizer modules can have strong effects on the performance characteristic results and large parts of the digitizer were originally developed in the early years of the GATE software prior to the beginning of the available history in the GATE `Git` source code repository[37]. As all GATE features are contributed by the scientific community based on the individual budgets and project funds available to the contributors (Sarrut et al., 2022), parts of the digitizer modules and features were without an active maintainer at the time of the rewrite, increasing the chance of software bugs introduced in the rewriting process. Thus, this re-evaluation represented an important test case for the stability and functionality of the new GATE digitizer, and the results were published in Kochebina et al. (2024), where the new GATE digitizer was introduced.

18.2. Dual-system and mixed coincidences

Installing a breast PET insert inside the Biograph mMR will potentially lead to degradations in the whole-body imaging due to additional attenuation in the FOV, resulting in reduced sensitivity, an increased number of scattered events, and the need for precise attenuation correction of the insert. However, the breast PET insert will allow to collect Type III coincidences between the whole-body PET and the breast PET insert itself. The performed dual-system simulations to investigate Type III coincidences revealed that these mixed coincidences between the breast PET insert and the whole-body PET scanner can be used to considerably improve the sensitivity by between 26 % and 52 %

[37]The GATE `Git` repository is available at `https://github.com/OpenGATE/Gate` (accessed on 2023-06-27).

and spatial resolution, with single-component improvements of the Type III spatial resolution between 0.7 mm and 3.1 mm, in the axillary lymph node region outside of the FOV of the breast PET insert. In addition to improved image quality, this can potentially improve the detection of small lesions in this region due to a reduced partial volume effect as a result of the improved spatial resolution.

When including the Type III events in the axillary lymph node region, the sensitivity can be increased by a range of 52 % and 26 % compared to Type I events only, depending on the source position and breast PET insert geometry. Geometry A had the highest Type III sensitivity for all evaluated source positions. The breast PET insert geometry was found to impact the Type I sensitivities, and Geometry A, introducing the highest amount of scintillation material (176 detector blocks) into the Biograph mMR, led to lower Type I sensitivities compared to Geometries B and C, especially at the source positions closer to the transaxial cFOV, where the central detectors of Geometry A block multiple LORs of the Biograph mMR. However, the central detectors of Geometry A resulted in an increased Type III sensitivity in this region. For Geometries B and C, the Type I sensitivities were similar with relative differences of below 2 %, however, close to the transaxial cFOV, Geometry B revealed an up to 23 % higher Type III sensitivity than Geometry C, demonstrating improved performance parameters for dual-system sensitivity.

The simulated Type I sensitivities of between 5.1 % and 8.3 % were higher than the measured system sensitivity of the Biograph mMR of 1.5 % as reported in Delso et al. (2011). This is due to the fundamentally different sensitivity performance measurements described in the NEMA NU-2 and NEMA NU-4 standards, rendering the comparison of the two sensitivities meaningless. While a 700 mm long line source filled with 4.8 MBq [^{18}F]FDG was used for the sensitivity measurement of the Biograph mMR based on the NEMA NU-2 standard (Delso et al., 2011), a point source with low activity was used in the simulations based on the NEMA NU-4 standard. The NEMA NU-2 standard leads to strongly reduced sensitivities for the Biograph mMR compared to the NEMA NU-4 standard, as the line source is extending the axial FOV, such that parts of the activity are located outside of the scanner FOV.

The two-layer DOI variants of the three investigated geometries were found to be interesting candidates, as the three-layer DOI variants revealed only slight

improvements in the mean spatial resolution over the two-layer DOI variants. In the two-layer DOI variants, the three geometries had similar spatial resolution performance in the axillary lymph node region, and showed strong improvements compared to the whole-body PET scanner with mean improvements of the spatial resolution component in x-direction of up to 2.9 mm, and up to 3.6 mm for a single source position. Therefore, the breast PET insert will improve the imaging quality also for axillary lymph node staging, as well as the detection of small metastases in the lymph nodes.

The read-out and digitizer modeling of the dual-system simulations represents a best-case scenario in several aspects of the system integration, while the simple and generic image reconstruction used to estimate the spatial resolution represents a worst-case scenario. In the simulation output and during coincidence processing, the clocks of the two PET systems were perfectly aligned and the only modeled uncertainty in the time stamps of the individual single events was due to the finite time resolution of the single scanners. For the real dual-system, synchronization of the scanner clocks, needed to align the list-mode events of the two devices, poses a technical challenge and will likely introduce jitter that was not modeled in the presented simulations. Although it was previously shown that the clock signal of the Biograph mMR can be directly used for the breast PET insert, the dual-system coincidence processing is not finalized and requires future work (Schmidt, 2022). Furthermore, the dual-system simulations did not include the limited signal bandwith for event data transmission and dead time modeling of the coincidence processor due to the unfinalized system specifications.

The simulated spatial resolution was limited by the generic image reconstruction and can therefore be considered a conservative estimate with potential for future geometry-specific improvements. The highly flexible CASToR image reconstruction code allowed for the atypical breast PET insert geometries as well as the mixed coincidences to be compared based only on the provided crystal dimensions, placements, orientations, and an optional attenuation map at 511 keV for attenuation correction. No normalization correction was applied and each crystal was connected in coincidence with every other crystal in the dual-system setup, except for crystals in the same detector block. This could be improved in future work to reduce scatter, as for the mixed coincidences, many of the available LORs can be defined as invalid *a priori*, because they do not penetrate the patient volume, e.g. LORs between the outer detector

blocks of the breast PET insert and the Biograph mMR detectors on the same side, and the lower layer of the breast PET insert blocks and the lowest blocks of the Biograph mMR. This can potentially improve the mixed-coincidence image reconstruction, as these LORs can only be caused by scattered or random coincidences. Once the final geometry of the breast PET insert has been decided, future work will include geometry-specific improvements to the image reconstruction.

To achieve comparable estimations of the spatial resolution for the Type III mixed coincidences and the Type I coincidences of the whole-body PET scanner, the same generic image reconstruction used for the Type III coincidences was also used for the Type I coincidences instead of the FBP algorithm. The image reconstruction for the Type III coincidences included attenuation correction of the breast PET insert geometries from precise attenuation maps produced by the GATE MuMap actor from the simulation input. Nevertheless, the simulations for the Type I coincidences were performed without breast PET insert integration in order to avoid underestimation of the Type I spatial resolution due to increased scatter and potentially imperfect attenuation correction.

Using longer crystals in the breast PET insert will increase the sensitivity of the Type II and the Type III coincidences. Following a back-of-the-envelope calculation using a linear attenuation coefficient of $\mu = 0.87\,\mathrm{cm}^{-1}$ for LSO (Melcher, 2000), the fraction of gamma rays depositing energy in the crystal is increased from 58 % for a 10 mm long crystal to 73 % for a crystal length of 15 mm, and to 82 % for a 20 mm long crystal. As only one of the two crystals of a mixed coincidence (Type III) would be extended, this directly corresponds to an estimated relative sensitivity increase of 25 % for the 15 mm crystal and 42 % for the 20 mm crystal compared to the sensitivity using a 10 mm long crystal. For Type II coincidences, the extension of both involved crystals leads to relative sensitivity improvements of 57 % and 101 % for crystals with lengths of 15 mm and 20 mm, respectively, compared to 10 mm long crystals. However, longer crystals will lead to a reduced Type I sensitivity due to the additional scintillation material inside the FOV of the whole-body scanner. Furthermore, the use of longer crystals will potentially deteriorate the Type III spatial resolution at the axillary lymph nodes outside of the breast PET insert FOV, as the LORs through this region are often projected on the long side of the breast PET insert crystals rather than their front faces, e.g. for LORs between the outer crystals of the breast PET insert and the upper crystals

of the Biograph mMR. Theoretically, this effect could be counteracted by incorporating additional DOI layers or continuous DOI technology, so that the lengths of the sub-crystal segments remain similar to the shorter crystal case, but this would require substantial changes to the detector design. Simulations with different crystal lengths are planned to quantify the expected degradation in spatial resolution with longer crystals and to investigate the potential of the discussed countermeasures. Furthermore, simulations with smaller detector blocks are planned, which will allow to improve the approximation of the circular shape. The sensitivity of the Type III coincidences could potentially be improved by placing either a plate or a curved arrangement of additional detector blocks below the breast PET insert, which will enable additional Type III LORs between the crystals in the plate and the upper part of the whole-body scanner.

Project III

Conclusion

Conclusion

19. Summary and conclusion

Three scientific projects using automated, scalable, and reproducible workflows implemented in the Snakemake workflow management system and in a custom workflow tool developed in the course of this thesis were discussed.

The CORRAREA correction is an empirical energy-dependent correction function for the XMM-Newton EPIC on-axis effective areas, derived from cross-calibration using a large sample of observations. In collaboration with the ESAC, a new CORRAREA correction function was derived, switching from the previously used stack-and-fit approach to the fit-and-stack method, and was released as part of the official XMM-Newton Current Calibration Files (CCFs). A generic workflow system was developed as part of the Large-sample Epic Analysis Pipeline (LEAP) tool, which allows for continuous validation of the CORRAREA correction functions after the implementation of future updates to the EPIC calibration or Science Analysis System (SAS). Using the new and highly automated CORRAREA workflow, the new CORRAREA correction was successfully validated on several sub-samples, demonstrating the robustness of the correction for different EPIC science modes, pile-up levels, and epochs. These sub-sample analyses revealed significant relative uncertainties in the science mode and time-dependent calibration at energies below the lower energy threshold of the CORRAREA correction of 2 keV, proving the suitability of LEAP and the CORRAREA workflow for probing calibration topics beyond CORRAREA. New sources from future source catalogue updates can be added to the sample with two manual one-time steps: visual screening and the definition of a physical source model. The generic XMM-Newton LEAP system allows for further studies beyond CORRAREA on large samples of XMM-Newton observations and can be extended to include observations from other X-ray instruments in future work.

For characterization of the eROSITA Filter Wheel Closed (FWC) background a new highly detailed mass model was derived from the final eROSITA CAD

model. Together with a new digitizer and data analysis workflow that offers precise modeling of detector effects and allowed to use the eROSITA Science Analysis Software System (eSASS) pattern matching algorithm, an MC simulation of the eROSITA FWC background was performed using Geant4. In contrast to pre-launch simulation studies, the simulated background agreed with the measurements within the uncertainties of the radiation and particle environment at the eROSITA orbit around L_2. Although the absolute strengths of the fluorescence lines in the FWC spectrum could not be reproduced even with detailed material compositions including all known impurities, the information about the relative contributions from individual volumes to the fluorescence lines provided valuable insights into the eROSITA FWC background and for the design of future X-ray missions. The digitizer and data analysis workflow provides a wide range of useful data that was not available for previous simulation studies, such as eSASS-compatible spectral products that will be used to further improve the spectral model of the eROSITA FWC background. The eSASS-compatible output together with a back link for every event to a pool of detailed simulation data on the Geant4 `Hit` level inside the detector will allow to tackle a variety of questions that will potentially help to further deepen the characterization and the understanding of the eROSITA background. The results presented in this thesis represent only the first steps of the exploitation of the produced simulation data.

MC simulations of three different geometries of a breast PET insert integrable into the Biograph mMR whole-body PET/MRI scanner were conducted using GATE to estimate the expected PET performance characteristics. Close to the center of the Field Of View (cFOV) the breast PET inserts revealed spatial resolutions between 1.4 mm and 2.0 mm depending on the geometry and DOI capability, which will lead to strongly improved imaging quality in this region compared to the whole-body PET scanner. The simulations revealed that it will be necessary to integrate Depth Of Interaction (DOI) capability in the detectors to prevent severe degradations of the spatial resolution towards the edges of the FOV due to the parallax error. Geometry A demonstrated the best absolute sensitivity of 3.1 % at the cFOV, while Geometries B and C had absolute sensitivities at the cFOV of 2.7 % and 2.2 %, respectively. For typical clinical scenarios, the breast PET insert is expected to operate below saturation and the background single count rates were between 17.1 Mcps for Geometry A and 14.9 Mcps for Geometry C. Multi-system simulations were

performed, where the breast PET insert and the whole-body PET scanner were connected in coincidence, to investigate the improvements of the mixed coincidences (Type III) between both scanners on the sensitivity and spatial resolution in the axillary lymph node region, outside of the FOV of the breast PET insert. Depending on the source position and geometry, the sensitivity of the whole-body PET could be increased by between 26 % and 52 % when including Type III coincidences. The mean spatial resolution components along the x, y, and z-directions were improved by up to 3.1 mm, 1.7 mm, and 1.0 mm, respectively, due to the Virtual Pinhole PET (VP-PET) effect. Overall, Geometry B in the two-layer DOI version was found to be a suitable compromise between PET performance, manufacturing effort, and cost, while Geometry A in the three-layer DOI version yielded the best PET performance of the investigated geometries. Based on the strongly improved spatial resolution both inside and outside of the breast PET insert FOV, the simulation study revealed improved breast imaging capabilities compared to standalone whole-body PET acquisitions of the breast.

With the still rapidly increasing available computational capacity at the time of writing this thesis, allowing for more precise and complex simulations and large-sample studies, the importance of automated, scalable, and reproducible workflows will only increase in the fields of high energy astrophysics, medical imaging, and computational physics in general in the coming years.

Conclusion

Bibliography

Bibliography

Bibliography

Adams, James H., J. Cosmic ray effects on microelectronics. Part 4, Dec. 1986. Published: Final Memorandum Report, Oct. 1983 - Oct. 1986 Naval Research Lab., Washington, DC.

Adriani, O., Barbarino, G. C., Bazilevskaya, G. A., et al. Time Dependence of the e^- Flux Measured by PAMELA during the July 2006-December 2009 Solar Minimum. *The Astrophysical Journal*, 810(2):142, Sept. 2015. doi: 10.1088/0004-637X/810/2/142.

Agostinelli, S., Allison, J., Amako, K., et al. Geant4—a simulation toolkit. *Nuclear Instruments and Methods in Physics Research Section A: Accelerators, Spectrometers, Detectors and Associated Equipment*, 506(3):250–303, July 2003. doi: 10.1016/S0168-9002(03)01368-8.

Aguilar, M., Ali Cavasonza, L., Ambrosi, G., et al. Properties of Cosmic Helium Isotopes Measured by the Alpha Magnetic Spectrometer. *Physical Review Letters*, 123(18):181102, Nov. 2019. doi: 10.1103/PhysRevLett.123.181102.

Aide, N., Lasnon, C., Veit-Haibach, P., et al. EANM/EARL harmonization strategies in PET quantification: from daily practice to multicentre oncological studies. *European Journal of Nuclear Medicine and Molecular Imaging*, 44(S1):17–31, Aug. 2017. doi: 10.1007/s00259-017-3740-2.

Aklan, B., Paulus, D. H., Wenkel, E., et al. Toward simultaneous PET/MR breast imaging: Systematic evaluation and integration of a radiofrequency breast coil: Toward simultaneous PET/MR breast imaging. *Medical Physics*, 40(2):024301, Feb. 2013. doi: 10.1118/1.4788642.

Aklan, B., Jakoby, B. W., Watson, C. C., et al. GATE Monte Carlo simulations for variations of an integrated PET/MR hybrid imaging system based on the Biograph mMR model. *Physics in Medicine and Biology*, 60(12):4731–4752, June 2015. doi: 10.1088/0031-9155/60/12/4731.

Aleskandarany, M. A., Vandenberghe, M. E., Marchiò, C., et al. Tumour Heterogeneity of Breast Cancer: From Morphology to Personalised Medicine. *Pathobiology*, 85(1-2):23–34, 2018. doi: 10.1159/000477851.

Allison, J., Amako, K., Apostolakis, J., et al. Geant4 developments and applications. *IEEE Transactions on Nuclear Science*, 53(1):270–278, Feb. 2006. doi: 10.1109/TNS.2006.869826.

Allison, J., Amako, K., Apostolakis, J., et al. Recent developments in Geant4. *Nuclear Instruments and Methods in Physics Research Section A: Accelerators, Spectrometers, Detectors and Associated Equipment*, 835:186–225, Nov. 2016. doi: 10.1016/j.nima.2016.06.125.

Apostolakis, J., Asai, M., Bogdanov, A., et al. Geometry and physics of the Geant4 toolkit for high and medium energy applications. *Radiation Physics and Chemistry*, 78(10):859–873, Oct. 2009. doi: 10.1016/j.radphyschem.2009.04.026.

Arnaud, K. Archives, surveys, catalogs, and software. In Arnaud, K., Smith, R., and Siemiginowska, A., editors, *Handbook of X-ray Astronomy*, pp. 114–130. Cambridge University Press, 1 edition, Sept. 2011. ISBN 978-0-521-88373-3 978-1-139-03423-4. doi: 10.1017/CBO9781139034234.007.

Arnaud, K. A., and Smith, R. K. Data reduction and calibration. In Arnaud, K., Smith, R., and Siemiginowska, A., editors, *Handbook of X-ray Astronomy*, pp. 59–85. Cambridge University Press, 1 edition, Sept. 2011. ISBN 978-0-521-88373-3 978-1-139-03423-4. doi: 10.1017/CBO9781139034234.005.

Astropy Collaboration, Price-Whelan, A. M., Lim, P. L., et al. The Astropy Project: Sustaining and Growing a Community-oriented Open-source Project and the Latest Major Release (v5.0) of the Core Package. *The Astrophysical Journal*, 935:167, Aug. 2022. doi: 10.3847/1538-4357/ac7c74. ADS Bibcode: 2022ApJ...935..167A.

Bailey, D. L., Townsend, D. W., Valk, P. E., and Maisey, M. N., editors. *Positron Emission Tomography*. Springer-Verlag, London, 2005. ISBN 978-1-85233-798-8. doi: 10.1007/b136169. URL http://link.springer.com/10.1007/b136169.

Baker, M. 1,500 scientists lift the lid on reproducibility. *Nature*, 533(7604):452–454, May 2016. doi: 10.1038/533452a.

Bakr, S., Cohen, D., Siegele, R., et al. Latest Geant4 developments for PIXE applications. *Nuclear Instruments and Methods in Physics Research Section B: Beam Interactions with Materials and Atoms*, 436:285–291, Dec. 2018. doi: 10.1016/j.nimb.2018.10.004.

Bakr, S., Cohen, D. D., Siegele, R., et al. Geant4 X-ray fluorescence with updated libraries. *Nuclear Instruments and Methods in Physics Research Section B: Beam Interactions with Materials and Atoms*, 507:11–19, Nov. 2021. doi: 10.1016/j.nimb.2021.09.009.

Bearden, J. A., and Burr, A. F. Reevaluation of X-Ray Atomic Energy Levels. *Reviews of Modern Physics*, 39(1):125–142, Jan. 1967. doi: 10.1103/RevModPhys.39.125.

Beaudoux, V., Blin, G., Barbrel, B., Kantor, G., and Zacharatou, C. Geant4 physics list comparison for the simulation of phase-contrast mammography (XPulse project). *Physica Medica*, 60:66–75, Apr. 2019. doi: 10.1016/j.ejmp.2019.03.026.

Boellaard, R. Optimisation and harmonisation: two sides of the same coin? *European Journal of Nuclear Medicine and Molecular Imaging*, 40(7):982–984, July 2013. doi: 10.1007/s00259-013-2440-9.

Boellaard, R., Delgado-Bolton, R., Oyen, W. J. G., et al. FDG PET/CT: EANM procedure guidelines for tumour imaging: version 2.0. *European Journal of Nuclear Medicine and Molecular Imaging*, 42(2):328–354, Feb. 2015. doi: 10.1007/s00259-014-2961-x.

Botsikas, D., Kalovidouri, A., Becker, M., et al. Clinical utility of 18F-FDG-PET/MR for preoperative breast cancer staging. *European Radiology*, 26(7):2297–2307, July 2016. doi: 10.1007/s00330-015-4054-z.

Bradshaw, M. J., Burwitz, V., Hartner, G., et al. Developments in testing x-ray optics at MPE's PANTER facility. In Pareschi, G., and O'Dell, S. L., editors, *Optics for EUV, X-Ray, and Gamma-Ray Astronomy IX*, p. 42, San Diego, United States, Sept. 2019. SPIE. doi: 10.1117/12.2531709.

Brun, R., and Rademakers, F. ROOT — An object oriented data analysis framework. *Nuclear Instruments and Methods in Physics Research Section A: Accelerators, Spectrometers, Detectors and Associated Equipment*, 389(1-2):81–86, Apr. 1997. doi: 10.1016/S0168-9002(97)00048-X.

Brunner, H., Boller, T., Coutinho, D., et al. eROSITA ground operations. In den Herder, J.-W. A., Nakazawa, K., and Nikzad, S., editors, *Space Telescopes and Instrumentation 2018: Ultraviolet to Gamma Ray*, p. 193, Austin, United States, July 2018. SPIE. doi: 10.1117/12.2315138.

Brzeziński, K., Oliver, J. F., Gillam, J., and Rafecas, M. Study of a high-resolution PET system using a Silicon detector probe. *Physics in Medicine and Biology*, 59(20):6117–6140, Oct. 2014. doi: 10.1088/0031-9155/59/20/6117.

Brzeziński, K., Oliver, J., Gillam, J., et al. Experimental evaluation of the resolution improvement provided by a silicon PET probe. *Journal of Instrumentation*, 11(09):P09016–P09016, Sept. 2016. doi: 10.1088/1748-0221/11/09/P09016.

Burak, W. E., Hollenbeck, S. T., Zervos, E. E., et al. Sentinel lymph node biopsy results in less postoperative morbidity compared with axillary lymph node dissection for breast cancer. *The American Journal of Surgery*, 183(1): 23–27, Jan. 2002. doi: 10.1016/S0002-9610(01)00848-0.

Campana, R. In-Orbit Background for X-Ray Detectors. In Bambi, C., and Santangelo, A., editors, *Handbook of X-ray and Gamma-ray Astrophysics*, pp. 1–27. Springer Nature Singapore, Singapore, 2022. ISBN 9789811645440. doi: 10.1007/978-981-16-4544-0_28-1.

Cash, W. Parameter estimation in astronomy through application of the likelihood ratio. *The Astrophysical Journal*, 228:939, Mar. 1979. doi: 10.1086/156922.

Catalano, O. A., Masch, W. R., Catana, C., et al. An overview of PET/MR, focused on clinical applications. *Abdominal Radiology*, 42(2):631–644, Feb. 2017. doi: 10.1007/s00261-016-0894-5.

Caudle, A. S., Cupp, J. A., and Kuerer, H. M. Management of Axillary Disease. *Surgical Oncology Clinics of North America*, 23(3):473–486, July 2014. doi: 10.1016/j.soc.2014.03.007.

Chang, J. M., Leung, J. W. T., Moy, L., Ha, S. M., and Moon, W. K. Axillary Nodal Evaluation in Breast Cancer: State of the Art. *Radiology*, 295(3): 500–515, June 2020. doi: 10.1148/radiol.2020192534.

Cherry, S. R., Sorenson, J. A., and Phelps, M. E. Positron Emission Tomography. In *Physics in Nuclear Medicine*, pp. 307–343. Elsevier, 2012. ISBN 978-1-4160-5198-5. doi: 10.1016/B978-1-4160-5198-5.00018-6.

Chytracek, R., Mccormick, J., Pokorski, W., and Santin, G. Geometry Description Markup Language for Physics Simulation and Analysis Applications. *IEEE Transactions on Nuclear Science*, 53(5):2892–2896, Oct. 2006. doi: 10.1109/TNS.2006.881062.

Clinthorne, N., Brzezinski, K., Chesi, E., et al. Silicon as an unconventional detector in positron emission tomography. *Nuclear Instruments and Methods in Physics Research Section A: Accelerators, Spectrometers, Detectors and Associated Equipment*, 699:216–220, Jan. 2013. doi: 10.1016/j.nima.2012.05.026.

Coccetti, F. The Fermiac or Fermi's Trolley. *Il Nuovo Cimento C*, 39(2):1–8, Sept. 2016. doi: 10.1393/ncc/i2016-16296-7.

Crippa, F., Gerali, A., Alessi, A., Agresti, R., and Bombardieri, E. The Role of FDG-PET for Axillary Lymph Node Staging in Primary Breast Cancer. In Bombardieri, E., Gianni, L., and Bonadonna, G., editors, *Breast Cancer*, pp. 157–167. Springer Berlin Heidelberg, Berlin, Heidelberg, 2008. ISBN 978-3-540-36780-2 978-3-540-36781-9. doi: 10.1007/978-3-540-36781-9_12.

Crusoe, M. R., Abeln, S., Iosup, A., et al. Methods included: standardizing computational reuse and portability with the Common Workflow Language. *Communications of the ACM*, 65(6):54–63, June 2022. doi: 10.1145/3486897.

Dauser, T., Falkner, S., Lorenz, M., et al. SIXTE: a generic X-ray instrument simulation toolkit. *Astronomy & Astrophysics*, 630:A66, Sept. 2019. doi: 10.1051/0004-6361/201935978.

Davis, J. E. The Formal Underpinnings of The Response Functions Used in X-Ray Spectral Analysis. *The Astrophysical Journal*, 548(2):1010–1019, Feb. 2001. doi: 10.1086/319002.

Delso, G., Fürst, S., Jakoby, B., et al. Performance Measurements of the Siemens mMR Integrated Whole-Body PET/MR Scanner. *Journal of Nuclear Medicine*, 52(12):1914–1922, Dec. 2011. doi: 10.2967/jnumed.111.092726.

Den Herder, J. W., Brinkman, A. C., Kahn, S. M., et al. The Reflection Grating Spectrometer on board XMM-Newton. *Astronomy & Astrophysics*, 365(1): L7–L17, Jan. 2001. doi: 10.1051/0004-6361:20000058.

Dennerl, K. Spectral fitting: Calibration uncertainties and Randomization, Sept. 2019.

Di Tommaso, P., Chatzou, M., Floden, E. W., et al. Nextflow enables reproducible computational workflows. *Nature Biotechnology*, 35(4):316–319, Apr. 2017. doi: 10.1038/nbt.3820.

Disselhorst, J. A., Newport, D. F., Schmid, A. M., et al. NEMA NU 4-2008 performance evaluation and MR compatibility tests of an APD-based small animal PET-insert for simultaneous PET/MR imaging. *Physics in Medicine & Biology*, 67(4):045015, Feb. 2022. doi: 10.1088/1361-6560/ac499d.

Dregely, I., Lanz, T., Metz, S., et al. A 16-channel MR coil for simultaneous PET/MR imaging in breast cancer. *European Radiology*, 25(4):1154–1161, Apr. 2015. doi: 10.1007/s00330-014-3445-x.

Drury, L. O. Origin of cosmic rays. *Astroparticle Physics*, 39-40:52–60, Dec. 2012. doi: 10.1016/j.astropartphys.2012.02.006.

Eidelman, S. I., and Shwartz, B. A. Interactions of Particles and Radiation with Matter. In Grupen, C., and Buvat, I., editors, *Handbook of Particle Detection and Imaging*, pp. 3–23. Springer Berlin Heidelberg, Berlin, Heidelberg, 2012. ISBN 978-3-642-13270-4 978-3-642-13271-1. doi: 10.1007/978-3-642-13271-1_1.

ESA: XMM-Newton SOC. Users Guide to the XMM-Newton Science Analysis System, Issue 18.0, 2023a. URL https://xmm-tools.cosmos.esa.int/external/xmm_user_support/documentation/sas_usg/USG/.

ESA: XMM-Newton SOC. XMM-Newton Users Handbook, Issue 2.21, 2023b. URL https://xmm-tools.cosmos.esa.int/external/xmm_user_support/documentation/uhb/.

Ferrari, A., Sala, P., Fasso, A., and Ranft, J. FLUKA: A Multi-Particle Transport Code. Technical Report SLAC-R-773, 877507, Dec. 2005. URL http://www.osti.gov/servlets/purl/877507-sC9S9L/.

Ferrario, I., Arcangeli, L., Citterio, O., et al. The eROSITA X-ray mirrors: technology and qualification aspects of the production of mandrels, shells and mirror modules. In Kadowaki, N., editor, *International Conference on Space Optics — ICSO 2010*, p. 59, Rhodes Island, Greece, Nov. 2017. SPIE. doi: 10.1117/12.2309183.

Fioretti, V., Bulgarelli, A., Malaguti, G., et al. The low Earth orbit radiation environment and its impact on the prompt background of hard x-ray focusing telescopes. p. 845331, Amsterdam, Netherlands, Sept. 2012. doi: 10.1117/12.926248.

Fioretti, V., Lotti, S., and Santin, G. AREMBES WP 7: Normalization of an isotropic flux in space in Geant4 simulations., May 2018.

Forbush, S. E. Cosmic-ray intensity variations during two solar cycles. *Journal of Geophysical Research*, 63(4):651–669, Dec. 1958. doi: 10.1029/JZ063i004p00651.

Freyberg, M., Perinati, E., Pacaud, F., et al. SRG/eROSITA in-flight background at L2. In den Herder, J.-W. A., Nakazawa, K., and Nikzad, S., editors, *Space Telescopes and Instrumentation 2020: Ultraviolet to Gamma Ray*, p. 163, Online Only, United States, Dec. 2020. SPIE. doi: 10.1117/12.2562709.

Freyberg, M. J., Müller, T., Perinati, E., et al. SRG/eROSITA micrometeoroid hits and effects. In den Herder, J.-W. A., Nakazawa, K., and Nikzad, S., editors, *Space Telescopes and Instrumentation 2022: Ultraviolet to Gamma Ray*, p. 232, Montréal, Canada, Aug. 2022. SPIE. doi: 10.1117/12.2630890.

Friedrich, P., Bräuninger, H., Budau, B., et al. Design and development of the eROSITA x-ray mirrors. p. 70112T, Marseille, France, July 2008. doi: 10.1117/12.788948.

Furse, D., Groh, S., Trost, N., et al. Kassiopeia: a modern, extensible C++ particle tracking package. *New Journal of Physics*, 19(5):053012, May 2017. doi: 10.1088/1367-2630/aa6950.

Furuta, M., Kitamura, K., Ohi, J., et al. Basic evaluation of a C-shaped breast PET scanner. In *2009 IEEE Nuclear Science Symposium Conference Record (NSS/MIC)*, pp. 2548–2552, Orlando, FL, Oct. 2009. IEEE. doi: 10.1109/NSSMIC.2009.5402027.

Fürst, F. XMM-CCF-REL-388 – Empirical correction of the EPIC effective area, Apr. 2022a. URL https://xmmweb.esac.esa.int/docs/documents/CAL-SRN-0388-1-4.pdf.

Fürst, F. XMM-SOC-CAL-TN-0230 – Empirical correction of the EPIC effective area based on NuSTAR observations, Apr. 2022b. URL https://xmmweb.esac.esa.int/docs/documents/CAL-TN-0230-1-3.pdf.

García Hernández, T., Vicedo González, A., Ferrer Rebolleda, J., et al. Performance evaluation of a high resolution dedicated breast PET scanner: Performance evaluation of a DbPET. *Medical Physics*, 43(5):2261–2272, Apr. 2016. doi: 10.1118/1.4945271.

Garmire, G. P., Bautz, M. W., Ford, P. G., Nousek, J. A., and Ricker, Jr., G. R. Advanced CCD imaging spectrometer (ACIS) instrument on the Chandra X-ray Observatory. p. 28, Waikoloa, Hawai'i, United States, Mar. 2003. doi: 10.1117/12.461599.

Giacalone, J., Fahr, H., Fichtner, H., et al. Anomalous Cosmic Rays and Heliospheric Energetic Particles. *Space Science Reviews*, 218(4):22, June 2022. doi: 10.1007/s11214-022-00890-7.

Gleeson, L. J., and Axford, W. I. Solar Modulation of Galactic Cosmic Rays. *The Astrophysical Journal*, 154:1011, Dec. 1968. doi: 10.1086/149822.

Gong, K., Cherry, S. R., and Qi, J. On the assessment of spatial resolution of PET systems with iterative image reconstruction. *Physics in Medicine and Biology*, 61(5):N193–N202, Mar. 2016. doi: 10.1088/0031-9155/61/5/N193.

Gonzalez, A. J., Gonzalez-Montoro, A., Vidal, L. F., et al. Initial Results of the MINDView PET Insert Inside the 3T mMR. *IEEE Transactions on Radiation and Plasma Medical Sciences*, 3(3):343–351, May 2019. doi: 10.1109/TRPMS.2018.2866899.

Goorley, T., James, M., Booth, T., et al. Features of MCNP6. *Annals of Nuclear Energy*, 87:772–783, Jan. 2016. doi: 10.1016/j.anucene.2015.02.020.

Grant, C. E., Miller, E. D., Bautz, M. W., et al. Towards precision particle background estimation for future x-ray missions: correlated variability between Chandra ACIS and AMS. In den Herder, J.-W. A., Nakazawa, K., and Nikzad,

S., editors, *Space Telescopes and Instrumentation 2022: Ultraviolet to Gamma Ray*, p. 89, Montréal, Canada, Aug. 2022. SPIE. doi: 10.1117/12.2629520.

Grkovski, M., Brzezinski, K., Cindro, V., et al. Evaluation of a high resolution silicon PET insert module. *Nuclear Instruments and Methods in Physics Research Section A: Accelerators, Spectrometers, Detectors and Associated Equipment*, 788:86–94, July 2015. doi: 10.1016/j.nima.2015.03.078.

Gruber, D. E., Matteson, J. L., Peterson, L. E., and Jung, G. V. The Spectrum of Diffuse Cosmic Hard X-Rays Measured with *HEAO 1*. *The Astrophysical Journal*, 520(1):124–129, July 1999. doi: 10.1086/307450.

Gryk, M. R., and Ludäscher, B. Workflows and Provenance: Toward Information Science Solutions for the Natural Sciences. *Library Trends*, 65(4):555–562, 2017. doi: 10.1353/lib.2017.0018.

Guainazzi, M., Saxton, R., Stuhlinger, M., et al. XMM-CAL-SRN-0321 – CORRAREA: a new tool to estimate the impact of effective area EPIC inter-calibration uncertainties, Sept. 2014. URL https://xmmweb.esac.esa.int/docs/documents/CAL-SRN-0321-1-2.pdf.

Guatelli, S., Mantero, A., Mascialino, B., Pia, M. G., and Zampichelli, V. Validation of Geant4 Atomic Relaxation Against the NIST Physical Reference Data. *IEEE Transactions on Nuclear Science*, 54(3):594–603, June 2007. doi: 10.1109/TNS.2007.894814.

Guller, U., Nitzsche, E., Moch, H., and Zuber, M. Is Positron Emission Tomography an Accurate Non-invasive Alternative to Sentinel Lymph Node Biopsy in Breast Cancer Patients? *JNCI Journal of the National Cancer Institute*, 95(14):1040–1043, July 2003. doi: 10.1093/jnci/95.14.1040.

Hanisch, R. J., Farris, A., Greisen, E. W., et al. Definition of the Flexible Image Transport System (FITS). *Astronomy & Astrophysics*, 376(1):359–380, Sept. 2001. doi: 10.1051/0004-6361:20010923.

Harris, C. R., Millman, K. J., van der Walt, S. J., et al. Array programming with NumPy. *Nature*, 585(7825):357–362, Sept. 2020. doi: 10.1038/s41586-020-2649-2.

Harris, J. R., Lippman, M. E., Morrow, M., and Osborne, C. K. *Diseases of the Breast*, volume Fifth edition. Lippincott Williams and Wilkins, Philadelphia, Pennsylvania, 2014. ISBN 978-1-4511-8627-7.

Harrison, R. L., Granja, C., and Leroy, C. Introduction to Monte Carlo Simulation. pp. 17–21, Bratislava (Slovakia), 2010. doi: 10.1063/1.3295638.

Heinitz, C. B. Empirical Cross-Calibration of XMM-Newton's EPIC Effective Areas and Search for a Compact Object Associated with the SNR G96.0+2.0. Nov. 2021. doi: 10.15496/PUBLIKATION-62088. Publisher: Universität Tübingen.

Heynderickx, D., Quaghebeur, B., Wera, J., Daly, E. J., and Evans, H. D. R. New radiation environment and effects models in the European Space Agency's Space Environment Information System (SPENVIS). *Space Weather*, 2(10): n/a–n/a, Oct. 2004. doi: 10.1029/2004SW000073.

Hong, S. J., Kwon, S. I., Ito, M., et al. Concept Verification of Three-Layer DOI Detectors for Small Animal PET. *IEEE Transactions on Nuclear Science*, 55(3):912–917, June 2008. doi: 10.1109/TNS.2008.920258.

Houck, J. C., and Denicola, L. A. ISIS: An Interactive Spectral Interpretation System for High Resolution X-Ray Spectroscopy. 216:591, Jan. 2000. Conference Name: Astronomical Data Analysis Software and Systems IX ADS Bibcode: 2000ASPC..216..591H.

Hubbard, M. ATHENA OU TN-16: A discussion of the isotropic normalisation issue for radiation transport in Geant4 for space applications, Oct. 2021.

Huh, S. S., Clinthorne, N. H., and Rogers, W. Investigation of an internal PET probe for prostate imaging. *Nuclear Instruments and Methods in Physics Research Section A: Accelerators, Spectrometers, Detectors and Associated Equipment*, 579(1):339–343, Aug. 2007. doi: 10.1016/j.nima.2007.04.073.

Hunter, J. D. Matplotlib: A 2D Graphics Environment. *Computing in Science & Engineering*, 9(3):90–95, 2007. doi: 10.1109/MCSE.2007.55.

International Organization for Standardization. Space environment (natural and artificial) — Galactic cosmic ray model (ISO Standard No. 15390:2004), 2004.

Ito, M., Lee, J. S., Kwon, S. I., et al. A Four-Layer DOI Detector With a Relative Offset for Use in an Animal PET System. *IEEE Transactions on Nuclear Science*, 57(3):976–981, June 2010. doi: 10.1109/TNS.2010.2044892.

Ivantchenko, A. V., Ivanchenko, V. N., Molina, J.-M. Q., and Incerti, S. L. Geant4 hadronic physics for space radiation environment. *International Journal of Radiation Biology*, 88(1-2):171–175, Jan. 2012. doi: 10.3109/09553002.2011.610865.

Jacobs, F., Sundermann, E., De Sutter, B., Christiaens, M., and Lemahieu, I. A Fast Algorithm to Calculate the Exact Radiological Path through a Pixel or Voxel Space. *Journal of computing and information technology*, 6 (1):89–94, 1998.

Jan, S., Santin, G., Strul, D., et al. GATE: a simulation toolkit for PET and SPECT. *Physics in Medicine and Biology*, 49(19):4543–4561, Oct. 2004. doi: 10.1088/0031-9155/49/19/007.

Jan, S., Benoit, D., Becheva, E., et al. GATE V6: a major enhancement of the GATE simulation platform enabling modelling of CT and radiotherapy. *Physics in Medicine and Biology*, 56(4):881–901, Feb. 2011. doi: 10.1088/0031-9155/56/4/001.

Janecek, M., Heyu Wu, and Yuan-Chuan Tai. A simulation study for the design of a prototype insert for whole-body PET scanners. *IEEE Transactions on Nuclear Science*, 53(3):1143–1149, June 2006. doi: 10.1109/TNS.2006.871899.

Jansen, F., Lumb, D., Altieri, B., et al. XMM-Newton observatory: I. The spacecraft and operations. *Astronomy & Astrophysics*, 365(1):L1–L6, Jan. 2001. doi: 10.1051/0004-6361:20000036.

Jiang, J., Samanta, S., Li, K., et al. Augmented Whole-Body Scanning via Magnifying PET. *IEEE Transactions on Medical Imaging*, 39(11):3268–3277, Nov. 2020. doi: 10.1109/TMI.2019.2962623.

Joye, W. A., and Mandel, E. New Features of SAOImage DS9. 295:489, Jan. 2003. Conference Name: Astronomical Data Analysis Software and Systems XII ADS Bibcode: 2003ASPC..295..489J.

Kawrakow, I. Accurate condensed history Monte Carlo simulation of electron transport. I. EGS nrc, the new EGS4 version. *Medical Physics*, 27(3):485–498, Mar. 2000. doi: 10.1118/1.598917.

Kendziorra, E., Clauss, T., Meidinger, N., et al. Effect of low-energy protons on the performance of the EPIC pn-CCD detector on XMM-Newton. p. 32, San Diego, CA, USA, Dec. 2000. doi: 10.1117/12.409132.

Kettula, K., Nevalainen, J., and Miller, E. D. Cross-calibration of *Suzaku* /XIS and *XMM-Newton* /EPIC using galaxy clusters. *Astronomy & Astrophysics*, 552:A47, Apr. 2013. doi: 10.1051/0004-6361/201220408.

Kirsch, M. G., Elfving, A., Kresken, R., et al. Extending the lifetime of ESA's X-ray observatory XMM-Newton. In *SpaceOps 2014 Conference*, Pasadena, CA, May 2014. American Institute of Aeronautics and Astronautics. doi: 10.2514/6.2014-1608.

Kirsch, M. G. F. XMM-Newton MOC and spacecraft status, May 2023. URL https://xmm-tools.cosmos.esa.int/external/xmm_calibration/calib/documentation/epic_cal_meetings/202305/MKirsch.pdf.

Kist, J. W., Van Der Vlies, M., Hoekstra, O. S., et al. Calibration of PET/CT scanners for multicenter studies on differentiated thyroid cancer with 124I. *EJNMMI Research*, 6(1):39, Dec. 2016. doi: 10.1186/s13550-016-0191-x.

Kochebina, O., Bonifacio, D. A. B., Konstantinou, G., et al. New GATE Digitizer Unit for versions post v9.3. *Frontiers in Physics*, 12:1294916, Mar. 2024. doi: 10.3389/fphy.2024.1294916.

Kolb, A., Wehrl, H. F., Hofmann, M., et al. Technical performance evaluation of a human brain PET/MRI system. *European Radiology*, 22(8):1776–1788, Aug. 2012. doi: 10.1007/s00330-012-2415-4.

Koolen, B. B., Vogel, W. V., Vrancken Peeters, M. J. T. F. D., et al. Molecular Imaging in Breast Cancer: From Whole-Body PET/CT to Dedicated Breast PET. *Journal of Oncology*, 2012:1–8, 2012. doi: 10.1155/2012/438647.

Koyama, K., Tsunemi, H., Dotani, T., et al. X-Ray Imaging Spectrometer (XIS) on Board Suzaku. *Publications of the Astronomical Society of Japan*, 59(sp1):S23–S33, Jan. 2007. doi: 10.1093/pasj/59.sp1.S23.

Kurtzer, G. M., Sochat, V., and Bauer, M. W. Singularity: Scientific containers for mobility of compute. *PLOS ONE*, 12(5):e0177459, May 2017. doi: 10.1371/journal.pone.0177459.

Kuznetsov, N. V., Popova, H., and Panasyuk, M. I. Empirical model of long-time variations of galactic cosmic ray particle fluxes. *Journal of Geophysical Research: Space Physics*, 122(2):1463–1472, Feb. 2017. doi: 10.1002/2016JA022920.

Köster, J., and Rahmann, S. Snakemake—a scalable bioinformatics workflow engine. *Bioinformatics*, 28(19):2520–2522, Oct. 2012. doi: 10.1093/bioinformatics/bts480.

Lee, E., Werner, M. E., Karp, J. S., and Surti, S. Design Optimization of a Time-Of-Flight, Breast PET Scanner. *IEEE Transactions on Nuclear Science*, 60(3):1645–1652, June 2013. doi: 10.1109/TNS.2013.2257849.

Lober, L. Investigating the time stability of the XMM-Newton effective area cross-calibration with CORRAREA. Master's thesis, University of Tuebingen, Feb. 2023.

Longair, M. S. *High Energy Astrophysics:*. Cambridge University Press, 3 edition, Feb. 2011. ISBN 978-0-521-75618-1 978-0-511-77834-6. doi: 10.1017/CBO9780511778346. URL https://www.cambridge.org/core/product/identifier/9780511778346/type/book.

Longinotti, A. L., de La Calle, I., Bianchi, S., Guainazzi, M., and Dovciak, M. FERO (Finding Extreme Relativistic Objects): statistics of relativistic broad Fe Kalpha lines in AGN. 32:62–64, Apr. 2008. Conference Name: Revista Mexicana de Astronomia y Astrofisica Conference Series ADS Bibcode: 2008RMxAC..32...62L.

Lumb, D. H. XMM-Newton in-orbit calibration. *ESA Bulletin*, 109:71–77, Feb. 2002. ADS Bibcode: 2002ESABu.109...71L.

Lönnblad, L. CLHEP—a project for designing a C++ class library for high energy physics. *Computer Physics Communications*, 84(1-3):307–316, Nov. 1994. doi: 10.1016/0010-4655(94)90217-8.

Mannheim, J. G., Schmid, A. M., Schwenck, J., et al. PET/MRI Hybrid Systems. *Seminars in Nuclear Medicine*, 48(4):332–347, July 2018. doi: 10.1053/j.semnuclmed.2018.02.011.

Mantero, A., Ben Abdelouahed, H., Champion, C., et al. PIXE simulation in Geant4. *X-Ray Spectrometry*, 40(3):135–140, May 2011. doi: 10.1002/xrs.1301.

Marshall, H. L., Chen, Y., Drake, J. J., et al. Concordance: In-flight Calibration of X-Ray Telescopes without Absolute References. *The Astronomical Journal*, 162(6):254, Dec. 2021. doi: 10.3847/1538-3881/ac230a.

Martelotto, L. G., Ng, C. K., Piscuoglio, S., Weigelt, B., and Reis-Filho, J. S. Breast cancer intra-tumor heterogeneity. *Breast Cancer Research*, 16(3):210, June 2014. doi: 10.1186/bcr3658.

Martucci, M., Munini, R., Boezio, M., et al. Proton Fluxes Measured by the PAMELA Experiment from the Minimum to the Maximum Solar Activity for Solar Cycle 24. *The Astrophysical Journal*, 854(1):L2, Feb. 2018. doi: 10.3847/2041-8213/aaa9b2.

Mason, K. O., Breeveld, A., Much, R., et al. The XMM-Newton optical/UV monitor telescope. *Astronomy & Astrophysics*, 365(1):L36–L44, Jan. 2001. doi: 10.1051/0004-6361:20000044.

Mathews, A. J., Komarov, S., Wu, H., O'Sullivan, J. A., and Tai, Y.-C. Improving PET imaging for breast cancer using virtual pinhole PET half-ring insert. *Physics in Medicine and Biology*, 58(18):6407–6427, Sept. 2013. doi: 10.1088/0031-9155/58/18/6407.

Maurin, D., Melot, F., and Taillet, R. A database of charged cosmic rays. *Astronomy & Astrophysics*, 569:A32, Sept. 2014. doi: 10.1051/0004-6361/201321344.

Maurin, D., Dembinski, H. P., Gonzalez, J., Mariş, I. C., and Melot, F. Cosmic-Ray Database Update: Ultra-High Energy, Ultra-Heavy, and Antinuclei Cosmic-Ray Data (CRDB v4.0). *Universe*, 6(8):102, July 2020. doi: 10.3390/universe6080102.

Meidinger, N., Andritschke, R., Elbs, J., et al. eROSITA camera design and first performance measurements with CCDs. p. 70110J, Marseille, France, July 2008. doi: 10.1117/12.787793.

Meidinger, N., Andritschke, R., Bornemann, W., et al. Report on the eROSITA camera system. p. 91441W, Montréal, Quebec, Canada, July 2014. doi: 10.1117/12.2055703.

Meidinger, N., Andritschke, R., Dennerl, K., et al. eROSITA camera array on the SRG satellite. *Journal of Astronomical Telescopes, Instruments, and Systems*, 7(02), May 2021. doi: 10.1117/1.JATIS.7.2.025004.

Melcher, C. L. Scintillation crystals for PET. *Journal of Nuclear Medicine: Official Publication, Society of Nuclear Medicine*, 41(6):1051–1055, June 2000.

Merlin, T., Stute, S., Benoit, D., et al. CASToR: a generic data organization and processing code framework for multi-modal and multi-dimensional tomographic reconstruction. *Physics in Medicine & Biology*, 63(18):185005, Sept. 2018. doi: 10.1088/1361-6560/aadac1.

Merloni, A., Lamer, G., Liu, T., et al. The SRG/eROSITA all-sky survey: First X-ray catalogues and data release of the western Galactic hemisphere. *Astronomy & Astrophysics*, 682:A34, Feb. 2024. doi: 10.1051/0004-6361/202347165.

Mesirov, J. P. Accessible Reproducible Research. *Science*, 327(5964):415–416, Jan. 2010. doi: 10.1126/science.1179653.

Metropolis, N. The Beginning of the Monte Carlo Method. *Los Alamos Science*, 15:125–130, 1987.

Metropolis, N., and Ulam, S. The Monte Carlo Method. *Journal of the American Statistical Association*, 44(247):335–341, Sept. 1949. doi: 10.1080/01621459.1949.10483310.

Miyake, K. K., Matsumoto, K., Inoue, M., et al. Performance Evaluation of a New Dedicated Breast PET Scanner Using NEMA NU4-2008 Standards. *Journal of Nuclear Medicine*, 55(7):1198–1203, July 2014. doi: 10.2967/jnumed.113.131565.

Moliner, L., González, A. J., Soriano, A., et al. Design and evaluation of the MAMMI dedicated breast PET: Design and evaluation of the MAMMI dedicated breast PET. *Medical Physics*, 39(9):5393–5404, Aug. 2012. doi: 10.1118/1.4742850.

Morawitz, J., Sigl, B., Rubbert, C., et al. Clinical Decision Support for Axillary Lymph Node Staging in Newly Diagnosed Breast Cancer Patients Based on ^{18} F-FDG PET/MRI and Machine Learning. *Journal of Nuclear Medicine*, 64(2):304–311, Feb. 2023. doi: 10.2967/jnumed.122.264138.

Moreau, D., Wiebels, K., and Boettiger, C. Containers for computational reproducibility. *Nature Reviews Methods Primers*, 3(1):50, July 2023. doi: 10.1038/s43586-023-00236-9.

Moses, W. W. Fundamental limits of spatial resolution in PET. *Nuclear Instruments and Methods in Physics Research Section A: Accelerators, Spectrometers, Detectors and Associated Equipment*, 648:S236–S240, Aug. 2011. doi: 10.1016/j.nima.2010.11.092.

Moy, L., Ponzo, F., Noz, M. E., et al. Improving Specificity of Breast MRI Using Prone PET and Fused MRI and PET 3D Volume Datasets. *Journal of Nuclear Medicine*, 48(4):528–537, Apr. 2007. doi: 10.2967/jnumed.106.036780.

Mrigakshi, A. I., Matthiä, D., Berger, T., Reitz, G., and Wimmer-Schweingruber, R. F. Assessment of galactic cosmic ray models: ASSESSMENT OF GALACTIC COSMIC RAY MODELS. *Journal of Geophysical Research: Space Physics*, 117(A8), Aug. 2012. doi: 10.1029/2012JA017611.

Muzic, R. F., and DiFilippo, F. P. Positron Emission Tomography-Magnetic Resonance Imaging: Technical Review. *Seminars in Roentgenology*, 49(3): 242–254, July 2014. doi: 10.1053/j.ro.2014.10.001.

Mölder, F., Jablonski, K. P., Letcher, B., et al. Sustainable data analysis with Snakemake. *F1000Research*, 10:33, Apr. 2021. doi: 10.12688/f1000research.29032.2.

Nasa High Energy Astrophysics Science Archive Research Center (Heasarc). HEAsoft: Unified Release of FTOOLS and XANADU. *Astrophysics Source Code Library*, p. ascl:1408.004, Aug. 2014. ADS Bibcode: 2014ascl.soft08004N.

National Electrical Manufacturers Association. NEMA Standard Publication NU 2-2007: Performance Measurements of Positron Emission Tomographs, 2007.

National Electrical Manufacturers Association. NEMA Standard Publication NU 4-2008: Performance Measurements of Small Animal Positron Emission Tomographs, Sept. 2008.

Nensa, F., Beiderwellen, K., Heusch, P., and Wetter, A. Clinical applications of PET/MRI: current status and future perspectives. *Diagnostic and Interventional Radiology*, 20(5):438–447, Aug. 2014. doi: 10.5152/dir.2014.14008.

Nevalainen, J., and Molendi, S. Studying X-ray instruments with galaxy clusters. *Astronomy & Astrophysics*, 676:A142, Aug. 2023. doi: 10.1051/0004-6361/202245099.

Nevalainen, J., David, L., and Guainazzi, M. Cross-calibrating X-ray detectors with clusters of galaxies: an IACHEC study. *Astronomy & Astrophysics*, 523: A22, Nov. 2010. doi: 10.1051/0004-6361/201015176.

Niederkohr, R. D., Hayden, S. P., Hamill, J. J., et al. Reproducibility of FDG PET/CT image-based cancer staging and standardized uptake values with simulated reduction of injected FDG dose or acquisition time. *American Journal of Nuclear Medicine and Molecular Imaging*, 11(5):428–442, 2021.

Nymmik, R., Panasyuk, M., Pervaja, T., and Suslov, A. A model of galactic cosmic ray fluxes. *International Journal of Radiation Applications and Instrumentation. Part D. Nuclear Tracks and Radiation Measurements*, 20 (3):427–429, July 1992. doi: 10.1016/1359-0189(92)90028-T.

Nymmik, R., Panasyuk, M., Pervaya, T., and Suslov, A. An analytical model, describing dynamics of galactic cosmic ray heavy particles. *Advances in Space Research*, 14(10):759–763, Oct. 1994. doi: 10.1016/0273-1177(94)90538-X.

Nymmik, R., Panasyuk, M., and Suslov, A. Galactic cosmic ray flux simulation and prediction. *Advances in Space Research*, 17(2):19–30, Jan. 1996. doi: 10.1016/0273-1177(95)00508-C.

Orsi, S. PAMELA: A payload for antimatter matter exploration and light nuclei astrophysics. *Nuclear Instruments and Methods in Physics Research*

Section A: Accelerators, Spectrometers, Detectors and Associated Equipment, 580(2):880–883, Oct. 2007. doi: 10.1016/j.nima.2007.06.051.

Park, S.-J., Rogers, W. L., Huh, S., et al. Performance evaluation of a very high resolution small animal PET imager using silicon scatter detectors. *Physics in Medicine and Biology*, 52(10):2807–2826, May 2007. doi: 10.1088/0031-9155/52/10/012.

Pavlinsky, M., Tkachenko, A., Levin, V., et al. The ART-XC telescope on board the SRG observatory. *Astronomy & Astrophysics*, 650:A42, June 2021. doi: 10.1051/0004-6361/202040265.

Perinati, E., Tenzer, C., Santangelo, A., et al. The radiation environment in L-2 orbit: implications on the non-X-ray background of the eROSITA pn-CCD cameras. *Experimental Astronomy*, 33(1):39–53, Mar. 2012. doi: 10.1007/s10686-011-9269-7.

Perinati, E., Barbera, M., Diebold, S., et al. Preliminary assessment of the ATHENA/WFI non-X-ray background. *Experimental Astronomy*, 44(3): 387–399, Dec. 2017. doi: 10.1007/s10686-017-9541-6.

Perkins, S. T., Cullen, D. E., Chen, M. H., et al. Tables and graphs of atomic subshell and relaxation data derived from the LLNL Evaluated Atomic Data Library (EADL), Z = 1–100. Technical Report UCRL–50400-Vol.30, 10121422, Oct. 1991. URL http://www.osti.gov/servlets/purl/10121422/.

Peñuelas, I., Domínguez-Prado, I., García-Velloso, M. J., et al. PET Tracers for Clinical Imaging of Breast Cancer. *Journal of Oncology*, 2012:1–9, 2012. doi: 10.1155/2012/710561.

Pia, M. G., Weidenspointner, G., Augelli, M., et al. PIXE Simulation With Geant4. *IEEE Transactions on Nuclear Science*, 56(6):3614–3649, Dec. 2009. doi: 10.1109/TNS.2009.2033993.

Pichler, B. J., Wehrl, H. F., Kolb, A., and Judenhofer, M. S. Positron Emission Tomography/Magnetic Resonance Imaging: The Next Generation of Multimodality Imaging? *Seminars in Nuclear Medicine*, 38(3):199–208, May 2008. doi: 10.1053/j.semnuclmed.2008.02.001.

Piconcelli, E., Jimenez-Bailón, E., Guainazzi, M., et al. Evidence for a multizone warm absorber in the *XMM-Newton* spectrum of Markarian 304. *Monthly Notices of the Royal Astronomical Society*, 351(1):161–168, June 2004. doi: 10.1111/j.1365-2966.2004.07764.x.

Picozza, P., Galper, A., Castellini, G., et al. PAMELA – A payload for antimatter matter exploration and light-nuclei astrophysics. *Astroparticle Physics*, 27(4):296–315, Apr. 2007. doi: 10.1016/j.astropartphys.2006.12.002.

Pinker, K., Bogner, W., Baltzer, P., et al. Improved Differentiation of Benign and Malignant Breast Tumors with Multiparametric ^{18} Fluorodeoxyglucose Positron Emission Tomography Magnetic Resonance Imaging: A Feasibility Study. *Clinical Cancer Research*, 20(13):3540–3549, July 2014. doi: 10.1158/1078-0432.CCR-13-2810.

Pivarski, J., Schreiner, H., Hollands, A., et al. Uproot, July 2023. URL https://zenodo.org/record/4340632.

Plucinsky, P. P., Bogdan, A., Marshall, H. L., and Tice, N. W. The complicated evolution of the ACIS contamination layer over the mission life of the Chandra X-ray Observatory. In Den Herder, J.-W. A., Nakazawa, K., and Nikzad, S., editors, *Space Telescopes and Instrumentation 2018: Ultraviolet to Gamma Ray*, p. 226, Austin, United States, July 2018. SPIE. doi: 10.1117/12.2312748.

Polyak, K. Heterogeneity in breast cancer. *Journal of Clinical Investigation*, 121(10):3786–3788, Oct. 2011. doi: 10.1172/JCI60534.

Pommranz, C. M. Monte Carlo Simulation Studies for Medical and Astrophysical Applications. Master's thesis, University of Tuebingen, Tübingen, Jan. 2019.

Pommranz, C. M., Tenzer, C., Diebold, S. J., et al. Simulation studies of the eROSITA particle-induced background using a highly detailed mass model. In den Herder, J.-W. A., Nakazawa, K., and Nikzad, S., editors, *Space Telescopes and Instrumentation 2022: Ultraviolet to Gamma Ray*, p. 231, Montréal, Canada, Aug. 2022. SPIE. doi: 10.1117/12.2630299.

Pommranz, C. M., Schmidt, F. P., Mannheim, J. G., et al. Design and performance simulation studies of a breast PET insert integrable into a clinical whole-body PET/MRI scanner. *Physics in Medicine & Biology*, Feb. 2023. doi: 10.1088/1361-6560/acba77.

Predehl, P., Sunyaev, R. A., Becker, W., et al. Detection of large-scale X-ray bubbles in the Milky Way halo. *Nature*, 588(7837):227–231, Dec. 2020. doi: 10.1038/s41586-020-2979-0.

Predehl, P., Andritschke, R., Arefiev, V., et al. The eROSITA X-ray telescope on SRG. *Astronomy & Astrophysics*, 647:A1, Mar. 2021. doi: 10.1051/0004-6361/202039313.

Pujara, A. C., Kim, E., Axelrod, D., and Melsaether, A. N. PET/MRI in Breast Cancer: PET/MRI in Breast Cancer. *Journal of Magnetic Resonance Imaging*, 49(2):328–342, Feb. 2019. doi: 10.1002/jmri.26298.

Ramos, C. D., Erdi, Y. E., Gonen, M., et al. FDG-PET standardized uptake values in normal anatomical structures using iterative reconstruction segmented attenuation correction and filtered back-projection. *European Journal of Nuclear Medicine*, 28(2):155–164, Feb. 2001. doi: 10.1007/s002590000421.

Ravindranath, B., Maramraju, S. H., Junnarkar, S. S., et al. A simultaneous PET/MRI breast scanner based on the RatCAP. In *2008 IEEE Nuclear Science Symposium Conference Record*, pp. 4650–4655, Dresden, Germany, Oct. 2008. IEEE. doi: 10.1109/NSSMIC.2008.4774460.

Read, A. M., Guainazzi, M., and Sembay, S. Cross-calibration of the *XMM-Newton* EPIC pn and MOS on-axis effective areas using 2XMM sources. *Astronomy & Astrophysics*, 564:A75, Apr. 2014. doi: 10.1051/0004-6361/201423422.

Rembielak, A., Green, M., Saleem, A., and Price, P. Diagnostic and therapeutic imaging in oncology. *Medicine*, 44(1):6–9, Jan. 2016. doi: 10.1016/j.mpmed.2015.10.010.

Ros, A., Barrientos, L., Borja-Lloret, M., et al. New probe for the improvement of the Spatial Resolution in total-body PET (PROScRiPT). *EPJ Web of Conferences*, 253:09004, 2021. doi: 10.1051/epjconf/202125309004.

Rosen, S., Saxton, R., and Smith, M. XMM-CCF-REL-396 – EPIC MOS response, Mar. 2023. URL https://xmmweb.esac.esa.int/docs/documents/CAL-SRN-0396-1-4.pdf.

Rosen, S. R., Webb, N. A., Watson, M. G., et al. The *XMM-Newton* serendipitous survey: VII. The third *XMM-Newton* serendipitous source catalogue. *Astronomy & Astrophysics*, 590:A1, June 2016. doi: 10.1051/0004-6361/201526416.

Ross, E., and Chaplin, W. J. The Behaviour of Galactic Cosmic-Ray Intensity During Solar Activity Cycle 24. *Solar Physics*, 294(1):8, Jan. 2019. doi: 10.1007/s11207-019-1397-7.

Sah, B.-R., Ghafoor, S., Burger, I. A., et al. Feasibility of ^{18} F-FDG Dose Reductions in Breast Cancer PET/MRI. *Journal of Nuclear Medicine*, 59 (12):1817–1822, Dec. 2018. doi: 10.2967/jnumed.118.209007.

Salmaso, B., Moretti, A., and Gaskin, J. Facilities for X-ray Optics Calibration. In Bambi, C., and Santangelo, A., editors, *Handbook of X-ray and Gamma-ray Astrophysics*, pp. 1–32. Springer Nature Singapore, Singapore, 2022. ISBN 9789811645440. doi: 10.1007/978-981-16-4544-0_14-1.

Salvadori, J., Labour, J., Odille, F., et al. Monte Carlo simulation of digital photon counting PET. *EJNMMI Physics*, 7(1):23, Dec. 2020. doi: 10.1186/s40658-020-00288-w.

Salvat, F., and Fernández-Varea, J. M. Overview of physical interaction models for photon and electron transport used in Monte Carlo codes. *Metrologia*, 46 (2):S112–S138, Apr. 2009. doi: 10.1088/0026-1394/46/2/S08.

Santin, G. Normalisation modelling sources, 2007.

Santos-Lleo, M., Schartel, N., Tananbaum, H., Tucker, W., and Weisskopf, M. C. The first decade of science with Chandra and XMM-Newton. *Nature*, 462(7276):997–1004, Dec. 2009. doi: 10.1038/nature08690.

Sarmiento, M. H., Arévalo, M., Arviset, C., et al. XMM-Newton Science Archive (XSA). 521:104, Oct. 2019. Conference Name: Astronomical Data Analysis Software and Systems XXVI ADS Bibcode: 2019ASPC..521..104S.

Sarrut, D., Bała, M., Bardiès, M., et al. Advanced Monte Carlo simulations of emission tomography imaging systems with GATE. *Physics in Medicine & Biology*, 66(10):10TR03, May 2021. doi: 10.1088/1361-6560/abf276.

Sarrut, D., Arbor, N., Baudier, T., et al. The OpenGATE ecosystem for Monte Carlo simulation in medical physics. *Physics in Medicine & Biology*, 67(18): 184001, Sept. 2022. doi: 10.1088/1361-6560/ac8c83.

Sato, T., Iwamoto, Y., Hashimoto, S., et al. Features of Particle and Heavy Ion Transport code System (PHITS) version 3.02. *Journal of Nuclear Science and Technology*, 55(6):684–690, June 2018. doi: 10.1080/00223131.2017.1419890.

Savvidy, K. G. The MIXMAX random number generator. *Computer Physics Communications*, 196:161–165, Nov. 2015. doi: 10.1016/j.cpc.2015.06.003.

Saxton, R. D. XMM-SOC-CAL-TN-0212 – Stability of the EPIC-pn camera, Mar. 2022. URL https://xmmweb.esac.esa.int/docs/documents/CAL-TN-0212-3-0.pdf.

Schartel, N., González-Riestra, R., Kretschmar, P., et al. XMM-Newton. In Bambi, C., and Santangelo, A., editors, *Handbook of X-ray and Gamma-ray Astrophysics*, pp. 1–38. Springer Nature Singapore, Singapore, 2022. ISBN 9789811645440. doi: 10.1007/978-981-16-4544-0_41-1.

Schellenberger, G., Reiprich, T. H., Lovisari, L., Nevalainen, J., and David, L. *XMM-Newton* and *Chandra* cross-calibration using HIFLUGCS galaxy clusters: Systematic temperature differences and cosmological impact. *Astronomy & Astrophysics*, 575:A30, Mar. 2015. doi: 10.1051/0004-6361/201424085.

Schmidt, F. P. Towards the Development of a Breast PET/MRI Insert for a Clinical Whole-Body PET/MRI Scanner. Apr. 2022. doi: 10.15496/PUBLIKATION-67654. Publisher: Universität Tübingen.

Schmidt, F. P., Krämer, J. C., Parl, C., Schmand, M., and Pichler, B. J. Evaluation of a modular all-in-one high-resolution PET detector and readout electronics setup. *Physics in Medicine & Biology*, 68(11):115011, June 2023. doi: 10.1088/1361-6560/acd432.

Schmitz, J., Schwab, J., Schwenck, J., et al. Decoding Intratumoral Heterogeneity of Breast Cancer by Multiparametric *In Vivo* Imaging: A Translational Study. *Cancer Research*, 76(18):5512–5522, Sept. 2016. doi: 10.1158/0008-5472.CAN-15-0642.

Schulz, V., Schug, D., Gebhardt, P., et al. Improving the Diagnosis of Breast Cancer using a dedicated PET/MRI – The EU Project HYPMED. pp. s–0040–1708301, Leipzig, Apr. 2020. doi: 10.1055/s-0040-1708301.

Scipioni, M., Corbeil, J., Allen, M. S., et al. Design and Development of the Human Dynamic NeuroChemical Connectome Scanner. In *2023 IEEE Nuclear Science Symposium, Medical Imaging Conference and International Symposium on Room-Temperature Semiconductor Detectors (NSS MIC RTSD)*, pp. 1–2, Vancouver, BC, Canada, Nov. 2023. IEEE. doi: 10.1109/NSSMICRTSD49126.2023.10337891.

Sedeta, E., Sung, H., Laversanne, M., Bray, F., and Jemal, A. Recent Mortality Patterns and Time Trends for the Major Cancers in 47 Countries Worldwide. *Cancer Epidemiology, Biomarkers & Prevention*, 32(7):894–905, July 2023. doi: 10.1158/1055-9965.EPI-22-1133.

Segars, W. P., Sturgeon, G., Mendonca, S., Grimes, J., and Tsui, B. M. W. 4D XCAT phantom for multimodality imaging research: 4D XCAT phantom for multimodality imaging research. *Medical Physics*, 37(9):4902–4915, Aug. 2010. doi: 10.1118/1.3480985.

Sembay, S., Guainazzi, M., Plucinsky, P., et al. Defining High-Energy Calibration Standards: IACHEC (International Astronomical Consortium for High-Energy Calibration). pp. 593–594, Bologna (Italy), 2010. doi: 10.1063/1.3475350.

Shepp, L. A., and Vardi, Y. Maximum Likelihood Reconstruction for Emission Tomography. *IEEE Transactions on Medical Imaging*, 1(2):113–122, Oct. 1982. doi: 10.1109/TMI.1982.4307558.

Šimko, T., Heinrich, L., Hirvonsalo, H., Kousidis, D., and Rodríguez, D. REANA: A System for Reusable Research Data Analyses. *EPJ Web of Conferences*, 214:06034, 2019. doi: 10.1051/epjconf/201921406034.

Smith, M., Pommranz, C., Heinitz, C., and Stuhlinger, M. XMM-CCF-REL-382 – Update of the CORRAREA Empirical EPIC Effective Area Correction, July 2021. URL https://xmmweb.esac.esa.int/docs/documents/CAL-SRN-0382-1-1.pdf.

Stodden, V., McNutt, M., Bailey, D. H., et al. Enhancing reproducibility for computational methods. *Science*, 354(6317):1240–1241, Dec. 2016. doi: 10.1126/science.aah6168.

Strüder, L., Briel, U., Dennerl, K., et al. The European Photon Imaging Camera on XMM-Newton: The pn-CCD camera. *Astronomy & Astrophysics*, 365(1):L18–L26, Jan. 2001. doi: 10.1051/0004-6361:20000066.

Stuhlinger, M., Smith, M., Guainazzi, M., et al. XMM-SOC-CAL-TN-0052 – Status of XMM-Newton instrument cross-calibration with SASv10.0, Dec. 2010. URL https://xmmweb.esac.esa.int/docs/documents/CAL-TN-0052.pdf.

Sung, H., Ferlay, J., Siegel, R. L., et al. Global Cancer Statistics 2020: GLOBOCAN Estimates of Incidence and Mortality Worldwide for 36 Cancers in 185 Countries. *CA: A Cancer Journal for Clinicians*, 71(3):209–249, May 2021. doi: 10.3322/caac.21660.

Sunyaev, R., Arefiev, V., Babyshkin, V., et al. SRG X-ray orbital observatory: Its telescopes and first scientific results. *Astronomy & Astrophysics*, 656: A132, Dec. 2021. doi: 10.1051/0004-6361/202141179.

Tai, Y.-C., Wu, H., and Janecek, M. Initial study of an asymmetric PET system dedicated to breast cancer imaging. *IEEE Transactions on Nuclear Science*, 53(1):121–126, Feb. 2006. doi: 10.1109/TNS.2006.869853.

Tai, Y.-C., Wu, H., Pal, D., and O'Sullivan, J. A. Virtual-Pinhole PET. *Journal of Nuclear Medicine*, 49(3):471–479, Mar. 2008. doi: 10.2967/jnumed.107.043034.

Tenzer, C., Warth, G., Kendziorra, E., and Santangelo, A. Geant4 simulation studies of the eROSITA detector background. p. 77420Y, San Diego, California, USA, July 2010. doi: 10.1117/12.857087.

Tenzer, J.-C. *Monte-Carlo background studies for space-based detectors in X-ray astronomy*. PhD thesis, Tübingen, 2008.

The Astropy Collaboration, Robitaille, T. P., Tollerud, E. J., et al. Astropy: A community Python package for astronomy. *Astronomy & Astrophysics*, 558: A33, Oct. 2013. doi: 10.1051/0004-6361/201322068.

The Astropy Collaboration, Price-Whelan, A. M., Sipőcz, B. M., et al. The Astropy Project: Building an Open-science Project and Status of the v2.0 Core Package. *The Astronomical Journal*, 156(3):123, Aug. 2018. doi: 10.3847/1538-3881/aabc4f.

Thomas, S. R., Owens, M. J., and Lockwood, M. The 22-Year Hale Cycle in Cosmic Ray Flux – Evidence for Direct Heliospheric Modulation. *Solar Physics*, 289(1):407–421, Jan. 2014. doi: 10.1007/s11207-013-0341-5.

Thompson, A., Attwood, D., Gullikson, E., et al. *X-ray Data Booklet*. Lawrence Berkeley National Laboratory, University of California, 3 edition, 2009.

Townsend, D. W. Positron Emission Tomography/Computed Tomography. *Seminars in Nuclear Medicine*, 38(3):152–166, May 2008. doi: 10.1053/j.semnuclmed.2008.01.003.

Turner, M. J. L., Abbey, A., Arnaud, M., et al. The European Photon Imaging Camera on XMM-Newton: The MOS cameras. *Astronomy & Astrophysics*, 365(1):L27–L35, Jan. 2001. doi: 10.1051/0004-6361:20000087.

Tylka, A., Adams, J., Boberg, P., et al. CREME96: A Revision of the Cosmic Ray Effects on Micro-Electronics Code. *IEEE Transactions on Nuclear Science*, 44(6):2150–2160, Dec. 1997. doi: 10.1109/23.659030.

Umutlu, L., and Herrmann, K., editors. *PET/MR Imaging: Current and Emerging Applications*. Springer International Publishing, Cham, 2018. ISBN 978-3-319-69640-9 978-3-319-69641-6. doi: 10.1007/978-3-319-69641-6. URL http://link.springer.com/10.1007/978-3-319-69641-6.

Vandenberghe, S., and Marsden, P. K. PET-MRI: a review of challenges and solutions in the development of integrated multimodality imaging. *Physics in Medicine and Biology*, 60(4):R115–R154, Feb. 2015. doi: 10.1088/0031-9155/60/4/R115.

Vandenbroucke, A., Innes, D., and Levin, C. S. Effects of external shielding on the performance of a 1 mm^3 resolution breast PET camera. In *IEEE*

Nuclear Science Symposuim & Medical Imaging Conference, pp. 3644–3648, Knoxville, TN, Oct. 2010. IEEE. doi: 10.1109/NSSMIC.2010.5874492.

Veronesi, U., De Cicco, C., Galimberti, V., et al. A comparative study on the value of FDG-PET and sentinel node biopsy to identify occult axillary metastases. *Annals of Oncology*, 18(3):473–478, Mar. 2007. doi: 10.1093/annonc/mdl425.

Wang, Y., Chiu, E., Rosenberg, J., and Gambhir, S. S. Standardized Uptake Value Atlas: Characterization of Physiological 2-Deoxy-2-[18F]fluoro-d-glucose Uptake in Normal Tissues. *Molecular Imaging and Biology*, 9(2): 83–90, Feb. 2007. doi: 10.1007/s11307-006-0075-y.

Watson, M. G., Auguères, J.-L., Ballet, J., et al. The XMM-Newton Serendipitous Survey: I. The role of XMM-Newton Survey Science Centre. *Astronomy & Astrophysics*, 365(1):L51–L59, Jan. 2001. doi: 10.1051/0004-6361:20000067.

Webb, N. A., Coriat, M., Traulsen, I., et al. The *XMM-Newton* serendipitous survey: IX. The fourth *XMM-Newton* serendipitous source catalogue. *Astronomy & Astrophysics*, 641:A136, Sept. 2020. doi: 10.1051/0004-6361/201937353.

Wehrl, H. F., Sauter, A. W., Divine, M. R., and Pichler, B. J. Combined PET/MR: A Technology Becomes Mature. *Journal of Nuclear Medicine*, 56 (2):165–168, Feb. 2015. doi: 10.2967/jnumed.114.150318.

Weisskopf, M. C., Brinkman, B., Canizares, C., et al. An Overview of the Performance and Scientific Results from the *Chandra X-Ray Observatory*. *Publications of the Astronomical Society of the Pacific*, 114(791):1–24, Jan. 2002. doi: 10.1086/338108.

Won, J. Y., Park, H., Lee, S., et al. Development and Initial Results of a Brain PET Insert for Simultaneous 7-Tesla PET/MRI Using an FPGA-Only Signal Digitization Method. *IEEE Transactions on Medical Imaging*, 40(6): 1579–1590, June 2021. doi: 10.1109/TMI.2021.3062066.

Wu, H., Pal, D., Song, T. Y., O'Sullivan, J. A., and Tai, Y.-C. Micro Insert: A Prototype Full-Ring PET Device for Improving the Image Resolution of a Small-Animal PET Scanner. *Journal of Nuclear Medicine*, 49(10):1668–1676, Oct. 2008a. doi: 10.2967/jnumed.107.050070.

Wu, H., Song, T. Y., Pal, D., et al. A high resolution PET insert system for clinical PET/CT scanners. In *2008 IEEE Nuclear Science Symposium Conference Record*, pp. 5442–5444, Dresden, Germany, Oct. 2008b. IEEE. doi: 10.1109/NSSMIC.2008.4774485.

Zeng, T., Zheng, J., Xia, X., et al. Design and system evaluation of a dual-panel portable PET (DP-PET). *EJNMMI Physics*, 8(1):47, Dec. 2021. doi: 10.1186/s40658-021-00392-5.

Zhang, J., Olcott, P. D., Chinn, G., Foudray, A. M. K., and Levin, C. S. Study of the performance of a novel 1mm resolution dual-panel PET camera design dedicated to breast cancer imaging using Monte Carlo simulation: Monte Carlo simulation study on dual-panel PET camera. *Medical Physics*, 34(2): 689–702, Jan. 2007. doi: 10.1118/1.2409480.

Zhang-Yin, J. State of the Art in 2022 PET/CT in Breast Cancer: A Review. *Journal of Clinical Medicine*, 12(3):968, Jan. 2023. doi: 10.3390/jcm12030968.

Zhao, X.-Y., Wang, H.-Y., Wu, F., et al. A geometric factor calculation method based on the isotropic flux assumption. *Chinese Physics C*, 37(12):126201, Dec. 2013. doi: 10.1088/1674-1137/37/12/126201.

Zhou, J., and Qi, J. Theoretical analysis and simulation study of a high-resolution zoom-in PET system. *Physics in Medicine and Biology*, 54(17): 5193–5208, Sept. 2009. doi: 10.1088/0031-9155/54/17/008.

Bibliography

Acknowledgements

This work is supported by the Bundesministerium für Wirtschaft und Klimaschutz through the Deutsches Zentrum für Luft- und Raumfahrt e.V. (DLR) under the grant numbers 50 QR 2102, 50 QR 1602, and 50 OX 2202.

This work is based on observations obtained with XMM-Newton, an ESA science mission with instruments and contributions directly funded by ESA Member States and NASA. This research has made use of data obtained from the 3XMM and 4XMM XMM-Newton Serendipitous Source Catalogs compiled by the 10 institutes of the XMM-Newton Survey Science Centre selected by ESA.

This work is based on data from eROSITA, the soft X-ray instrument aboard SRG, a joint Russian-German science mission supported by the Russian Space Agency (Roskosmos), in the interests of the Russian Academy of Sciences represented by its Space Research Institute (IKI), and the Deutsches Zentrum für Luft- und Raumfahrt (DLR). The SRG spacecraft was built by Lavochkin Association (NPOL) and its subcontractors, and is operated by NPOL with support from the Max Planck Institute for Extraterrestrial Physics (MPE).
The development and construction of the eROSITA X-ray instrument was led by MPE, with contributions from the Dr. Karl Remeis Observatory Bamberg & ECAP (FAU Erlangen-Nuernberg), the University of Hamburg Observatory, the Leibniz Institute for Astrophysics Potsdam (AIP), and the Institute for Astronomy and Astrophysics of the University of Tübingen, with the support of DLR and the Max Planck Society. The Argelander Institute for Astronomy of the University of Bonn and the Ludwig Maximilians Universität Munich also participated in the science preparation for eROSITA.

Furthermore, I acknowledge support by the High Performance and Cloud Computing Group at the Zentrum für Datenverarbeitung of the University of Tübingen, the state of Baden-Württemberg through bwHPC and the German Research Foundation (DFG) through grant no. INST 37/935-1 FUGG.

Interdisciplinary science is of vital importance today, and I feel privileged to have had the opportunity to work simultaneously in the fields of astrophysics, medical physics, computational physics, and calibration as part of this thesis. I am aware that such a concept is far from common in today's scientific system, so I am grateful to everyone who supported this work and for all the contributions along the way. Thank you for making this research a wonderful journey. In particular, I would like to express my gratitude and appreciation to the following people:

- Prof. Dott. Andrea Santangelo and Prof. Dr. Bernd Pichler for providing the unique opportunity to work on interdisciplinary research projects as part of a collaboration between both institutes. Thank you for your supervision, your advice, for the continued support, and for the review of this thesis.
- PD Dr. Christoph Schäfer for the review of this thesis.
- Prof. Dr. Magdalena Rafecas for the review of this thesis.
- Dr. Chris Tenzer for your mentoring, support, proofreading, your approachability in case of questions, for managing and supporting the collaboration, and for being a constant source of motivation. Thank you for the productive and fun times at the institute and at several conferences and meetings that we visited together in the past years.
- Dr. Fabian Schmidt for supervising the PET related parts of this work. Thank you for your support, proofreading, suggestions and ideas, and the great times at several conferences.
- Dr. Sebastian Diebold for the productive discussions, for your deep insights into particle physics and simulations, for your openness to all kinds of questions, and for the occasional tennis match.
- Dr. Julia Mannheim for your suggestions and guidance at the regular WSIC detector physics group meetings and Obergurgl retreats, and for proofreading.
- Dr. Michael Smith for the fruitful collaboration on the CORRAREA project and the productive meetings at ESAC.
- Dr. Michael Freyberg for your support and encouragement in the regular background/foreground meetings.

- Dr. Konrad Dennerl for providing adapted versions of the `pattern` and `energy` eSASS routines that can be used with simulation data as part of the eROSITA digitizer and data analysis workflow, and for suggesting the electron charge cloud model.
- Dr. Emanuele Perinati for fruitful discussions about the eROSITA background simulations and for providing the proton input spectrum.
- Leon Lober for source screening and the definition of spectral models for recent observations.
- Tim Wildfang for supporting the transformation of the eROSITA CAD model into a GDML model usable for Geant4 simulations.
- Benjamin Mican and Christian Rohé at MPE for providing the final eROSITA CAD model together with the corresponding material mapping and manufacturer specifications of the materials.
- Michael Yeung for providing the most recent version of the cleaned eROSITA FWC data sets.
- Dr. David Sarrut and the OpenGATE community for creating one of the most welcoming and encouraging FLOSS communities I have experienced so far.
- the "Vintage A112" office members Inga, Fabian, and Heiko for the productive and especially the fun times in Office A112.
- all of the members of the IAAT for making the institute a friendly and memorable place to work.
- all of the members of the WSIC and especially the detector physics group who, despite the spatial distance and across different research fields, have always made me feel welcome and part of the group.
- Camill Kaipf for your insights into the use of automated computational workflow systems in bioinformatics and the (kind of) weekly lunch.
- Johanna Pommranz for language proofreading of the thesis.

This work would not have been possible without the continuous support and understanding of my friends, family, and especially my beloved wife Sabrina. *Vielen Dank – für alles!*